QC
1
.U56
V.64A
no.4

Volume 64A
Number 4
July–Aug. 1960

THE UNIVERSITY
OF MICHIGAN
AUG 10 1960
LIBRARY

Journal of Research

of the

NATIONAL BUREAU OF STANDARDS

A. PHYSICS AND CHEMISTRY

Journal of Research

of the

National Bureau of Standards

A. Physics and Chemistry

JULY–AUG. • 1960

VOLUME • 64A

NUMBER • 4

Editor: U. Fano

Associate Editors: L. M. Kushner
J. M. Richardson

Publication dates:
Feb. 1, Apr. 1, June 1, Aug. 1, Oct. 1, Dec. 1, 1960.

JOURNAL OF RESEARCH

The National Bureau of Standards Journal of Research reports research and development in the fields of activity shown at right. Also included from time to time are survey articles on topics closely related to the Bureau's scientific and technical programs.

The Journal is published in four separate sections as follows:

A. Physics and Chemistry

Contains papers of interest primarily to scientists working in these fields. Issued six times a year. Annual subscription: domestic, $4.00; foreign, $4.75.

B. Mathematics and Mathematical Physics

Presents studies and compilations designed mainly for the mathematician and the theoretical physicist. Issued quarterly. Annual subscription: domestic, $2.25; foreign, $2.75.

C. Engineering and Instrumentation

Reports research and development results of interest chiefly to the engineer and the applied scientist. Issued quarterly. Annual subscription: domestic, $2.25; foreign, $2.75.

D. Radio Propagation

Reports work in radio propagation, upper atmospheric physics, and communications. Issued six times a year. Annual subscription: domestic, $4.00; foreign, $4.75.

U.S. DEPARTMENT OF COMMERCE
Frederick H. Mueller, Secretary

NATIONAL BUREAU OF STANDARDS
A. V. Astin, Director

Functions and Activities

The functions of the National Bureau of Standards are set forth in the Act of Congress, March 3, 1901, as amended. These include the development and maintenance of the national standards of measurement and the provision of means and methods for making measurements consistent with these standards; the determination of physical constants and properties of materials; the development of methods and instruments for testing materials, devices, and structures; advisory services to government agencies on scientific and technical problems; invention and development of devices to serve special needs of the Government; and the development of standard practices, codes, and specifications. The work includes basic and applied research, development, engineering, instrumentation, testing, evaluation, calibration services, and various consultation and information services. The Bureau also serves as the Federal technical research center in a number of specialized fields. The scope of activities of the National Bureau of Standards is suggested in the following listing of the divisions and sections engaged in technical work.

Washington, D.C.

Electricity and Electronics. Resistance and Reactance. Electron Devices. Electrical Instruments. Magnetic Measurements. Dielectrics. Engineering Electronics. Electronic Instrumentation. Electrochemistry.

Optics and Metrology. Photometry and Colorimetry. Optical Instruments. Photographic Technology. Length. Engineering Metrology.

Heat. Temperature Physics. Heat Measurement. Cryogenic Physics. Rheology. Molecular Kinetics. Free Radicals Research. Equation of State. Statistical Physics. Molecular Spectroscopy.

Radiation Physics. Neutron Physics. Radiation Theory. Radioactivity. X-ray. High Energy Radiation. Nucleonic Instrumentation. Radiological Equipment.

Chemistry. Organic Coatings. Surface Chemistry. Organic Chemistry. Analytical Chemistry. Inorganic Chemistry. Electrodeposition. Molecular Structure and Properties of Gases. Physical Chemistry. Thermochemistry. Spectrochemistry. Pure Substances.

Mechanics. Sound. Mechanical Instruments. Fluid Mechanics. Engineering Mechanics. Mass and Scale. Capacity, Density, and Fluid Meters. Combustion Controls.

Organic and Fibrous Materials. Rubber. Textiles. Paper. Leather. Testing and Specifications. Polymer Structure. Plastics. Dental Research.

Metallurgy. Thermal Metallurgy. Chemical Metallurgy. Mechanical Metallurgy. Corrosion. Metal Physics.

Mineral Products. Engineering Ceramics. Glass. Refractories. Enameled Metals. Constitution and Microstructure.

Building Technology. Structural Engineering. Fire Protection. Air Conditioning, Heating, and Refrigeration. Floor, Roof, and Wall Coverings. Codes and Safety Standards. Heat Transfer. Concreting Materials.

Applied Mathematics. Numerical Analysis. Computation. Statistical Engineering. Mathematical Physics.

Data Processing Systems. SEAC Engineering Group. Components and Techniques. Digital Circuitry. Digital Systems. Analog Systems. Applications Engineering.

Atomic Physics. Spectroscopy. Radiometry. Mass Spectrometry. Solid State Physics. Electron Physics. Atomic Physics.

Office of Basic Instrumentation. • Office of Weights and Measures.

Boulder, Colorado

Cryogenic Engineering. Cryogenic Equipment. Cryogenic Processes. Properties of Materials. Gas Liquefaction.

Radio Propagation Physics. Upper Atmosphere Research. Ionosphere Research. Regular Prediction Services. Sun-Earth Relationships. VHF Research. Radio Warning Services. Airglow and Aurora. Radio Astronomy and Arctic Propagation.

Radio Propagation Engineering. Data Reduction Instrumentation. Radio Noise. Tropospheric Measurements. Tropospheric Analysis. Propagation-Terrain Effects. Radio-Meteorology. Lower Atmosphere Physics.

Radio Standards. High-Frequency Electrical Standards. Radio Broadcast Service. Radio and Microwave Materials. Atomic Frequency and Time Standards. Electronic Calibration Center. Microwave Circuit Standards.

Radio Communication and Systems. Low Frequency and Very Low Frequency Research. High Frequency and Very High Frequency Research. Modulation Systems. Antenna Research. Navigation Systems. Systems Analysis. Field Operations.

Order all publications from the Superintendent of Documents,
U.S. Government Printing Office, Washington 25, D.C.

Use of funds for printing this publication approved by the Director of the Bureau of the Budget (June 24, 1958).

DEPOSITED BY THE
UNITED STATES OF AMERICA

JOURNAL OF RESEARCH of the National Bureau of Standards—A. Physics and Chemistry
Vol. 64A, No. 4, July–August 1960

Gamma Irradiation of Hexafluorobenzene[1]

R. E. Florin, L. A. Wall, and D. W. Brown

(March 27, 1960)

Mixtures of hexafluorobenzene and benzene were irradiated in liquid phase by means of a Co^{60} gamma source at 20° and at 218° C. Perfluoroheptane and various binary mixtures involving perfluoroheptane, hexafluorobenzene, benzene, and cyclohexane were also irradiated at 20° C. Hexafluorobenzene resembled benzene very closely in its behavior upon radiolysis. Generally the fluorocarbon-hydrocarbon mixtures evolved much more SiF_4 (indicating the formation of HF, which reacts with the glass vessel) than the pure fluorocarbon components. The polymer from hexafluorobenzene-benzene mixtures was probably rich in cyclohexadiene and cyclohexene units, resembling that from pure benzene, and its composition ratio exhibited a strong "alternating" tendency. The results are discussed in terms of free-radical and excited-state mechanisms. At 218° C hexafluorobenzene and also its mixtures with benzene showed qualitative differences from their behavior at 20° C, although the G values for SiF_4 and polymer remained moderate.

1. Introduction

Fully fluorinated aromatic compounds have only recently become accessible. Because of their combination of C—F bonds and aromatic resonance structure they have attracted interest as possible heat-resistant materials. It has been observed that certain polyphenyls $(C_6F_4)_x$ are stable at high temperatures [1][2] and that the mass spectrum of these compounds shows relatively little fragmentation under electron impact [2]. The latter observation is reminiscent of benzene itself, and contrasts strongly with the extensive fragmentation of saturated fluorocarbons in the mass spectrometer [3, 4].

Since electrons are an important intermediate in the action of ionizing radiation, it can be expected that hexafluorobenzene derivatives, like their hydrocarbon analogs, will be relatively resistant to radiation, and may surpass them under some combinations of high temperature and radiation. Any improvement in materials for use under such conditions would be desirable.

The radiation chemistry of fluorocarbons has been studied very little until very recently, except for a few polymers and monomers [5 to 14]. Halogen compounds, including a few monofluoro derivatives, have been investigated and generally have been found to exhibit a very high sensitivity to radiation [15]. Benzene has been studied very extensively, both because of its low sensitivity and the possibility that it can exhibit a "protective" effect in mixtures. Likewise, a few higher aromatic hydrocarbons have been studied [16 to 18]. In radiation chemical studies in general, atom and free-radical mechanisms have been fairly well accepted [19], though seldom unequivocally proven. Besides the great wealth of data on hydrocarbon radical reactions [20], there have recently been a number of studies on reactions of aliphatic fluorocarbon radical [21 to 29].

The present situation is that fluorocarbons seem more resistant than hydrocarbons to heat, and also aromatic compounds more resistant than aliphatic. Under ionizing radiation, aliphatic hydrocarbons give off relatively large amounts of hydrogen; aromatic hydrocarbons lose very little hydrogen, but form polymers in moderate yield. Aliphatic fluorocarbons suffer breaks in the carbon chain and lose slight to moderate amounts of fluorine in ionic form [7 to 9]. The aromatic hydrocarbons biphenyl and terphenyl are resistant enough to radiation at high temperatures to be of some interest as reactor coolants [18]. The order of magnitude of the radiation yield, G, in molecules per 100 ev absorbed, is indicated in table 1 for the several processes. In this paper, we report some observations on the irradiation of C_6F_6, C_7F_{16}, and their mixtures with other materials.

TABLE 1. *Radiation yields for several processes*

Process	G value		
	C_nH_{2n+2}	C_6H_6	C_nF_{2n+2}
C—C scission	<1	0.02	1.7
H_2 or F_2	5	.04	.1
Polymer or crosslinks	5	1	0

2. Experimental Procedure

In general, samples were prepared on a vacuum line and irradiated to doses of about 100 to 300 megaroentgens (Mr). Products volatile at —80° and 25° C were analyzed by mass spectrometer. Nonvolatile residues were isolated by distillation of the liquid and characterized by infrared spectra and elemental analysis. The hexafluorobenzene used was from a specially purified center cut of material synthesized in our laboratory [30] and subjected to repeated fractional freezing. Its constants were bp=80.5° C/759 mm, n_{23}^{D}=1.3781. The benzene used was the commercial product (c.p.), not further purified. The perfluoroheptane used was the product of Minnesota Mining & Manufacturing Co. and was used as received. The cyclohexane used was an NBS standard sample.

[1] This work was sponsored by the Aeronautical Research Laboratory, Wright Air Development Center, U.S. Air Force.
[2] Figures in brackets indicate the literature references at the end of this paper.

For the irradiations at room temperature, the liquids were dried several weeks over P_2O_5 in break-seal tubes and distilled on the vacuum line into weighing bulbs of 30-ml capacity. These bulbs were fitted with standard taper joints and Hoke bellows valves connected via copper or Kovar glass seals. Samples were made up by distilling *in vacuo* into irradiation vessels of several kinds, then degassing, cooling with liquid nitrogen, opening for about 1 minute to a measured pressure of a few centimeters of argon, and sealing or closing off. Weights of components of the mixture, obtained by difference, were checked against the total weight of the radiation vessel. Discrepancies of a few milligrams were common, probably because of absorption of the volatile liquids in stopcock grease.

The radiation vessels for use at 218° C were 3-mm thick-walled glass tubes. At room temperature nickel capsules of about 10- to 15-ml capacity were used. They were silver-soldered to 1.5-mm x 40-mm nickel tubes and then through 4.7-mm o.d. Kovar seals to long 3-mm o.d. Pyrex end sections which were designed for opening into the mass spectrometer inlet system. In one irradiation experiment under a high pressure of hydrogen, a third type of radiation vessel was used, consisting of a Monel bomb, 12-mm o.d. x 6-mm i.d. x 300 mm in length, closed by a Hoke bellows valve. The simple capillary tube had the advantages of strength and small size but had a large potentially reactive wall surface and also could not be opened for analysis without some exposure to air. The composite capsules were mostly corrosion resistant, vacuumtight, and easily fitted to the mass spectrometer but were very fragile after use. The existence of a partial internal glass surface had some advantages as well as drawbacks. Any HF formed was converted to the easily measured SiF_4, while any reactive fluorocarbon intermediates of short life probably underwent further reaction in the liquid system before they could diffuse to the glass surface. It was noticed that corrosion was especially severe in the special graded glass of the Kovar seal. The Monel bomb vessel had the advantage of strength and all-metal construction but probably was subject to slow leaks over long periods. It is uncertain whether it would have remained tight with the valve exposed to high temperatures.

The sample tubes to be irradiated were placed in a can and lowered into the uniform central region of a 2,000-curie cobalt-60 source consisting of upright rods arranged in a circle and shielded by water. Heat, when needed, was provided within the can by a thermostat furnace capable of reaching 500° C. Electrical leads were carried through a pipe leading to the surface of the water. The exposure dose rate was determined by the ferrous sulfate dosimeter using $G=15.5$, and by a time correction for decay of the cobalt. The dose rate was 0.576 Mr/hr on December 11, 1956. The variations with geometry (mainly vertical extension) and container wall shielding were significant only for the Monel bomb containers. The absorbed dose was calculated with the aid of best values for the elements, derived from ref [31]. Typical factors in ev $g^{-1}Mr^{-1}\times10^{-20}$ were: C_nH_{2n}, 0.623; C_6H_6, 0.589; C_nF_{2n}, 0.526; and C_6F_6, 0.530.

After irradiation, which required several weeks, the samples were brought to the mass spectrometer whenever the design of the vessel was appropriate, and mass spectra taken with contents at −80° and +25° C. Where the container was not adapted for this, the contents were first transferred on an auxiliary vacuum line. Many of the Kovar-seal containers in which hydrocarbon-fluorocarbon mixtures were exposed to high doses were broken during irradiation or subsequent handling because of corrosion at the glass-metal seals. To calculate the mass spectrometer results for gaseous products, reliance was placed upon the argon introduced as an internal standard. For liquid products, the examination at 25° C yielded only relative values, distorted by fractionation effects. The opened tubes were emptied by suction, and the liquid content was frozen and sublimed at reduced pressure to isolate the nonvolatile residue. The empty tubes were rinsed with benzene repeatedly, yielding small additional amounts of residue. The residues were analyzed [3] for C, H, and F, and infrared spectra [4] were also taken in films and Nujol mulls.

In the mass spectrometric procedure, bulbs containing a large liquid sample were connected to the inlet system of the mass spectrometer before breaking the seal. Analyses of volatiles were then made with the sample bulb first cooled to −80° C and then warmed to 25° C. The analysis of material volatile at −80° C should give a reasonably accurate estimate of gaseous products for all samples in which the liquid was completely frozen at that temperature. This includes all samples containing hexafluorobenzene, benzene, and cyclohexane only. However, perfluoroheptane, although the reported freezing point is −55°, is often still liquid at −80° C and therefore can hold large quantities of gases in solution. For samples containing perfluoroheptane, therefore, the mass spectrometric analyses at −80° C may seriously underestimate the yields of gases. This error will be greatest for the samples rich in perfluoroheptane and for the higher boiling gases such as CF_4 (bp −128° C), SiF_4 (subl −95° C), C_2F_6 (bp −76.3° C), and CF_3H (bp −84.4° C).

For similar reasons, the volatiles at 25° C have merely qualitative interest. Products less volatile than the starting material will appear in greatly reduced concentration. The results will be especially uncertain for products of intermediate volatility, which are depleted in supply because of the previous analysis at −80° C, but favored by high relative volatility at 25° C.

Polymeric residues in irradiated samples were analyzed by combustion methods. In many instances, the sum of C, H, and F is low by several percent. The deficit may be attributed either to poor accuracy of fluorine analyses or to oxygen absorbed during the period between opening of samples and analysis. The polymeric product from irradi-

[3] Combustion analyses were by E. R. Deardorff, NBS.
[4] Spectra were obtained by John J. Comeford and W. J. Pummer, NBS.

ated benzene is highly reactive with oxygen [16], and the related material from fluorocarbons could react not only with oxygen but with moisture as well. These reactions should have been minimized in the present work by the fact that the longest storage of samples was in the crystalline or glassy form. It will therefore be assumed in calculations that the total deficit is due to low fluorine analyses.

A nearly self-consistent account can be given of the composition of C_6F_6–C_6H_6 residues by postulating combination of molecules and elimination of HF. The calculations will be deferred until the discussion of these mixtures. In most other mixtures, the polymer analysis is consistent with several possibilities, but extremes can be calculated.

The metallic interior surfaces of the containers appeared unchanged after irradiation. A monomolecular layer of metal fluoride may possibly have been present, but this could not contribute important errors at the doses used in this work.

All of the systems containing some fluorocarbon and some glass produced SiF_4.

In the capillary tubes containing C_6F_6 at 218° C, this product may have been formed by direct reaction of excited molecules with the wall. In the composite metal bulb reactors, the long diffusion path makes it very unlikely that short-lived intermediates of any kind could reach the glass parts in significant quantity. Among possible agents attacking the glass are F_2, HF, and perhaps especially reactive fluorocarbon molecules.

Radicals or fluorocarbon molecules attacking glass should produce CO or CO_2, as well as SiF_4:

$$4CF_3\cdot + 3SiO_2 \longrightarrow 3SiF_4 + 2CO + 2CO_2. \quad (1)$$

The steps would involve gradual replacement of O by F in the glass lattice until a volatile SiF_4 molecule is produced:

$$-\overset{|}{\underset{|}{C}}-F + -\overset{|}{\underset{|}{Si}}-O- \longrightarrow -\overset{|}{\underset{|}{C}}-O- + -\overset{|}{\underset{|}{Si}}-F. \quad (2)$$

Reactions not producing oxides of carbon are also possible:

$$C_2F_5\cdot + -\overset{|}{\underset{|}{Si}}-O- \longrightarrow C_2F_4 + -\overset{|}{\underset{|}{Si}}-F + -O-. \quad (3)$$

The reaction of F_2 with glass would apparently produce oxygen as a byproduct:

$$2F_2 + SiO_2 \longrightarrow SiF_4 + O_2. \quad (4)$$

This oxygen could react with radicals to form oxides of carbon or oxygenated fluorocarbon compounds. Despite the known slowness of the glass-fluorine reaction, it appears likely that it should occur in appreciable amounts over the long radiation times. Even in view of the uncertainties implied by the above reactions, it seems reasonable to consider each SiF_4 molecule as derived from 4 HF in mixtures with hydrocarbons, and from $2F_2$ in pure fluorocarbon systems, unless equivalent amounts of CO or CO_2 are observed. The CO and CO_2 were usually observed only in very small amounts relative to SiF_4. The reaction involving HF should produce water as a by-product:

$$4HF + SiO_2 \longrightarrow 2H_2O + SiF_4. \quad (5)$$

Conversion of HF to SiF_4 is presumed to be nearly complete, although some fixation in the form of alkali fluosilicates is conceivable. The above reactions show that the later stages of the irradiation may be complicated by gradually increasing amounts of oxygen and water.

Most of the materials were irradiated only at room temperature, but hexafluorobenzene and the C_6F_6–C_6H_6 mixtures were irradiated at both 20° and 218° C.

3. Results and Discussion

3.1. Hexafluorobenzene

From pure hexafluorobenzene the observed products were a nonvolatile residue (the so-called "polymer," table 2) and SiF_4 (tables 3 and 4) with a little CO and CO_2, which may have been derived from fluorine atoms or molecules or unstable fluorocarbon intermediates. At 20° the release of fluorine was almost negligible, $G(SiF_4)=0.01$, but at 218° it became 0.21 molecules/100 ev. The yield of polymer was about the same at both temperatures within the large experimental error at 218° and was about twice that from benzene. G(polymer)=2.01 at 20°, 1.3 ± 0.5 at 218°. The character of the polymer changed greatly with temperature, being a light yellow, low-melting ($<100°$) glass at 20°, and a nearly black finely granular precipitate at 218°. The elemental analysis of the 20° polymer was near

TABLE 2. *Polymer from irradiated hexafluorobenzene and benzene at 20° C* [a]

C_6F_6 in feed, mole fraction	1.00	0.667	0.114
C_6F_6 in polymer, mole fraction	0.922	0.527	0.422
Polymer weight, g	.7051	.6822	.860
%C	40.2	55.3	61.2
%H	[b] 0.3	2.	2.7
%F [c]	55.	38.4	31.2
Base moles	.00394	.00524	.00731
HF moles lost per mole	0	.230	.296

[a] Exposure dose 275 Mr.
[b] Presumed absent from fresh polymer.
[c] For further calculations, F is taken as 100—C—H.

TABLE 3. *Radiation yields from hexafluorobenzene and benzene at 20° C* [a]

C_6F_6 in feed, mole fraction	1.00	0.667	0.114	0[e]
C_6F_6 in polymer, mole fraction	0.922	0.527	0.422	0
G(polymer)[b]	2.01	2.73	2.79	[c] .93
G(C_6F_6 units)	1.85	1.44	1.18	
G(HF lost)[d]		0.628	.826	
$4G(SiF_4)$[e]	.045	Present	1.334	
$2G(H_2)$	.0014	Lost	.126	[c] .088

[a] Exposure dose 275 Mr; dose factors for C_6H_6, 0.589×10^{20} ev/g-Mr; for C_6F_6, 0.530×10^{20} ev/g-Mr.
[b] C_6H_6 and C_6F_6 units.
[c] From Gordon et al., ref. [17].
[d] From polymer analysis.
[e] From gas analysis.

TABLE 4. *Radiation yields from hexafluorobenzene and benzene at 218° C* [a]

C_6F_6 mole fraction	1.00	0.256	0
$4G(SiF_4)$	0.84	0.105	0
$G(CO)$	.054	.0063	0
$G(CO_2)$	.022	.0048	0
$G(H_2)$	0	.0075	.0022
$G(C_2H_2)$	0	.0048	.017
G(polymer)[b]	1.3±0.5	1±0.5	1.3

[a] Exposure dose 350 Mr. [b] C_6H_6 and C_6F_6 units.

that of the parent compound (table 2). The deficit, 100—C—F—H, and H content may represent contaminations in handling, difficulties of quantitative fluorine determination, or in the case of the deficit possibly oxygen absorption during storage [16, 17]. The quantity of the 218° C polymer was not sufficient for analysis.

Infrared spectra of the polymer and a synthetic perfluoropolyphenyl are compared in figure 1. Both have strong peaks at 6.6 and at 10.15 μ, but the radiation polymer has a broader absorption generally and numerous additional peaks at 5.7, 7.5, 8.8, 12.8, 13.3, and 13.7 μ. Most of the absorption bands are consistent with a C—F bond adjacent to either an aromatic or an olefinic carbon atom. The infrared absorption offers no reliable basis for a distinction.

There appear to be no small fluorocarbon molecules analogous to the C_2H_2 and CH_4 found with benzene. The similarity of C_6F_6 to C_6H_6 was striking—very low yields of volatile products, and a moderate yield of polymer; G(polymer)=2.01 for C_6F_6, and 0.93 for C_6H_6.

It is recognized that nearly the total effect of ionizing radiation on organic matter is due to the secondary electrons. Their first effect is to form positive ions which can be important intermediates in the gas phase [32] but are more likely to recapture electrons in liquid phase and form neutral radicals and atoms. Although the number of excited molecules (singlet and triplet) may considerably exceed the number of unexcited radicals formed [19], it is often possible to restrict attention to atoms and radicals as the effective chemical intermediates. Feng [13, 14] has briefly considered ionic intermediates, pointing out that atom formation is

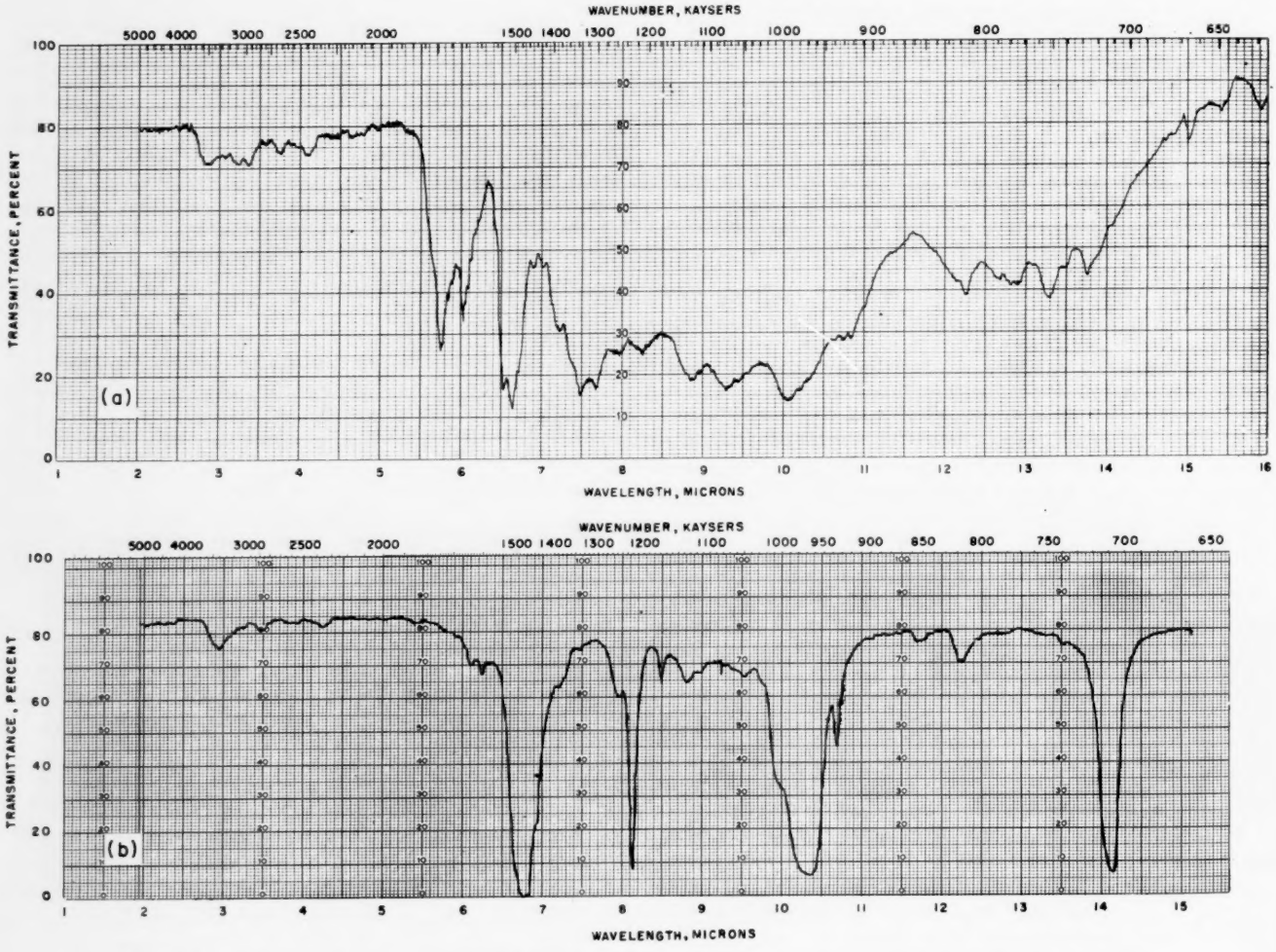

FIGURE 1. *Infrared absorption spectra of hexafluorobenzene radiation polymer and of perfluoropolyphenyl.*

a. C_6F_6 radiation polymer. b. I-$(C_6F_4)_{11}$-I.

energetically less favorable for carbon-fluorine than for other carbon-halogen bonds, and other investigators [16, 17] have introduced excited states in the discussion of the radiolysis of benzene.

The radiolysis of hexafluorobenzene offers few novelties beyond its hydrocarbon analog; both the free-radical mechanisms and excited-state mechanisms [16, 17] seem admissible with little choice. The outlines of a free-radical mechanism, following Burton's [16] treatment of C_6H_6, would be

$$C_6F_6 \longrightarrow C_6F_5\cdot + F\cdot, \quad (6)$$

$$C_6F_6 + F\cdot \longrightarrow C_6F_7\cdot, \quad (7)$$

$$R\cdot + C_6F_6 \longrightarrow RC_6F_6\cdot (R\cdot = C_6F_5\cdot, C_6F_7\cdot, C_6F_6C_6F_5\cdot), \quad (8)$$

$$R\cdot + R\cdot \longrightarrow RR, \quad (9)$$

$$R\cdot + F\cdot \longrightarrow RF. \quad (10)$$

Reactions (7) and (8), by analogy with the hydrogen atom-benzene reaction, probably have an activation energy of several kilocalories at most. The activation energy of reaction (8) would be reduced for C_6F_6 in an excited state. The low yield (G=2.01) does not require a chain reaction; however, the structure of the polymer (less volatile than biphenyl, melting below 100° to a moderately viscous liquid) requires a few addition steps like reaction (8). No abstraction reaction has been introduced:

$$R\cdot + C_6F_6 \rightarrow RF + C_6F_5\cdot \quad (11)$$

External evidence against reaction (11) is twofold. In the first place, in hydrocarbon analogs reaction (11) is slower than (8) at room temperature and below, e.g., addition dominates in the photochlorination of benzene [20] and the reaction of H atoms with frozen benzene [33]. The ratio, addition/abstraction, may be about 7.5 in radiolysis of mixtures of C_6H_6 and C_6D_6 [34].

Observation of $C_6H_5CF_3$ in the radiolysis of mixtures of CF_4 and C_6H_6 [13, 14] may require abstraction from C_6H_6 if the mechanism is of the free-radical type. Abstraction of H from C_6H_6 is postulated in the radiolysis of dilute aqueous benzene, the ultimate products being C_6H_5OH and $(C_6H_5)_2$ [35]. In both these instances, the attacking radical is highly electronegative.

The second evidence against reaction (11) is that fluorine atoms are not readily abstracted from perfluoroparaffins by ordinary atoms and radicals such as H [36], CH_3 [37], CF_3 [28], and C_2F_5 [27, 29]. Presumably, the fluorine atoms of aromatic fluorocarbons are likewise resistant. For the abstraction reaction

$$H\cdot + CF_4 \longrightarrow HF + CF_3\cdot \quad (12)$$

E>17 kcal, and the reaction is not observed up to 400° C [36].

For C_2F_4 [38] and C_6H_5F [39] reacting with H atoms, the evidence is for an efficient addition rather than abstraction.

In summary, it therefore seems unlikely that fluorine will be abstracted from either C_6F_6 or C_7F_{16}, except perhaps by "hot" atoms or radicals. Thus, there remains a radical mechanism with dissociation, addition, and recombination steps, yielding a polymer largely nonaromatic. The very low yield of SiF_4 requires that C_6F_6 should be a very efficient trap for F atoms. If the F atoms are formed in an efficient cage of C_6F_6 molecules, reactions (7) and (10) can predominate over reaction (13)

$$F\cdot + F\cdot \longrightarrow F_2, \quad (13)$$

without requiring any great inequality of rate constants.

Gordon and others [17, 40] have written a mechanism for C_6H_6 radiolysis involving excited states only. The same mechanism can be written for C_6F_6:

$$C_6F_6 \longrightarrow C_6F_6^*, \quad (14)$$

$$C_6F_6^* + C_6F_6 \longrightarrow (C_6F_6)_2. \quad (15)$$

Hydrocarbon analogs of the dimer have been reported. An advantage of the excited-state mechanism is that the nearly complete absence of SiF_4 (derived from corrosive fragments) is explained simply when fragments are not formed.

At higher temperatures (218° C) the argument against the radical mechanism does not apply, as considerably more SiF_4 is formed. The actual behavior of C_6F_6 at higher temperatures offers some difficulties. The black granular insoluble polymer suggest a highly condensed aromatic ring structure formed by extensive elimination of fluorine, yet the yield of polymer is about the same as that at low temperature, and the SiF_4 equals somewhat less than 1 F atom per C_6F_6 ring (see table 4).

3.2. Hexafluorobenzene and Hydrogen

Hexafluorobenzene and hydrogen produced more SiF_4 (from HF) than hexafluorobenzene, but less than in mixtures with hydrocarbons (see table 5, cf. tables 3 and 4). The pressure of hydrogen was 34 atm at —80° C, corresponding to 0.0223 mole in the sample, and the amount of hexafluorobenzene was 0.0176 mole. Assuming pertinent properties of the C_6F_6 to be the same as those of C_6H_6, reasonable estimates for the composition are

	in vapor phase	*in liquid phase*
C_6F_6	5.67×10–5 mole	0.0176 mole
H_2	0.223 mole	.00017 mole

TABLE 5. *Radiation yields from hexafluorobenzene and hydrogen 20° C* [a]

	C_6F_6	$C_6F_6+H_2$
$4G(SiF_4)$	0.045	0.440
$G(CO_2)$	.004	.004
$G(CO)$	.0012	0
G(polymer) [b]	2.01	2.30

[a] Exposure dose 319 Mr; hydrogen pressure 34 atm.
[b] C_6F_6 units.

The dose was 319 Mr. Much of the vapor was in a less intense radiation field. For the calculations in table 5, it is assumed that all radiation was absorbed by C_6F_6 as liquid.

The value of $G(SiF_4)$ is 0.11 as against 0.01 for pure C_6F_6 and 0.33 for a mixture of C_6F_6 and C_6H_6.

Conceivable steps producing the HF may be:

$$F\cdot + H_2 \longrightarrow HF + H\cdot, \tag{16}$$

$$C_6F_5\cdot + H_2 \longrightarrow C_6F_6H + H\cdot, \tag{17}$$

$$C_6F_7\cdot + H_2 \longrightarrow C_6F_7H + H\cdot, \tag{18}$$

$$C_6F_7\cdot + H_2 \longrightarrow C_6F_6 + HF + H\cdot, \tag{19}$$

$$C_6F_6{}^* + H_2 \longrightarrow H_2{}^* + C_6F_6, \quad H_2{}^* \searrow 2H\cdot \tag{20}$$

$$C_6F_6{}^* + H_2 \longrightarrow HF + H\cdot + C_6F_5. \tag{21}$$

These reactions must compete with addition reaction (8) and must be roughly comparable with reactions for HF production in hydrocarbon mixtures, e.g.,

$$F\cdot + C_6H_6 \longrightarrow HF + C_6H_5. \tag{22}$$

Any H atoms produced in reactions (16) to (20) may react by addition or abstraction:

$$H\cdot + C_6F_6 \longrightarrow C_6F_6H\cdot, \tag{23}$$

$$H\cdot + C_6F_6 \longrightarrow C_6F_5 + HF. \tag{24}$$

The radiation received in the vapor is relatively unimportant, estimated at 16×10^{20} ev as compared with 554×10^{20} ev in the liquid. In the liquid, the H_2/C_6F_6 mole ratio is about 0.01, as against much higher ratios in the mixtures with C_6H_6 and C_6H_{12}. For comparable HF production in the two cases this would require that k_{16} be considerably greater than k_{22}. For reactions (16) and (22) the activation energies may be near 6 kcal/mole or less. Somewhat analogous reactions with chlorine are:

$$Cl\cdot + H_2 \longrightarrow HCl + H\cdot;\ E \approx 6 \text{ kcal [41]}, \tag{25}$$

$$Cl\cdot + CH_4 \longrightarrow CH_3\cdot + HCl;\ E < 8 \text{ kcal [42]}. \tag{26}$$

Of the other reactions, (17) should be discounted because of the failure to find C_6F_5H experimentally. Activation energies for reactions related to (17) and (18) have been estimated [28]:

$$CF_3\cdot + RH \longrightarrow CF_3H + R\cdot. \tag{27}$$

For the various hydrocarbons RH the activation energies of the reaction in kilocalories per mole are C_2H_6, 7.5; C_6H_6, 7.7; H_2, 8.8; and CH_4, 10.3. Although the basis of the estimates has been criticized [20], comparable work [23 to 29] is consistent with values somewhere near these. The abstraction reactions are generally expected to be slower than the additions to C_6F_6, as discussed earlier for pure C_6F_6.

The formation of HF can also be accounted for by excited-state mechanisms such as in reactions (20) and (21); there is, unfortunately, no explicit literature for comparison. The attempt to account for HF without C_6F_5H remains somewhat unconvincing, as reaction (21) could be followed by a combination of C_6F_5 and H.

3.3. Hexafluorobenzene and Benzene

The data for these mixtures are shown in tables 2 and 3. For comparison, results on C_6H_6 are reproduced from the work of other investigators [17]. The polymer analyses are low by 4.3 to 4.9 percent. Since fluorine analyses tend to be low, it is assumed for calculation that the true fluorine value is that obtained from the difference between (C plus H) and 100. Some of the deficit may, however, have arisen from oxidation of the polymer prior to analysis, which could have lowered the C, F, and H, and simultaneously introduced O and some H. To arrive at G(polymer) values, it was assumed formally that polymer is produced by withdrawing x moles of C_6F_6 and y moles of C_6H_6 from the liquid and rejecting z moles of HF. If H and F are lost in other forms and unequal amounts, small inconsistencies arise. On the basis proposed, one can calculate yields of each type of unit in the polymer and of HF lost per unit.

$$\text{Base moles polymer} = x + y = \frac{\text{moles C}}{6} = \frac{\%\text{C} \times \text{weight}}{100 \times 6 \times 12},$$

$$\frac{\text{Moles HF lost}}{\text{Base mole polymer}} = z = 3\left\{\frac{\text{moles C} - \text{moles F} - \text{moles H}}{\text{moles C}}\right\},$$

$$\frac{\text{Moles } C_6F_6}{\text{Base mole polymer}} = \frac{x}{x+y} = \frac{1}{2}\left\{\frac{\text{moles C} + \text{moles F} - \text{moles H}}{\text{moles C}}\right\}.$$

For all the mixtures, G(polymer) is higher than for either pure component, and $G(SiF_4)$ is very much larger than in pure C_6F_6 (see fig. 2). The SiF_4 was almost certainly formed from HF. The color of the polymer solution became darker with increasing C_6H_6 content, and the polymer during frozen benzene evaporation remained stiffer and spongier, never collapsing to a clear glass.

The composition of the polymer remained near 1:1 for C_6H_6/C_6F_6, even for wide variations in feed ratio (table 2, fig. 3). At increasing C_6H_6 feed content, the H/C and F/C ratios of polymer gradually declined, reflecting the increased removal of H and F mentioned in connection with the SiF_4 yields. As with the pure C_6F_6, the mixture did not show any CF_4 or C_2F_2, and only the mixture with the high C_6H_6 content, 0.886 mole fraction, showed CH_4 or

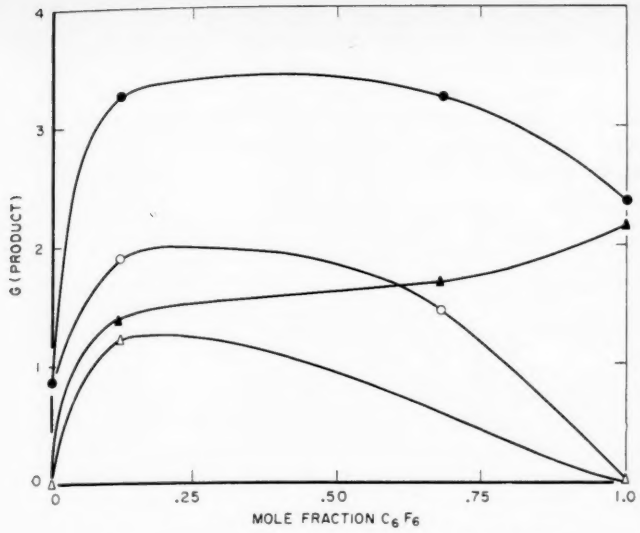

FIGURE 2. *Radiation yields from* $C_6F_6+C_6H_6$.

●, G(polymer, total), ○, G(polymer C_6H_6 units), ▲, G(polymer C_6F_6 units), △, $4G(SiF_4)$.

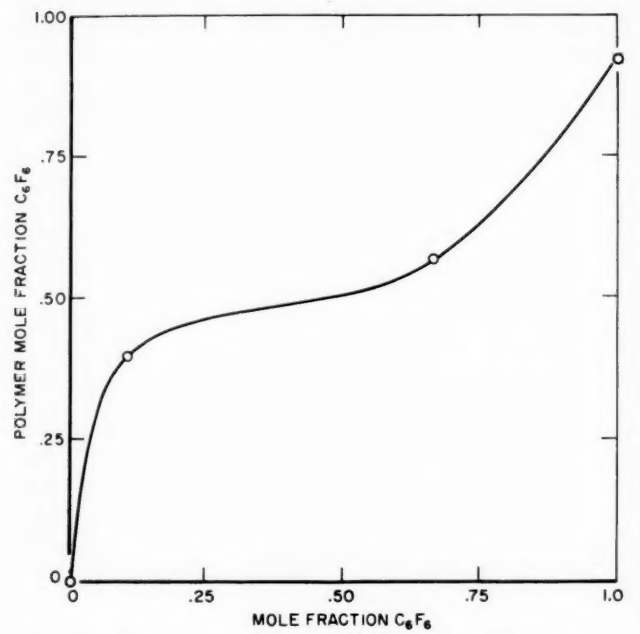

FIGURE 3. *Composition of polymer from* $C_6F_6+C_6H_6$.

C_2H_2. Surprisingly, neither C_6F_5H nor C_6H_5F was found.

The behavior of polymer composition is reminiscent of vinyl copolymerization with a strong alternating tendency. By analogy, a mechanism can be written in which large "crossed" propagation rate constants are responsible for the composition, i.e., where k_{29}, $k_{31} > k_{28}$, k_{30}.

$$\sim C_6F_6\cdot + C_6F_6 \xrightarrow{k_{28}} C_6F_6-C_6F_6\cdot, \qquad (28)$$

$$\sim C_6F_6\cdot + C_6H_6 \xrightarrow{k_{29}} C_6F_6-C_6H_6\cdot, \qquad (29)$$

$$\sim C_6H_6\cdot + C_6H_6 \xrightarrow{k_{30}} C_6H_6-C_6H_6\cdot, \qquad (30)$$

$$\sim C_6H_6\cdot + C_6F_6 \xrightarrow{k_{31}} C_6H_6-C_6F_6\cdot. \qquad (31)$$

Polarity differences often favor addition of unlike units. In partial support, Szwarc [21] finds the methyl affinities of C_6F_6 and C_2F_4 to be 14 and 10 times greater than the methyl affinities of C_6H_6 and C_2H_4. The corresponding $CF_3\cdot$ affinities do not seem to be known. For these low-molecular weight polymers, favorable crossed terminations could also influence the polymer composition.

There are several possible mechanisms involving excited states. Formally, a "crossed" generation of excited molecules could be favored by an energy transfer mechanism [43]. Against this concept is the fact that the overall formation of polymer is nearly independent of changing composition. It has also been pointed out in criticism that a symmetrical mutual energy transfer should not occur very generally [40]. Thus, an initial formation of triplet excited states or radicals of the two species in equivalent amounts by mutual transfer of excitation is unlikely. However, the chemical reactivity of triplet excited states may depend on some of the same considerations which apply to free radicals, among which polarity differences are included.

As in the other cases, a decision between the triplet state and radical mechanism is difficult. The obvious qualitative difference is that molecules are dissociated into fragments when forming radicals but not when forming excited states. The presence or absence of fragments is thus one criterion for distinction. Aside from this, it may be necessary to depend upon highly detailed knowledge of the two types of intermediates. Here, the formation of HF is weak evidence for the presence of some free radicals, while the absence of C_6H_5F and C_6F_5H is evidence against dissociation. A possible nonradical source of HF is from the reaction of excited molecules with other excited or ground-state molecules:

$$C_6H_6^* + C_6F_6 \longrightarrow C_6H_5-C_6F_5+HF. \qquad (32)$$

At low conversions, there are many more C_6 molecules than any other species. The fact that the polymer formed is mainly higher than C_{12} indicates that the C_{12} species once formed must retain chemical activity. A radical-addition mechanism allows this to occur in a self-evident way:

$$C_6H_5\cdot + C_6F_6 \longrightarrow C_6H_5-C_6F_6\cdot \qquad (33)$$

In a pure triplet-state mechanism, it is not evident that the C_{12} species would remain in an excited state with a long lifetime. Possibly excited C_6 could transfer excitation preferentially to ground-state C_{12} molecules. Both the relative absence of fragments and the growth of larger species could be explained if excited molecules initially combine to form a biradical which subsequently grows by ordinary radical addition.

The high G(HF) in mixtures could be formally accounted for by a Bagdassarian [43] or Magat [40] excitation mechanism. An atom and radical mechanism can account for this feature with emphasis on the steps:

$$C_6F_6 \longrightarrow C_6F_5\cdot + F\cdot, \quad (6)$$

$$F\cdot + C_6H_6 \longrightarrow C_6H_5\cdot + HF, \quad (22)$$

$$F\cdot + C_6H_6 \longrightarrow C_6H_6F\cdot, \quad (34)$$

$$F\cdot + C_6F_6 \longrightarrow C_6F_7\cdot. \quad (7)$$

Here $k_{22} < k_7 < k_{34}$, but all are of substantial magnitude. To illustrate, a calculation with $k_7 = 0.1\ k_{34}$, $k_{22} = 0.05\ k_7$ predicts a rather flat maximum production of HF near 0.7 mole fraction C_6F_6.

The data for the mixtures of C_6F_6 and C_6H_6 at 218° C are very rough because of the small sample size and difficulties of manipulation (see table 4). As with pure C_6F_6 at this temperature, the polymer was insoluble and dark. The G values for both polymer and volatile products seem to vary linearly with composition.

It is not surprising that $G(SiF_4)$ from C_6F_6 should be higher at high temperature (compare tables 3 and 4), but it is difficult to understand why $G(SiF_4)$ from the mixtures is less than at room temperature. The polymer from the mixtures resembles that from C_6F_6 at this temperature, and is presumably rich in condensed ring structures or conjugated unsaturation, the formation of which requires elimination of F_2 or HF. Thus, the $G(SiF_4)$ suggests no change from mixtures at 20° C, while the insolubility and color suggest more HF elimination. The dark color of the polymer from mixtures does suggest some conjugated unsaturation even at 20° C. The principal remaining anomaly may then be the relatively high $G(SiF_4)$ from pure C_6F_6 at 218° C. This could be attributed to union of F atoms as F_2, to more efficient escape from a C_6F_6 cage to the wall, or to the onset of C—C cleavage like that which produced C_2H_2 from benzene. The C_2F_2 and similar fragments could be reactive with the walls of the apparatus.

3.4. Hexafluorobenzene and Cyclohexane

From C_6F_6 and cyclohexane, the principal products were SiF_4 (G=0.322), H_2 (G=1.92), and polymer (G=3 to 5) (see table 6). The G value for the SiF_4 is not very different from that of C_6F_6 and benzene. The polymer composition can be discussed by an extension of the method used for C_6F_6 and C_6H_6, if C—C chain scission products can be neglected. Let each C_6 unit of polymer be build from f moles of C_6F_6 and $(1-f)$ moles of C_6H_{12}, rejecting i atoms of F and j atoms of H. Then

$$f = \frac{F}{C} + \frac{i}{6},$$

$$f \geq \frac{F}{C}$$

$$f = 1 - \frac{1}{2}\frac{H}{C} - \frac{j}{12},$$

$$f \leq 1 - \frac{1}{2}\frac{H}{C}.$$

Similar limiting formulas can be constructed for other systems.

The G value for H_2(1.92) plus that derived for HF (1.29) is a little less than the usual $G(H_2)$ [44] for cyclohexane multiplied by the electron fraction ($5.5 \times 0.636 = 3.5$). This may correspond to a weak protective effect. Of the H_2, some may be formed by a molecular mechanism, but the HF should be from an abstraction by either of the following reactions:

$$F\cdot + C_6H_{12} \longrightarrow HF + C_6H_{11}\cdot, \quad (35)$$

$$H\cdot + C_6F_6 \longrightarrow HF + C_6F_5\cdot. \quad (24)$$

As discussed earlier for hexafluorobenzene and hydrogen, the evidence for reaction (24) or any abstraction from C_6F_6 is weak; for example, in the failure to detect C_6F_5H here. For the same reasons, radicals from C_6H_{12} are not likely to abstract fluorine to form alkyl and cyclohexyl fluorides. The failure to find RF is not quite conclusive because $C_6H_{11}F$ is rather unstable and smaller scission products of any one kind would be small in amount. On the whole, reaction (35) is preferred as the source of HF. The mechanism of protection may still be either of the sponge type or by addition, as with C_6H_6.

TABLE 6. *Radiation yields from hexafluorobenzene and cyclohexane at 20° C*[a]

C_6F_6, mole fraction	0[b]	0.192	0.234	0.655
$4G(SiF_4)$	0	[c]	1.29	[c].
$G(H_2)$	5.2, 5.9	[c]	1.92	[c].
$G(CH_4)$	0.09, 0.02	[c]	0.005	[c].
$G(C_2H_4)$	0.21, 0.14	[c]	0.007	[c].
G(polymer) [d]	1.66 [b]	4.9	6.1	3.1.
Polymer F/C [e]	0	0.336	0.368	0.479.
Polymer H/C [e]		1.279	1.148	0.925.
Polymer, mole fraction C_6F_6	0	0.34 to 0.36	0.37 to 0.43	0.48 to 0.54.

[a] Exposure dose 174.5 Mr.
[b] Ref[19], pp. 18 and 20.
[c] Container failed before analysis.
[d] C_6 units.
[e] Mole ratio.

3.5. Perfluoroheptane

The data of table 7 are rather uncertain because of the large number of possible products and the general ambiguity of mass spectrometer analyses for saturated fluorocarbons. All of these compounds furnish large amounts of fragment ions, especially CF_3^+, and little parent ion. However, the G values for SiF_4, CF_4, and perhaps C_2F_6 are more reliable, as these components were determined at −80°, where most of the higher fluorocarbons are not volatile enough to interfere. The reported G value may, however, be low because of differential solubility of gases in the liquid at −80°; by contrast, both C_6F_6 and C_6H_6 have high freezing points and at −80° would have crystallized, expelling dissolved gases.

TABLE 7. *Radiation yields from hexafluorobenzene and perfluoroheptane at 20° C* [a]

C_6F_6, mole fraction	0	0.38	0.74	1.00
$4G(SiF_4)$	[b] 0.668	1.232 [b]	0.352	0.040
$G(CO_2)$	[b] .028	0.025 [b]	0.003	.0012
$G(CF_4)$	.195	0.131	0.085	0
$G(C_2F_6)$	[b] .081	0.122 [b]	0.008	0
G(polymer) [c]	2.0	3.2 to 3.8	3.0 to 3.5	2.01
Polymer F/C [d]	2.102	1.624	1.361	.93
Polymer mole fraction C_6F_6	0	<0.55	<0.75	1

[a] Exposure dose 330 to 408 Mr; dose factor for C_6F_6, 0.530×10^{20} ev/g Mr; for C_7F_{16}, 0.526.
[b] May be low because of solubility.
[c] As C_6 or C_7 units.
[d] Mole ratio.

The character of the polymer was similar to that reported by other workers. Most boiled in the range 179° to 250°, and the material was a viscous liquid at 4° C. For comparison, $n-C_{12}F_{26}$ boils at 175° and freezes at 42°, and $n-C_{16}F_{34}$ boils at 240° and freezes at 115°. The failure of the sample to freeze may indicate branched structures, but is not very conclusive in a mixture.

In addition to the data of table 7, the analyses of liquid in table 8 are of qualitative interest, although both the amounts and identities quoted are subject to large uncertainties of interpretation. Presumably,

TABLE 8. *Liquid phase from radiolysis of hexafluorobenzene and perfluoroheptane* [a]

C_7F_{16} prepared	mole fraction	1.00	0.62
C_7F_{16} found	mole %	9.9	19.3
C_6F_6 found	mole %	0	9.3
C_6F_{14} found	mole %	7.0	10.2
C_5F_{12} [b] found	mole %	6.0	5.7
C_3F_8 found	mole %	9.0	1.5
C_2F_6 found	mole %	2.19	~0

[a] See table 7, footnote [a], for radiation conditions. Samples analyzed by mass spectra of vapor at 25° C.
[b] Or *cyclo*-C_5H_{10}.

fractionation effects would weight unduly the lowest boiling components and minimize those above C_7. The values of $G(CF_4)=0.195$ and of $G(SiF_4)=0.167$ for C_7F_{16} are high relative to those for C_6F_6 (table 7). The main products are thus SiF_4 and higher and lower saturated fluorocarbons. The mass spectrometer finds almost no olefinic molecules. It is possible that more sensitive and reliable indications would be given by infrared or by bromine or permanganate titrations. Stoichiometry requires that the extra fluorine content of the C_1 to C_6 perfluoroparaffins and the loss to SiF_4 be compensated either by equivalent condensation to higher perfluoroparaffins or formation of double bonds. The following reactions are to be considered, where rates can vary with the size of the radicals R_i and R_j:

C—C scission:

$$C_7F_{16}\longrightarrow R_i\cdot+R_{7-i}\cdot. \tag{36}$$

C—F atom splitting:

$$C_7F_{16}\longrightarrow sec-C_7F_{15}\cdot+F\cdot, \tag{37}$$

$$C_7F_1\longrightarrow prim-C_7F_{15}\cdot+F\cdot. \tag{38}$$

Recombination:

$$F\cdot+F\cdot\longrightarrow F_2, \tag{13}$$

$$R_i\cdot+F\cdot\longrightarrow R_iF, \tag{39}$$

$$R_i\cdot+R_j\cdot\longrightarrow R_i-R_j. \tag{40}$$

Disproportionation:

$$R_i\cdot+R_j\cdot\longrightarrow C_iF_{2i}+C_jF_{2j+2}, \tag{41}$$

$$F\cdot+R_i\cdot\longrightarrow C_iF_{2i}+F_2. \tag{42}$$

Radical attack on F_2:

$$R_i\cdot+F_2\longrightarrow R_iF+F\cdot. \tag{43}$$

Transfer:

$$R_i\cdot+C_7F_{16}\longrightarrow C_7F_{15}\cdot+R_iF. \tag{44}$$

The transfer reaction (44) is unlikely because of energetics, as previously discussed. Disproportionation (41) and (42) would generate olefinic molecules and so should be unimportant here; moreover, there is convincing experimental evidence against reaction (41) [23 to 29]. The remaining reactions, coupled with material balance, all require conservation of total number of molecules, and thus a compensation between product molecules larger and smaller than C_7. Larger molecules were found in the distillation residue although not by the mass spectrometer.

To extend the conclusion about conservation of number of molecules from C_7F_{16} to high polymers appears inconsistent with the familiar rapid degradation of polytetrafluoroethylene and polychlorotrifluoroethylene. The difficulty could be met by asserting that sufficient oxygen or hydrocarbon material was present in all polymer experiments to combine or undergo H abstraction with the polymer radicals and thus lower the molecular weight; or that the radicals were trapped in the solid matrix and could then undergo various other reactions ordinarily of low probability; or that a relatively very small increase in the number of molecules and double bonds occurs in all cases but is easily noticed only in the polymer. In this connection it has been noticed recently that polytetrafluoroethylene irradiated in vacuo is degraded very much less rapidly than in air [45]. Nevertheless, a thorough search for olefinic molecules in irradiated perfluoroheptane would be desirable.

The set of possible reactions is still too complicated for easy treatment, even when simplified by assumptions such as random splitting and equal reactivity of all radicals. Substantial amounts of all perfluoroparaffins C_1 to C_{14} could be expected. By assuming that all C—C and C—F bonds split with equal probability, and that all lower radicals disappear only by reaction with F atoms with equal rate constants, one arrives at an initial fragment distribution:

$$F : prim—C_7 : sec—C_7 : \text{all lower alkyl} : CF_3 = 16 : 6 : 10 : 12 : 2$$

and a product distribution in which all lower perfluoroalkanes occur equally and $G(CF_4)=2/46$ times the G value of total initial atoms and radicals. The observed $G(CF_4)=0.195$ might thus indicate an initial G value for total atoms and radicals as high as 4.5.

In a liquid phase, the products will be governed by the chances for diffusion before recombination of fragments. The predominant reactions will thus be

$$C_7F_{16} \longrightarrow C_7F_{15}\cdot + F\cdot, \qquad (37, 38)$$

$$C_7F_{16} \longrightarrow C_6F_{13}\cdot + CF_3\cdot (\text{for } i=1) \qquad (36a)$$

$$F\cdot + F\cdot \longrightarrow F_2, \qquad (13)$$

$$F\cdot + CF_3\cdot \longrightarrow CF_4 \text{ (for } i=1), \qquad (39a)$$

$$2C_7F_{15}\cdot \longrightarrow C_{14}F_{30}[\text{ (for } i, j=7), \qquad (40a)$$

$$2C_6F_{13}\cdot \longrightarrow C_{12}F_{26} \text{ (for } i, j=6). \qquad (41a)$$

It can be seen that these reactions account for much of the product SiF_4, CF_4, and high-boiling residue.

3.6. Perfluoroheptane and Benzene

The mixture of perfluoroheptane and benzene was heterogeneous but of considerable qualitative interest. The principal products from irradiation were SiF_4 (at a G value about twice that of pure C_7F_{16}), polymer, numerous lower fluorocarbons, and CF_3H (table 9). The last named compound had a G value of 0.158 by calculation from analyses at −80°C; however, the sample, when later warmed to 25° C, contained large amounts of CF_3H in the vapor phase, and a rough estimate from the 25° C analysis suggested a $G(CF_3H)$ in the region of 2.

TABLE 9. *Radiation yields from hydrocarbon-perfluoroheptane mixtures at 20° C* [a]

C_7F_{16}, mole fraction	0.716	0.560	0.685	0.188	0.213.
Second component	C_6H_6	C_6H_6	c-C_6H_{12}	c-C_6H_{12}	c-C_6H_{12}.
Dose.....Mr	339	174	339	339	174.
$4G(SiF_4)$	(b)	2.62	(b)	(b)	(b).
$G(H_2)$		0.09			
$G(CF_3H)$		0.158 [d]			
$G(CF_4)$		0.189			
$G(C_2F_6)$		0.021 [d]			
$G(C_2F_4)$		0.017 [d]			
$G(CH_4)$		0			
$G(C_2H_4)$		0			
G(polymer) [e]	4.2 to 4.9.	5.8 to 6.8	2.7 to 3.1.	2.8 to 3.2	4.7 to 5.4. [e]
Polymer H/C	0.340	0.305	0.866	1.326	
Polymer F/C	1.337	1.357	0.951	0.502	
Polymer, mole fraction C_7F_{16}	0.55 to 0.62.	0.56 to 0.66.	0.38 to 0.53.	0.19 to 0.30.	

[a] All samples have two liquid phases.
[b] Large; failure through glass seal corrosion.
[c] In C_6 or C_7 units, from weight and carbon analysis.
[d] May be much too low; large content remains in room temperature analysis.
[e] From weight, assuming analysis of preceding column.

Inasmuch as CF_3H boils at −84°, and C_7F_{16}, the major component of the mixture, is sometimes liquid at −80°, it is not unreasonable that most of the CF_3H present at −80° would be held in solution in the C_7F_{16}. For the same reason, G values for C_2F_6 and C_2F_4 should probably also be much higher. The CF_3H indicates a clear-cut abstraction reaction from C_6H_6:

$$CF_3\cdot + C_6H_6 \longrightarrow CF_3H + C_6H_5\cdot \qquad (45)$$

It is obvious from the presence of CF_4, C_2F_6, etc., that the direct recombinations, F·+R· and R·+R·, still occur to some extent. A comparison with column 1 of table 7, especially the fairly reliable CF_4 values, may indicate essentially no protection of C_7F_{16} by either C_6F_6 or C_6H_6. The SiF_4 values of table 9 indicate a sensitization, but the solubility of SiF_4 in C_7F_{16} under the conditions of analysis complicates the result, and both G values must be used with caution. Although C_7F_{16} in benzene had only moderate G values for products, C_7F_{16} in styrene was found to promote polymerization with a partial electron-fraction G value of 20±10[46] . The present C_7F_{16} environment should be in some ways similar.

If the high estimate of $G(CF_3H)$ of about 2 is correct for C_7F_{16} in benzene, it may be consistent with the polymerization $G=20$ for C_7F_{16} in styrene, for the various modes of C—C and C—F scission can form many other radicals as well as the CF_3. If the low value in table 8 is more nearly right, then the high results with styrene may require a special energy-transfer effect. In the radiolysis of mixtures of C_6H_6 with $C_6H_5CF_3$, CF_4, and chlorofluorocarbons, Feng [13, 14] has reported G(radicals) of the order of 1 by the DPPH disappearance method in contrast with the high G(radicals) usually observed for other halocarbons [40]. Although Feng's CF_4 effects were observed at unknown high dilution and the difference from pure C_6H_6 was close to the experimental error, his G values for $C_6H_5CF_3$ and CF_4 in any event were not large, and thus differ from the case of the chlorocarbons. Considering all the evidence, it seems best to suppose that our true $G(CF_3H)$ is considerably less than 2, that G(radicals) is usually low for fluorocarbons, and that the high G(radicals)=20 for C_7F_{16} in styrene polymerization may be due to special energy transfer effects, valid for styrene but not benzene.

It was further reported by Feng that the irradiation of CF_4 and C_6H_6 produced C_6H_5F and $C_6H_5CF_3$, detected by infrared, with G values rising to 1.5 [13, 14]. In the present mixture, C_6H_5F was not found, although its formation by combination of $F+C_6H_5$ is not unreasonable. In the present study, the C_6H_5F would have been associated with large proportions of unchanged liquid and perhaps not detected with high sensitivity. The reported high G value of C_6H_5F from so dilute a solution of CF_4 is surprising. Possibly other compounds, such as polymer structures formed by addition, could have absorbed at C—H and C—F frequencies close to those of $C_6H_5CF_3$ and C_6H_5F, with a very large absorption coefficient.

3.7. Perfluoroheptane and Cyclohexane

The mixtures of perfluoroheptane and cyclohexane were heterogeneous. The only data are those upon polymer, table 9, as all containers were broken by corrosion of glass seals, even after rela-

tively small doses of the order of 70 Mr. Presumably the yield of HF was considerably higher than any reported in the tables. Comparison of the polymer yields in columns 4 and 5 suggest that G(polymer) declines with increased dose.

3.8. Perfluorobenzene and Perfluoroheptane

With perfluorobenzene and perfluoroheptane (table 7) there appears to be an initial rise in $G(C_2F_6)$ as the C_6F_6 content is increased. This is believed to be an artifact due to solubility, as the freezing of C_6F_6 will concentrate the gaseous solutes in the remaining liquid and vapor. The data on SiF_4 and CF_4 are subject less strongly to the same kind of error, which may seriously underestimate these products where much C_7F_{16} is present. There is at least no strong "protective" effect. Since F atoms should be present, it appears that they combine with each other and with aliphatic radicals more readily than they add to C_6F_6. On the other hand, a rapid addition of F to C_6F_6 is needed in the radical mechanism for C_6F_6 radiolysis to explain the low SiF_4 yield. This inconsistency may call into question any purely radical mechanism for the radiolysis of C_6F_6 and favor a triplet-state mechanism there. A similar argument may apply to the radiolysis of C_6H_6, which exhibits a protective effect less drastic than might be expected from the radiolysis of the pure component. The very low hydrogen yields from pure C_6H_6 may be due mainly to failure to split off hydrogen atoms, rather than to rapid reaction with them. The yield of radicals from C_6H_6 detected by ordinary methods is somewhat low; G=0.33–0.89 by iodine [47] and DPPH disappearance [40]. Possibly it is also of about this same magnitude in mixtures where C_6H_6 exhibits a protective effect. The "sponge" mechanism of protection in C_6H_6 mixtures has been discussed recently in terms of relations between excited states [40].

The failure of protection in the present mixture suggests that protection, where it occurs, is of the sponge type and not due to extreme reactivity of the aromatic ring with atoms and radicals, and that the characteristics of aromatic radiation chemistry (considerable polymer, very little hydrogen or halogen) depend more upon reactions which proceed via triplet states than upon atom and radical reactions.

4. Conclusions

The data presented here show that representative pure liquid fluorocarbons are not especially sensitive toward ionizing radiation. In the paraffinic series, the indicated C—C scissions are about equal in n-C_7F_{16} and n-C_7H_{16}, as judged by the respective $G(CF_4)$ and $G(CH_4)$; and the indicated C—F scissions of the fluorocarbon are much less than the C—H scissions of the hydrocarbon. The low yield of C—F scission products (SiF_4) may be a cage effect phenomenon. The diffusion away of the hydrogen atom of a C—H pair must be an easier process than the corresponding diffusion of a fluorine atom. Results in the gas phase would be interesting for comparison. Even less C—F scission than that found here is suggested by the fact that Simons and Taylor [5], irradiating perfluoroaliphatic compounds in all-aluminum containers, found no evidence whatever of corrosive fluorine.

Aside from differences of purity or analytical sensitivity, both sets of observations appear consistent with the existence of a small steady-state concentration of F_2, which disappeared in one instance by diffusion to the glass parts of the apparatus and conversion to SiF_4, and in the other by attack of fluorocarbon radicals to form lower perfluoroalkanes. Some minimal C—F scission seems necessary to account for the considerable amount of C_{13} and C_{14} coupling products from C_7F_{16}. Irradiated polytetrafluoroethylene seems to undergo C—F scissions exclusively, according to electron resonance observations [48]. This behavior is again consistent with a cage effect, as F from a C—F scission can diffuse away, while the radical pair from a C—C scission is held more rigidly and recombines.

Some of the early indications of fluorocarbon sensitivity were due to the presence of oxygen. Recent studies of the tensile strength of irradiated polytetrafluoroethylene show the loss of tensile is very rapid in the presence of oxygen and hardly perceptible for long periods in its absence [45]. The strong oxygen effect is reminiscent of the degradation of very pure chlorinated compounds exposed to light, air, and moisture. For fluorocarbons under irradiation it may be speculated that the radical recombination rate is somewhat slower than for hydrocarbons, allowing more effective competition by oxygen reactions.

Aromatic fluorocarbons have the same kind of resistance to ionizing radiation as the aromatic hydrocarbons, yielding very little gas and a moderate amount of low polymer. G(polymer) is 2.01 for C_6F_6, as against 0. 93 for C_6H_6. The polymers from both materials are close to the starting material in elemental analysis. There has been some speculation in the literature concerning the degree of aromatic character present in perhaloaromatic compounds [49]. At least those aspects of aromatic character concerned with radiation resistance seem to remain in the totally fluorinated analog.

Recalling the considerable resistance of polystyrene to radiation, one might predict a similar resistance in polymers containing perfluoroaromatic groups.

Experimentally, poly(2,3,4,5,6-pentafluorostyrene) has a G value for free radicals observed by electron spin resonance, almost as low as polystyrene itself [50], which suggest that the general radiation resistance might be similar. Studies on mechanical and solution properties of large samples would be of interest, as would studies on poly(perfluorostyrene) if it should become available. Presumably, polymers with perfluoroaromatic rings in the main chain, rather than a side chain, would show a better combined resistance to heat and radiation than any styrene derivative. Polyphenyls and perfluoro-

polyphenylene ethers are the obvious structural possibilities of this kind.

It is not surprising that mixtures of fluorocarbons with hydrocarbons are usually less stable to radiation than the pure components themselves, for the production of hydrogen fluoride is now possible. It is likely that most partially fluorinated compounds would have the same weakness. In spite of the general tendency toward increased sensitivity, hexafluorobenzene appears to repress somewhat the production of hydrogen from cyclohexane. The increased polymer production in mixtures is in most cases a complicated phenomenon, but in the benzene-hexafluorobenzene mixtures it exhibits a strong tendency toward equal numbers of benzene and hexafluorobenzene units, as in alternating copolymerization. A likely reason for this behavior is the enhancement of radical or triplet-state reactivities by polarity differences.

At ordinary temperatures, atom and radical mechanisms modified by cage effects seem able to account for the results. Mechanisms involving triplet states, as outlined by other authors for benzene, are perhaps preferable for the perfluoroaromatic systems, especially because of the very slight occurrence of fragmentation. Ionic mechanisms, proposed by Feng for certain hydrocarbon fluorocarbon mixtures, have not been considered here at length because of the fairly satisfactory explanation by other mechanisms and the very short lifetimes to be expected for ions generally in condensed systems.

At higher temperatures (218° C), the radiation chemistry of hexafluorobenzene is not well understood, but the material retains a fairly good resistance toward inorganic fluoride production and the usual tendency for polymer production. Pure fluorocarbon materials are thus not especially sensitive to radiation, and aromatic fluorocarbons are quite resistant.

5. References

[1] M. Hellmann, A. J. Bilbo, and W. J. Pummer, J. Am. Chem. Soc. **77,** 3650 (1955).
[2] P. Bradt and F. L. Mohler, Anal. Chem. **27,** 875 (1955).
[3] F. L. Mohler, V. H. Dibeler, and R. M. Reese, J. Research NBS **49,** 343 (1952).
[4] V. H. Dibeler, R. M. Reese, and F. L. Mohler, J. Chem. Physics **26,** 304 (1957).
[5] J. H. Simons and E. H. Taylor, J. Phys. Chem. **63,** 636 (1959).
[6] D. S. Ballantine, A. Glines, P. Colombo, and P. Manowitz, Further studies of the effect of gamma radiation on vinyl polymer systems, BNL–294 (Mar. 1954).
[7] J. W. Ryan, Modern Plastics **31,** 152 (Oct. 1935).
[8] K. Matsumae, M. Watanabe, A. Nishioka, and T. Ichimiga, J. Polymer Sci. **28,** 653 (1958).
[9] J. Byrne, T. W. Costikyan, C. B. Hanford, D. L. Johnson, and W. L. Mann, Ind. Eng. Chem. **45,** 2549 (1953).
[10] E. I. du Pont de Nemours and Co., Inc., Brochure on Viton A, p. 11 ca. 1957.
[11] A. Charlesby, Great Britain Atomic Energy Research Establishment Report AERE M/R 978 (1953).
[12] A. Charlesby, Nucleonics **12,** No. 6, p. 18 (June 1954).
[13] P. Y. Feng and L. Mamula, J. Chem. Phys. **28,** 507 (1958).
[14] P. Y. Feng, The radiation chemistry of fluorinated organic compounds, 2d UN Conference on Atomic Energy (June 1958).
[15] L. Bouby, A. Chapiro, M. Magat, E. Migirdicyan, A. Prevot-Bernas, L. Reinisch, and J. Sebban, Geneva Conference on Peaceful Utilization of Nuclear Energy, Vol. **7,** p. 612 (1955).
[16] W. N. Patrick and M. Burton, J. Am. Chem. Soc. **76,** 2626 (1954).
[17] S. Gordon, A. R. van Dyken, and T. F. Doumani, J. Phys. Chem. **62,** 20 (1958).
[18] E. L. Colichman and R. Fish, Pyrolytic and radiolytic decomposition rate studies on Ortho-, meta-, and paraterphenyls, U.S. AEC Report NAA–SR–1287 (1955).
[19] M. Burton, Radiolyse de Liquides Organiques, Chapter 1 in M. Haissinksy (editor) Actions Chimiques et Biologiques des Radiations, 2me Serie, Masson et Cie, Paris (1958).
[20] E. W. R. Steacie, Atomic and Free Radical Reactions, 2d ed. (Reinhold Publishing Co., New York, N.Y., 1954).
[21] M. Szwarc, private communication.
[22] J. Smid and M. Szwarc, J. Am. Chem. Soc. **79,** 1534 (1957).
[23] P. Ayscough and E. W. R. Steacie, Proc. Roy. Soc. **A234,** 476 (1956).
[24] P. B. Ayscough, J. C. Polanyi, and E. W. R. Steacie, Can. J. Chem. **33,** 743 (1955).
[25] P. B. Ayscough, Can. J. Chem. **33,** 1566 (1955).
[26] P. B. Ayscough, J. Chem. Phys. **24,** 944 (1956).
[27] G. Giacometti and E. W. R. Steacie, Can. J. Chem. **36,** 1493 (1958).
[28] G. O. Pritchard, H. O. Pritchard, H. I. Schiff, and A. F. Trotman-Dickenson, Trans. Faraday Soc. **52,** 849 (1955).
[29] G. H. Miller, G. O. Pritchard, and E. W. R. Steacie, Z. physik. Chem. **15,** 262 (1958).
[30] M. Hellman, E. Peters, W. J. Pummer, and L. A. Wall, J. Am. Chem. Soc. **79,** 5654 (1957).
[31] Report of the International Commission on Radiological Units and Measurements (ICRU) 1956; NBS Handbook **62,** 10 to 17, 1956.
[32] D. P. Stevenson and D. O. Schissler, J. Chem. Physics **23,** 1353 (1955).
[33] K. H. Geib and P. Harteck, Ber. **66B,** 1815 (1933).
[34] W. N. Patrick and M. Burton, J. Phys. Chem. **58,** 424 (1954).
[35] P. V. Phung and M. Burton, Radiation Research **7,** 199 (1957).
[36] J. Dacey and J. Hodgins, Can. J. Research **B28,** 173 (1950).
[37] R. A. Sieger and J. G. Calvert, J. Am. Chem. Soc. **76,** 5197 (1954).
[38] P. E. Allen, H. W. Melville, and J. C. Robb, Proc. Roy. Soc. **A218,** 311 (1953).
[39] E. Boehm and K. Bonhoeffer, Z. physik. Chem. **119,** 385 (1926).
[40] M. Magat, L. Bouby, A. Chapiro, and N. Gislon, Z. Elektrochem. **62,** 307 (1958).
[41] W. H. Rodebush and W. C. Klingelhoefer, J. Am. Chem. Soc. **55,** 130 (1930); S. Glasstone, K. J. Laidler, and H. Eyring, Theory of rate processes (McGraw-Hill, New York, N.Y., p. 236, 1941).
[42] H. J. Schumacher, Z. Angew. Chem. **53,** 501 (1940).
[43] T. S. Nikitina and C. S. Bagdassarian, Rec. Travaux sur la Chimie des Radiations, ec. Sci. URSS, Moscow, p. 183 (1955).
[44] J. P. Manion and M. Burton, J. Phys. Chem. **56,** 560 (1952).
[45] L. A. Wall and R. E. Florin, J. Applied Polymer Science **2,** 251 (1959).
[46] L. A. Wall and D. W. Brown, to be published.
[47] E. N. Weber, P. F. Forsyth, and R. H. Schuler, Radiation Research **3,** 68 (1955).
[48] H. N. Rexroad and Walter Gordy, J. Chem. Phys. **30,** 399 (1959).
[49] W. H. Pearlson, in Fluorine Chemistry, **1,** 477, ed. J. H. Simons (Academic Press, Inc., New York, N.Y., 1950).
[50] L. A. Wall, R. E. Florin, and D. W. Brown, to be published.

WASHINGTON, D.C. (Paper 64A4–49)

JOURNAL OF RESEARCH of the National Bureau of Standards—A. Physics and Chemistry
Vol. 64A, No. 4, July–August 1960

Behavior of Isolated Disturbances Superimposed on Laminar Flow in a Rectangular Pipe [1]

Grover C. Sherlin

(April 8, 1960)

An investigation was conducted in a horizontal transparent rectangular pipe to study the behavior, in laminar flow, of an isolated turbulent-like disturbance produced by injecting a quantity of dye into the pipe 39 feet from the entrance. As the resulting mass of colored water moved downstream, time-distance measurements were made for the front of the dye mass and for the rear of the disturbance. The experimental setup, which is described in some detail, permitted reasonable control over the mean flow rate from which Reynolds number was calculated. The utilization of the data unfolded a functional relationship among three quantities: The ratio of the velocity of the rear of the disturbance to the velocity of the front of the dye U_R/U_F; the distance from the origin, X_F; and the Reynolds number R. The similarity of this work to that being done by Lindgren in Stockholm is mentioned.

1. Introduction

The investigation described herein is the outcome of what was originally intended to be a study of turbulent motions in pipe flow using dye techniques in water. While it turned out to be difficult to learn much about the turbulence itself by this method, it was possible to study the initiation of turbulence and to distinguish between turbulent and nonturbulent points of the stream. The investigation was therefore turned to a study of these phenomena, specifically to the observation and study of a disturbance which when introduced at a given point propagated downstream and either died out or developed into an isolated slug of turbulent flow.

The fact that flow in a pipe can be intermittently laminar or turbulent has been known for many years. Only recently, however, with the work of Rotta [1][2] and Lindgren [2,3] has the intermittency been portrayed in the light of downstream-convected regions of turbulent fluid separated by regions of laminar fluid. The turbulence in such cases originates sporadically at various locations in the pipe, and the regions are distributed randomly and occur with increasing frequency as the Reynolds number becomes greater. With a sufficient distance downstream from the origin of a disturbance and at a Reynolds number above some critical value the turbulent regions have grown together and the flow has become continuously turbulent. Similar phenomena are presumed to occur in smooth conduits of any cross-sectional shape.

The purpose of the investigation reported here was to study the development and propagation of a single turbulent region which had a known origin in time and space and could thereafter be followed and observed over a long course. Interest in the behavior of such a region arises primarily from the fact that it is presumably a fundamental link in the process by which flow becomes turbulent.

The observations were made in a long rectangular pipe with a well-faired entrance. An effort was made to reduce ambient disturbances so as to raise the limiting Reynolds numbers for laminar flow to as high a value as possible. The observations were made only in the region where there appeared to be fully developed pipe flow. The set of consecutive observations on a single disturbance will be called a "run".

2. Apparatus

2.1. Rectangular Pipe and Constant-Level Supply Tank

A circulating system using water from the city mains was constructed in the summer and fall of 1953. The system consisted of a constant-level supply tank, a horizontal rectangular transparent pipe, discharge controls, and tanks for storage and for regulation of flow. A simplified layout of the major components is shown in figure 1.

The constant-level tank was a rectangular-sided steel vessel 36 in. by 48 in. by 75 in. in size. A rectangular hole near the bottom led into the horizontal pipe through a plastic bellmouthed connection 33 in. long.

Water was delivered to the tank through two short lengths of vertically standing perforated pipes. A cloth bag about 10 in. in diameter and 36 in. long was fitted over each pipe to provide a fairly uniform distribution of flow. To improve the flow distribution, a porous barrier about 4 in. thick, made of $\frac{5}{8}$ in. glass spheres, was formed across the tank 42 in.

[1] Sponsored in part by the Air Force Office of Scientific Research.
[2] Figures in brackets indicate the literature references at the end of this paper.

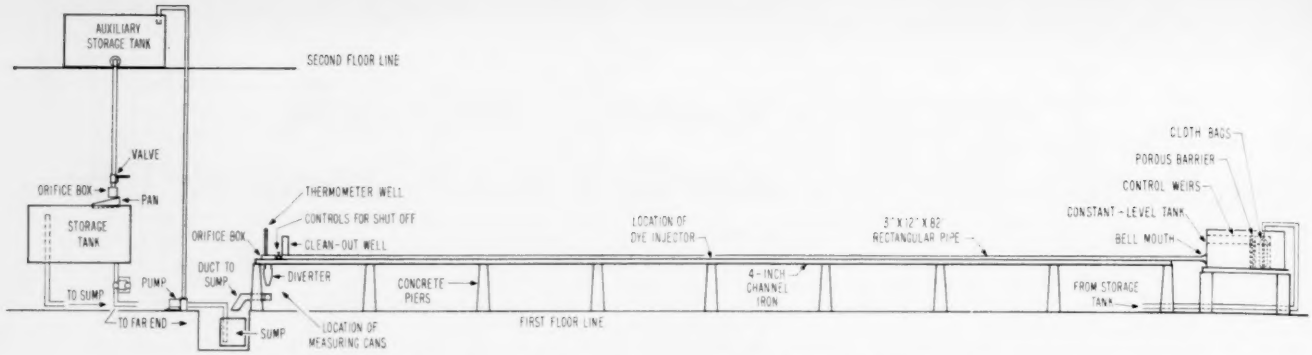

FIGURE 1. *Layout of major components of the circulating system.*

upstream from the bellmouth. Above the water level and near the bellmouth was mounted a hook gage graduated in thousandths of a foot.

The horizontal transparent pipe was 82 ft long. Internally it was 3 in. high and 12 in. wide. It was constructed of acrylic plastic sections approximately 68 in. long. Irregularities at the junctures of the sections were kept to a minimum. The pipe was supported 45 in. above the laboratory floor by two parallel rails of 4-in. channel iron which were suspended across concrete piers placed in a straight line at 9-ft intervals.

At 3-ft intervals along the length of the plastic pipe, 12-in. lengths of stainless steel tubing, 0.008 in. inside diameter, were inserted through the top and bottom walls on the centerline. Nigrosine black dye flowed by gravity from a reservoir into the tubing. Through a hole in the wall of each piece of tubing the dye issued into the water, moved along with the flow, and produced a straight horizontal black line when the flow was laminar. Simple packing glands on the pipe wall prevented leaks and permitted adjustment of the dye streamers in the vertical plane.

At a point 39 ft from the entrance of the pipe a special dye injecting device was located for the purpose of creating a disturbance to the water flow. The essential features of this device were a toy balloon that could be filled with a measured volume of red dye, a 6-in. length of 1½-in. plastic tube to confine the balloon when under pressure, and a cylindrical lead weight to force the dye out of the balloon. Rubber tubing connected the balloon with a ⅛-in. pipe nipple set flush in the bottom of the rectangular plastic pipe on the centerline.

From the location of the injection device to the end of the plastic pipe, vertical lines were drawn on both sides of the pipe at 1-ft intervals. These lines were used to mark the passage of dye masses along the plastic pipe.

2.2. Discharge Instrumentation

At the discharge end of the pipe were controls for shut-off, a thermometer well, an orifice box, a diverter, measuring cans, and ducts to carry water to a sump for recirculation.

The controls for shut-off were a manifold arrangement of five 1¼-in. brass gate valves that were connected at each opening, through short nipples, to corresponding holes in two 3 by 12 by ⅛-in. brass plates. One plate was screwed to the end of the rectangular pipe, the other plate to the upstream side of the orifice box.

Glued to the top of the orifice box was a vertical transparent plastic pipe that served as a thermometer well for a 59° to 115° F thermometer, graduated in twentieths of a degree. The bottom of the box was a brass plate with 15 symmetrically placed orifices, in five sizes of 1/16-, ⅛-, ¼-, ½-, and 1-in. diam, respectively. The three orifices of each size were spaced equidistantly on one of five concentric circles. Below each orifice was brazed a short nipple of sufficient inside diameter to allow free exit of water. Each nipple was covered with a pipe cap when not in use.

The diverter was directly below the orifice box. It was used to obtain samples of water for weighing to determine the mean velocity in the pipe. The water-carrying components of the diverter were constructed of acrylic plastic; the structural supports, bearings, and other parts were made of metal. A ball bearing mounted on the moving arms of the diverter actuated momentarily a microswitch as the arms shifted through the central or neutral position in directing the water flow to either side of the transparent pipe.

The water to be weighed was collected in galvanized cans, 15 in. long, 6 in. wide, and 14 in. deep, as it flowed from the diverter. Two plywood cars, one on each side of the transparent pipe, each held 15 cans as well as a special container which was placed under the diverter to receive water at the beginning or end of an experiment. The special containers each had a discharge spout at the bottom leading through duct work into the sump. During the experimental run, sample cans on alternate sides of the transparent pipe were successively moved into position under the diverter spout until all were filled. Each time the diverter was shifted to spill water into a different can, the microswitch on the diverter was actuated and a pulse was transmitted to the time-interval pen in a single-channel recorder. Thus,

as the measuring cans were filled progressively with about 35 lb of water, the time required to fill each can was indicated by the distance between marks on the recorder chart.

2.3. Modification to Apparatus

After the apparatus had been set up, several modifications in the equipment and its use were found necessary in order to obtain the desired measurements. For example, to secure a smooth, steady flow of water through the system, an auxiliary storage tank was added on the floor above the main setup. Water flowed from this tank through an orifice box to a circular tank below, which was 96 in. in diameter and 54 in. high, and thence to the constant-level tank that supplied the transparent pipe. The orifice box permitted a reproducible regulation of the flow rate. Water issued from the box downward in jets which were converted to tranquil horizontal flow after the jets impinged on a large horizontal flat pan in contact with the water surface in the circular tank. An overflow pipe in the circular tank helped maintain the water level so that while observations were being made a steady flow of water under constant pressure was delivered to the constant-level tank. A 2-in. galvanized pipe, controlled by a parallel arrangement of a 2-in. and a ¾-in. gate valve, connected the circular tank to the constant-level tank.

In the constant-level tank the flow of water over the control weirs at first generated secondary currents which distorted the flow pattern through the bell-mouth. However, it was found that the quantity of water overflowing the weirs could be reduced to a mere trickle by carefully adjusting the supply valve. This trickle of water did not cause distortion of the flow pattern, but it did assure the observer that the water level in the tank and the pressure in the rectangular pipe were being kept very nearly constant.

Experience showed that when fresh water was added to the system to make up for overflow losses, a laminar flow regime would not develop so long as the water temperature varied by as much as 0.2° in 10 min. It was therefore necessary to circulate the fresh water through the system until a temperature equilibrium was obtained.

It was found that the black dye streamers were affected by the elevation of the flask that supplied the dye. If the flask was below a particular point, water from the rectangular pipe would enter the dye tube, whereas if the flask was too high, the dye would emerge as a jet and cause disturbances in the dye stream. To obtain sharp, straight streamers in regions of laminar flow, special supports were devised to permit careful adjustment of the elevation of the flask.

Throughout the study efforts were made to reduce or eliminate vibrations and noises that might disturb the water and set up regions of instability. However, within the range of flow rates at which laminar flow was obtained, normal vibrations and noises in the laboratory seemed to have less effect on the stability of laminar flow than did distorted velocity distribution at the pipe entrance, foreign matter or particles in the pipe, excessive temperature gradients, or possibly other unidentified factors.

3. Experimental Procedure and Observations

Five observers were used in the experiments. Three observers followed the progress of the slug of red dye and the resulting disturbance as the dye moved downstream. Each of the three marked the time of an observed event by a signal impressed on a single-channel recorder, the signal from each being attenuated a characteristic amount by series resistors for purposes of identification. A fourth observer recorded the temperature at approximate 30-sec intervals throughout the run.

As soon as straight, parallel dye streams throughout the length of the rectangular pipe indicated the presence of laminar flow, the sampling of water was begun by the fifth observer. Immediately following the filling of the second sample can, a measured quantity of red dye was squirted forcefully into the rectangular pipe by the dye injector. Then foot by foot the first observer marked, on the recorder, the passage of the red dye downstream. After 3 or 4 ft of travel, the front of the dye stream took on a parabolic or bullet-nosed appearance that was sharply defined in the vertical plane.

It was noticed that some time after the front end of the red dye passed each of the tubes supplying black dye, a fresh streamer of black dye would wave violently like a flag in a wind storm. The second observer recorded the time and location of this phenomenon for each fresh dye streamer as an indication of the passage of the front of the mass of disturbed water.

The third observer followed the rear of the disturbance, i.e., the boundary between sharp, straight dye lines upstream and the disordered dye lines downstream. He marked the time on the recorder for each foot this boundary progressed downstream. There was some uncertainty as to when the boundary first existed because the mechanism of turbulent regeneration in the particular rectangular pipe used in this investigation was a succession of pulses, each of which acted on the straight dye streamer to start a bulge at a point 6 or 8 in. upstream from the last irregularity in the dye streamer. The bulge would increase in amplitude and suddenly the whole region between the initial pulse and the previously disturbed mass downstream would appear to be identically disturbed. Although some of the straight dye streamers behind the disturbance were being distorted continuously, the rate at which this occurred was such that the whole disturbed mass of water moved downstream and could be followed to within a foot of the exit where the flow began to accelerate into the 1¼-in. openings. Eventually the disturbed mass of water passed on out the exit, leaving the flow in the pipe free from disturbance.

The collected water samples were weighed on a Howe beam scale. The density and viscosity of the

water at the measured temperature were assumed to conform, within the limits of experimental error, to the values given in standard tables; consequently they were not measured.

It was originally planned to make triplicate runs for each flow rate studied. The three runs of each set were to differ from one another only as a result of using different control orifices that had the same nominal diameter but different locations in the orifice box. However, flow conditions in the transparent pipe were found to vary with the location of the control orifices in the box. It was therefore not feasible to make use of the triplicates in analyzing the data. Instead, some runs were repeated to obtain a measure of reproducibility.

4. Data Processing

4.1. Reynolds Number

It is well known that the parameter which characterizes the relative importance of viscous action in a moving fluid is the Reynolds number. It will be used in this paper to aid in physically classifying the 27 different runs and will be denoted by the symbol R as defined by

$$R=\frac{\rho d\overline{U}}{\mu},$$

where ρ=density, d=4×hydraulic radius, $\overline{U}$=mean velocity in the pipe, and μ=absolute viscosity. The hydraulic radius is the ratio of the cross-section area, A, of the pipe to the wetted perimeter, P, so that $d=4A/P$.

The value of $\overline{U}$ was determined from weighed samples of water taken at successive time intervals. A fourth-degree polynomial was fitted to the data with the aid of SEAC to obtain $W=f(T)$, where W is the total mass of water collected at the end of time T. The mean velocity was then obtained by

$$\overline{U}=\frac{dW/dT}{A\rho}$$

and the Reynolds number by

$$R=\frac{4(dW/dT)}{\mu P}.$$

The Reynolds number associated with the runs illustrated in this paper are mean values representing the conditions existing during the run.

4.2. Time-Distance Relations

To make use of the data obtained in these 27 runs, several relationships were considered for study. The simplest relationship, time and distance, was graphed for each of the runs with time as a function of distance traveled by the vertex of the parabolic-shaped front of the dye. Also time was graphed as a function of the distance traveled by the front of the disturbance, and by the rear of the disturbance. Some of these graphs are reproduced here in figures 2 and 3 to illustrate some charactersitics of isolated disturbances superimposed on laminar flow.

The several samples of the time-distance relationship in figure 2 illustrate the general behavior and the irregularities that at times appear. Common to all of the graphs shown for the front of the dye is the essentially straight line of points indicating that the velocity of the front of the dye was constant throughout each run. In contrast to this regularity, the graphs of the front and the rear of the disturbance varied considerably. For example, during run 1R a spot of spontaneous turbulence was noticed approaching the rear of the disturbance from upstream. The discontinuity in the graph marks the joining of this spot with the main turbulent slug, and the step in the curve is the time required for the spot to pass the observation point and leave the upstream part of the pipe free of disturbance. A larger step is seen to occur in run 12, this time from a spontaneous disturbance originating farther upstream from the injector-caused disturbance and accordingly producing a longer disturbed region and requiring more time to pass by the observation point.

Another feature is illustrated by an early termination of the data for the rear of the disturbance in certain runs. This signifies that disordered motions could no longer be observed and apparently had died out as in runs 7R, 8, 9, 17, and 17R. The phenomenon was generally associated with the lower Reynolds numbers, with run 7 appearing to be just enough above a borderline to escape the effect. The curves of figure 2 show that the behavior of the disturbances can be divided roughly into two types: Those at the higher Reynolds numbers where the rear of the disturbance moved at approximately a constant rate, and those at the lower Reynolds numbers where the rear moved at a rate changing with distance along the pipe.

4.3. Growth of the Disturbance

The primary purpose of obtaining the data illustrated in figure 2 was to determine what happened to the disturbance after it left the point of origin and progressed downstream through the pipe. By observing the dye streamers it was apparent that the disturbance produced a turbulent region consisting initially of the turbulent motions caused by the fluid injection. While the subsequent behavior was not completely consistent, as shown by figure 2, it was apparent that turbulent motions would persist causing the extent of the region to grow. Since growth in length was an indication of whether the motions were dying out or reinforcing themselves, the time-distance data were used to determine the length of the region as a function of the distance of travel and the Reynolds number.

By referring to figure 3, which is an example of a run free from extraneous effects, one may see that at any given time T after the introduction of the disturbance the front of the dye is at a distance

X_F and the rear of the turbulent region is at a distance X_R from the origin. Therefore at time T the region between the front and rear occupies the length $(X_F - X_R)$.

The data for each run were smoothed by least-square computations on SEAC. The values of T as expressed by a fourth-degree polynomial in X_F are denoted T_F; T_R is the similarly adjusted value of T as a function of X_R. The adjusted values of T were used as a parameter to get a smoothed relationship between simultaneous values of X_F and X_R. Having obtained values of X_R corresponding to values of X_F, successive values of $(X_F - X_R)$ could be determined for each of the integral values of X_F. The successive differences of the values of $(X_F - X_R)$ provided a measure of the change in length of the region for successive distances along the pipe, X_F.

Figure 4 is a summary plot showing how the change in length of the disturbed region $\Delta(X_F - X_R)$ varies with X_F along the pipe. For run 14 the value of $\Delta(X_F - X_R)$ appears to approach some constant value as X_F increases. There is uncertainty about

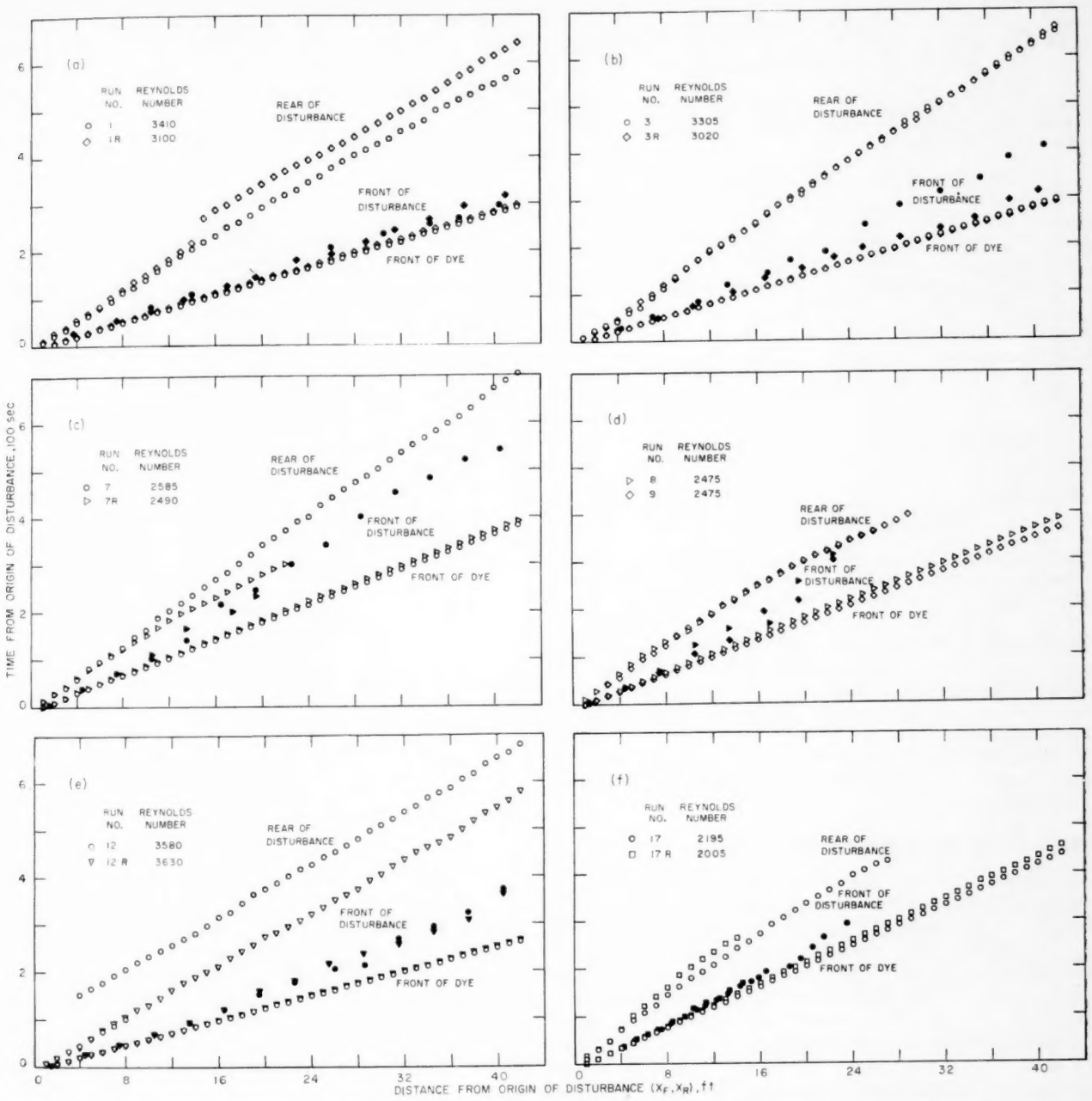

FIGURE 2. *Time-distance relationships for twelve runs showing variations in behavior of an isolated disturbance superimposed on laminar flow.*

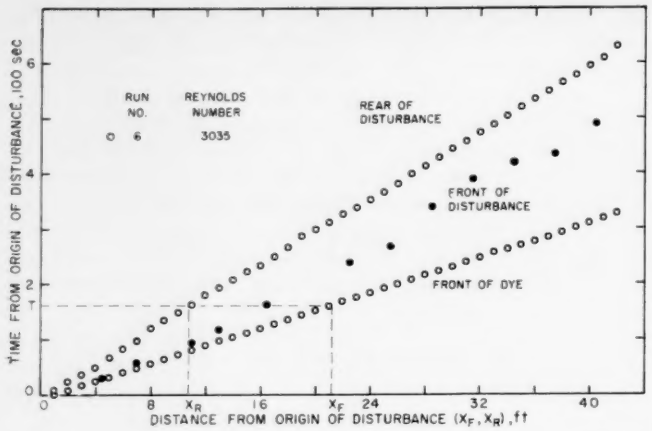

FIGURE 3. *Time-distance relationship for a single run to show that at time* T *the region between* X_F *and* X_R *occupies the length* $(X_F - X_R)$.

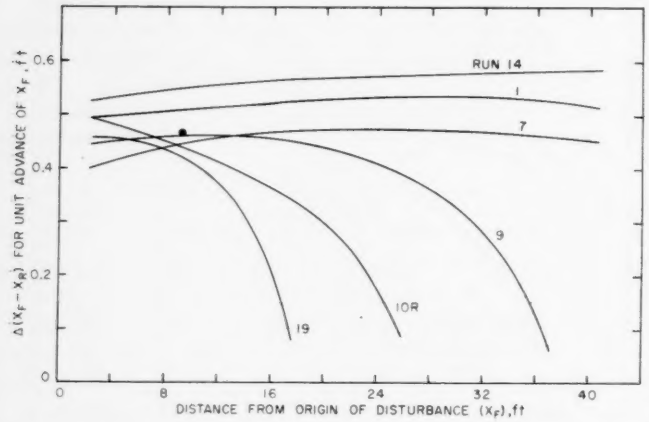

FIGURE 4. *Selected runs to show that the relationship of the change in length of* $(X_F - X_R)$ *to the distance traveled by the front,* X_F, *suggests a system of curves.*

the possible behavior of runs 1 and 7 beyond the range shown, but in runs 9, 10R, and 19 the quantity $\Delta(X_F - X_R)$ appears to approach zero as X_F increases. This method of processing the data demonstrates experimentally that at the low rates of flow a disturbance will cease to grow, but if the flow rate is high enough, the disturbance will increase in length at a steady rate.

4.4. Velocity of Propagation of Disturbed Regions

At this stage of the analysis, a mathematical functional relationship has not been found between X_F and T_F, between X_R and T_R, or between X_R and X_F; however, the relation has been expressed through tabulated data and by approximating polynomials. The derivatives of the polynomials, dX_R/dT_R and dX_F/dT_F, could be expected to give reasonably close approximations of the velocities U_R and U_F. The ratio of these velocities as a function of R was first considered for the location $X_F=5$. When these were plotted, the wide scatter of points for the 27 runs formed no recognizable pattern. To explore the possibility that some recognizable order might be found to exist among these quantities as the disturbances moved downstream, computations were made for four additional locations along the pipe. These progressive relationships formed the patterns shown in figures 5(a) to 5(e).

While the scatter of the points was large, due mainly to the irregularities illustrated in figure 2, it was possible to draw curves that enclosed the majority of the points in each plot. These curves were extended beyond the Reynolds-number range of the experiment on the basis of the indicated trend, as X_F increased, and on the assumption that at low Reynolds numbers the ratio of velocities would be essentially unity and at the higher Reynolds numbers the ratio would approach some constant value, such as 0.4, asymptotically. For each of the five locations along the pipe the initial envelope curves were sketched and then a curve of the following form was fitted to them:

$$U_R/U_F = 1 - 0.6 \exp(-b/R^c), \qquad (1)$$

where the coefficient 0.6 was chosen to make curves of U_R/U_F approach the asymtotic value indicated in figure 5 and b and c were chosen after successive approximations. A representative mean curve (curve B in each plot) was computed using parameters that placed it approximately half way between the two envelopes. Where these "B" curves are collected in figure 5(f), a crossing over is seen to occur in the neighborhood of Reynolds number of 2,700, suggesting that this might indicate critical values. To explore this possibility, the particular values $R=2{,}700$ and $U_R/U_F=0.51$, were substituted in eq (1) to produce an equation containing b and c. By solving the equation for b and substituting in eq (1) again, the following relationship is obtained

$$\frac{U_R}{U_F} = 1 - 0.6 \exp\left[-\frac{(2{,}700)^c \log^{\frac{1}{2}}(0.6/0.49)}{R^c}\right]. \qquad (2)$$

Equation (2) has been plotted in figure 6 for odd integral values of c from 1 to 15. It turns out that the curves for $c=3$ and $c=7$ approximate very closely the curves for $X_F=5$ and $X_F=25$ of figure 5(f), which suggests a functional relation of c and X_F. Equation (2) may be rewritten without affecting the relationships to give

$$\frac{U_R}{U_F} = 1 - 0.6 \exp[-\log(0.6/0.49) \exp(c \log\left(\frac{2{,}700}{R}\right)]. \qquad (3)$$

This form of the equation was found to be useful in computing U_R/U_F when R is held constant and c varies as a function of X_F. The tabulated values of figure 5(f) give a numerical relation of c to X_F for five values of X_F. These are plotted in figure 7 and a curve has been drawn as a reasonable interpretation of the behavior of the function in the extrapolated range. Using values of c taken from the curve for X_F at 2-ft intervals, a system or family of curves was computed for 16 values of R from 1,200 to 4,200. These are the curves shown in figure 8.

Several features are at once evident from this family of curves. The lower the Reynolds number the more rapidly U_R/U_F approaches unity with distance downstream. For the Reynolds number 2,700 the straight line $U_R/U_F=0.51$ divides the field into two parts wherein the curves in the upper part approach unity and those in the lower part decrease to a lower value than that existing at the origin. These trends are taken to be an indication of changes in the vigor of the motions. For example, an upward trend of the curves, which indicates a faster downstream convection of the rear, is taken to mean a damping out of the disturbance.

To assist in the discussion to follow, these same phenomena have been represented on an approximate time basis in figure 9. Here T_F is the averaged time taken by the front to travel to the point X_F. The approximation, which for the intended purpose of the figure is assumed to be permissible, involved using a constant factor, K, to reduce Reynolds number to velocity of the front in each case.

5. Discussion of Results

Figures 8 and 9 permit certain inferences to be drawn about the behavior of turbulent disturbances in a pipe. First of all there is the not unexpected

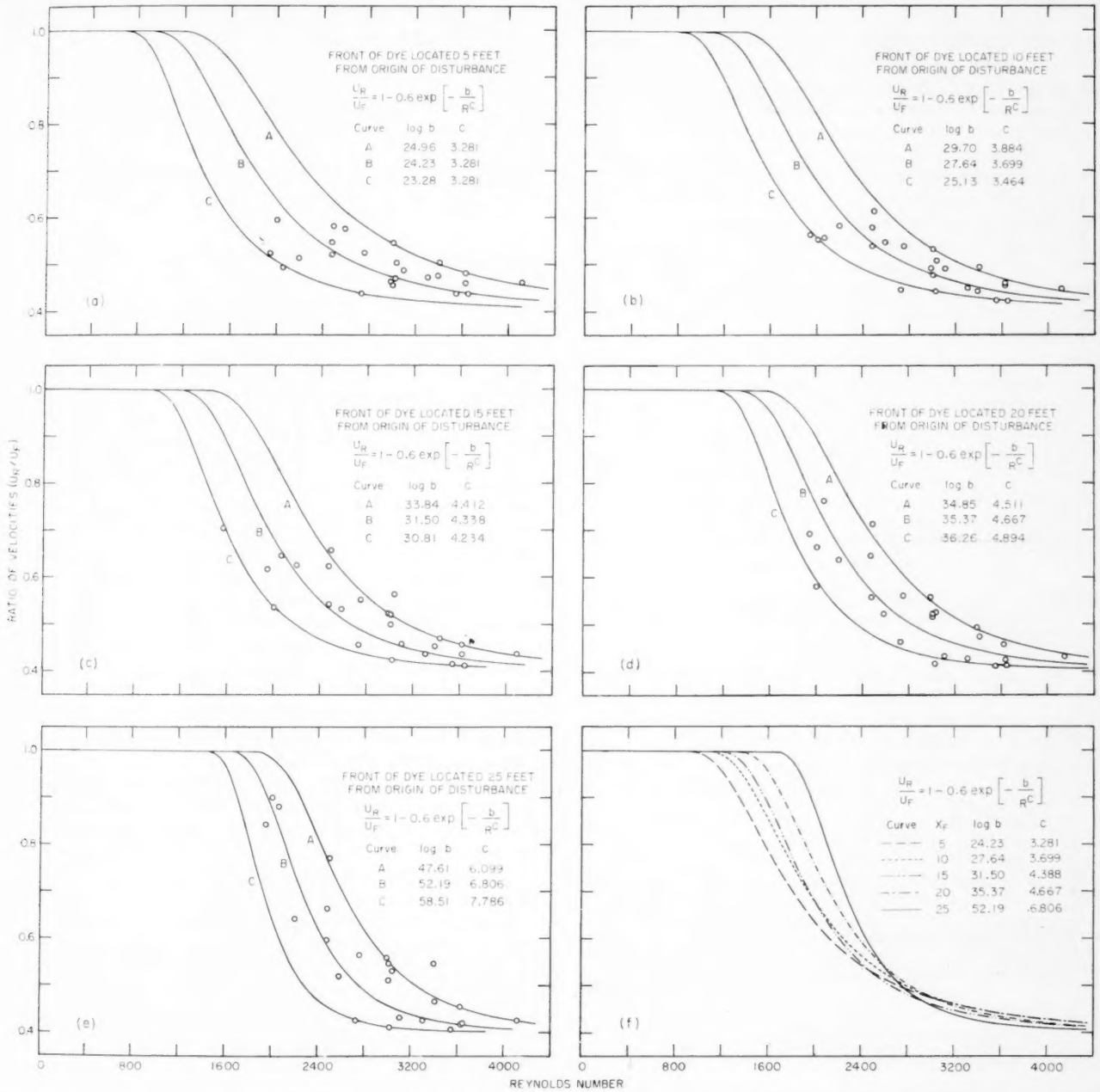
FRONT OF DYE LOCATED 5 FEET FROM ORIGIN OF DISTURBANCE
$\frac{U_R}{U_F} = 1 - 0.6 \exp\left[-\frac{b}{R^C}\right]$
Curve log b C
A 24.96 3.281
B 24.23 3.281
C 23.28 3.281
(a)
FRONT OF DYE LOCATED 10 FEET FROM ORIGIN OF DISTURBANCE
$\frac{U_R}{U_F} = 1 - 0.6 \exp\left[-\frac{b}{R^C}\right]$
Curve log b C
A 29.70 3.884
B 27.64 3.699
C 25.13 3.464
(b)
FRONT OF DYE LOCATED 15 FEET FROM ORIGIN OF DISTURBANCE
$\frac{U_R}{U_F} = 1 - 0.6 \exp\left[-\frac{b}{R^C}\right]$
Curve log b C
A 33.84 4.412
B 31.50 4.338
C 30.81 4.234
(c)
FRONT OF DYE LOCATED 20 FEET FROM ORIGIN OF DISTURBANCE
$\frac{U_R}{U_F} = 1 - 0.6 \exp\left[-\frac{b}{R^C}\right]$
Curve log b C
A 34.85 4.511
B 35.37 4.667
C 36.26 4.894
(d)
FRONT OF DYE LOCATED 25 FEET FROM ORIGIN OF DISTURBANCE
$\frac{U_R}{U_F} = 1 - 0.6 \exp\left[-\frac{b}{R^C}\right]$
Curve log b C
A 47.61 6.099
B 52.19 6.806
C 58.51 7.786
(e)
$\frac{U_R}{U_F} = 1 - 0.6 \exp\left[-\frac{b}{R^C}\right]$
Curve X_F log b C
5 24.23 3.281
10 27.64 3.699
15 31.50 4.388
20 35.37 4.667
25 52.19 6.806
(f)
RATIO OF VELOCITIES (U_R/U_F)
REYNOLDS NUMBER
0 800 1600 2400 3200 4000
0.4 0.6 0.8 1.0

FIGURE 5. *Sets of curves at 5-ft intervals of X_F showing the development of a trend that suggests the curve fitting to eq (1); and showing the emergence of critical values when the "B" curves are brought together.*

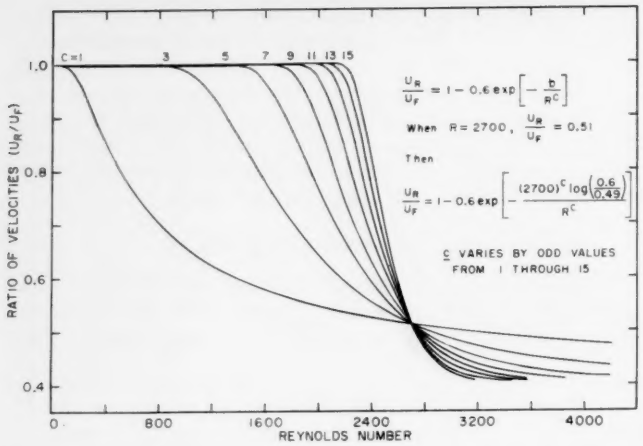

FIGURE 6. *System of curves resulting from eq (2) when the parameter "c" is varied through odd integral values.*

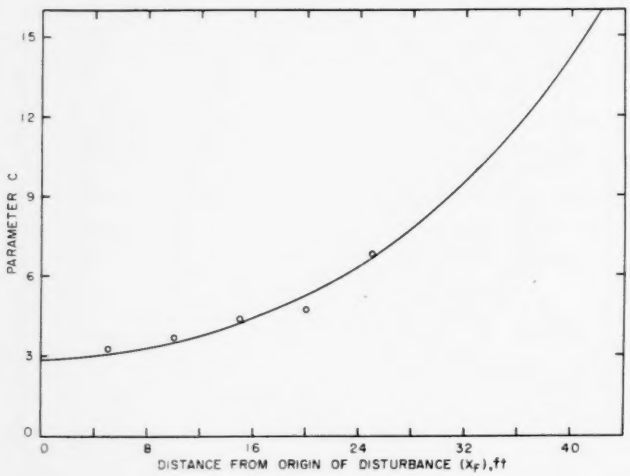

FIGURE 7. *An extrapolation of the values of parameter "c" to cover the 42-ft range of X_F in this investigation.*

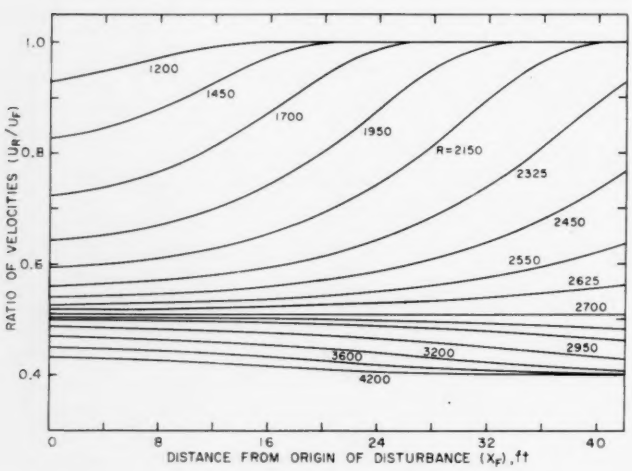

FIGURE 8. *A system of curves computed for particular value of Reynolds number when for eq (3) the values of parameters "c" are taken from figure 7 at 2-ft intervals of X_F.*

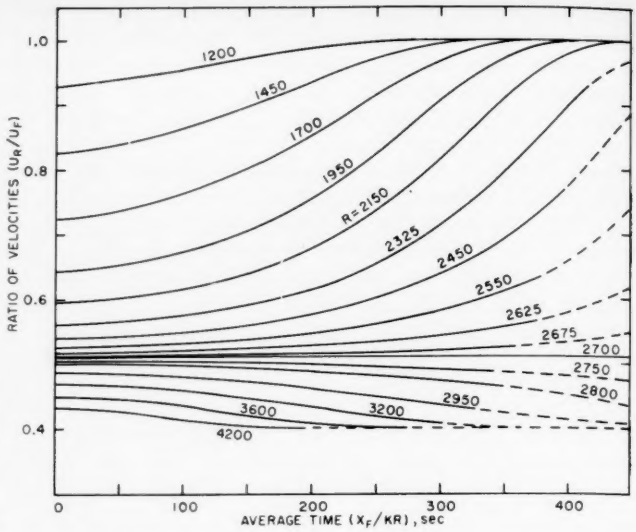

FIGURE 9. *A system of curves differing from those of figure 8 by having for the abscissa an averaged time (X_F/KR) where for each curve the values of K and R are constant.*

emergence of a critical Reynolds number above which turbulent motions once started will persist indefinitely and below which they will eventually die out. The value of 2,700 found here falls within the range of the values published in [4] for straight pipes of various cross section. More significant, however, from the standpoint of novelty is the behavior of a disturbance below and above the critical value. When a stirring motion (here termed the disturbance) is introduced at a very low Reynolds number, it quickly dies out. As the Reynolds number is increased, it persists longer and longer. This shows that there is a reinforcement of the motions which increases with Reynolds number and which, while not sufficient to balance the damping action of viscosity, is sufficient to prolong the life of the motion. The disturbance motion will eventually die out at all Reynolds numbers below a critical value such as 2,700. The effect at higher Reynolds numbers, where U_R/U_F progresses toward lower values, may be interpreted to mean that the initial strength was not as great as that capable of being maintained by the shear flow.

Several factors not accounted for in this paper, such as the initial strength of the disturbance, must affect the trends; therefore the diagrams should not be regarded as universal even for this particular pipe. The phenomena exhibited here are, however, believed to be universally applicable to pipe flow.

Among the foregoing phenomena, perhaps the one that has been least apparent in past experiments on pipe flow, and therefore not previously emphasized, is the one showing that below a critical value the life of a disturbance is influenced by the Reynolds number. This aspect of turbulence in pipes has usually been dismissed by stating that below the critical Reynolds number the flow will return to the laminar state no matter how much it has been disturbed. Little has been written previously on how

a turbulent-like motion, when once introduced, will exist below the critical Reynolds number. Figures 8 and 9 show that the lifetime of a disturbance is prolonged more and more as the Reynolds number increases. This effect can be of some importance in practical situations where mixing is involved, either accidental or intentional, and may modify the flow field for various distances from the source of the disturbance. Just what the nature of the source might be and how disturbances might occur in practice are subjects requiring further investigation.

The most comprehensive previous work on the propagation and character of turbulent slugs is that of Lindgren [2, 3] conducted in straight round pipes. He used the birefringent characteristics of bentonite clay suspended in water to observe turbulent "flashes". One aspect of his results on the velocity of the front and rear of such flashes relative to the mean-flow velocity is shown in figure 10 by the dashed curves. The results of the experiment reported here are shown by the points and the solid curve. Lindgren's observations pertain to flashes that occurred randomly, presumably from disturbed entrance conditions, and the ones shown were made in a 6-mm tube 8.5 m from the entrance. The part of the data from this investigation, shown in the figure, pertains to the case where the dye front had traveled 15 ft from the origin. For these conditions the results for $U_R/\overline{U}$ obtained in the two investigations are much alike. Lindgren's front velocity, designated here as U_{FT}, is really the velocity of the leading end of the turbulent field. A comparable quantity, represented by the solid symbols in figures 2 and 3, could not be reliably calculated from the author's data. The velocity of the front of the dye, U_F is included in figure 10 as the ratio $U_F/\overline{U}$. The horizontal line is the theoretical value of $U_c/\overline{U}(=1.772)$ for laminar flow in the rectangular pipe as given in [5], where U_c is the velocity at the center. The agreement between U_F and U_c shows that the dye front extended forward into the laminar regime and thus outran the turbulent field.

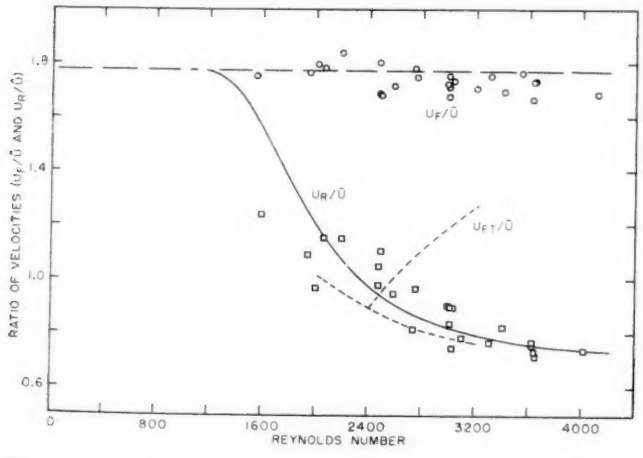

FIGURE 10. *A comparison of author's data for* $U_R/\overline{U}_F$ *with that of Lindgren (ref. 2); and for* $U_F/\overline{U}$ *with the theoretical value computed from ref. 5.*

6. Conclusions

From observations of turbulent motions, created artificially at an upstream point in a rectangular pipe and allowed to pass on downstream in an otherwise fully developed laminar flow, the following conclusions are drawn:

1. It could be ascertained definitely from dye indicators that there developed a slug of turbulent pipe flow, preceded and followed by laminar flow.

2. The turbulent slug will grow indefinitely in length as it moves along the pipe if the Reynolds number of the flow is above a critical value, estimated to be 2,700. Below this critical value the growth eventually ceases.

3. Dye injected with the disturbance and also introduced as streamers is suitable for observing the rear of the slug but is poorly suited for observing the front end of the disturbance. The farthest progress of the dye, which is here called the front, is in laminar flow and moving with the centerline velocity.

4. The ratio of the velocity of the rear to the velocity of the front serves as a criterion of the vigor of the turbulent motions, and therefore is an indication of whether the motions are being sustained or are dying out as the slug moves downstream.

5. A velocity of the rear less than that of the front is taken to mean that the turbulent motions are "alive"; if the velocity of the rear increases with distance, they are dying out; if it is constant, they are maintaining their original vigor; and if it is decreasing with distance, they are growing in strength.

6. The survival time of the initially stimulated turbulent motions depends on the Reynolds number. There is a survival time below the critical value which increases as the Reynolds number increases. At the critical value and above, the survival time is infinite.

The author acknowledges the assistance of Walter Washington, Edwin Ford, and Stanley Benowitz in carrying out the experimental program. Grateful acknowledgment is extended also to W. J. Youden whose counseling provided an essential contribution to the manner of taking and processing data, and to G. B. Schubauer who proposed a study of this kind and offered many valuable suggestions throughout the course of the investigation.

7. References

[1] J. Rotta, Experimenteller Beitrag zur Entstehung turbulenter Strömung im Rohr., Ingenieur-Archiv **24**, 258, (1956).

[2] E. Rune Lindgren, The transition process and other phenomena in viscous flow, Arkiv för Fysik **12**, 1 (1957).

[3] E. Rune Lindgren, Liquid flow in tubes, II, Arkiv för Fysik **15**, 37 (1959).

[4] S. Goldstein, Modern developments in fluid dynamics **1**, 319 (Oxford Univ. Press, 1938).

[5] H. L. Dryden, F. D. Murnaghan, H. Bateman, Hydrodynamics, Bull. National Research Council, No. 84 (Feb. 1932).

WASHINGTON, D.C. (Paper 64A4–50)

JOURNAL OF RESEARCH of the National Bureau of Standards—A. Physics and Chemistry
Vol. 64A, No. 4, July–August 1960

Standard of Spectral Radiance for the Region of 0.25 to 2.6 Microns

Ralph Stair, Russell G. Johnston, and E. W. Halbach

(March 1, 1960)

This paper contains information relating to the setting up of standard blackbodies for use through the temperature range of about 1,400° to 2,400° K and their use in the calibration of tungsten strip lamps as laboratory standards of spectral radiance for the wavelength region of 0.25 to 2.6 microns. A graphite blackbody is described and representative data are given on the spectral characteristics of the new lamp standard as compared to blackbodies at several selected temperatures.

1. Introduction

Fifty years ago the principal need in the evaluation of radiant energy was a convenient standard against which a radiometer might be calibrated. Although several crude standards of total radiance in the form of oil lamps or candles existed about 1900, the establishment of the carbon filament lamp [1, 2, 3][1] provided a convenient working standard for a limited range of total radiance. Then, as today, the blackbody was considered the reference standard, but its use was relegated only to the few primary scientific laboratories. The carbon filament standard has received wide acceptance in scientific research, not only in this country but throughout the world. It has been, and remains, extremely useful, but within recent years has been recognized as being inadequate to cover many new uses wherein spectral energy distributions were required.

It is to fulfill this latter requirement that a new secondary standard of spectral radiance in the form of a tungsten strip lamp has been set up. Again the blackbody has been employed as the reference source in the development of the new standard.

It has been established that the total and spectral radiation characteristics of a blackbody may be defined in terms of certain equations or laws. Planck's radiation law relates the radiance N_λ at a particular wavelength to the absolute temperature T by the relationship

$$N_\lambda = \frac{C_1 \lambda^{-5}}{e^{C_2/\lambda T} - 1},$$

wherein C_1 and C_2 are the first and second radiation constants having the dimensions watts/cm² and cm/degree, respectively. The exact values attached to these depend not only on the units employed in expressing N_λ, but also upon the most probable values of the various fundamental atomic constants.

In the present case the following values have been employed for the various parameters in the Planck equation:

λ = wavelength in cm;
$C_1 = 1.19088 \times 10^{-12}$ watt/cm²;
$C_2 = 1.4380$ cm/°K;
N_λ = watt cm^{-2} ster^{-1}/cm wavelength interval.

Much research has been carried out on tungsten lamps, in particular regarding the spectral emissivity of tungsten [4, 5, 6, 7, 16, 17, 18]. Although all the results are not in perfect agreement, it is generally agreed that with reasonable caution the emissivity of pure clean tungsten ribbon remains fairly constant throughout the life of the lamp. Recently, in many laboratories [8, 10, 11, 12, 15] the determination of the spectral distribution of radiant energy from a tungsten filament lamp has been obtained through making use of the published values of the emissivity of tungsten and the observed color temperature or brightness temperature of the filament. These calculations are based upon a doubtful assumption that all samples of tungsten are identical in emissivity. No account was taken of the effects of impurities present, or of the size and shape of the filament or of its mechanical or crystalline structure [4, 6]. All these properties affect markedly the true spectral and total emissivity. Furthermore, it has been found that interreflections within the lamp envelope [6] affect the total spectral radiation from a particular tungsten strip. In order to obtain the correct spectral radiance of a lamp, it becomes necessary that the particular lamp as set up for use be calibrated against a blackbody.

2. Apparatus and Method

Before discussing the apparatus and method employed in comparing a group of tungsten ribbon strip lamps with blackbodies at various temperatures a discussion is in order relative to the type of lamp chosen.

Investigations by Worthing [4a] many years ago resulted in the accumulation of considerable information relating to the radiation characteristics of tungsten, in particular in regard to the effects of the angle (polarization, etc.) from which the filament is

[1] Figures in brackets indicate the literature references at the end of this paper.

viewed. These results proved the necessity of using a flat-ribbon filament to insure a reproducible source. A lamp was designed at the National Bureau of Standards a number of years ago which entailed the foregoing qualities and was accepted for commercial production by the General Electric Co. as their type G.E. 30A/T24/3. This lamp was chosen for use as the new standard (see fig. 1). It has a mogul bipost base and a nominal rating of 30 amp at 6 v. Radiant energy is emitted from the flat strip filament through a 1¼-in. fused silica window placed parallel to and at a distance of about 3 to 4 in. from the plane of the filament. This separation of the window (necessitated by a graded seal) assists greatly in reducing the deposit of metallic tungsten on the lamp window as the lamp ages.

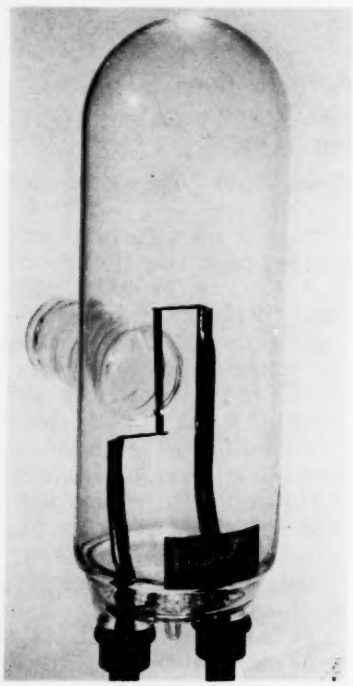

FIGURE 1. *Tungsten ribbon strip lamp standard of spectral radiance.*

The principal apparatus employed in comparing the radiant energy from the lamp with that of the blackbody was set up as shown in figure 2 to cover the spectral region from 0.7 to 2.6 μ. The lamp and the blackbody were mounted side by side on an optical bench (constructed from a lathe bed and table) so they could alternately be placed at the focal point of the auxiliary optical system. In figure 3 is shown the monochromator mounted on the optical bench with the auxiliary optics rigidly secured on the front of the monochromator. This arrangement was employed for the spectral region of 0.25 to 0.75 μ wherein a high-temperature graphite blackbody was used. It was possible to move the monochromator so that the lamp and the blackbody would be alternately at the correct object distance of the auxiliary optics.

The auxiliary optics consisted of a plane mirror and a spherical mirror having a 71-cm radius of curvature. The placing of the lamp and the blackbody alternately at the same position insured equal light paths and the use of identical optics.

The blackbody indicated in figure 2, which was operated up to 1,400° K, was constructed of a casting of an alloy of 80 percent nickel and 20 percent chromium and had a 3-in. outside diameter, was 6 in. in length, and had a wall thickness of ½ in. The

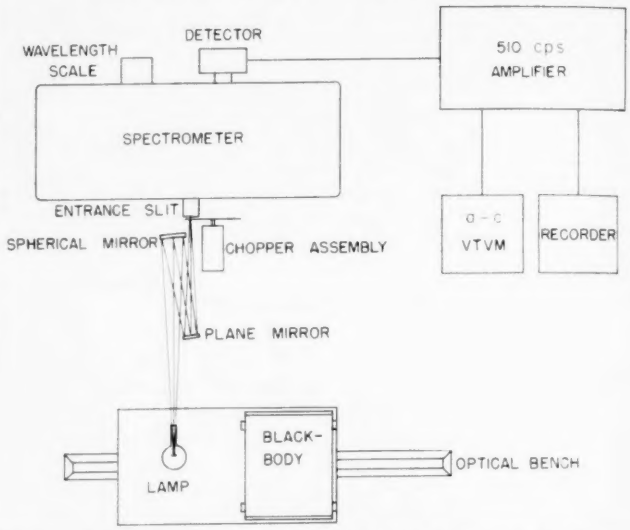

FIGURE 2. *Instrumental set-up of blackbody, monochromator, lamp and associated equipment for the wavelength region of 0.7 to 2.6 microns.*

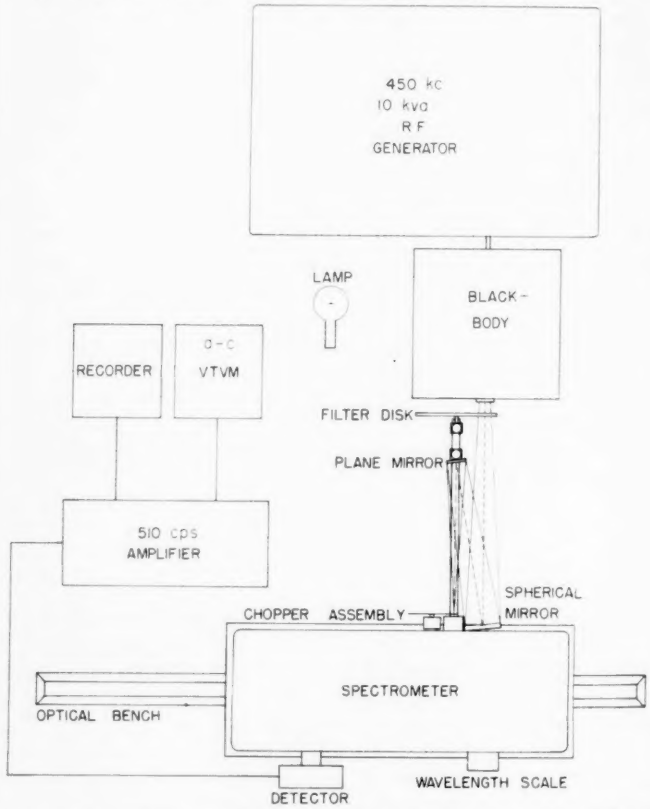

FIGURE 3. *Instrumental setup of blackbody, monochromator, lamp and associated equipment for the wavelength region of 0.25 to 0.75 micron.*

low reflectivity of this oxidized metal coupled with the small aperture (3/16 in. by 1/2 in.) as compared with the internal surface area resulted in a blackbody of extremely high effective emissivity. The high heat capacity of the associated furnace gave the blackbody a very high thermal stability, making manual temperature regulation easy. Further information on a similar blackbody employed as a standard at longer wavelengths has been published elsewhere [14].

The blackbody employed for the shorter wavelengths and shown in figures 3 and 4 was constructed of high purity graphite. It consists of a cylindrical enclosure 4 1/2 in. long and 1 1/2 in. in diameter, having walls 3/16 in. thick. The exit end of the tube has a 3/8-in. opening shielded by a conical graphite endpiece 3/4 in. long (see fig. 4.) The very low reflectivity of the graphite (rough machined surface) and the relatively small aperture (as compared to the total internal surface) resulted in a blackbody of high effective emissivity.

This graphite blackbody is heated by induction inside a water-cooled coil by a radiofrequency generator operating at 450 kc. The blackbody tube is insulated by firmly packed boron nitride powder inside a high temperature porcelain tube (closed at one end) 4 in. in outside diameter and 6 in. in length. An alundum ceramic tube placed midway between the graphite core and the high temperature porcelain tube increased the mechanical stability of the unit.

Depreciation of the graphite at high temperature was reduced by enclosing the blackbody unit in an airtight chamber (see fig. 4) through which dry helium was passed. The concentration of oxygen was further reduced by heating copper coils within the chamber preceding each operation of the blackbody.

The spectral transmittance of the fused silica window of the enclosure was measured and the necessary corrections were made for temperature measurements and spectral radiance.

This blackbody is many times larger than the small tungsten enclosures often used in high temperature work. A much larger opening can be employed thereby making possible the use of the entire slit of the usual spectroradiometer.

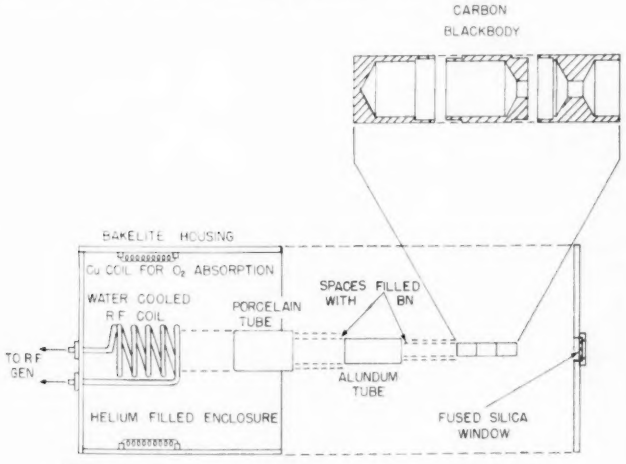

FIGURE 4. *Graphite high temperature blackbody.*

Leiss double quartz prism monochromators with relative aperture ranges of *F*/6.4 to *F*/7.2 were employed as shown in figures 2 and 3. The detector used at the exit slit of the monochromator for the wavelengths from 0.7 to 2.6 μ was an uncooled lead sulfide cell, while for the wavelength range of 0.25 to 0.75 μ a photomultiplier, type 1P28 was employed [9]. In all cases care was taken (through the use of filters to reduce the light intensity when required, and by other means) in using the photomultiplier to make certain that the detector was not exposed to excessive radiation which might produce a change or nonlinear character in the photoelectric response.

The radiant energy beam was mechanically chopped at 510 cps and the detector signal amplified by a special tuned amplifier [15]. Usually the output signal was read on an a-c vacuum tube voltmeter and manually recorded. However, equipment was available (and occasionally used) for recording the data with a strip chart recorder connected to the d-c output of the tuned amplifier.

The temperature of the blackbody used at 1,400° K (and below) was determined by a platinum versus platinum 10 percent rhodium thermocouple calibrated by the heat division of the National Bureau of Standards. The same laboratory calibrated the optical pyrometer employed to determine the temperatures from 1,400° to 2,400° K in the graphite blackbody. Check measurements between the optical pyrometer and the thermocouple usually were in agreement within 2° to 3° K. Calibrations of the optical pyrometer by the heat division before and following the measurements reported in this paper were in agreement to about 1° K.

Tests using thermocouples placed at various positions and by observations with the optical pyrometer indicated closely uniform temperatures within the low temperature blackbody. Similar tests with the optical pyrometer indicated a similar uniform condition within the high-temperature enclosure.

Each lamp was seasoned by operation on alternating current at 35 amp (about 2,470° K) for 2 hr. During calibration the lamp current was controlled manually through the use of variable and stepdown transformers as described in a later paragraph (see fig. 5).

Each lamp was set up with the envelope vertical and with the section of the filament viewed horizontally through the center of the lamp window being employed in the measurements (no note was made of a notch placed in one edge of the lamp filament for another use). Through the use of the external optics (plane mirror and spherical mirror) a full size image of this section of the lamp filament was focused upon the entrance slit of the spectroradiometer. Hence, the physical dimensions of the spectrometer slit (set at about 0.5 mm by 5 mm) determined the source area employed in the measurements. Since the optical arrangement was identical for the lamp and the blackdody equal areas of the two sources were always being compared.

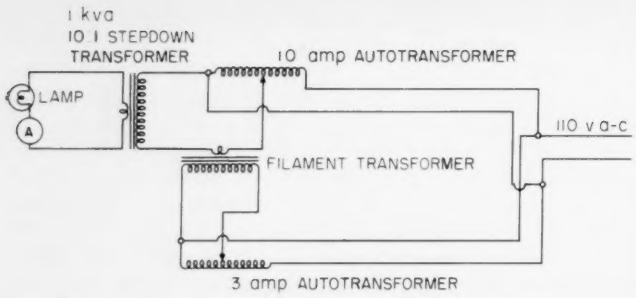

FIGURE 5. *Electrical circuit for lamp operation to give smooth current control.*

Readings were alternately taken on the blackbody and on the lamp for each wavelength setting throughout the spectral range. The blackbodies were operated at several selected temperatures so that the radiance from the lamp and the blackbody were approximately equal in a given region of the spectrum. At each wavelength a number of readings were taken (with changes in the temperature of the blackbody) such that in some cases the radiance of the lamp was greater than that of the blackbody while in others it was less than that of the blackbody. This procedure enabled us to keep the effect of any departure from linearity within the electronics in the detector circuitry as small as practicable.

3. Results

Data obtained upon two lamps as compared with the blackbodies are given in table 1. Other lamps result in slightly higher or lower values depending upon the characteristics of the particular lamp chosen. For the laboratory lamp standards more than 20 comparisons between the lamps and blackbodies were made within the shorter wavelength region (0.25 to 0.75μ). About 10 to 12 independent comparisons were made at the longer wavelengths. Due to the small magnitued of scatter of the results, little is to be gained by additional measurements.

The data of table 1 are tabulated in terms of radiance, microwatts per square centimeter at a distance of 1 m from a square millimeter area source, and for a wavelength interval of 0.1μ. Hence the radiant energy values are in a form directly applicable for use with a spectroradiometer of fixed entrance slit. Those who desire to make solid angle measurements may change the tabulated values to erg cm^{-2} $ster^{-1}\mu^{-1}sec^{-1}$ as reported by DeVos [6] simply by multiplying the recorded value by 10^8. Similarly, the data recorded in the DeVos tables may be reduced to the units employed herein by multiplying by 10^{-8} (within about 0.1 percent resulting from slightly different atomic constants employed in the DeVos calculations).

Although the data for all wavelengths are given on the same basis as regards the wavelength interval of 0.1 μ, in the experimental setup the actual instrumental spectral slit widths ranged from about 0.001 μ at 0.25 μ to 0.060 μ at 2.6 μ (being about 0.020 μ at 1.0 μ). The use of the 0.1 μ interval affects the absolute values but little for wavelengths longer than about 1 μ. However, for the shorter wavelengths where the spectral energy curve exhibits a greater degree of curvature, higher accuracy may be obtained

TABLE 1. *Spectral radiance of blackbodies and tungsten lamps* $= N_\lambda = P \times 10^{-q}$ *expressed in microwatts per square centimeter at 1 meter for a 1-mm² source and for a wavelength interval of 0.1 micron*

Wavelength	1,400° K blackbody		1,600° K blackbody		1,800° K blackbody		2,000° K blackbody		2,200° K blackbody		2,400° K blackbody		Lamp #20 25 amp		Lamp #20 30 amp		Lamp #16 35 amp	
μ	P	q	P	q	P	q	P	q	P	q	P	q	P	q	P	q	P	q
0.250	1.7493	12	2.9736	10	1.6145	8	3.9432	7	5.3871	6	4.7597	5					4.13	5
.260	6.9821	12	9.7412	10	4.5360	8	9.7969	7	1.2103	5	9.8342	5					9.59	5
.270	2.4973	11	2.9018	9	1.1720	7	2.2592	6	2.5429	5	1.9119	4					1.88	4
.280	8.1013	11	7.9434	9	2.8113	7	4.8756	6	5.0331	5	3.5211	4					3.40	4
.290	2.4084	10	2.0160	8	6.3092	7	9.9166	6	9.4458	5	6.1797	4					5.84	4
.300	6.6199	10	4.7810	8	1.3340	6	1.9128	5	1.6901	4	1.0386	3					9.72	4
.320	4.0740	9	2.2519	7	5.1031	6	6.1953	5	4.7772	4	2.6206	3					2.34	3
.350	4.0766	8	1.5976	6	2.7707	5	2.7157	4	1.7577	3	8.3334	3					7.00	3
.400	8.1943	7	2.0301	5	2.4646	4	1.8160	3	9.3067	3	3.6326	2					2.76	2
.450	7.8861	6	1.3677	4	1.2582	3	7.4259	3	3.1737	2	1.0648	1					7.27	2
.500	4.5642	5	5.9508	4	4.3847	3	2.1670	2	8.0096	2	2.3808	1	8.00	3	4.04	2	1.56	1
.550	1.8812	4	1.9255	3	1.1764	2	5.0096	2	1.6399	1	4.4073	1	1.88	2	8.14	2	2.72	1
.600	5.6287	4	4.7836	3	2.5267	2	9.5681	2	2.8441	1	7.0506	1	3.64	2	1.39	1	4.05	1
.650	1.4227	3	1.0214	2	4.7345	2	1.5838	1	4.4118	1	1.0192		6.24	2	2.13	1	5.66	1
.700	3.0045	3	1.8808	2	7.8326	2	2.4523	1	6.2392	1	1.3586		9.56	2	2.99	1	7.17	1
.750	5.6866	3	3.1435	2	1.1889	1	3.4470	1	8.2366	1	1.7026		1.35	1	3.74	1	8.59	1
.800	9.6470	3	4.8017	2	1.6731	1	4.5420	1	1.0284		2.0323		1.66	1	4.38	1		
.900	2.2294	2	9.2845	2	2.8163	1	6.8433	1	1.4153		2.5938		2.22	1	5.42	1		
1.000	4.1215	2	1.4883	1	4.0409	1	8.9872	1	1.7290		2.9841		2.74	1	6.12	1		
1.100	6.5110	2	2.0924	1	5.1891	1	1.0736		1.9472		3.2003		3.12	1	6.38	1		
1.200	9.1769	2	2.6762	1	6.1679	1	1.1992		2.0713		3.2694		3.32	1	6.41	1		
1.300	1.1883	1	3.1923	1	6.8898	1	1.2761		2.1154		3.2273		3.36	1	6.24	1		
1.400	1.4428	1	3.6135	1	7.3864	1	1.3103		2.0974		3.1089		3.39	1	5.94	1		
1.500	1.6672	1	3.9295	1	7.6649	1	1.3101		2.0349		2.9425		3.16	1	5.55	1		
1.600	1.8534	1	4.1431	1	7.7585	1	1.2839		1.9429		2.7499		2.96	1	5.04	1		
1.700	1.9982	1	4.2641	1	7.7037	1	1.2393		1.8331		2.5465		2.74	1	4.52	1		
1.800	2.1024	1	4.3055	1	7.5363	1	1.1825		1.7144		2.3427		2.45	1	3.94	1		
1.900	2.1690	1	4.2819		7.2874	1	1.1185		1.5929		2.1454		2.20	1	3.45	1		
2.000	2.2023	1	4.2071	1	6.9828	1	1.0508		1.4731		1.9585		1.97	1	3.03	1		
2.100	2.2072	1	4.0941	1	6.6434	1	9.8224	1	1.3576		1.7842		1.78	1	2.65	1		
2.200	2.1888	1	3.9531	1	6.2857	1	9.1466	1	1.2482		1.6235		1.58	1	2.37	1		
2.300	2.1516	1	3.7930	1	5.9212	1	8.4935	1	1.1458		1.4764		1.40	1	2.13	1		
2.400	2.0999	1	3.6214	1	5.5593	1	7.8705	1	1.0508		1.3425		1.26	1	1.92	1		
2.500	2.0372	1	3.4432	1	5.2060	1	7.2833	1	9.6317	1	1.2211		1.13	1	1.66	1		
2.600	1.9667	1	3.2633	1	4.8657	1	6.7335	1	8.8277	1	1.1113		1.02	1	1.52	1		

if the tabulated values be converted to a shorter wavelength interval corresponding more nearly to that employed in obtaining the data.

In the original comparisons with the blackbody the cone of radiant energy from the lamp was limited to approximately 5° and near normal to the plane of the lamp filament. If, in use, a larger angle is required it should be ascertained that the flux density is uniform and free of polarization throughout the added aperture.

Although the calibrations of the standards are given in terms of radiant power per cm² for the various wavelengths at a distance of 1 m, the lamps may be used at any convenient distance provided proper correction is made for the new distance. However, if there is excessive water vapor in the laboratory atmosphere, errors may result at the wavelengths of water vapor absorption. In the original calibrations any water vapor absorption effects cancelled out for the greater part since the measurements were made using essentially identical air paths.

The quality of the two blackbodies used in this work was determined by the method outlined by André Gouffé [13] and the first and second order approximations of the quality of the low temperature blackbody was found to be 0.999. The quality of the high temperature graphite blackbody was 0.996.

The certification of the optical pyrometer was given as ±2° from 1,000° to 1,400° K and ±6° from 1,400° to 2,300° K. This gives rise to an uncertainty of ½ to 2 percent in the longer wavelengths while in the shorter wavelengths the uncertainty increases to 1 to 4 percent. The uncertainty for the thermocouple was less than ±3° which would result in an uncertainty in the radiance not in excess of 2 percent.

If one assumes an ability to read the meters employed as two-fifths of the smallest division, this would lead to an uncertainty never more than 1.0 percent. The ability of the electronics to reproduce an output when a given signal is applied to the input is of the order of 1.0 percent.

It is estimated that the maximum uncertainty in the results ranges from about 8 percent at the shortest wavelengths to about 3 percent at the longest wavelengths.

4. Use of the Standards of Spectral Radiance

The auxiliary optics employed with this standard may be composed of two units such as those employed in the original calibrations (see figs. 2, 3, and 6), namely a plane mirror and a spherical mirror (each aluminized on the front surface). If the spherical mirror is placed at a distance from the lamp filament equal to its radius of curvature and the plane mirror set about one-third to two-fifths this distance from the spherical mirror, and facing it (at an angle of 10° or less), an image of the filament equal in size to that of the filament itself may be focused upon the spectrometer slit. Little distortion of the filament image occurs provided good optical surfaces are employed and all reflection angles are kept to less than 10°.

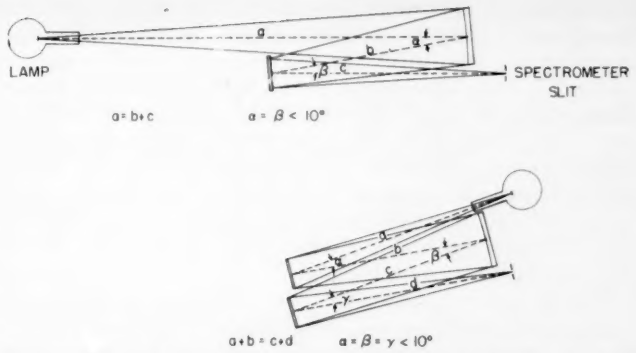

FIGURE 6. *Auxiliary optics when using a lamp standard of spectral radiance in the calibration of a spectroradiometer; and for determining the spectral reflectivity of the aluminized mirrors employed.*

In general, the radius of curvature of this auxiliary spherical mirror should be greater than the focal length of the spectrometer employed so that no loss of radiant energy will result through overfilling the spectrometer optics. Furthermore, as noted above, the aperture of this mirror should be kept within a total conical angle of about 5°.

No diaphragm or other shielding is required in the use of these standards, except for a shield to prevent direct radiation from the lamp, not falling on the concave mirror from entering the spectrometer, since in their use an optical image of the filament is focused upon the spectrometer slit.

In order to calibrate a spectroradiometer with this standard lamp, a knowledge of the spectral reflective characteristics of the mirror surfaces is required in order to evaluate the radiant energy properly at the spectrometer slit. A good aluminized surface should have a spectral reflectivity above 87 percent throughout the spectral region of 0.5 to 2.6 μ but which increases slightly with wavelength except for a slight dip in the region of 0.8 to 1.0μ. In practice the proper reflectance losses can best be determined through the use of a third mirror (a second plane mirror) which may be temporarily incorporated into the optical setup from time to time. (See fig. 6 for a possible arrangement of the auxiliary optics when including the third mirror to determine its spectral reflectance.)

In experiments where sources of radiation are being compared, no knowledge of the spectral reflectance of the auxiliary mirrors, the spectrometer transmission characteristics, or the spectral sensitivity of the detector is required. Furthermore when the same auxiliary optics are employed no measure need be taken of the spectrometer slit widths, or slit areas, provided the slit is fully and uniformly filled in both cases.

Operation of these standards should be on alternating current to obviate filament crystallizing effects which occur when the operation is on direct current. To reduce line voltage a stepdown transformer (1-kva capacity) having a ratio of 10 to 1 or a 50-amp variable transformer may be employed. (See fig. 5.) Then to give fine control a second variable transformer (10-amp capacity) is wired into the circuit to control the input of the heavy duty

transformer. For still finer control a third variable transformer may be employed with a radio filament transformer to add (or subtract) a small voltage (0 to 2.5 v) to the primary voltage fed into the stepdown transformer. It was found that this method was very effective in accurately controlling the larger lamp currents. The heavy-duty (1 kva) stepdown transformer is preferred to that of a 50-amp variable transformer since the latter is subject to contact damage when operated for long intervals of time at high current values.

These lamp standards are expensive laboratory equipment and it is suggested that they be operated at the lower current value in order to prolong their usual life. Only for short intervals should they ever be operated above 30 amp (about 2,200° K), and then only to calibrate a similar lamp as a working standard. In general even at lower currents a working standard should be prepared and used, except for purposes of checking the operation of such working standard.

5. Conclusions

The tungsten strip lamp is a useful working standard for use in spectral radiance measurements within the region of 0.25 to 2.6μ. At wavelengths shorter than 0.25μ the available radiant energy from heated tungsten is too low for practical uses. At longer wavelengths than about 2.6μ the low emissivity of tungsten, together with window absorption and reradiation effects render the use of this type of lamp impractical. Some other source, in air or employing a special window, will be found more practical. The recent measurements on the spectral emissivity of platinum from 2.0 to 15.0μ provides one possible standard for radiance at long wavelengths [14].

The method of calibration against a blackbody is direct and leaves no question relating to filament temperature or tungsten emissivity. The energy of the lamp is equated to that of the blackbody. The principal uncertainty in the results lie within the accurate determination of the blackbody temperatures and the measurement of the current through the lamp filament.

The authors thank Milton Burdick and H. S. Parker of the Engineering Ceramics Section of the Bureau for useful suggestions in developing the high temperature blackbody, and also William F. Roeser of the Building Technology Division for constructive criticisms.

6. References

[1] W. W. Coblentz, Measurements on standards of radiation in absolute value, Bull. Bur. Stds. **11,** 87 (1914) SP227.

[2] W. W. Coblentz and R. Stair, The present status of the standards of thermal radiation maintained by the Bureau of Standards, BS J. Research **11,** 79 (1933) RP578.

[3] Ralph Stair and Russell G. Johnston, Effects of recent knowledge of atomic constants and humidity on the calibrations of the National Bureau of Standards Thermal Radiation Standards, J. Research NBS **53,** 211 (1954) RP2535.

[4] A. G. Worthing, The true temperature scale of tungsten and its emissivity powers at incandescent temperatures, Phys. Rev. **10,** 377 (1917); Deviation from Lambert's law and polarization of light emitted by incandescent tungsten, tantalum and molybdenum and changes in the optical constants of tungsten with temperature, J. Opt. Soc. Am. **13,** 635 (1926).

[5] H. C. Hamaker, Reflectivity and emissivity of tungsten (Inaug Diss, Utrecht, Holland, 1934).

[6] J. C. DeVos, Evaluation of the quality of a blackbody, Physica **20,** 669 (1954). A new determination of the emissivity of tungsten ribbon, physica **20,** 690 (1954); relation between brightness, temperature, true temperature and colour temperature of tungsten. Luminance of tungsten, Physica **20,** 715 (1954).

[7] Robert D. Larrabee, Spectral emissivity of tungsten, J. Opt. Soc. Am. **49,** 619 (1959).

[8] R. Stair and W. O. Smith. A tungsten-in-quartz lamp and its applications in photoelectric radiometry, J. Research NBS **30,** 449 (1943) RP1543.

[9] Ralph Stair, Thomas C. Bagg, and Russell G. Johnston, Continuous measurement of atmospheric ozone by an automatic photoelectric method, J. Research NBS **52,** 133 (1954) RP2481.

[10] W. J. Condell, Jr., Tungsten spectral intensity calibration methods, U. Md. Report, REMP–3 1959.

[11] William J. Condell and Francis T. Byrne, Spectral intensity of ac operated tungsten lamps, J. Opt. Soc. Am. **47,** 1,135 (1957).

[12] Louis E. Barbrow, Memorandum on a procedure for obtaining spectral radiant intensity of tungsten filament, J. Opt. Soc. Am. **49,** 1,122 (1959).

[13] André Gouffé, Aperture corrections for artificial blackbodies, Revue d'Optique, **24,** Nos. 1–3 (1945).

[14] A. Maki, Ralph Stair, and Russell G. Johnston, Apparatus for the measurement of the normal spectral emissivity in the infrared, J. Research NBS **64C**, 99 (1960).

[15] Ralph Stair, Photoelectric spectroradiometry and its application to measurement of fluorescent lamps, J. Res. NBS **46,** 437 (1951) RP2212.

[16] F. Hoffman and H. Willenberg, Uber Messungen an Temperaturstrahlen im Ultraviolett, Physik Z. **35,** 1 (1934). Das Emissionsvermogen des Wolframs im Ultraviolett bei hohen Temperature, Physik Z. **35,** 713 (1934).

[17] L. S. Ornstein, Tables of the emissivity of tungsten as a function of wavelength from 0.23–2.0μ in the region of temperature 1,600°–3.000° K, Physica **3,** 561 (1936).

[18] C. Zwikker, Physiche Eigenshappen Van Wolfraam by Hooge Temperaturen (thesis, Amsterdam, 1925).

Washington, D.C. (Paper 64A4–51)

JOURNAL OF RESEARCH of the National Bureau of Standards—A. Physics and Chemistry
Vol. 64A, No. 4, July–August 1960

Photovoltaic Effect Produced in Silicon Solar Cells by X- and Gamma Rays [1]

Karl Scharf

(January 25, 1960)

The open-circuit voltage and photocurrent produced in a silicon solar cell by X- and gamma rays were measured as a function of exposure dose rate, cell temperature, angle of incidence of radiation, and photon energy. This photoresponse was stable and proportional to the exposure dose rate, which was applied up to a maximum of 1.8×10^6 roentgen per minute for X-rays and 4×10^2 roentgen per minute for Co^{60} gamma rays. At an exposure dose rate of 1 roentgen per minute the response was of the order of 10^{-5} volt for the open-circuit voltage and 10^{-8} ampere for the photocurrent. At high exposure dose rates of Co^{60} gamma rays, radiation damage became apparent. The temperature dependence of the photoresponse was controlled by the temperature dependence of the cell resistance. The directional dependence of the photoresponse varied with the quality of radiation and for Co^{60} gamma rays was very small for angles from 0° to 70°. The photoresponse decreased with increasing photon energy but changed only little between 200 and 1,250 kilo electron volts. The ratio of the response to X-rays of 38 kilo electron volts effective energy and that to Co^{60} gamma rays was approximately 6:1. An approximate value of the thickness of the effective p–n junction layer is deduced from the energy dependence.

1. Introduction

The investigation reported in this paper was carried out in order to test the suitability of silicon solar photocells for dosimetry of X- and gamma rays.

Silicon solar cells are photovoltaic cells of the p–n junction type. When irradiated with photons of an energy sufficient to produce electron-hole pairs in silicon, a photocurrent is produced without application of an external electrical power supply. The photocurrent or the photovoltage developed between the two sides of the junction can be used as a measure of the intensity of the incident radiation.

Photovoltaic cells are frequently used for measurements of the intensity of visible light. Only few quantitative investigations have been made of the response of photovoltaic cells to X- and gamma rays. More detailed investigations were carried out on cuprous-oxide [1, 2] [2] and selenium [1, 3, 4] cells of the metal-semiconductor contact type and on germanium [5] and gallium arsenide [6] p–n junction photocells. Large area selenium cells had the greatest overall sensitivity but showed a very slow photoresponse to X-rays, similar to that observed in photoconductive cells. Photovoltaic p–n junction cells were less sensitive than selenium cells but had response times of the order of milliseconds [6].

No detailed investigation of the response of silicon solar cells to X- and gamma rays has been reported. The investigation of these cells seemed to be promising for different reasons. The silicon solar cell is a large area photovoltaic cell which has a high current output and a short response time [7]. It was also expected that due to the low atomic number of silicon ($Z_{Si}=14$), the response of silicon solar cells would be less dependent on incident photon energy than that of other photovoltaic cells.

Measurements are reported of the response of silicon solar cells to X- and gamma-rays as a function of (1) the exposure dose rate of the radiation, (2) the cell temperature, (3) the angle of incidence of the radiation, and (4) the incident photon energy.

2. General Considerations

A silicon solar cell consists of a large area n-type silicon disk with a very thin p-type layer on its surface [8]. In balancing an equilibrium between the different carrier concentrations in the p-type and n-type silicon, a strong electrostatic field is established in the transition zone (fig. 1). The electric junction field is due to a potential difference with the higher potential on the side of the n-type layer. This potential difference, sometimes called the "diffusion potential," is of the order of 1 v in silicon. This can be seen from the configuration of the electron energy bands in the p–n junction as shown in figure 1. In the equilibrium state, the Fermi level E_F is constant throughout the p- and n-type layers and the barrier height ΔE is slightly smaller than the energy gap E_G, which is 1.1 ev for silicon.

The p–n junction has a current-voltage characteristic of an electric rectifier with the forward current flowing from the p-type to the n-type layer. If the p–n junction is irradiated with photons of an energy larger than E_G, electron-hole pairs are produced which are separated by the junction field. Electrons are driven to the n-type and holes to the p-type layer. In this way a voltage difference is produced between the two sides of the junction, the p-side becoming positive and the n-side negative. This photovoltage biases the p-n junction in the forward direction and opposes the diffusion voltage.

[1] Supported in part by the U.S. Atomic Energy Commission.
[2] Figures in brackets indicate the literature references at the end of this paper.

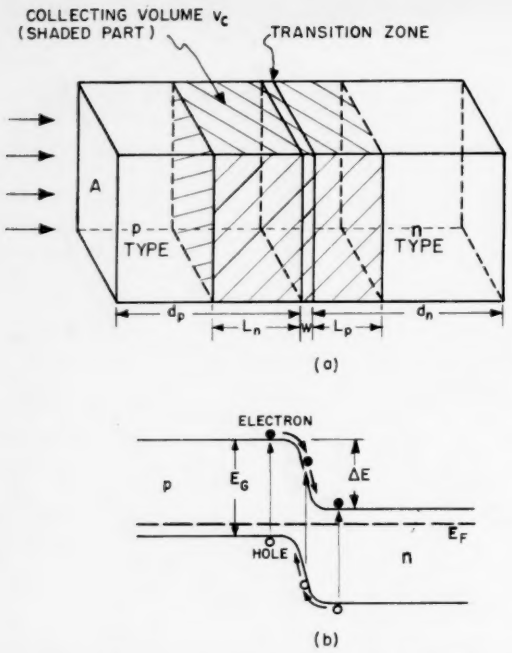

FIGURE 1. (a) *Geometry of* p–n *junction photocell showing the photoelectric effective collecting volume* v_c *determined by the minority carrier diffusion lengths* L_n *and* L_p. (b) *Equilibrium configuration of electron energy bands in a* p–n *junction.*

The current carriers produced by the radiation and separated by the junction field represent the generated photocurrent in the reverse direction of the junction. In restoring the equilibrium state, the photovoltage produces a current through the junction in the forward direction. Provided that no external load is connected to the cell, the open-circuit voltage (photoelectromotive force) reaches a steady value at which the generated photocurrent equals the junction current produced by the photovoltage. If a load resistance is connected across the junction, part of this current flows through the external load and the photovoltage is reduced.

The electrical characteristic of a p–n junction photovoltaic cell can be derived by considering the equivalent circuit shown in figure 2. The photocell is represented as a constant current generator.

The generated photocurrent I_s divides into the junction current I_j and the external load current I. R_j is the voltage dependent junction resistance in the forward direction and R_L is the load resistance. It may be assumed that the series cell resistance R_s and shunt resistance R_{sh} need not be considered if $R_s \ll R_L \ll R_{sh}$, a condition usually fulfilled.

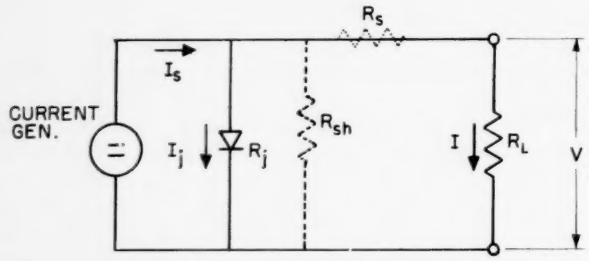

FIGURE 2. *Equivalent circuit of* p–n *junction photocell.*

According to the theory of the p–n junction [9], one obtains

$$I_j = I_0 \left[\exp(qV/kT) - 1\right]. \tag{1}$$

I_0 is the saturation current of the junction in the reverse direction, q the electronic charge, k the Boltzman constant, T the absolute temperature, and V the photovoltage. The photocurrent I measured in the external load is then

$$I = I_s - I_j = I_s - I_0[\exp(qV/kT) - 1]. \tag{2}$$

From this equation one obtains for the photovoltage measured across the cell terminals

$$V = \frac{KT}{q} \ln\left(\frac{I_s - I}{I} + 1\right). \tag{3}$$

Two special cases are usually considered:

(a) Open circuit condition:

$$R_L = \infty; \quad I = 0; \quad I_s = I_j$$

$$V \equiv V_0 = \frac{KT}{q} \ln\left(\frac{I_s}{I_0} + 1\right). \tag{4}$$

For $(I_s/I_0) \ll 1$, one obtains

$$V_0 = \frac{KT}{q} \cdot \frac{I_s}{I_0} \tag{4a}$$

(b) Short circuit condition:

$$R_L = 0; \quad I_j = 0; \quad V = 0; \quad I = I_s \tag{5}$$

The open-circuit voltage V_0 and the generated current I_s, usually called the short-circuit current, are considered as characteristic measures for the photoresponse of the cell.

The theory of the photovoltaie effect assumes that, in addition to carriers produced inside the junction, all minority carriers produced outside it but able to reach the junction by diffusion, are contributing to the photocurrent. The photoelectric effective area is therefore determined by the diffusion lengths of the minority carriers, the diffusion length being defined as the average distance that carriers diffuse before recombining.

If the mean free path of the radiation (equal to the reciprocal of the absorption coefficient measured in cm^{-1}) is large compared with the diffusion lengths one obtains for the width L of the effective area

$$L = L_n + L_p + W. \tag{6}$$

L_n is the diffusion length of electrons in the p-type layer, L_p the diffusion length of holes in the n-type layer, and W is the width of the junction (fig. 1). Usually W is very small compared with L_p and L_n

and can be neglected. In solar cells $d_p < L_n$, if d_p is the thickness of the p-layer. The value of L is therefore approximately

$$L = L_p + d_p. \tag{6a}$$

The generated current I_s will comprise all minority carriers produced by radiation in the collecting volume

$$v_c = A(L_p + d_p) = AL, \tag{7}$$

provided that the whole junction area A is being irradiated. It has also been shown that the saturation current I_0 will comprise all minority carriers thermally generated in the same collecting volume v_c.

Considering eqs (2) and (3) one obtains [10]

$$I = qAg_0L - qAgL'[\exp(qV/kT) - 1] \tag{8}$$

and

$$V = \frac{kT}{q} \ln\left(\frac{qAg_0L - I}{qAgL'} + 1\right) \tag{9}$$

if

$$gL' = g_pL_p + g_nd_p \tag{10}$$

where g_0 is the rate of generation of electron-hole pairs due to radiation and is equal to their number produced by the radiation per cubic centimeter per second, and g_p and g_n are the thermal generation rates of holes in the n-layer and electrons in the p-layer, respectively.

From eqs (8) and (9) one obtains for the generated or short circuit current

$$I_s = qAg_0L = qg_0v_c \tag{11}$$

and for the open-circuit voltage

$$V_0 = \frac{kT}{q} \ln\left(\frac{g_0L}{gL'} + 1\right) \tag{12}$$

For $(g_0L/gL') << 1$, the approximation can be made

$$V_0 = \frac{KT}{q} \cdot \frac{g_0L}{gL'}. \tag{12a}$$

The above relations were derived for the photovoltaic effect produced by visible light but are also valid for irradiation with X- and gamma rays. In the case of visible light each absorbed photon excites one electron from the valence band into the conduction band and thus produces one electron-hole pair. High-energy photons will mostly ionize low lying atomic energy levels (K- and L-levels) producing photoelectrons or will interact with atomic electrons mainly in higher levels by a Compton scattering process producing recoil electrons and Compton photons. Pair production will have to be considered for photons of energy larger than 1.02 Mev. High-energy electrons, produced in these interactions, transfer part of their energy to the crystal lattice of silicon, but lose most of their energy by impact ionization thus producing low energy current carriers.

High-energy electrons, which pass the p–n junction are negligibly influenced by the low potential barrier of approximately 1 ev. Only low-energy carriers are acted upon by the junction field in such a way that they contribute to the photocurrent. Equations (8) and (9) are, therefore, also applicable in the case of high-energy radiation, provided that g_0 refers to the generation rate of low-energy carriers produced by the high-energy electrons. The collecting volume v_c will be the same as in the case of visible light.

3. Experimental Procedure

The photocells investigated were commercial round silicon solar cells [3] with a sensitive area of 7.9 cm². The silicon disk of the cell was approximately 0.7 mm thick and was encapsulated in a metal casing. The front of the cell was closed with a glass window 1.25 mm thick. The whole cell was wrapped in black insulation tape in order to prevent the access of light.

The X-ray sources were a 250-kv Machlett tube with an inherent filtration of 3-mm Al and a 50-kv Machlett beryllium window-type tube with an inherent filtration of 1-mm Be. The tubes were tungsten target tubes operated by a stabilized constant voltage supply. A calibrated 100-curie Cs^{137} and a calibrated 200-curie Co^{60} source were used as gamma ray sources.

Unless otherwise stated, exposure dose rates were measured with Victoreen r-meters which had been calibrated for each investigated type of radiation against the NBS standard free air chambers.[4] All measurements were carried out with an irradiation of the whole sensitive cell area.

The open circuit voltage was measured by an electric compensation method. The photocurrent was determined either directly with a microammeter or sensitive galvanometer or by measuring the voltage drop across a known load resistance with a potentiometer.

4. Results and Discussion

4.1 Exposure Dose Rate Dependence

Figure 3 shows the open-circuit voltage V_0 and the photocurrent I as a function of the exposure dose rate for 250 kv unfiltered X-rays (fig. 3a) and Co^{60} gamma rays (fig. 3b). The exposure dose rate of the X-rays was measured with the NBS 250 kv standard free air chamber and was varied by changing the tube current. In the case of Co^{60} gamma rays, the exposure dose rate was varied by changing the distance between source and photocell. The exposure dose rates at different distances were obtained from the calibration curve of the source. Exposure dose rates were increased up to approximately 10^4 r/hr for the X-rays and up to 400 r/hr for the Co^{60} gamma rays.

[3] Type S–1A cells manufactured by Hoffman Electronics Corp. (Semiconductor Division).

[4] The calibrations of the r-meters were carried out by Mr. LeRoy DeLaVergne of the Radiological Equipment Section of the National Bureau of Standards.

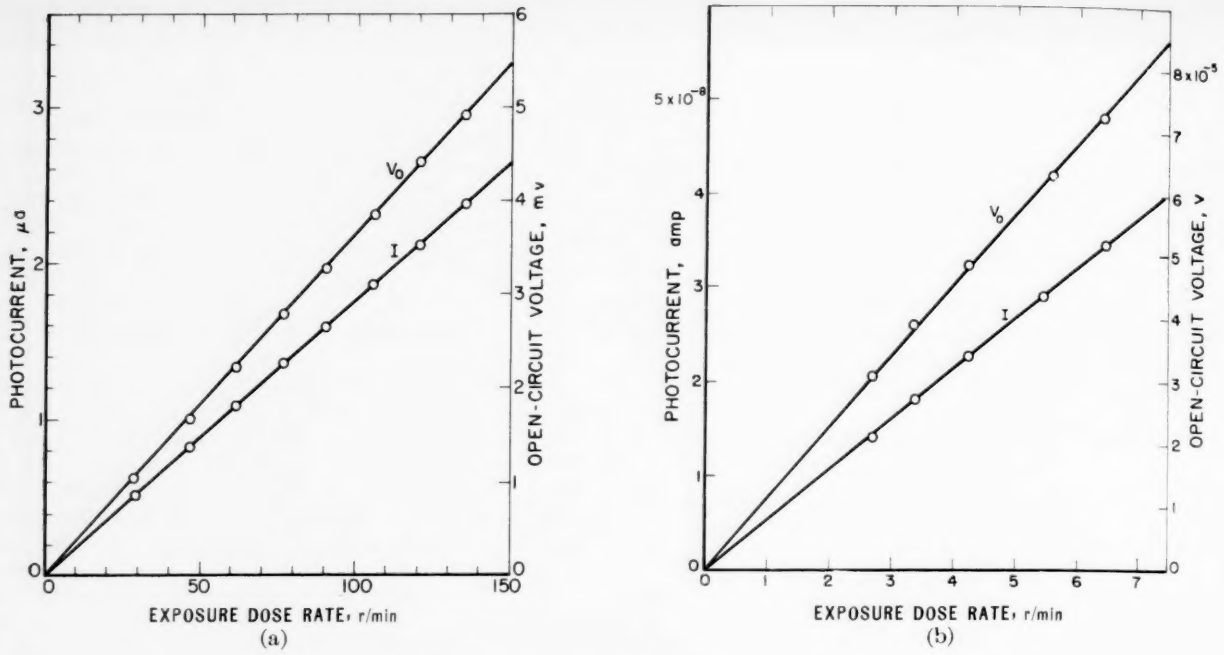

FIGURE 3. *Dependence of open-circuit voltage* V_o *and photocurrent* I *on exposure dose rate measured at room temperature* (a) *with 250-kv unfiltered X-rays (load resistance* R_L*=890 ohms), and* (b) *with* Co^{60} *gamma rays* (R_L*=532 ohms).*

Open circuit voltage and photocurrent produced by X- and gamma rays were proportional to the exposure dose rate. The photoresponse remained constant during the irradiation and was reproducible within the accuracy of the measuring instruments and the constancy of the radiation source.

In order to obtain the generated or short circuit current I_s from the measured photocurrent I, the current-voltage characteristic of the cell must be known. Figure 4 shows the current-voltage characteristics of the photocell measured at different temperatures for very low voltages. The characteristic is linear and its slope gives the zero voltage resistance R_c of the photocell. At the low photovoltages encountered in this investigation, the cell resistance may be assumed as voltage independent and equal to the zero voltage junction resistance R_j, provided that R_s and R_{sh} need not be considered. Substituting in eq (2) the relations

$$I_j = V/R_j \quad \text{and} \quad I = V/R_L$$

one obtains

$$I_s = I(1 + R_L/R_j) \tag{13}$$

and

$$V_0 = I_s R_j \tag{14}$$

when R_L is the load resistance. Equation (13) shows that I_s differs from I by a constant factor, which is determined by the ratio R_L/R_j. According to eq (14), V_0 is proportional to I_s and both should show the same functional behavior, if R_j is constant.

The junction resistance R_j of the investigated cell was approximately 1,000 ohms at room temperature. The values of the photocurrent I shown in figure 3 have, according to eq (13), to be multiplied by a factor of 1.89 (R_L=890 ohms) for X-rays (fig. 3a) and 1.53 (R_L=532 ohms) for gamma rays (fig. 3b), in order to obtain the short circuit currents I_s. This means that measurements shown in figure 3 indicate the proportionality between the short circuit current I_s and exposure dose rate as well. In case the series resistance R_s and shunt resistance R_{sh} must be taken into account, the impedance of the combined resistances needs to be considered. The proportionality between I and I_s and V_0 and I_s would still be maintained.

Measurements were further carried out with X-rays obtained from a beryllium window-type tube operated at 50 kv (fig. 5). Because of the small inherent filtration of this tube, the radiation comprised a greater amount of low-energy radiation which was strongly absorbed in the cell. V_0 and I were measured at high exposure dose rates up to 1.8×10^6 r/hr. The attenuation of the radiation in the glass window of the cell was taken into account. Photocurrents increased linearly with exposure dose rate with different load resistances up to 10^4 ohm. The open circuit voltage showed for higher exposure dose rates a nonlinear dependence following the logarithmic relation of eq (4). The highest response obtained in these measurements with R_L=50 ohm was approximately I=90 μa and V_0=70 mv. At 1.8×10^6 r/hr exposure dose rate, the maximum matched load power output was 1.7 μw. This corresponds to a conversion efficiency of approximately 0.02 percent. For higher energy radiation the conversion efficiency decreases due to the reduced absorption of the radiation.

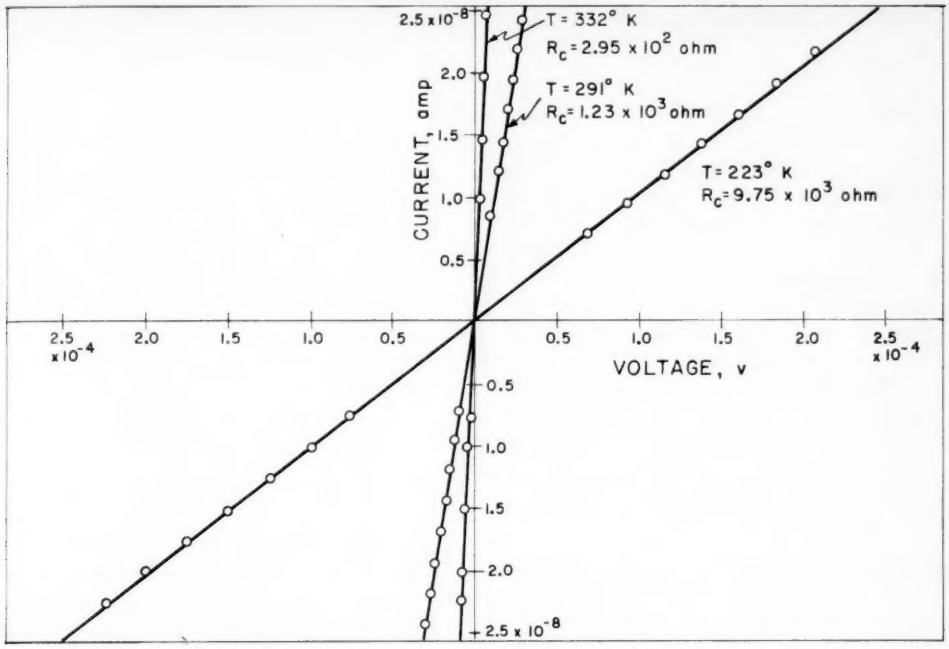

FIGURE 4. *Current-voltage characteristics of the investigated silicon solar cell measured at different cell temperatures* T, *with indication of respective cell resistance* R_c.

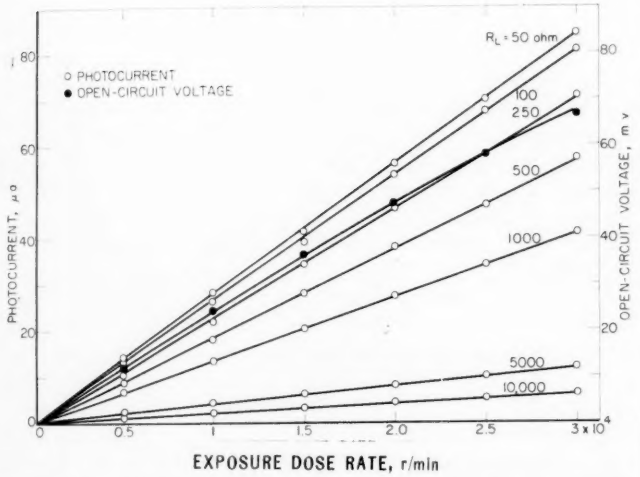

FIGURE 5. *Exposure dose rate dependence of open-circuit voltage and photocurrent measured at room temperature with different load resistances at high exposure dose rates of 50-kv unfiltered X-rays obtained from a beryllium-window-type tube.*

The maximum photocurrent observed at these high exposure dose rates remained constant during irradiation over several hours. The open-circuit voltage showed a slow decrease in time of irradiation, which was apparently due to an increase of the cell temperature. When the radiation was shut off and the cell allowed to cool down, the open-circuit voltage recovered to the original value at a subsequent irradiation.

Open-circuit voltage and photocurrent produced by gamma rays obtained from a water-shielded 2,000 curie Co^{60} source at an exposure dose rate of approximately 6×10^5 r/hr, showed a considerable decay with time of irradiation. Simultaneously with the decay of the photoresponse the electrical resistance of the cell decreased. Such transient response, apparently due to radiation damage, was not observed in measurements with gamma rays at low exposure dose rates and is also not in agreement with measurements reported by other authors. Moody et al. [11] found a constant response of silicon solar cells to Co^{60} gamma rays at an exposure dose rate of approximately 10^5 r/hr. Loferski and Rappaport [12] found that the photoresponse of silicon solar cells to visible light remained unaffected by simultaneous irradiation with 750 kv and 2 Mev X-rays. The response of silicon solar cells to high-energy radiation at high exposure dose rates is being further investigated by the author.

4.2. Temperature Dependence

V_0 and I produced by Cs^{137} gamma rays were measured for different cell temperatures between −50° C and 60° C. The silicon solar cell was placed inside a wooden box in which the temperature could be regulated by means of a thermostat. Dry ice was used for obtaining temperatures below room temperature. The gamma-ray source was placed outside the box.

The results of these measurements are shown in figure 6. V_0 decreased nearly exponentially with increasing temperature. The photocurrent I measured with a load resistance of $R_L=532$ ohms was approximately constant up to 10° C and decreased then with increasing temperature. The temperature dependence of V_0 and I will, according to eqs (13) and (14), be determined by the temperature dependence of R_j. The generated current I_g may be

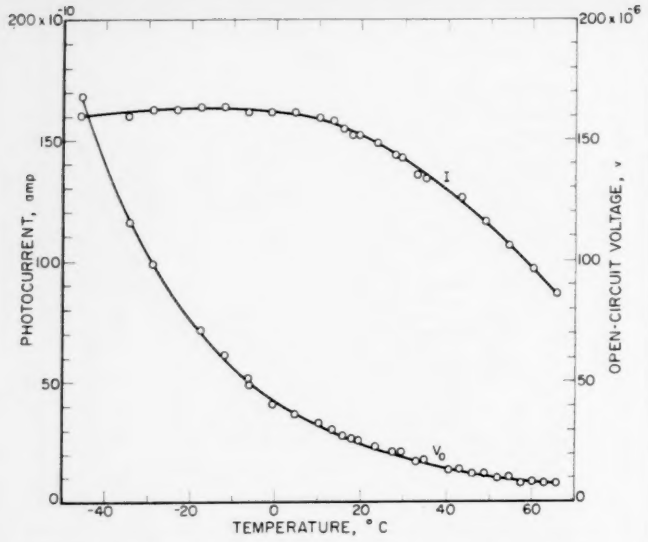

FIGURE 6. *Temperature dependence of open-circuit voltage* V_o *and photocurrent* I (R_L=*532 ohms*) *produced by Cs* ^{137} *gamma rays.*

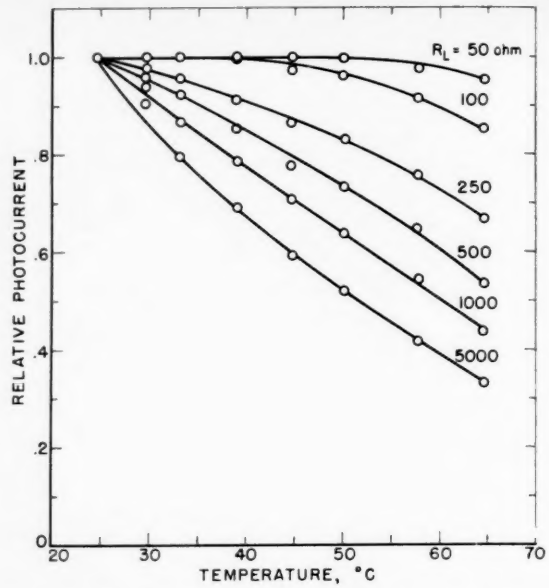

FIGURE 7. *Relative change of photocurrent with cell temperature measured with 250-kv unfiltered X-rays for different load resistances.*

assumed to be independent of temperature, because the generation rate g_0 and the diffusion length L_P (eq (11)) remain approximately constant over a limited range of temperature. R_j decreases nearly exponentially with increasing temperature causing the exponential decrease of V_0 (eq (14)). The temperature dependence of I is determined by the ratio R_L/R_j (eq (13)). R_L/R_j increases with increasing temperature and the photocurrent therefore decreases. With decreasing temperature the ratio R_L/R_j decreases and the photo current increases approaching the value of I_s. However, at lower temperatures the series resistance R_s, originally assumed as negligibly small, increases too and eq (13) has to be modified as,

$$I_s=I\left(1+\frac{R_L+R_s}{R_j}\right). \tag{13a}$$

The temperature dependence of I is now determined by the ratio $(R_L+R_s)/R_j$. The rate of increase of I with decreasing temperature is reduced and I reaches a maximum at low temperatures as seen in figure 6.

The temperature dependence of I with different load resistances R_L was measured with 250 kv unfiltered X-rays. The relative values of I are shown in figure 7, the photocurrent at 25° C being normalized to unity. With R_L=50 ohms, the photocurrent remained constant from 25° C up to approximately 50° C and then decreased slowly at higher temperatures. With increasing R_L, the temperature dependence becomes stronger. For very large R_L, the photovoltage $V=IR_L$ approaches the value of V_0 and the photocurrent shows a temperature dependence similar to that of V_0. The influence of the load resistance on the temperature dependence of the photocurrent can in the same way, as shown above, be explained by the temperature dependence of R_j.

4.3. Directional Dependence

The directional dependence of V_0 and I measured for different qualities of radiation is shown in figure 8. The photocell was turned at different angles θ around an axis going through the center of the cell perpendicular to the direction of the incident radiation. V_0 and I changed in the same way with changing θ. The relative values shown in figure 8 therefore apply to both.

The directional dependence measured with 50-kv unfiltered X-rays from a beryllium-window-type tube approximately follows a cosine law. There is less directional dependence for 250-kv unfiltered X-rays and the response to Co^{60} gamma rays is practically independent of θ up to 70°. At larger angles the attenuation in the metal casing becomes apparent. For more penetrating radiation, a response is also observed with irradiation of the backside of the cell. The directional dependence for backside irradiation is similar to that for frontside irradiation.

The directional dependence of the photoresponse can be explained by considering the energy absorbed in the effective p-n junction layer. The incident energy flux density will be proportional to cos θ, while the path length of the radiation inside the effective layer will be $d/\cos\theta$, if d is the thickness of the effective layer. The energy E_a absorbed in this layer will therefore show a directional dependence,

$$E_a \propto \cos\theta[1-\exp(-\mu d/\cos\theta)],$$

where μ is the absorption coefficient of silicon. For large values of $\mu d/\cos\theta$, the directional dependence

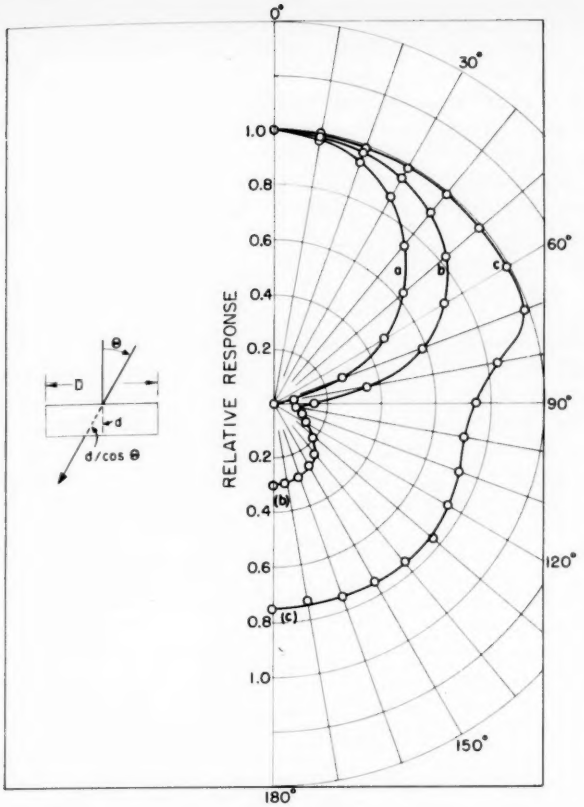

FIGURE 8. *Relative values of photoresponse (open-circuit voltage* V_o*, photocurrent* I *and generated photocurrent* I_s*) for different angles of incidence of (a) 50-kv unfiltered X-rays from a beryllium-window-type tube, (b) 250-kv unfiltered X-rays, and (c)* Co^{60} *gamma rays.*

of E_a approaches a cosine law. For $\mu d/\cos\theta \ll 1$ one can make the approximation

$$[1-\exp(-\mu d/\cos\theta)] \sim \mu d/\cos\theta$$

and E_a becomes independent of θ. For large values of θ one has to consider that the silicon disk has a finite diameter D and the radiation will enter the disk from the side. For angles approaching 90°, the photoresponse is a function of $\cos(90-\theta)$ and of the disk diameter D.

The directional dependence of the response to Co^{60} gamma rays is in good agreement with the above relations. However they do not fully account for the directional dependence observed with low-energy X-rays. This can be explained by the fact that the radiation has to pass absorbing materials before entering the silicon disk. The energy absorbed in the effective layer is thus reduced by a direction dependent factor $\exp(-\mu_1 d_1/\cos\theta)$ if μ_1 and d_1 are the absorption coefficient and thickness of the absorbing materials, i.e., the glass window and metal casing of the cell. For large values of $\mu_1 d_1$, as in the case of low-energy X-rays, the directional dependence of the photoresponse is therefore strongly influenced by the absorption in the cell casing.

4.4. Energy Dependence

The photoresponse of the silicon solar cell to radiations of different photon energies was measured with heavily filtered X-rays and Cs^{137} and Co^{60} gamma rays. Tube voltages, filtrations, half value layers (HVL) in copper, and corresponding effective energies for the different investigated radiations are shown in table 1. The applied exposure dose rates were between 0.5 and 5 r/min.

The open-circuit voltage and photocurrent per unit exposure dose rate showed the same energy dependence. Their relative values, normalized to unity for 100-kv X-rays, are the same for both. They are shown in figure 9 as a function of the effective photon energy. The absorption of the radiation in the glass window, measured after dismantling

TABLE 1. *Qualities of investigated radiations*

Constant X-ray tube voltage	Filtration [a] (mm)			Approximate half-value layer (HVL)	Approximate effective photon energy ($h\nu_{eff}$)
			X-rays		
kv	Cu	Sn	Pb	*mm* Cu	*kev*
50			0.125	0.16	38
60	0.32		.125	.26	46
65	.32		.125	.31	49
75	.81		.125	.47	58
80			.52	.55	62
100			.52	.72	70
150	4.00	1.53		2.4	122
200	.59	4.00	.69	4.1	170
250	.62	1.00	2.67	5.4	210
			Gamma rays		
Cs^{137}					661
Co^{60}					1250

[a] Additional to inherent tube filtration of 3 mm Al.

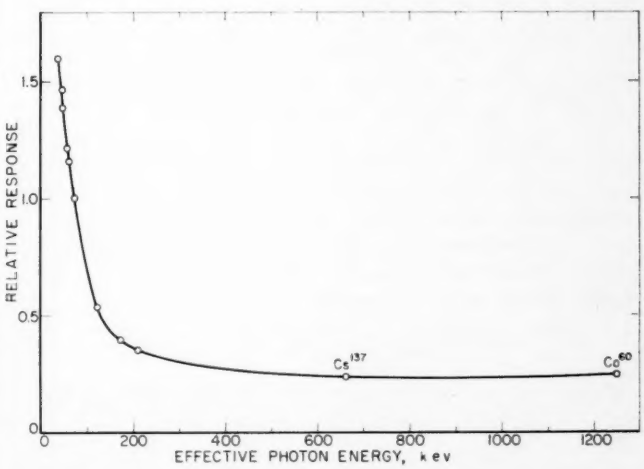

FIGURE 9. *Energy dependence of relative values of photoresponse (open-circuit voltage* V_o*, photocurrent* I*, and generated photocurrent* I_s*) obtained from measurements at room temperature with constant load resistance.*

Values for 100-kv filtered X-rays (effective photon energy $h\nu_{eff}$=70 kev) are normalized to unity.

the cell, was taken into account. The photocurrent was always measured with the same load resistance (532 ohms). The relative values given in figure 9 show, in accordance with eq (13), the energy dependence of the generated photocurrent I_s as well. The normalized values measured for the 100 kv X-rays ($h\nu_{eff}$=70 kev) per unit exposure dose rate of 1 r/min and R_L=532 ohm were:

$$(V_0)_{100}=4.12\times10^{-5}v; \quad (I)_{100}=2.34\times10^{-8} \text{ amp}; \quad (I_s)_{100}=3.58\times10^{-8} \text{ amp}.$$

The response of the silicon solar cell changes slightly between 1.25 Mev and 0.20 Mev and then rises more steeply with decreasing effective energies. The response to Co^{60} gamma rays is about 7 percent higher than to Cs^{137} gamma rays. The higher value for Co^{60} gamma rays could not be explained satisfactorily.

The energy dependence of the photoresponse is determined by the energy dependence of the generation rate g_0, as seen from eqs (11) and (12). In the case of light, the number of electron-hole pairs produced in the collecting volume v_c is equal to the number of photons absorbed within v_c. With high-energy radiation, the photons absorbed within v_c produce high-energy electrons, part of which are able to leave the collecting volume before dissipating all their energy within v_c. At the same time electrons produced outside of v_c enter v_c and produce secondary electrons there. The net generation rate g_0 is proportional to the net amount of energy dissipated in v_c. In the case of electronic equilibrium, the energy lost by electrons leaving v_c is compensated by the gain of energy from electrons entering v_c. In this case one obtains

$$g_0=\frac{E_a}{\epsilon v_c} \tag{15}$$

where E_a is the radiation energy absorbed per second in the collecting volume v_c, and ϵ is the average energy required to produce one electron-hole pair. Considering the small dimensions of v_c, the value of g_0 may be assumed as constant within v_c.

For the discussion of the energy dependence of the photoresponse, the relation between the absorbed energy and the generated photocurrent I_s will be considered further because of the simple relation (eq 11) between g_0 and I_s. The radiation energy E_a which is absorbed per second in v_c and is transformed into electron energy is

$$E_a=J_0(\mu_{en}/\rho)_{Si}v_c\rho \tag{16}$$

where J_0 is the intensity of the incident radiation, in erg per square centimeter and per second, ρ the density of silicon (2.42 g/cm^3) and $(\mu_{en}/\rho)_{Si}$ the mass energy absorption coefficient of silicon in square centimeters per gram defined as: [5]

$$(\mu_{en}/\rho)_{Si}=(\tau/\rho)_{Si}+(\sigma_a/\rho)_{Si}+(\kappa_a/\rho)_{Si}; \tag{17}$$

[5] The influence of acceptor and donor impurities on the absorption coefficient was assumed as negligible because of their very small concentration.

$(\tau/\rho)_{Si}$, $(\sigma_a/\rho)_{Si}$ and $(\kappa_a/\rho)_{Si}$, are the respective mass absorption coefficients referring to photoelectric absorption, energy absorbed by Compton scattered recoil electrons and absorption by pair production. In the investigated energy range, $(\kappa_a/\rho)_{Si}$ is zero except for Co^{60} gamma rays.

According to the definition of the roentgen unit, the following relation [13] can be substituted in eq (16):

$$J_0=\frac{87.7\ R}{(\mu_{en}/\rho)_{air}} \text{ erg/sec, cm}^2 \tag{18}$$

if R is the exposure dose rate in roentgens per second and $(\mu_{en}/\rho)_{air}$ the mass energy absorption coefficient of air. Substituting the value of g_0 from eq (15) in eq (11) and considering eqs (16) and (18) one obtains the generated photocurrent I_s by expressing the absorbed energy in electron volts and the electronic charge in coulombs as

$$I_s=2.11\times10^{-5}\ R(v_c/\epsilon)\ f \text{ amp}. \tag{19}$$

where f is the ratio $(\mu_{en}/\rho)_{Si}/(\mu_{en}/\rho)_{air}$. For non-monochromatic filtered X-rays the energy spectrum of the radiation has to be considered in calculating f as

$$f=\frac{\int_0^{E_{max}} J_0(E)[\mu_{en}(E)/\rho]_{Si}\,dE}{\int_0^{E_{max}} J_0(E)[\mu_{en}(E)/\rho]_{air}\,dE} \tag{20}$$

if E is the photon energy and E_{max} is determined by the operating voltage of the X-ray tube.

Relative values of the generated photocurrent per unit exposure dose rate are shown in figure 10 as function of f. The calculation of f was in general based on spectral distributions $J_0(E)$ calculated by the Kramer's [14] method as has been done by Ehrlich and Fitch [15] for some of the investigated radiations. The calculations for the 100-kv and 150-kv X-rays were based on spectral distributions reported by Hettinger and Starfelt [16]. The influence of the absorption in the glass window on the spectral distribution was taken into account. The energy absorption coefficients of silicon were calculated from data given by White Grodstein [17] and Nelms [18]. Values of $(\mu_{en}/\rho)_{air}$ were taken from the ICRU report [13]. The integration was carried out graphically by planimetry.

According to figure 10, the relative values of I_s are not proportional to f as would be expected from eq (19). The reason for this is apparently the nonfulfillment of the electronic equilibrium condition on which eq (19) is based. The actual generation rate g_0 differs from that calculated by eq (15). The ratio of the actual and calculated value of the generation rate shall be designated as K and be called *ionization coefficient*. Introducing K into eqs (15) and (19), one obtains for the actual generation rate

$$g_0=\frac{KE_a}{\epsilon v_c} \tag{15a}$$

and

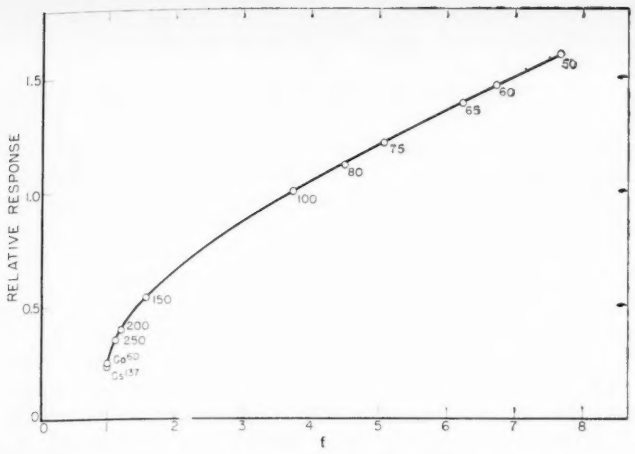

FIGURE 10. *Relation between photoresponse and radiation energy absorbed per unit exposure dose rate in the photoelectric effective silicon layer.*

This energy is a function of '*f*', the ratio of the mass energy absorption coefficients of silicon and air. Values of *f* were calculated by taking into account the spectral distribution of the radiations. Numbers near the measured points indicate the operating voltages for filtered X-rays, as referred to in table 1.

$$I_s = 2.11\times10^{-5}\dot{R}(v_c/\epsilon)Kf \quad \text{amp.} \qquad (19a)$$

The ionization coefficient K is energy dependent as can be deduced from the graph in figure 10. The relative value of the generated current is, according to eq (19a),

$$\frac{I_s}{(I_s)_{100}} = \frac{Kf}{K_{100}f_{100}} \qquad (21)$$

if the index 100 refers to the values for the 100-kv X-rays ($h\nu_{\text{eff}}=70$ kev) and all values of I_s are measured at the same exposure dose rate. The relative values of the ionization coefficient K/K_{100} can now be calculated from eq (21) by using the measured values of $I_s/(I_s)_{100}$ and the calculated values of f. Figure 11 shows the value of K/K_{100} for different effective energies. It has a maximum at approximately 120 kev and decreases for smaller and higher energies. The Co^{60} point is again higher than that for Cs^{137}.

It may be assumed that the ionization coefficient K is determined by the loss of ionization due to the deviation from the electronic equilibrium condition and by the gain in ionization from absorption inside the effective layer of Compton scattered photons produced inside and outside v_c.

In the investigated energy range, the absorption of radiation takes place by photoelectric absorption and Compton scattering. In the transition range between predominant photoelectric absorption and predominant Compton scattering, the average energy of the primary electrons does not change much. This is shown in table 2 which gives for monochromatic radiations the approximate values of the fractions of energy absorbed in silicon by photoelectric absorption and Compton scattering, the average energy of photoelectrons and Compton recoil electrons, and the average energy of all

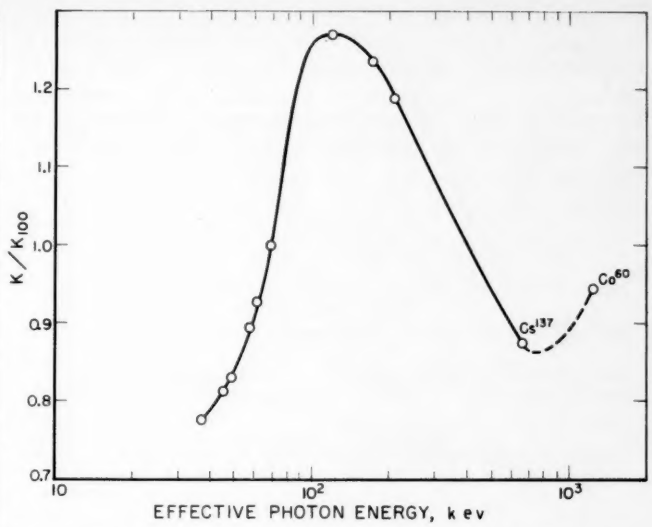

FIGURE 11. *Energy dependence of relative ionization coefficient* K/K_{100}.

K_{100} is the ionization coefficient for 100-kv filtered X-rays ($h\nu_{\text{eff}}=70$ kev).

TABLE 2. *Average energies of primary electrons produced by radiation in silicon in single interactions*

Photon energy $h\nu$	Fraction of energy absorbed		Average electron energy		
	Photo-electrons	Compton-electrons	Photo-electrons	Compton-electrons	Total of photo- and Compton-electrons
kev	%	%	*kev*	*kev*	*kev*
30	99.3	0.7	28.2	1.5	24.6
40	97.6	2.4	38.2	2.6	28.4
50	94.3	5.7	48.2	4.0	29.1
100	53.8	46.2	98.2	13.8	25.5
150	20.5	79.5	148.2	27.2	32.6
200	8.8	91.2	198.2	43.6	46.8
250	5.5	94.5	248.2	62.0	64.6

electrons produced in single interactions (primary electrons). The average energy of recoil electrons was calculated as $\overline{E}_c = h\nu\ (\sigma_a/\rho)_{\text{Si}}/(\sigma_T/\rho)_{\text{Si}}$ if $(\sigma_T/\rho)_{\text{Si}}$ is the total Compton mass absorption coefficient of silicon

$$(\sigma_T/\rho)_{\text{Si}} = (\sigma_s/\rho)_{\text{Si}} + (\sigma_a/\rho)_{\text{Si}} \qquad (22)$$

and $(\sigma_s/\rho)_{\text{Si}}$ is the mass absorption coefficient referring to the energy of scattered Compton photons. The energy of photoelectrons was approximately calulated as $\overline{E}_{ph} = h\nu - I_k$, if I_k is the ionization energy of a K-electron which can be assumed for silicon as 1.8 kev.

The average electron energy changes only slightly for photon energies between 30 and 150 kev. There will thus not be much change in this range in the net loss of ionization due to high-energy electrons. It may, therefore, be assumed that the energy dependence of the ionization coefficient K is mainly determined by absorption of scattered Compton photons. The relative increase of the absorbed energy E_a (eq (16)) due to reabsorption of scattered

Compton photons will be dependent on the ratio $(\sigma_s/\mu_{en})_{Si}$. Figure 12 shows the relative values of the ionization coefficient K/K_{100} as a function of $(\sigma_s/\mu_{en})_{Si}$. The values of $(\sigma_s/\mu_{en})_{Si}$ were calculated by taking into account the spectral distribution of the radiation as has been done in the calculation of f (eq (20)).

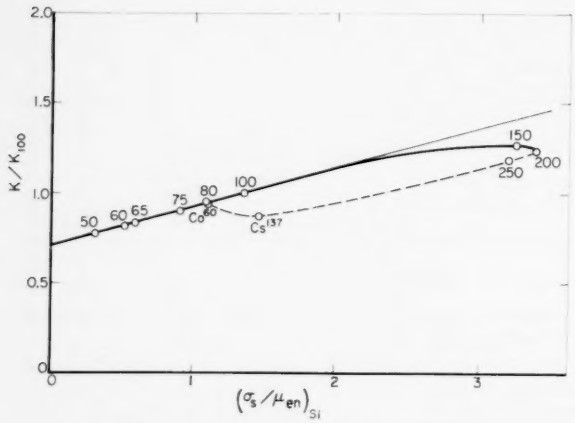

FIGURE 12. *Relative ionization coefficients,* K/K_{100}, *as a function of* $(\sigma_s/\mu_{en})_{Si}$, *the ratio of energy scattered by Compton photons and energy transferred to electrons (photoelectrons and Compton recoil electrons).*

For the calculation of values of $(\sigma_s/\mu_{en})_{Si}$, the spectral distributions of the radiations were taken into account. Numbers shown near the points indicate the operating voltages for X-rays (table 1).

For lower energies, the values of K/K_{100} show a linear dependence on $(\sigma_s/\mu_{en})_{Si}$ which has a maximum value at approximately $h\nu=150$ kev. For the linear part of the graph at lower energies, one can assume the relation

$$K/K_{100}=\alpha[1+\beta(\sigma_s/\mu_{en})_{Si}] \tag{23}$$

with $\alpha=0.71$ and $\beta=0.29$. For higher energies the K/K_{100} values are lower than those given by relation (23). Assuming that for very low photon energies $K=1$, one obtains by linear extrapolation to $(\sigma_s/\mu_{en})_{Si}=0$:

$$\alpha=1/K_{100} \text{ and } K=1+\beta(\sigma_s/\mu_{en})_{Si}.$$

From the value of α one obtains $K_{100}=1.41$. With this value, one can calculate K for all investigated radiations from the known values of K/K_{100}. They increase from 1.09 for the 50-kv X-rays to a maximum value of 1.79 for the 150-kv X-rays and fall off to 1.21 for Cs^{137} gamma rays. The value of $\beta=0.29$ indicates that for the investigated low-energy X-rays, 29 percent of the energy of Compton photons scattered in all directions are reabsorbed in the collecting volume v_c.

The collecting volume v_c and the thickness L of the effective layer can be calculated by introducing the values of K in eq (19a) and calculating I_s from eq (13). The energy required to produce one electron-hole pair is assumed as $\epsilon=2.25$ ev, a value found by Chynoweth and McKay [19] for the electron threshold energy for electron-hole pair production in silicon. Thus, one obtains

$$v_c=4.4\times10^{-2}\text{cm}^3 \text{ and } L=5.5\times10^{-3}\text{cm}.$$

The diffusion lengths in the investigated cell were not known. However, the above value of L, mainly determined by the diffusion length L_p of holes in the n-type layer, is of the same order of magnitude as usually given by other authors [20] (10^{-2} to 10^{-3} cm). Gremmelmaier [21] calculated the diffusion lengths in a silicon solar cell in a similar way from the photoresponse to Co^{60} gamma rays. However, in his calculations he used the total absorption coefficient without taking into consideration an ionization coefficient and assumed a value $\epsilon=3.6$ ev. He claimed agreement with measured values of L_p within 20 percent.

5. Conclusions

The stable and linear response of silicon solar cells to X-rays and low-level gamma rays makes it possible to use such cells for quantitative measurements of such radiations. The maximum exposure dose rates applied in this investigation were 1.8×10^6 r/hr for unfiltered 50 kv X-rays from a beryllium window-type tube, 6×10^4 r/hr for unfiltered 250-kv X-rays, and 4×10^2 r/hr for Co^{60} gamma rays. The relatively low electron energy threshold ($\sim$145 kev) for radiation damage in silicon [22] may put a limit on the use of silicon solar cells for gamma radiations of photon energies above approximately 400 kev.

The limit for a measurable response at low exposure dose rate levels is determined by the sensitivity of the measuring instruments. The response observed in this investigation for an exposure dose rate of 1 r/min was of the order of 10^{-5} volts for the open-circuit voltage and 10^{-8} amp for the photocurrent. Because of the great temperature dependence of the open-circuit voltage, it is preferable to use the photocurrent for radiation measurements. However, it will be difficult to reduce the load resistance sufficiently to make the photocurrent temperature independent because of the usual high impedance of sensitive current measuring instruments.

The response of the silicon solar cell showed a smaller directional dependence for X- and gamma rays than for visible light which follows a cosine law [7]. For Co^{60} gamma rays, the photoresponse remained constant over a wide angle of incidence of radiation.

The silicon solar cells show a better energy dependence than other solid state devices used for measurement of high-energy radiation. The ratio between the response to 50-kv X-rays ($h\nu_{eff}=38$ kev) and that to Co^{60} gamma rays was approximately 6:1 compared with an approximate value of 25:1 for the same ratio reported for cadmium sulfide photoconductive cells [23] and photographic films [15]. Because of their high-atomic number, a high ratio may also be expected for germanium ($Z_{Ge}=32$) and selenium ($Z_{Se}=34$) photocells.

Silicon solar cells of the same manufacture and of the same type showed different electrical characteristics and accordingly different sensitivity with the same measuring setup. The measurements reported in this investigation were all carried out on one and the same cell.

The response of silicon solar cells to X- and gamma rays could be improved by making certain adjustments to the cell, which is actually designed for use with visible light. In high energy radiation cells, the p-type and n-type layers should be larger than the diffusion lengths by an amount which is equal to the range of the most energetic electron produced by the radiation. In this way electronic equilibrium condition could be approached. The ionization coefficient and the collecting volume would thus be increased and the cell would become more sensitive for high-energy radiation. A special design of the cell casing could improve the directional and energy dependence of the photoresponse. The overall sensitivity could be increased by using multicell arrangements and stacking of cells in case of irradiation with high-energy gamma rays. The silicon solar cell could be specially useful in monitoring and relative measurements of radiation, having also the advantage of being independent of an external electric power supply.

6. References

[1] K. Scharf and O. Weinbaum, Z. Physik **80,** 465 (1933).
[2] H. Felsinger, Ann. Physik **29,** 81 (1937).
[3] G. Blet, J. Phys. Radium **14,** 368 (1953).
[4] R. Feinberg, Nature **181,** 1057 (1958).
[5] J. Drahokoupil, M. Malkowska and J. Tauc, Czech. J. Phys. **7,** 57 (1957).
[6] H. Pfister, Z. Naturforsch. **11a,** 434 (1956).
[7] M. B. Prince and M. Wolf, J. Brit. I.R.E. **18,** 583 (1958).
[8] M. B. Prince, J. Appl. Phys. **26,** 534 (1955).
[9] W. Shockley, Bell System Tech. J. **28,** 435 (1949).
[10] R. L. Cummerow, Phys. Rev. **95,** 16 (1954).
[11] J. W. Moody, G. L. Kendall and R. K. Willardson, Nucleonics **16,** No. 10, 101 (1958).
[12] J. J. Loferski and P. Rappaport, RCA Review **19,** 536 (1958).
[13] Report of the International Commission on Radiological Units and Measurements (ICRU), NBS Handb. 62 p. 11, (1956).
[14] H. A. Kramers, Phil. Mag. **46,** 836 (1923).
[15] M. Ehrlich and S. H. Fitch, Nucleonics **9,** No. 3, 5 (1951).
[16] G. Hettinger and N. Starfelt, Acta Radiol. **50,** 381 (1958).
[17] G. White Grodstein, NBS Circ. **583** (1957).
[18] A. T. Nelms, NBS Circ. **542** (1952).
[19] A. G. Chynoweth and K. G. McKay, Phys. Rev. **108,** 29 (1957).
[20] P. Rappaport, RCA Review **20,** 373 (1958).
[21] R. Gremmelmaier, Proc. I.R.E. **46,** 1045 (1958).
[22] J. J. Loferski and P. Rappaport, Phys. Rev. **111,** 432 (1958).
[23] L. E. Hollander, Nucleonics **14,** No. 10, 68 (1956).

WASHINGTON, D.C.

(Paper 64A4–52)

JOURNAL OF RESEARCH of the National Bureau of Standards—A. Physics and Chemistry
Vol. 64A, No. 4, July–August 1960

Phase Equilibria in Systems Involving the Rare-Earth Oxides. Part I. Polymorphism of the Oxides of the Trivalent Rare-Earth Ions

R. S. Roth and S. J. Schneider

(April 5, 1960)

The polymorphic relationships of the pure rare-earth oxides have been reinvestigated using X-ray diffraction methods for identification of phases. The oxides of the trivalent rare earth ions crystallize in three different types: A, B, and C. Each oxide has only one truly stable polymorph: La_2O_3, Ce_2O_3, Pr_2O_3, and Nd_2O_3 belong to the A type; Sm_2O_3, Eu_2O_3, and Gd_2O_3 to the B type; Tb_2O_3, Dy_2O_3, Ho_2O_3, Er_2O_3, Tm_2O_3, Yb_2O_3, and Lu_2O_3 to the C type. In addition Nd_2O_3, Sm_2O_3, Eu_2O_3, and Gd_2O_3 have low-temperature, apparently metastable, C-type polymorphs. The low-temperature form inverts irreversibly to the stable form at increasingly higher temperatures for decreasing cation radius.

1. Introduction

During the course of a study of phase equilibria in various rare-earth oxide systems, it was necessary to reinvestigate the polymorphic relationships of the pure rare-earth oxides. These materials had been previously investigated by Goldschmidt, Ulrich, and Barth [1][1] in 1925. More recently Shafer and Roy [2] have investigated some of the rare-earth oxide phases by hydrothermal means and they report some discrepancies from the original work of Goldschmidt et al.

Goldschmidt et al., [1] divided the rare-earth oxides into three main polymorphic types, A, B, and C. The oxides of the larger rare-earth cations (A type) were reported to be hexagonal and the oxides of the smallest ones (C type) cubic. The intermediate (B type) oxides had unknown symmetry. No X-ray diffraction data were given for the A- or B-type polymorphs and only unit-cell dimensions were given for the C-type cubic polymorph. The structures of the A and C types were first reported by Zachariasen [3]. Pauling [4] suggested a different structure for the A-type rare-earth oxides and this structure was confirmed by Koehler and Wollan [5] by means of neutron diffraction.

The B-type rare-earth oxide was originally observed in two different forms, reported as B_1 and B_2 by Goldschmidt et al. [1]. The B_2 type was designated as the lower temperature form but was never observed as a single phase. As no X-ray data were given for either phase, it has been rather difficult for subsequent research workers to identify these phases. Douglass and Staritzky [6] grew single crystals of a polymorph of Sm_2O_3 which they concluded was the B type of Goldschmidt et al., and reported this modification to be monoclinic. The structure of this B-type polymorph was reported by Cromer [7].

[1] Figures in brackets indicate the literature references at the end of this paper.

2. Specimen Preparation and Test Methods

The spectrographic analyses of the oxides used in this study are listed in part II of this work [8]. The oxalates were specially purified materials supplied by E. L. Weise of the Chemistry Division of NBS. All rare-earth oxides and salts had a purity of 99.9 percent or better, with two exceptions. The samarium oxalate contained about one percent europium and, in one experiment, a neodymium oxide of about 98 percent purity was used.

For heat treatments performed in air below 1,000° C, the specimen was placed in a covered platinum crucible and heated in a commercial resistance furnace. For temperatures between 1,000° and 1,650° C an 80 percent Pt–20 percent Rh wire-wound resistance furnace was used. The specimen was contained in a platinum tube hung on fine platinum wire and was usually quenched after heating. In both furnaces the specimen was always placed immediately adjacent to the thermocouple so that the temperatures reported are probably accurate to at least ±10° C. Above 1,650° C an inductively heated iridium crucible was utilized and the temperature measured with an optical pyrometer. An arc image furnace was used in an attempt to obtain melted drops of several of the oxides.

The specimens were examined at room temperature by means of an X-ray powder diffractometer using Ni-filtered Cu radiation. The phases identified are interpreted as representing the conditions of the material at the temperature of heating. Any nonquenchable phases cannot be determined by this technique. Indexed X-ray diffraction powder patterns were used to identify the three possible polymorphs of the rare-earth oxides. The hydroxides and oxyhydroxides were identified by reference to the X-ray patterns (unindexed) listed by Schafer and Roy [2].

548228—60——4

3. Experimental Data

All of the experiments performed in the present work are listed in table 1. The experiments are listed in order of increasing cation atomic number (or decreasing ionic radius), and in order of increasing temperature of heat treatment for each starting material. Continual reference to this table will be of value in clarifying the following discussion.

TABLE 1. *Experimental data on the polymorphic relations of the rare-earth oxides*

Starting material	Heat treatment [1]		Pressure [2]	Phases identified by X-ray powder diffraction	Remarks
	Temp.	Time			
	°C	hr			
$La(OH)_3$ [3]	200	144		$La(OH)_3$	
Do	300	144		$LaO(OH)+La(OH)_3$	Very poor X-ray pattern.
Do	350	168		LaO(OH)	
Do	400	168		do	
Do	450	168		do	
Do	500	168		do	
$La(NO_3)\cdot 2NH_4NO_3\cdot 4H_2O$	450	20		Unidentified	Does not contain either C- or A-type rare-earth oxide.
Do	450	192		do	
$La(NO_3)\cdot 6H_2O$	450	20		do	Not A- or C-type rare-earth oxide.
$Ce_2(C_2O_4)_3\cdot 10H_2O$	500	96	10^{-4} mm Hg	CeO_2	Cerous oxalate must be heated in hydrogen to maintain trivalent state.
Pr_6O_{11}	1,010	.83	10^{-5} mm Hg	A-type Pr_2O_3	
$Nd(C_2O_4)_3\cdot 10H_2O$	500	40		C-type Nd_2O_3	
Do	500	168		[4] Unidentified+C-type Nd_2O_3	
Do	600	120		C-type Nd_2O_3	
Do	700	144		C-type Nd_2O_3+A-type Nd_2O_3	No B-type Nd_2O_3.
Do	800	144		A-type Nd_2O_3+C-type Nd_2O_3	Do.
$Nd(C_2O_4)_3\cdot 10H_2O$	1,300	.083		A-type Nd_2O_3	
$Nd(C_2O_4)_3\cdot 10H_2O$ [5]	600	168	20,000 psi	$Nd(OH)_3$	Sealed in Pt tube with H_2O added.
Do. [5]	600	168	20,000 psi	NdO(OH)	Sealed in Pt tube without adding H_2O.
Do. [5]	950	42	5,000 psi	do	
Do. [6]	950	42	5,000 psi	do	Sealed in Pt tube with H_2O.
Do. [6]	950	42	5,000 psi	A-type Nd_2O_3	Sealed in Pt tube without adding H_2O.
$Nd(OH)_3$ [7]	600	16		C-type Nd_2O_3	
Do	950	48	5,000 psi	$NdO(OH)+Nd(OH)_3$	Heated in unsealed Pt tube.
Do. [8]	950	48	5,000 psi	NdO(OH)+A-type Nd_2O_3	Sealed in Pt tube without adding H_2O.
Do	600	288		C-type Nd_2O_3	
Sm_2O_3	1,000	2		B-type Sm_2O_3	
Do	1,500	1.5		do	
Sm_2O_3	([9])			C-type Sm_2O_3?	Very poorly crystalline.
Do	500	4		C-type + B-type Sm_2O_3	
Do	500	168		do	B-type probably present in "as received" material.
$Sm_2(C_2O_4)_3\cdot 10H_2O$	500	336		C-type Sm_2O_3	
Do	600	168		do	
Do	700	192		do	
Do	750	216		do	
Do	800	192		do	
Do	900	168		do	
Sm_2O_3 [5]	600	168	20,000 psi	SmO(OH)	Sealed in Pt tube with H_2O.
Do. [5]	600	168	20,000 psi	C-type Sm_2O_3+SmO(OH)	Sealed in Pt tube without adding H_2O.
Do. [6]	950	6	5,000 psi	B-type Sm_2O_3+SmO(OH)	Do.
Sm_2O_3	([10])	([10])		B-type Sm_2O_3	Bar previously calcined at 1475° C for 15 hr.
Eu_2O_3	1,000	2		C-type Eu_2O_3	
Do	1,500	1.5		B-type Eu_2O_3	
Eu_2O_3	1,050	114.5		C-type Eu_2O_3	
Gd_2O_3	1,000	2		C-type Gd_2O_3	
Do	1,500	1.5		B-type Gd_2O_3	
Gd_2O_3	1,000	68		C-type Gd_2O_3	
Do	1,100	42		do	
Do	1,200	42		do	
Do	1,250	72		C-type+B-type Gd_2O_3	No sign of B_2-type Gd_2O_3.
Do	1,319	64		B-type Gd_2O_3	
Do	1,200	336		B-type Gd_2O_3+C-type Gd_2O_3+A-type Gd_2O_3.	C- and A- Gd_2O_3 only surface effect.
Gd_2O_3	600	168	20,000 psi	GdO(OH)	Sealed in Pt tube with H_2O added.
Do	600	168	20,000 psi	C-type Gd_2O_3	Sealed in Pt tube without adding H_2O.
Do	950	6	5,000 psi	do	Do.
$Gd(OH)_3$ [5]	850	.167		C-type Gd_2O_3	
Tb_4O_7	1,500	1.5		2 cubic phases (?)	
Do	1,500	0.33		C-type Tb_2O_3	Heated in argon atmosphere.

See footnotes at end of table.

TABLE 1. *Experimental data on the polymorphic relations of the rare-earth oxides*—Continued

Starting material	Heat treatment [1]		Pressure [2]	Phases identified by X-ray powder diffraction	Remarks
	Temp.	Time			
	° C	hr			
Dy_2O_3	1,000	2		C-type Dy_2O_3	
Do	1,500	1.5		do	
Dy_2O_3	([11])	([11])		do	Bar previously calcined at 1475° C for 15 hr.
Ho_2O_3	1,200	6		C-type Ho_2O_3	
Do	1,500	6		do	
Er_2O_3	1,200	6		C-type Er_2O_3	
Do	1,500	6		do	
Tm_2O_3	1,100	4		C-type Tm_2O_3	
Do	1,500	6		do	
Yb_2O_3	1,100	4		C-type Yb_2O_3	
Do	1,500	6		do	
Lu_2O_3	1,100	4		C-type Lu_2O_3	
Do	1,500	6		do	
Y_2O_3	1,350	10		C-type Y_2O_3	
Do	2,000	0.25		do	

[1] The heat treatment for each specimen includes all previously listed lower temperature heatings for the same starting material.
[2] All specimens were treated at atmospheric pressure except where indicated in this column.
[3] A-type La_2O_3 boiled in distilled H_2O for 2 hr; dried overnight at 110° C; X-ray powder diffraction pattern shows only $La(OH)_3$.
[4] Unidentified phase probably due to reaction with atmosphere after removal from furnace and before subjecting to X-ray diffraction. This was the only specimen in the series to wait several days between heat treatment and X-ray examination.
[5] Calcined at 600° C in Pt crucible, but probably partially rehydrated before being sealed in Pt tube.
[6] Calcined at 600° C in Pt crucible, recalcined at 600° C overnight in Pt tube and sealed.
[7] Impure A-type Nd_2O_3 boiled in distilled H_2O for 2 hr, dried overnight at 110° C. X-ray powder diffraction patterns show only $Nd(OH)_3$.
[8] $Gd(OH)_3$ formed by dissolving Gd_2O_3 in HCl and precipitating with $(NH_3)OH$, precipitate washed and dried under infrared lamp.
[9] As received.
[10] Melted drop in arc image furnace.
[11] Melted(?) drop in arc image furnace.

4. Comparison with Previous Results

4.1. La_2O_3

Lanthanum oxide was reported [by Goldschmidt et al., [1] to occur only in the A-type rare-earth oxide structure. However, Lohberg [9] reported preparing a C-type La_2O_3 by decomposing lanthanum ammonium nitrate at 450° C during a 20-hr heat treatment. This experiment was also performed by the present authors but no C-type rare-earth oxide could be identified in the X-ray pattern. Apparently the nitrate was not completely decomposed at 450° C and no rare-earth oxide structure was formed.

An attempt was also made to form the C-type La_2O_3 polymorph by decomposing the hydroxide at low temperatures. However, as the data in table 1 indicate, $La(OH)_3$ decomposes to LaO(OH) between 200° and 300° C. This LaO(OH) is stable up to at least 500° C, too high a temperature to produce C-type La_2O_3. It must be concluded that considerable doubt exists as to whether pure La_2O_3 can be formed in the C-type polymorph. This question cannot be answered unless a method is found to produce La_2O_3 by decomposing a lanthanum compound below 500° C.

4.2. Ce_2O_3 and Pr_2O_3

Goldschmidt et al. [1] have suggested that B-type Ce_2O_3 might be obtained by a heat treatment of several days duration in a stream of hydrogen at about 600° C. They report the A-type of Ce_2O_3, obtained by heating ceric oxide in a stream of hydrogen at 1,250° C for 30 min. No attempt has been made to heat cerium oxide in hydrogen in the present work. One attempt to form Ce_2O_3 from cerous oxalate at 500° C in vacuum (10^{-4} mm Hg) was unsuccessful, resulting in CeO_2. Data on Nd_2O_3 (see sec. 4.3.) indicate that it is very unlikely that Ce_2O_3 could form the B structure. However, it may be possible that the C type can form at low temperatures.

Praseodymium oxide was formed in the A type in the present work by heating Pr_6O_{11} in vacuum (10^{-5} mm) at 1,010° C. As in the case of Ce_2O_3 it seems unlikely that the B type would exist. However, the C type may very possibly form at low temperatures.

4.3. Nd_2O_3

Neodymium oxide was found by Goldschmidt et al. [1] to be stable in the B type over a large temperature range, transforming to the A type at about 1,000° C, although it could be found metastably in short runs as high as 1,300° C. The C modification of Nd_2O_3 was first described by Lohberg [9], who obtained this structure type at 700° and 875° C and found that it transformed directly to the A type at about 940° C. Lohberg was unable to prepare Nd_2O_3 in the B modification.

Shafer and Roy [2] have studied the stability of the phases in some rare-earth oxide—water systems by hydrothermal techniques. They report B-type Nd_2O_3 to be stable at intermediate temperatures and pressures (for instance 950° C—5,000 lb/in.^{2}).

In the present work, Nd_2O_3 was found to transform from the C type directly to the A type at atmospheric pressure and approximately 650° C. Attempts to form the B-type oxide by reproducing the experiments of Goldschmidt et al. [1] and Shafer and Roy [2] resulted in either C- or A-type Nd_2O_3 or else $Nd(OH)_3$ or NdO(OH).

Shafer and Roy report an X-ray powder diffraction pattern for B-type Nd_2O_3. This work was performed before the publication of the monoclinic parameters of B-type Sm_2O_3 by Douglass and Staritzky [6] and the B-Nd_2O_3 pattern was not indexed. However, a comparison of Shafer and Roy's pattern with those of the known B-type oxides indicates that it does have the B structure. Therefore, it must be concluded that the B polymorph is stable in the range indicated by Shafer and Roy. The reason it could not be synthesized in the present work probably depends on the rate of reaction of this phase with H_2O. Shafer and Roy were probably able to obtain the B-type Nd_2O_3 by allowing the steam to escape first and then temperature quenching the dry specimen. With the equipment available for the present work, this was not possible and the specimen was in contact with hot water for several minutes during cooling. A specimen of B-type Nd_2O_3 prepared by Shafer and Roy in their original work was sent to the present authors. However it was found that the specimen now contained only NdO(OH), probably having hydrated over the years at atmospheric pressure. In compositions reported in part II of this study [8], it was observed that B-type solid solutions containing 90 percent or more of Nd_2O_3 had a much stronger tendency to hydrate than did the A or C modifications of Nd_2O_3.

It may be concluded, therefore, that pure Nd_2O_3 at atmospheric pressure will be formed only in the C and A polymorphic types. However under hydrothermal conditions the B type may occur at intermediate temperatures. Whether the B type could occur in pure Nd_2O_3-H_2O mixtures in a closed system cannot be determined at the present time as the water cannot be driven out fast enough in such a system to prevent hydration. As the B-type Nd_2O_3 does not occur, under atmospheric conditions, it seems unlikely that the B type would form at all with Pr_2O_3 or Ce_2O_3.

4.4. Sm_2O_3

Goldschmidt et al., report both the C and B modifications for Sm_2O_3. They state that type C will not transform to B with heat treatments of several days duration at 800° C, 700° C, or 600° C. However, they state that a mixture of B and C types was formed by heating the hydroxide as low as 735° C. In the present work the C polymorphic type formed from samarium oxalate did not transform to the B structure with 1 to 2 weeks heat treatment at several temperatures up to 900° C. A sample of C-Sm_2O_3 whose diffuse powder diffraction lines indicated poor crystallinity readily formed the B type at 1,000° C in a few hours.

It appears that the C–B transformation in Sm_2O_3 is a rate process depending on the crystallinity of the C type. Poorly crystallized C-type material quickly transforms to the B type at relatively low temperatures whereas the more crystalline C-type samples will be transformed only with greater difficulty.

Goldschmidt et al. were unable to transform the B-Sm_2O_3 back to the C type even with many days annealing. They concluded that with Sm_2O_3 the C–B transformation may be monotropic. The fact that the C–B transformation temperature apparently depends on the crystallinity of the starting material is another indication of the monotropic nature of the reaction.

Goldschmidt et al. suggested that, for Sm_2O_3, the stable phase was type A at the melting point and this quickly transformed to B on cooling. A quickly cooled drop of Sm_2O_3, melted in an arc-image furnace in the present work, showed X-ray powder diffraction lines of the B type only. It therefore seems unlikely that pure Sm_2O_3 can be quenched in the A-structure, if such a structure exists. Only high temperature X-ray measurements at approximately 2,300° C could answer the question of the occurrence of the A structure.

4.5. Eu_2O_3

Europium oxide was obtained as the C type by Goldschmidt et al., at 735° C and 750° C, and as the B type at 1,100° C. Curtis and Tharp [10] reported the C–B transformation temperature for Eu_2O_3 as approximately 1,050° C. In the present work the C modification of Eu_2O_3 did not transform to B even after 114.5 hr at 1,050° C. The C–B transformation in Eu_2O_3 may also depend on crystallinity. However, by combining the data from the present experiments with those of Curtis and Tharp [10] the transformation temperature can be concluded to be about 1,075° C.

4.6. Gd_2O_3

Goldschmidt et al. [1] found the C-type Gd_2O_3 to be stable at 600° and at 750° C. However, their X-ray powder pattern of gadolinium oxide which had been heated to 800° to 900° C showed strongly the lines of a crystalline phase which apparently had relatively high symmetry and was called B_2 type oxide. Crystal type B_1 was observed by Goldschmidt et al. in a specimen heated at 1,300° C.

Guentert and Mozzi [11] reported high temperature X-ray diffraction experiments on Gd_2O_3. The monoclinic form, identified with Goldschmidt's B_1, did not occur at 1,200° C but was partially formed at 1,400° C. They concluded that their results indicated a direct transition from the cubic to the monoclinic form, without any evidence for the existence of the B_2 type.

In the present work the C–B transformation in Gd_2O_3 was observed in heatings of several days to take place at approximately 1,250° C. Again no evidence of the B_2 type was found in experiments involving the C–B transformation. Dr. T. F. W. Barth [12] has suggested, in a private communica-

tion, that "Perhaps the B_2 phase simply is caused by impurities." The present authors were unable to obtain the data for the d values which were identified by Goldschmidt et al., as being characteristic of the B_2 phase. Therefore the B_2 phase cannot be definitely explained.

As the C–B transformation was not found to be reversible in Sm_2O_3 it was thought that the reversibility of this transformation in Gd_2O_3 should be checked. A pellet of the B-type Gd_2O_3 was heated just below the transformation temperature at 1,200° C for 2 weeks. The body of the pellet was found to contain only the B-crystal type. However, the surface of the pellet showed both C and A polymorphic types in addition to the B-type (fig. 1). As the (002) peak was much stronger than the (101), it appears the A-Gd_2O_3 was highly oriented on the surface of the pellet. From this data the present authors conclude that A-Gd_2O_3 is only a metastable phase and that the C–B transformation is not truly reversible.

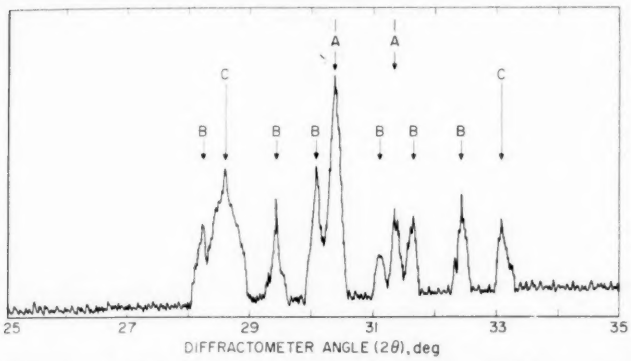

FIGURE 1. *Portion of an X-ray diffraction powder pattern from the surface of a pellet of* Gd_2O_3 *heated at 1,200° C for 2 weeks, showing a mixture of all three crystal types A, B, and C.*
Ni-filtered Cu radiation.

4.7. Tb_2O_3

In the present study, Tb_4O_7 was converted to a phase having the C-type crystal structure by heating in argon at 1,500° C. However it is possible that this reaction did not proceed completely to Tb_2O_3 and may represent a solid solution of Tb_2O_3 with excess oxygen.

4.8. Dy_2O_3, Ho_2O_3, Y_2O_3

These three oxides have been found to occur only in the C-type modification. However, Goldschmidt et al. state that the B_1–C transformation of dysprosium oxide appears to proceed spontaneously. This was based on the observation that: "After heating at the platinum melting point, dysprosium oxide showed modification C, possibly pseudomorphic after B."

In the present work, a bar of Dy_2O_3 was heated in an arc image furnace and very quickly cooled. Due to the thermal shock characteristics of Dy_2O_3 the hot portion of the bar broke up with explosive force, so that it could not be determined whether melting had occurred. However, modification C was the only type identified in the X-ray pattern. It may be concluded that pure Dy_2O_3 can form only the C-type structure, although very small amounts of impurities may possibly enable a B type to become stable. Both Ho_2O_3 and Y_2O_3 have been found to crystallize only in the C type.

4.9. Er_2O_3, Tm_2O_3, Yb_2O_3, and Lu_2O_3

These rare earth oxides have been found only in the C type. Goldschmidt et al. examined Yb_2O_3 at low temperatures to see if a further type D would appear, with negative results. There is no evidence to suggest any other modification of the pure rare-earth oxides and the present work (table 1) is not in disagreement with the conclusion that the C-type is the only modification to appear in the oxides of the smaller rare-earth ions.

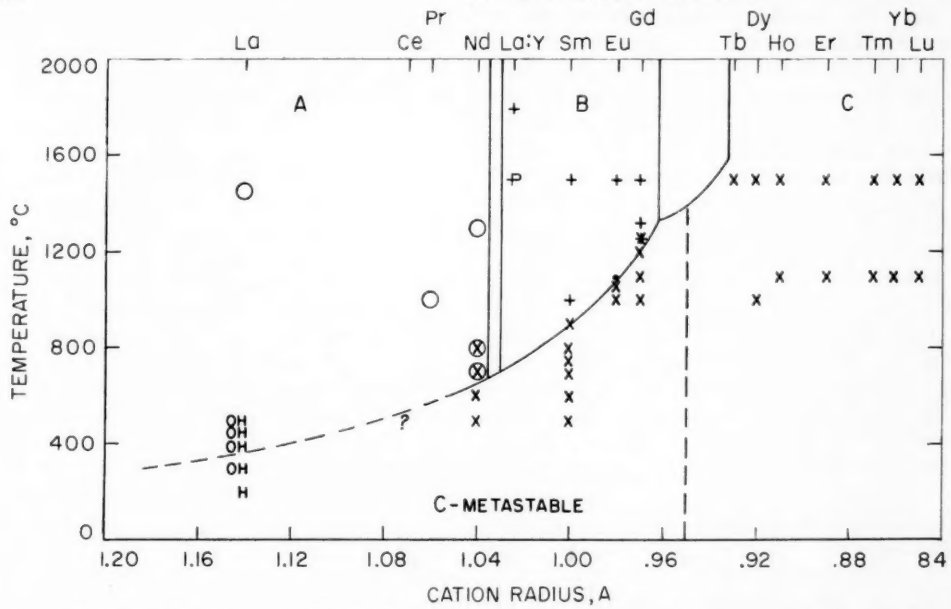

FIGURE 2. *Stability relations of the A, B, and C polymorphic forms of the rare-earth sesquioxides.*
○, A type; +, B type; X, C type; P, perovskite; La:Y, 1:1 La_2O_3:Y_2O_3; H, hydroxide; OH, oxyhydroxide; ?, structure and oxidation state unknown.

5. General Conclusions

5.1. Stability of the Polymorphic Types

The stability relations of the polymorphs encountered in this study are summarized in figure 2. In this figure the temperature has been plotted on the ordinate and the radii of the rare-earth ions (instead of the atomic number as was done by Goldschmidt) have been plotted on the abscissa. The radii used here are those given by Ahrens [13]. This diagram shows the A-type rare-earth oxide structure to be stable for the larger ions, the B type for the intermediate ions, and the C type for the smaller ions. In addition, the C-type structure is shown to occur metastably at low temperatures for all the A- and B-type oxides except La_2O_3. This oxide could not be formed by decomposition at low enough temperatures to confirm the existence of the C type. The A–B and B–C boundaries are shown as two-phase areas to correspond with the diagrams drawn for part II of this study [8] which show the relationships of these polymorphs in all possible binary and ternary combinations. The upper stability temperature of the metastable C field, for any given oxide, probably depends upon the starting material. The C–B reaction has not been reversed experimentally and is probably monotropic.

Goldschmidt et al. [1] state that the three crystal types A, B, and C show "succeeding thermal relations," A being stable at the highest temperatures, B at intermediate temperatures, and C at the lowest temperatures. This conclusion cannot be drawn from the present study. Rather, the three crystal types show relations only to the cation size, A for the largest ions, B for the intermediate ions, and C for the smaller ions. As the low→high reaction of the C polymorph to either B or A is probably monotropic, the C polymorph should not be considered as a stable phase for these oxides.

During the interval between the publication of Goldschmidt's work [1] and the indexing of the X-ray powder pattern of the B type by Douglass and Staritzky [6], the B polymorph was almost totally ignored and the rare-earth oxides were generally classified into two types, A and C. There is no longer any excuse for this binary classification. As has been shown by the present work, as well as that of Goldschmidt et al. [1], Shafer and Roy [2], and others, the trivalent rare-earth oxides must be classified into the three groups A, B, and C with the B type recognized as a stable crystal phase. The B polymorph is more stable in impure materials than it is in the pure rare earths, as is shown for various binary and ternary systems studied by the present authors [8]. This stability of the B type in impure systems may account for the report of a B polymorph in the oxides of the larger rare-earth ions such as Nd_2O_3.

Goldschmidt, Ulrich, and Barth have given the impression that the three crystal types in the rare-earth oxides, in general, showed enantiotropic relations. However, no enantiotropic reactions were found in the present work. The C–B transformation occurs readily enough. However, the B–C transformation was not obtained except as a surface reaction in Gd_2O_3 involving the formation of the A polymorph as well. Goldschmidt et al. claimed this reaction was enantiotropic on the basis of a spontaneous B–C reaction in dysprosium oxide. The present work shows no indication of a B type for Dy_2O_3.

No A–B or B–A reaction was found in the present work. Goldschmidt observed this reaction to proceed in both directions with Nd_2O_3. As it seems that B-Nd_2O_3 can exist in the pure oxide only under hydrothermal conditions the reversibility of this reaction cannot be checked. The A–B transformation, which was reported by Goldschmidt et al., to take place spontaneously in Sm_2O_3, also was not observed.

The transformation C–A observed in the present work for Nd_2O_3 was not observed at all by Goldschmidt. The A-type Nd_2O_3 cannot be converted to C-type Nd_2O_3 without going through an intermediate hydrated state.

Shafer and Roy [2] have concluded that the inversions in the rare-earth oxides "appear to be genuine reversible polymorphic transitions." This conclusion appears to be based on an experiment in which B-type Nd_2O_3 was transformed to C-type Nd_2O_3 hydrothermally. However it must be realized that in the process of heating this specimen the B-Nd_2O_3 was necessarily first transformed to a hydrated crystalline type, so that the reversibility of the direct transformation is left open to question. It may be concluded therefore that all the polymorphic reactions of the trivalent rare-earth oxides are irreversible and probably monotropic.

5.2. Unit-Cell Parameters and Radii of the Trivalent Rare-Earth Cations

The unit-cell dimensions of the various polymorphs of the rare-earth oxides are listed in table 2. All of these values are derived from data obtained in the present study with the exception of the B-type Nd_2O_3, which was calculated from the X-ray pattern listed by Shafer and Roy [2].

The unit-cell dimensions of the C-type cubic polymorphs are plotted in figure 3 against the radii of the cations, as listed by Ahrens [13]. It can be seen that the unit cell dimensions of the oxides of the rare-earth ions from Nd^{+3} to Lu^{+3} fall on a straight line. The straight line relationship is required for the C-type polymorphs, as Ahrens' radii were originally calculated from unit-cell dimensions of the C-type oxides. The fit to a straight line would be more exact if the radii were given to three decimal points as suggested by Templeton and Dauben [14]. The Tb_2O_3 parameter is the only one significantly off the straight line as indicated by the arrows. Either the radius of Tb^{+3} listed by Ahrens is too small or else the reduction of the present specimen was not complete. It should be pointed out that an extension of this straight line to the radius of La^{+3} predicts the unit cell dimension of C-type La_2O_3 close to the value of 11.4 A reported by Lohberg [9].

The values of the unit-cell dimensions of Y_2O_3 and In_2O_3 do not fall on this line when the radii given by

TABLE 2. *Unit-cell dimensions of the rare-earth oxides*

Oxide	Radius of cation[1]	A type		B type				C type	
		a	c	a	b	c	β	a	a, least squares[2]
		A	*A*	*A*	*A*	*A*		*A*	*A*
La_2O_3	1.14	3.93	6.12						
Ce_2O_3	1.07								
Pr_2O_3	1.06	3.85	6.00						
Nd_2O_3	1.04	3.82	5.98	14.35	3.666	8.99	100.34°	11.080	
Sm_2O_3	1.00			14.16	3.621	8.84	100.05°	10.934	
Eu_2O_3	0.98			14.06	3.601	8.80	100.15°	10.860	
Gd_2O_3	.97	3.76	5.89	14.06	3.572	8.75	100.10°		10.8122
Tb_2O_3	.93							10.729	
Dy_2O_3	.92								10.6647
Ho_2O_3	.91								10.6065
Y_2O_3	[3](.91)								10.6021
Er_2O_3	.89								10.5473
Tm_2O_3	.87								10.4866
Yb_2O_3	.86								10.4334
Lu_2O_3	.85								10.3907
In_2O_3	[3](.77)								10.1178

[1] Radii of the cations taken from Ahrens [13] except where noted.
[2] The data were fitted by least squares by Cohen's extrapolation method as discussed by Azároff and Buerger, The Powder Method. (McGraw-Hill Book Co., Inc., New York, N.Y., 1958).
[3] These are the radii derived from the unit-cell dimensions in the present study.

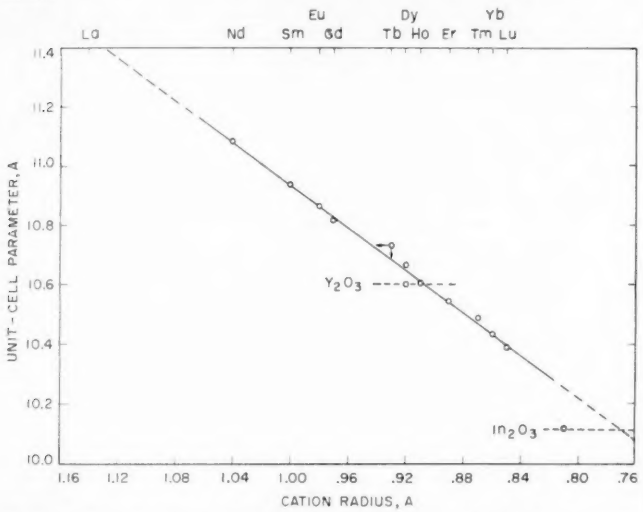

FIGURE 3. *Linear relationship between the unit-cell dimensions and the cation radius for the C-type cubic rare-earth oxide structures.*

Ahrens for Y^{+3} and In^{+3} are utilized. It must be concluded that both Y^{+3} and In^{+3} have slightly different effective radii when occurring in oxides of the C-type structure, and probably also in other oxide structure types. The radius of Y^{+3} is found to be just slightly smaller than that of Ho^{+3}, 0.91 A. The extension of the straight line intersects the unit-cell dimension of In_2O_3 at 0.77 A rather than the value of 0.81 A given by Ahrens. Using the unit-cell parameters of Sc_2O_3 (9.81 A) and Mn_2O_3 (9.43A) listed by Donnay and Nowacki [15] the effective radii of Sc^{+3} and Mn^{+3} in rare-earth-oxide-type compounds are found to be approximately 0.68 A and 0.56 A, respectively.

Templeton and Dauben [14] have calculated ionic radii of the rare-earth ions using a value of 0.21441 *a* (for the C-type rare-earth oxide structure) for the cation-oxygen distance. They emphasize that the relative difference between any two trivalent rare-earth cations can be found much more accurately than the absolute radii. For this reason the more generally accepted values of Ahrens, as modified by figure 3, are used for the present work.

In figure 4 the unit-cell parameters of the B-type oxides are plotted against the ionic radii. The *a*, *b*, and *c* parameters all increase significantly with increasing cation radius. The change in β is almost negligible. In addition to the unit cell dimensions of Nd_2O_3, Sm_2O_3, Eu_2O_3, and Gd_2O_3, the dimensions of the B-type phase reported to occur at 1:1 $La_2O_3:Y_2O_3$[2] [16] are plotted using an average radius for the two cations. It can be seen that the *a* and β parameters for 1:1 $La_2O_3:Y_2O_3$ occur at very significantly larger values than would be expected from the plot of the pure oxides. It will be shown in part II [8] that many solid solutions of the B type have this different relationship.

It can be inferred from figure 5 that the unit-cell dimensions of the A-type rare-earth oxides also

[2] The unit-cell parameters of the B-type 1:1 $La_2O_3:Y_2O_3$, previously heated at 1,800° C for 1 hr, are: a=14.41 A, b=3.643 A, c=8.93 A, β=101.09°.

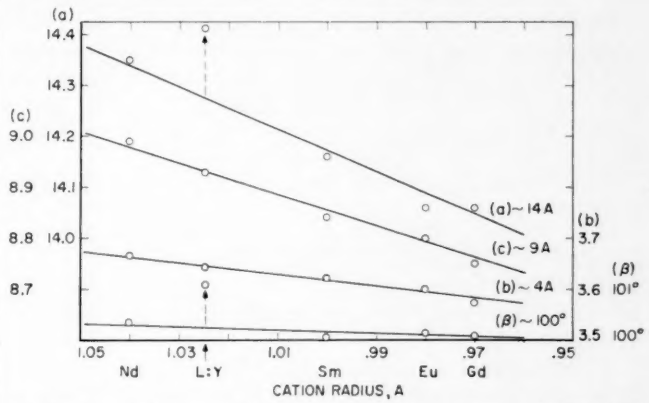

FIGURE 4. *Linear relationship between the unit-cell dimensions and the cation radius for the B-type monoclinic rare-earth oxide structures.*

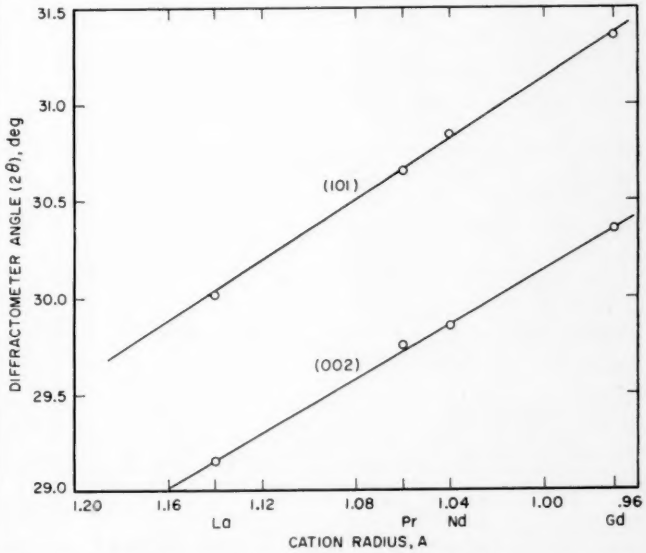

FIGURE 5. *Linear relationship between the diffraction angle 2θ and cation radius for the (002) and (101) peaks of the A-type hexagonal rare-earth oxide structures.*

change linearly with change in the radius of the cation. It may be seen that the (002) and (101) values observed for the metastable A-type Gd_2O_3 fall on the same straight lines as those drawn through the values for the stable A-type oxides.

6. Summary

The polymorphic forms of the oxides of the trivalent rare-earth ions have been reinvestigated. The overall picture of polymorphism in trivalent rare-earth oxides is slightly changed as compared with the original study of Goldschmidt et al. [1]. Lanthanum oxide has been found to occur only in the A-type hexagonal structure. Neodymium oxide forms the C-type cubic structure at low temperatures and inverts irreversibly to the A-type at about 650° C. The B-type monoclinic structure reported for Nd_2O_3 was not encountered in the present work. Samarium oxide, Eu_2O_3, and Gd_2O_3 crystallize in the C-type at low temperatures and invert directly and irreversibly to the B-type monoclinic structure at about 950°, 1,075°, and 1,225° C, respectively. The A-type structure was not found to occur at high temperatures in Sm_2O_3 but was found to occur metastably in Gd_2O_3 as a surface reaction when the B type was held at 1,200° C for several weeks. All the rare-earth oxides which have cations smaller than Gd^{+3} showed only the C-type cubic modification.

The transformation of the low-temperature C-type structure to either A or B type was concluded to be a rate process, depending on the degree of crystallinity of the C polymorph. This transformation appears to be irreversible, probably monotropic. No enantiotropic transformations were encountered in this study.

The unit-cell dimensions of the oxides of all three types are shown to vary linearly with the radius of the cation. The linear relationship holds true regardless of whether the polymorph is stable or metastable.

7. References

[1] V. M. Goldschmidt, F. Ulrich, and T. Barth, Geochemical distribution of the elements, Pt. IV. On the crystal structure of the oxides of the rare earth metals, Skrifter Norske Videnskaps-Akad. Oslo. I. Mat. Naturv. Kl., No. 5 (1925).

[2] M. W. Shafer and R. Roy, Rare earth polymorphism and phase equilibria in rare-earth oxide-water systems, J. Am. Ceram. Soc. **42,** 563 (1959).

[3] W. H. Zachariasen, Investigations of the crystal structure of the sesquioxides and the ABO_3 compounds, Skrifter Norske Videnskaps-Akad. Oslo. I. Mat. Naturv. Kl., No. 4 (1928).

[4] L. Pauling, The crystal structure of the *A*-modification of the rare earth sesquioxides, Z. Krist. **69,** 415 (1928).

[5] W. C. Koehler and E. O. Wollan, Neutron diffraction study of the structure of the A-form of the rare earth sesquioxides, Acta Cryst. **6,** 741 (1953).

[6] R. M. Douglass and E. Staritzky, Crystallographic Data: 112 samarium sesquioxide, Form B, Anal. Chem. **28,** 552 (1956).

[7] D. T. Cromer, The crystal structure of monoclinic Sm_2O_3, J. Phys. Chem. **61,** 753 (1957).

[8] S. J. Schneider and R. S. Roth, Phase equilibria in systems involving the rare earth oxides. Pt. II. Solid state reactions in trivalent rare earth oxide systems, J. Research NBS **64A,** 317 (1960).

[9] K. Lohberg, On the C-modification of the sesquioxides of neodymium and lanthanum, Z. Phys. Chem. (B) **28,** 402 (1935).

[10] C. E. Curtis and A. G. Tharp, Ceramic properties of europium oxide, J. Am. Ceram. Soc. **42,** 151 (1959).

[11] O. J. Guentert and R. L. Mozzi, The monoclinic modification of gadolinium sesquioxide Gd_2O_3, Acta Cryst. **11,** 746 (1958).

[12] T. F. W. Barth, Private communication (Dec. 7, 1958).

[13] L. H. Ahrens, The use of ionization potentials, Pt. I, Ionic radii of the elements, Geochim. Cosmochim. Acta **2,** 155–169 (1952).

[14] D. H. Templeton and C. H. Dauben, Lattice parameters of some rare earth compounds and a set of crystal radii, J. Am. Chem. Soc. **76,** 5237 (1954).

[15] J. D. H. Donnay and W. Nowacki, Crystal data, Geol. Soc. Am. Mem. 60 (1954).

[16] S. J. Schneider and R. S. Roth, Perovskite-type compounds in binary rare earth oxide systems, J. Am. Ceram. Soc. **43,** 115 (1960).

WASHINGTON, D.C. (Paper 64A4–53)

JOURNAL OF RESEARCH of the National Bureau of Standards—A. Physics and Chemistry
Vol. 64A, No. 4, July–August 1960

Phase Equilibria in Systems Involving the Rare-Earth Oxides. Part II. Solid State Reactions in Trivalent Rare-Earth Oxide Systems

S. J. Schneider and R. S. Roth

(April 5, 1960)

Selected mixtures in 21 binary and 9 ternary rare-earth oxide systems were studied by X-ray diffraction after heat treatment at 1,650° C and above. Two graphs were drawn to show specific regions of stability for the various structure types. Each gives the average ionic radius of constituent cations versus the mole percent of the smaller cation. One diagram is essentially divided into areas of solid solution of the A, B, and C rare-earth oxide structure types. The other indicates a field of perovskite-type compounds bordered by regions of A, B, or C solid solutions. These diagrams were used to predict the subsolidus phase diagrams of a number of systems. A total of forty-one subsolidus binary and one ternary rare-earth oxide systems were given. A tolerance factor equal to 0.77 was assigned as the minimum value for the formation of a perovskite-type compound.

1. Introduction

To date, no comprehensive study has been performed on the phase equilibrium relations between the oxides of the trivalent rare-earth ions. Most of the information available on these materials has centered about studies on the single oxides or on limited portions of systems involving only one trivalent rare-earth oxide. The authors, in a previous study [1],[1] have reinvestigated the polymorphic characteristics of the individual trivalent rare-earth oxides and essentially confirmed the earlier works of Goldschmidt [2] and of Shafer and Roy [3]. It has been definitely established that at elevated temperatures the stable forms of the rare-earth oxides have the following symmetries: La_2O_3, Ce_2O_3, Pr_2O_3, Nd_2O_3—hexagonal; Sm_2O_3, Eu_2O_3, Gd_2O_3—monoclinic; and Tb_2O_3, Dy_2O_3, Ho_2O_3, Er_2O_3, Tm_2O_3, Yb_2O_3, Lu_2O_3—cubic. The hexagonal, monoclinic, and cubic forms are referred to as the A, B, and C rare-earth oxide structures, respectively.

Ionic size is probably by far the most important factor in determining the behavior of any mixture of the rare-earth oxides at elevated temperatures. According to Ahrens [4] the radii of the trivalent rare-earth ions are: La^{+3}—1.14 A; Ce^{+3}—1.07 A; Pr^{+3}—1.06 A; Nd^{+3}—1.04 A; Sm^{+3}—1.00 A; Eu^{+3}—0.98 A; Gd^{+3}—0.97 A; Tb^{+3}—0.93 A; Dy^{+3}—0.92 A; Ho^{+3}—0.91 A; Er^{+3}—0.89 A; Tm^{+3}—0.87 A; Yb^{+3}—0.86 A; and Lu^{+3}—0.85 A.[2] Because of the relatively small differences between the radii of the various cations, it can be assumed that solid solution would be prevalent in a number of rare-earth oxide systems. In most cases, systems of oxides having like structure types probably form a complete series of solid solutions between the end members. As reported in a previous note [5], compounds occur only in those systems where there is a large difference in size between the constituent cations. These compounds ($LaErO_3$, $LaTmO_3$, $LaYbO_3$, and $LaLuO_3$) are all isostructural, having a perovskite-type structure, probably with orthorhombic symmetry.

The purpose of this investigation was to survey the solid state reactions that occur under equilibrium conditions for different mixtures of the trivalent rare-earth oxides and to establish the subsolidus phase equilibrium diagrams for various systems.

2. Materials

The oxides used in this study were examined by a general qualitative spectrochemical method and were estimated to contain impurity elements in the following ranges of concentration:

La_2O_3 —0.001–0.01% each Al, Ca, and Si; 0.0001–0.001% each Ag, Cu, and Mg; questionable Pr.

Nd_2O_3 —0.01–0.1% Eu; 0.001–0.01% each Ho, La, Si, and Yb; 0.0001–0.001% each Ca, Cu, Fe, Lu, Mg, Tm, and Y; <0.0001% each Ag and Mn; questionable Al, Cr, Er, and Ni.

Sm_2O_3 —0.01–0.1% Dy; 0.001–0.01% each Gd, La, Si, and Tm; 0.0001–0.001% each Eu, Fe, Ho, Mg, Y, and Yb; <0.0001% each Ca, Cu, and Mn; questionable Ag, Al, and Ni.

Gd_2O_3 —0.03% Tb; 0.05% Eu; 0.001–0.01% each Cu and Si; <0.0001% Al.

Dy_2O_3 —0.006% Y; 0.13% Ho; 0.01% Er and Tm; and 0.001–0.01% each Cu and Si.

Ho_2O_3 —0.07% Er; 0.001–0.01% Si.

Er_2O_3 —0.001–0.01% each Mn and Si.

Tm_2O_3 —0.01–0.1% each Er and Lu; 0.001–0.01% each Dy, Ho, La, Si, Y, and Yb;

[1] Figures in brackets indicate the literature references at the end of this paper.
[2] These values are used throughout this paper.

0.0001–0.001% each Ca, Cu, Fe, and Mg; <0.0001% Ag; and questionable Eu, Gd, and Mn.

Yb_2O_3 —0.001–0.01% each Er, Lu, Si, and Tm; 0.0001–0.001% each Cu, Fe, Mg, and Y; <0.0001% each Ca and Mn; and questionable Ag and Ce.

Lu_2O_3 —0.01–0.1% Er; 0.001–0.01% each Dy, Si, Y, and Yb; 0.0001–0.001% each Cu, Mg, and Tm; <0.0001% Ca; and questionable Ag, Eu, and Mn.

It should be noted that the rare-earth elements do not all have equivalent sensitivities in the spectrochemical method of analysis. It is possible that impurity elements such as Pr, Nd, Sm, Eu, Gd, etc., could be present in some of the above listed oxides in amounts of 0.01 percent or higher and still not be detected.

3. Test Methods

Specimens were prepared from either 0.75 or 1.0 g batches of various combinations of the rare-earth oxides. Calculated amounts of each oxide component, corrected for loss due to volatile material, were weighed to the nearest milligram. Each batch was mixed, pressed at 10,000 lb/in.^{2} into a ⅜-in.-diameter pellet, and fired at 1,350° C for a minimum of 6 hr. The specimens were then ground, remixed, again pressed into pellets, and finally fired at 1,650° C for 6 hr. In a number of instances, in order to obtain equilibrium, it was necessary to heat the pellets to 1,900° C for several minutes.

The 1,350° and 1,650° C heat treatments were performed in an air atmosphere using an electrically heated tube furnace wound with 80% Pt–20% Rh wire. An induction furnace having, as the susceptor, a small iridium metal crucible (½-in. diameter by $1\frac{1}{16}$ in. high), was used for the 1,900° C heat treatments.

Equilibrium was considered to have been reached when the X-ray pattern of the specimen showed no change with successive heat treatment or when the X-ray powder data were consistent with the results predicted from a previous set of experiments. All specimens were examined at room temperature by X-ray diffraction with a Geiger-counter diffractometer employing nickel-filtered copper radiation. The various phases were identified by comparison of their X-ray patterns with similar indexed patterns of the pure oxides and perovskite-type compounds.

The boundaries of two-phase areas in a given binary system were determined either by the disappearing-phase method or a variation of the parametric method. The former method consists of studying mixtures which differ in composition only by small increments. The boundaries are established between two adjacent compositions that contain one and two phases, respectively. The parametric method locates the boundaries from a knowledge of the unit-cell parameters of a phase, the average ionic radius and the composition that corresponds to that radius. Roth and Schneider [1] have shown that the unit-cell parameters of the A-, B-, and C-type rare-earth oxides lie on a straight line when plotted against Ahrens' ionic (cation) radii. According to Vegard's law, the parameters of solid solutions of these structure types should also plot on the same curve. Once a two-phase area is located by trial and error and the unit cell parameters measured, the average ionic radius of each phase can be determined from the radius-parameter plot. Inasmuch as the unit-cell parameters of the phases in a two-phase area do not change with composition, the boundary compositions can be calculated from the average ionic radius of each phase in any mixture in a two-phase area.

4. Results and Discussion

4.1. Composition-Stability Diagram

Because of the great similarity in behavior of different mixtures of the rare-earth oxides, a convenient method was devised whereby the subsolidus phase relations of more than one system could be given on a single diagram. The method selected was a plot of the ionic radii of the constituent cations versus composition. The derivation of a composition-stability diagram is illustrated in figure 1. The center portion of figure 1 shows the plot of the ionic radius of La^{+3} on the left ordinate and the radii of Sm^{+3}, Gd^{+3}, and Dy^{+3} on the right. The straight lines connecting the radii values represent isothermal cuts through the La_2O_3-Sm_2O_3 and La_2O_3-Dy_2O_3 systems. Composition is indicated on the abscissa in the usual manner. For convenience, the radius of the larger cation of any particular combination of oxides was always plotted on the left ordinate. The conventional type subsolidus phase diagrams, as determined in the present study, for the La_2O_3-Sm_2O_3 and the La_2O_3-Dy_2O_3 systems are shown in the upper and lower portions of the figure. The two-phase regions of both systems are located on the center diagram by simple projections, in the manner illustrated. The loci of similar boundary points then define the fields of stability for the A_{ss}, B_{ss}, and C_{ss} structure types for all the intermediate systems (such as the La_2O_3-Gd_2O_3 system) which are included within the triangle La^{+3}-Sm^{+3}-Dy^{+3}.

Throughout this investigation the equilibrium phases present in a given composition were predicted from rough drafts similar to figure 1 (center) and then investigated experimentally. As more data were accumulated, figure 1 was continually revised and expanded in scope to include all binary systems of La_2O_3 with Sm_2O_3 and smaller rare-earth oxides. When the predicted and experimental results were in close agreement, the composition-stability diagram for La_2O_3 containing binary systems was considered complete.

In a similar manner, a composition-stability diagram was prepared for sets of binary systems containing Nd_2O_3, Sm_2O_3, Gd_2O_3, etc. Each of these two-dimensional plots represent a plane in a three dimensional figure defined by the orthogonal axes: Radius of large cation, average cation radius of mix-

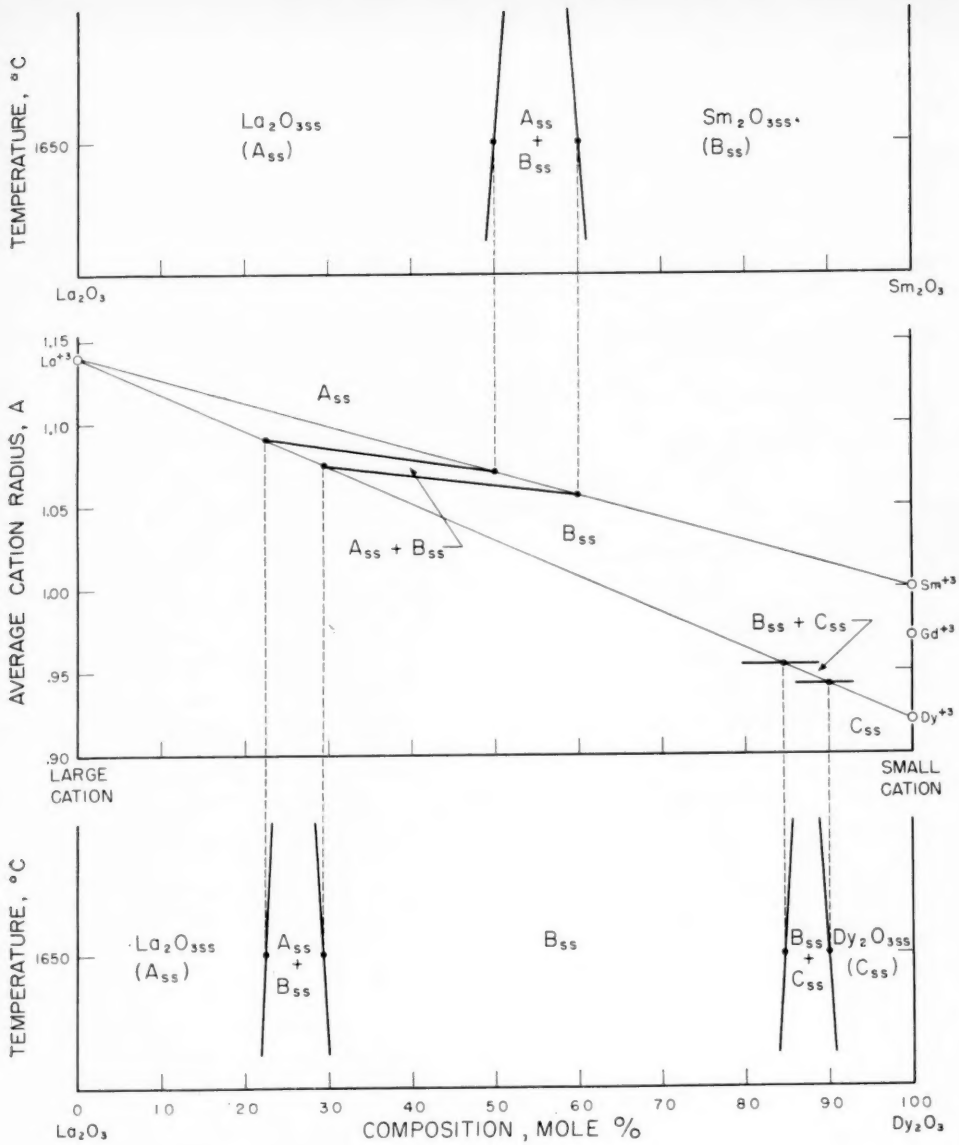

FIGURE 1. *Derivation of a composition-stability diagram from the* La_2O_3-Sm_2O_3 *and* La_2O_3-Dy_2O_3 *systems.*

The exsolution curves of both systems were drawn arbitrarily. The true curvature was not determined.

ture, and composition (mole fraction of small cation). This diagram is illustrated in figure 2. For simplicity only two composition-stability planes are shown. The projection of all of these planes would result in a composite diagram which then defines the phase assemblages for all possible binary systems.

Figures 3 and 4 when superimposed give the completed composite diagram of this general type, as derived from all the experimental data listed in tables 1 and 2. These figures show the fields of stability for the various structure types at room temperature for specimens heat-treated at 1,650° and/or 1,900° C. The boundary lines separating the different fields represent the "best" fit through the several data points as established by the disappearing-phase or the parametric method. Although these two figures ignore such things as pos-

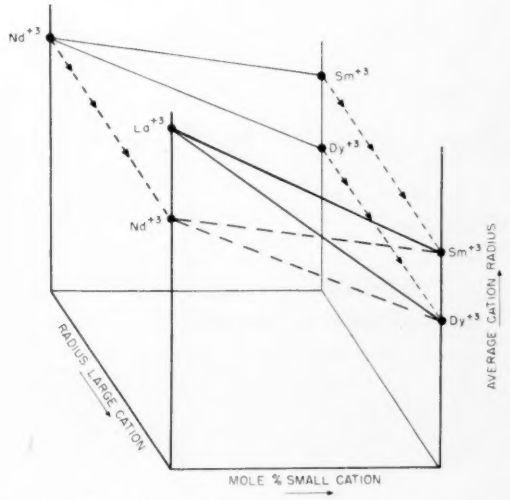

FIGURE 2. *Three-dimensional representation of a composite composition-stability diagram.*

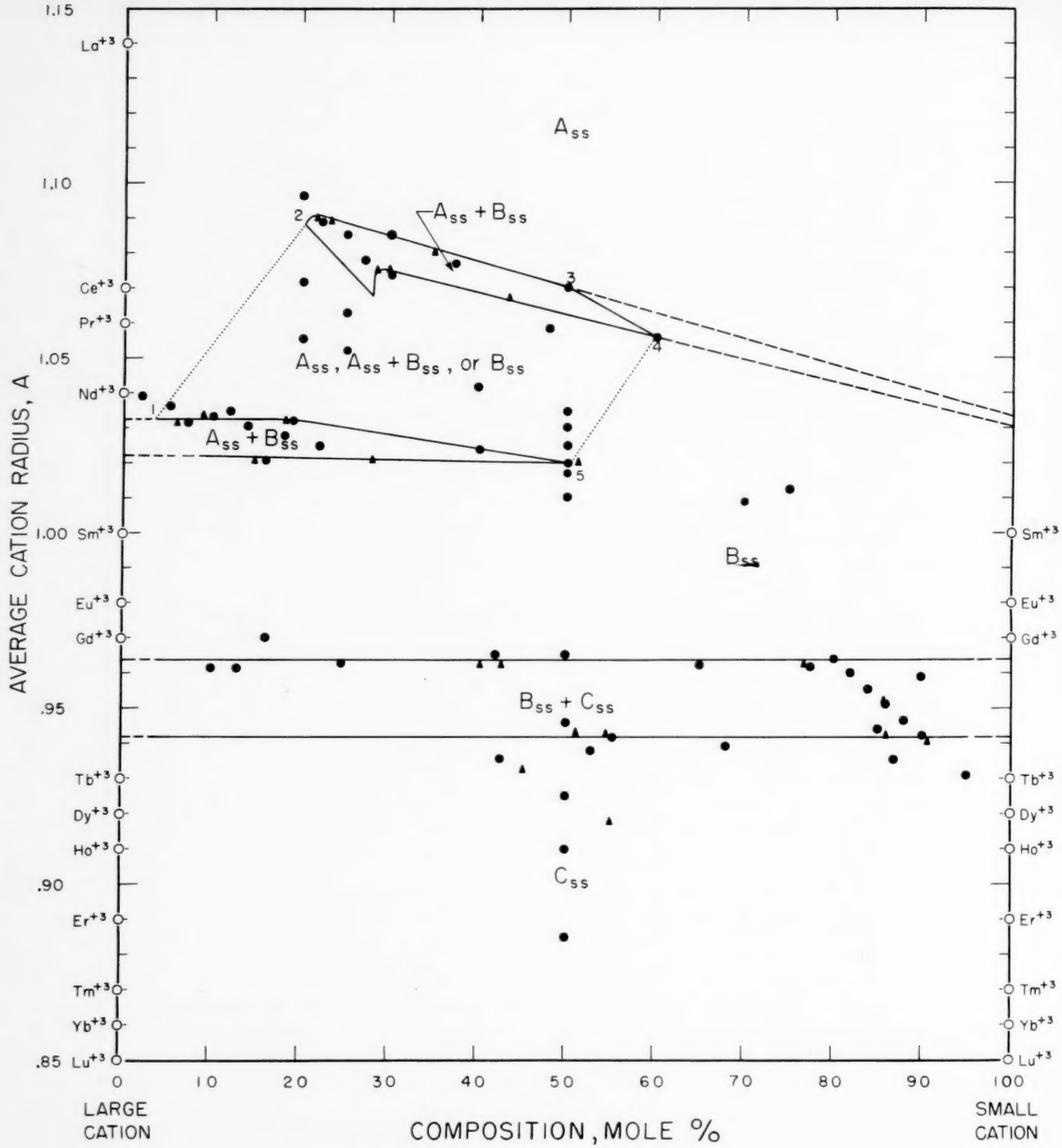

FIGURE 3. *Composition-stability diagram for systems containing only the A, B, or C structure type.*

The diagram is applicable to all systems in which the difference in radii of constituent cations is less than 0.22 A. Area 12345 invalid where radius of large cation >1.04 A and <1.14 A.

●, Compositions studied; ▲, parametric determinations.

Guide for predicting the phases present in any multicomponent mixture of oxides of the trivalent rare-earth ions:

(1) Locate the average radius of all A-type cations present on the left ordinate and the average radius of all other cations (B and C type) on the right. On the line connecting these points, locate the total mole percentage of cations other than A-type. (Note that A-type cations cannot be plotted on the right ordinate.)

(2) If no A-type cations are present, locate the average cation radius of all the B-type cations present on the left ordinate and the average cation radius of all C-type cations on the right. On the line connecting these points, locate the total mole percentage of cations other than B-type.

(3) If either A-, B-, or C-type cations are present alone, locate the point on the left ordinate corresponding to the average cation radius.

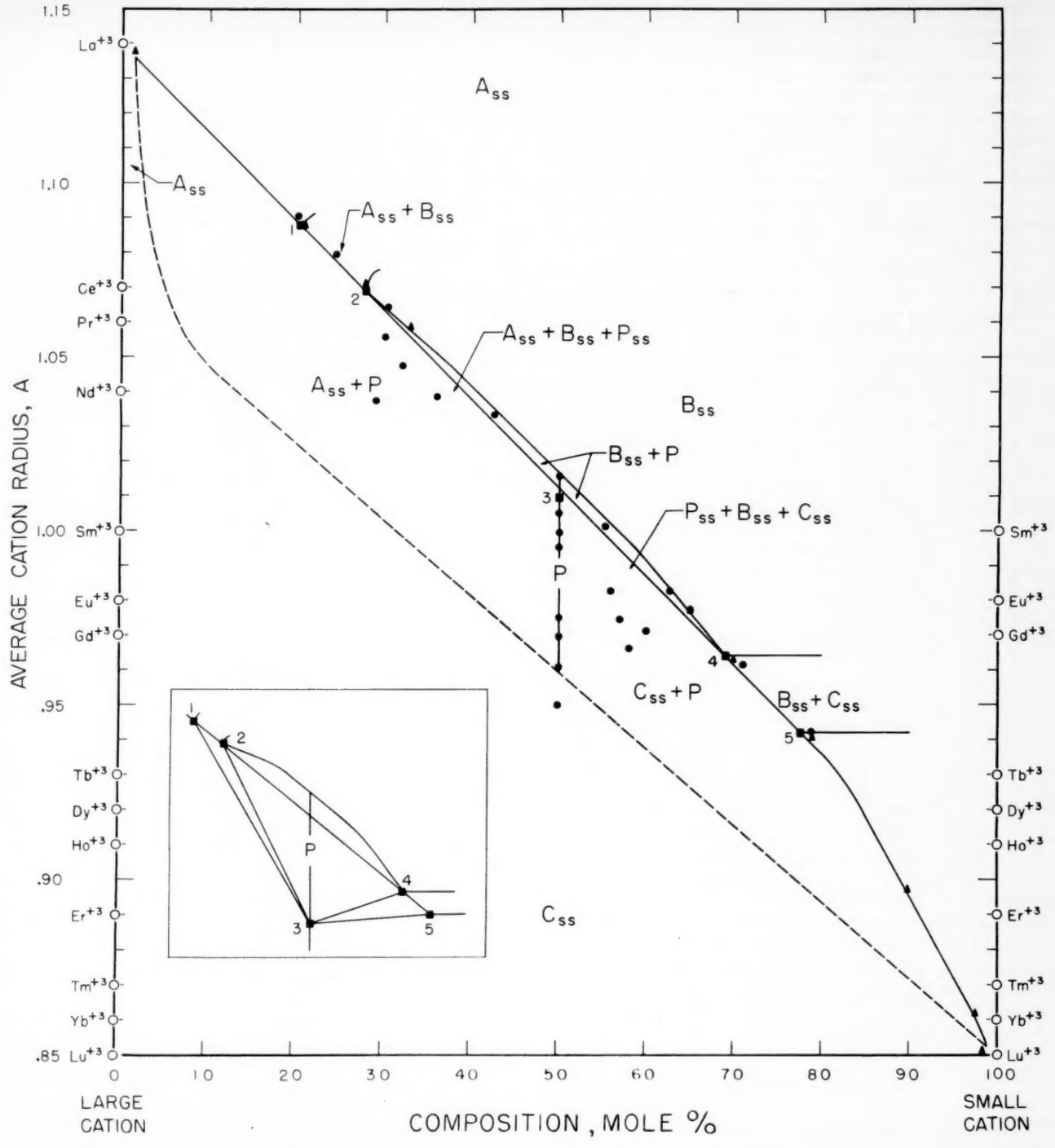

FIGURE 4. *Composition-stability diagram for systems containing perovskite-type compounds.*

The diagram is applicable to all systems in which the difference in radii of constituent cations is equal to or greater than 0.22 A. The inset indicates an exaggerated view of the three-phase areas which are bounded by the triangles 1, 2, 3 and 3, 4, 5.

●, Compositions studied; ▲, parametric determinations.

Guide for predicting the phases present in any multicomponent mixture of oxides of the trivalent rare-earth ions:

(1) Locate the average radius of all A-type cations present on the left ordinate and the average radius of all other cations (B and C type) on the right. On the line connecting these points, locate the total mole percentage of cations other than A-type. (Note that A-type cations cannot be plotted on the right ordinate.)

(2) If no A-type cations are present, locate the average cation radius of all the B-type cations present on the left ordinate and the average cation radius of all C-type cations on the right. On the line connecting these points, locate the total mole percentage of cations other than B-type.

(3) If either A-, B-, or C-type cations are present alone, locate the point on the left ordinate corresponding to the average cation radius.

sible variations in composition of solid solutions with temperatures, they are useful guides for approximate predictions of the behavior of unknown rare-earth oxide systems at high subsolidus temperatures.

Binary, ternary, and, in theory, four or more component systems are believed to be equally well described by figures 3 and 4. The three guides for predicting the phase relations of any multicomponent system involving oxides of the trivalent rare-earth ions are given in the legends of the figures. It should be emphasized that these rules must be followed implicitly.

Figure 3 pertains only to the A, B, and C structure types. It is applicable to all systems in which the difference between the average radius of the large and small cation is less than 0.22 A. When the difference is greater than this value a perovskite-type compound may form, and figure 4 is then used to predict the phase relationships.

Figure 3 shows two fields of $A_{ss}+B_{ss}$ separated by an area in which either A_{ss}, $A_{ss}+B_{ss}$, or B_{ss} may be present. These fields represent the two phase areas for the La_2O_3 and the Nd_2O_3 sets of binary systems shown in figure 2. The data showed that this area (1–2–3–4–5 of figure 3) is made up of several $A_{ss}+B_{ss}$ fields, the locations of which depend upon the group of systems under consideration. Complete subsolidus phase diagrams cannot be incorporated into figure 3 if A-type cations are involved which have an average radius greater than 1.04 A (Nd^{+3}) and less than 1.14 A (La^{+3}). This excludes certain portions of systems of A-type oxides or their solid solutions with the B- and C-type rare-earth oxides.

Figure 5 indicates how the $A_{ss}+B_{ss}$ field is believed to shift in this region. More experimental data are needed, however, to predict accurately the location and curvature of the boundary lines.

The two triangles formed by joining the points 1, 2, and 3 and points 3, 4, and 5 of figure 4 define the three-phase areas, $A_{ss}+B_{ss}+P_{ss}$ and $P_{ss}+B_{ss}+C_{ss}$, respectively. An exaggerated view of these triangles is shown by the inset. These areas are necessary in certain systems of three or more components where three phases in equilibrium are required by the phase rule. Also, the lower dashed portion of the figure should contain three-phase areas, as well as $B_{ss}+P$ areas. However, no data were available to confirm this.

4.2. B-Type Solid Solutions

The radii of the cations of the B-type oxides vary between fairly narrow limits, 0.97 A for Gd^{+3} to 1.00 A for Sm^{+3}. With reference to figure 3, it is evident that in B-type solid solutions, the radii extend to much larger values. The largest average radius of B_{ss} found in the present study is approximately 1.075 A. Mixtures having an average cation radius approaching this value are found in B-type solid solutions in the La_2O_3-Dy_2O_3 and La_2O_3-Ho_2O_3 binaries. In multicomponent systems involving La^{+3} and small cations whose average radius is equal to about 0.91 A or 0.92 A, this same radius of 1.075 A

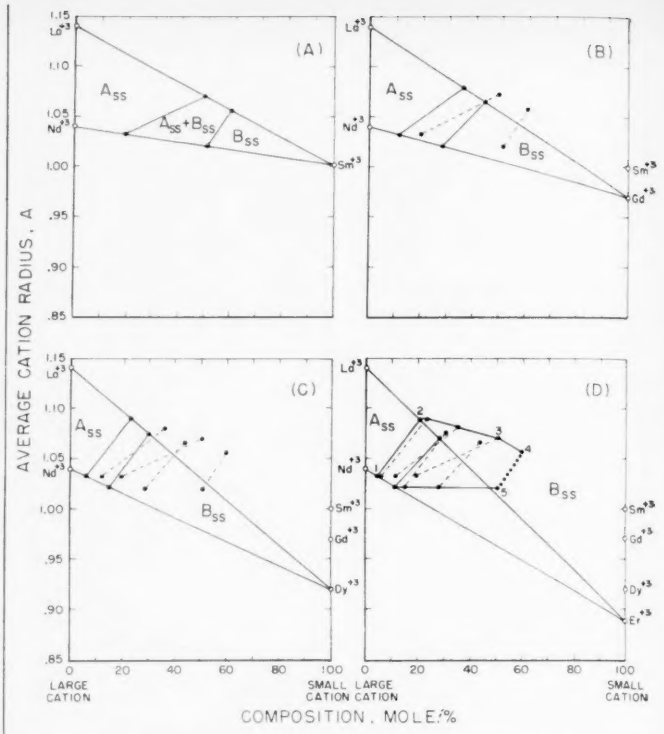

FIGURE 5. *Predicted limits of* $A_{ss}+B_{ss}$ *area of ternary systems.*

(A) La_2O_3-Nd_2O_3-Sm_2O_3, (B) La_2O_3-Nd_2O_3-Gd_2O_3, (C) La_2O_3-Nd_2O_3-Dy_2O_3, (D) La_2O_3-Nd_2O_3-Er_2O_3.
Dashed lines represent boundaries carried over from previous figures. ●, limit of solid solution determined for binary systems. Area 12345 represents same region shown in figure 3

can be predicted as the limit of the B_{ss}-type field. It is noteworthy that a mixture of an A type (La_2O_3) with a C type (Dy_2O_3 or Ho_2O_3) can give a B-type solid solution that has larger unit-cell dimensions than any mixture of the same A-type oxide with a B-type oxide such as La_2O_3 with Sm_2O_3.

In general, the B-type solid solutions having the smallest unit-cell dimensions in a given system have approximately equal lattice parameters, regardless of the systems under consideration. These small B-types have average cation radii equal to about 0.964 A and are found in mixtures of either A or B type with C-type oxides. The primary exception found in the present study is in the Sm_2O_3-Lu_2O_3 system where the B-type solid solution of 1:1 ratio has an average cation radius of about 0.935 A. This solid solution has considerably smaller unit-cell dimensions than the smallest B-type oxide, Gd_2O_3, or any other B-type solid solution. Goldschmidt [2] indicated that Dy_2O_3 formed a B-type oxide at elevated temperatures, which presumably would have unit-cell dimensions about equal to those of the 1: 1 Sm_2O_3–Lu_2O_3 mixture. The authors [1] however could not make a B-type Dy_2O_3[3].

Both the smallest and largest B-type solid solu-

[3] A 1:1 mixture of Dy_2O_3 and In_2O_3 after heat treatment at 1,650° C showed a mixture of $B_{ss}+C_{ss}$, with the B_{ss} having parameters equivalent to an average cation radius of about 0.88 A. This is the smallest average radius for a B-type solid solution yet reported. It extends well into the C_{ss} region of figure 3.

tions appear to occur in systems where the difference between the radii of the large and small cations (fig. 3) approaches a maximum value. When the difference is at or near a maximum, compound formation is likely. This fact is illustrated by the La_2O_3–Er_2O_3 [5] and the Sm_2O_3–In_2O_3 [6] systems where a perovskite-type compound occurs as a stable phase. The difference between the radii of large and small cations in each of these systems is just slightly greater than equivalent values for the La_2O_3-Ho_2O_3 and the Sm_2O_3-Lu_2O_3systems.

One further correlation can be made between the B-type solid solutions and compound formation. Figure 6 shows a plot of 2θ values for several X-ray reflections of different B-type solid solutions versus their corresponding average cation radii. For comparison the appropriate values for Sm_2O_3, Eu_2O_3, and Gd_2O_3 are included. Each reflection is denoted by its respective indices ($11\bar{2}$, 310, 003, $40\bar{2}$, 401, and 111). The primary anomaly presented by this figure is in the 401 and $40\bar{2}$ separation. The systems fall into two groups having either a narrow or a wide split between the 401 and $40\bar{2}$, dependent upon the mixture under consideration.

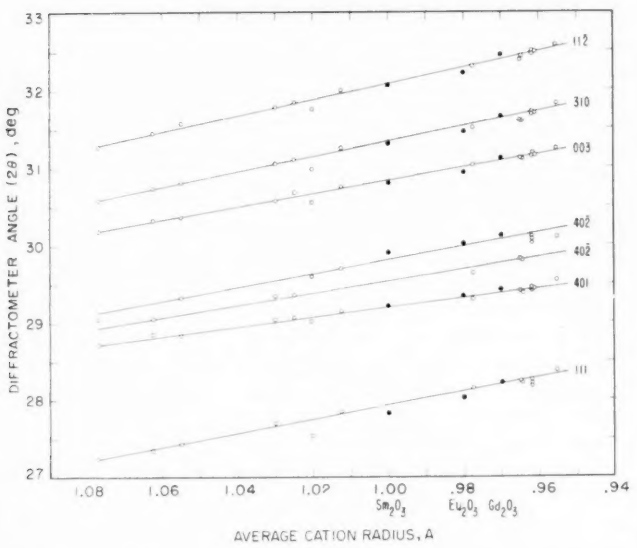

FIGURE 6. *Diffraction angle 2θ of certain X-ray powder lines as a function of average cation radius for* Sm_2O_3, Eu_2O_3, Gd_2O_3, *and B-type solid solutions.*

Indices of each X-ray line are indicated by number adjacent to the corresponding curve. ○, solid solutions; ●, pure oxides.

The narrow split apparently occurs in systems in which a perovskite-type compound might be reasonably expected to occur. These systems for the most part essentially border the perovskite field as shown by figure 4. They are: La_2O_3-Dy_2O_3, La_2O_3-Ho_2O_3, La_2O_3–Er_2O_3, Nd_2O_3-Er_2O_3, Nd_2O_3-Yb_2O_3, Nd_2O_3–Lu_2O_3, and Sm_2O_3–Lu_2O_3. The one exception to this grouping is the La_2O_3–Dy_2O_3 system which contains B-type solid solutions of both categories. The narrow split is prevalent throughout most of the La_2O_3–Dy_2O_3 system. At about the 1:3 La_2O_3–Dy_2O_3 composition the separation between the 401 and $40\bar{2}$ lines widens in a continuous manner until the maximum is reached at the two-phase $B_{ss}+C_{ss}$ border. The 401–$40\bar{2}$ split for Sm_2O_3, Eu_2O_3, and Gd_2O_3 is of the wide variety. This is entirely consistent with the other data in that these oxides do not form a perovskite-type compound. Even though all of the B-type solid solutions appear to be isostructural it is suggested that there are in fact two separate varieties, both of which may occur in the same system.

4.3. Perovskite-Type Compounds

Figure 4 generally pertains to those systems which contain perovskite-type compounds as stable phases. As mentioned earlier, four compounds of the perovskite type, $LaErO_3$, $LaTmO_3$, $LaYbO_3$, and $LaLuO_3$ have been reported [5] in double oxides of the trivalent rare-earth ions. Figure 4 indicates that only one other double oxide, $CeLuO_3$, would be expected to form a stable perovskite-type compound. All other stable phases having a perovskite structure would occur in rare-earth oxide systems of three or more components. A stable perovskite-type structure should form in all trivalent rare-earth oxide systems in which the difference between the average radius of the large and small cations is equal to or greater than 0.25 A. This conclusion is substantiated by the La_2O_3-Er_2O_3, La_2O_3-Tm_2O_3, La_2O_3-Yb_2O_3, and La_2O_3-Lu_2O_3 binary systems. For certain systems such as the La_2O_3-Nd_2O_3-Lu_2O_3 ternary, the minimum difference is decreased to 0.22 A. In essence, when the difference in radii is within the range 0.22 to 0.25 A a stable perovskite-type compound may or may not form. These might be termed border systems and should be studied individually.

Goldschmidt [7] derived a tolerance factor for the perovskite structure which is given by the following formula:

$$t=\frac{R_a+R_O}{2(R_b+R_O)}$$

where

t = tolerance factor
R_a = ionic radius of larger cation
R_b = ionic radius of small cation
R_O = ionic radius of oxygen (=1.40 A).

As t approaches unity the tendency for the formation of a perovskite-type structure becomes greater. The lower limit for the tolerance factor in $A^{+2}B^{+4}O_3$ perovskite structures ranges between 0.71 and 0.77 [6]. No similar minimum values have been assigned to perovskite-type structures in double oxides of the trivalent rare-earth ions. Roth [6] reported t values as high as 0.94 for $LaAlO_3$ (rhombohedral) and as low as 0.76 for $SmInO_3$ (orthorhombic). Apparently 1:1 mixtures of oxides of the trivalent rare-earth

ions will always form a stable perovskite-type compound when the tolerance factor is 0.79 or greater. Those mixtures having a t value of 0.77 or 0.78 may possibly form such a compound, although it may well be a metastable phase. Based on data in the La_2O_3-Nd_2O_3-Lu_2O_3 system, it is concluded that $CeLuO_3$ is a stable perovskite-type compound. The 1:1 mixture of La_2O_3 and Ho_2O_3 did not form a perovskite compound, even as a metastable phase. Yet each of these mixtures has a t value of 0.78. It is possible that a perovskite-type phase may form in ternary mixtures having a tolerance factor lower than the minimum value for binary systems. Although there remain several apparent inconsistencies, a tolerance factor of 0.77 is probably the lowest possible value for a 1:1 rare-earth oxide mixture to form a perovskite-type structure.

Neither radius difference nor tolerance factor gives satisfactory criteria for determining the boundary of the perovskite field in figure 4. The difficulty lies perhaps in the inaccuracy of the ionic radius values. Ahrens' radii used in this paper are admittedly not entirely correct. However, other values such as those reported by Templeton and Dauben [8] do not fit the data any better. Differences in the thermal expansion characteristics and partially covalent character of the bonds are both important factors to be considered.

4.4. Phase Diagrams

Figures 7 through 12 give subsolidus phase diagrams for various binary systems involving the trivalent rare-earth oxides. In many instances, the diagrams were completely estimated from either figure 3 or figure 4. When actual experimental data were available (tables 1 and 2), the diagrams, or portions thereof, were drawn to fit these data. Data points are indicated by circles on the diagrams. On the whole, the diagrams must be considered as predicted and for that reason are shown by dashed lines. The general appearance of each diagram is probably correct even though the positions of the boundary lines may be slightly in error. Any possible variations of solid solubility with temperature have been ignored in this work.

Of all the binary systems given, the Sm_2O_3-rare-earth oxide group, figure 9, is most in doubt. The position of the two-phase area, $B_{ss}+C_{ss}$, for the Sm_2O_3-Lu_2O_3 system is unexpectedly shifted to the right (lower radii) from the position predicted by figure 3. If the other systems of this group behave in a consistent manner, the position of this two-phase region should also be located at somewhat lower percentages of Sm_2O_3.

Figure 12 gives a model ternary system, La_2O_3-Sm_2O_3-Lu_2O_3 as predicted by experimental data from rare-earth oxide systems. It was drawn by plotting the boundary points (circles) of binary systems having La_2O_3 as one end member. These binary systems are indicated by the joins (solid lines) between La_2O_3 and the other listed oxides. The dotted portion shows the position of the two-phase area, $B_{ss}+C_{ss}$, that conforms to the data found for the Sm_2O_3-Lu_2O_3 system. It should be noted that the position of the intersection of the two three-phase areas and the P_{ss} line (point 3) is only estimated. It may lie anywhere along that line. No data were available to fix its position.

It should be emphasized that figure 12 is simply another way of plotting the experimental data listed in tables 1 and 2, which pertain primarily to binary systems. It seems likely that the true La_2O_3-Sm_2O_3-Lu_2O_3 ternary system would have the same general appearance as figure 12, although differing in certain details. In binary systems the B_{ss} field has been observed to occur throughout a wider range of average radii than the equivalent values of the B-type single oxides. Furthermore, the B_{ss} in the Sm_2O_3-Lu_2O_3 system extends to lower average radii than found in most other binary rare-earth oxide systems. Therefore, it is suggested that the B_{ss} field in figure 12 may extend in the true ternary to even wider ranges than are indicated by the dashed lines. In addition, the limit of the perovskite field may be expected to increase towards higher Sm_2O_3 content (lower tolerance factors).

5. Summary

A survey was made of the subsolidus reactions that occur in various systems involving oxides of the trivalent rare-earth ions. Mixtures in 21 binary and 9 ternary systems were investigated. Specimens were heat treated at 1,650° C or above and examined at room temperature by X-ray powder diffraction.

On the basis of the survey, two composite composition-stability diagrams were drawn. These are plots of the average ionic radii of the constituent cations versus mole percent of the smaller cation. A join between left and right ordinate values represents an isotherm for the binary system whose cations have radii corresponding to the two limiting ordinates. The diagram may be also applied to some multicomponent systems, with the limiting ordinates representing the average ionic radii of the large and small cations present.

One composition-stability diagram is divided into fields of A_{ss}, B_{ss}, and C_{ss} oxide structure types with appropriate two-phase areas. This diagram is applicable to all systems in which the difference between the radii of the large and small cations is less than 0.22 A. The other diagram shows a large field of perovskite-type compounds bordered by regions of A_{ss}, B_{ss}, or C_{ss}. The data indicated that a perovskite-type compound always occurred in 1:1 mixtures having a tolerance factor equal to or greater than 0.79. A tolerance factor of 0.77 appears to be the lowest possible value for even a metastable perovskite-type phase to form. In addition, B-type solid solutions apparently can be grouped according to the amount of separation of the $40\bar{1}$–$40\bar{2}$ doublet in the X-ray powder pattern.

The composition-stability diagrams were used to predict a number of the subsolidus phase diagrams of the 41 binary and 1 ternary rare-earth oxide systems which are given.

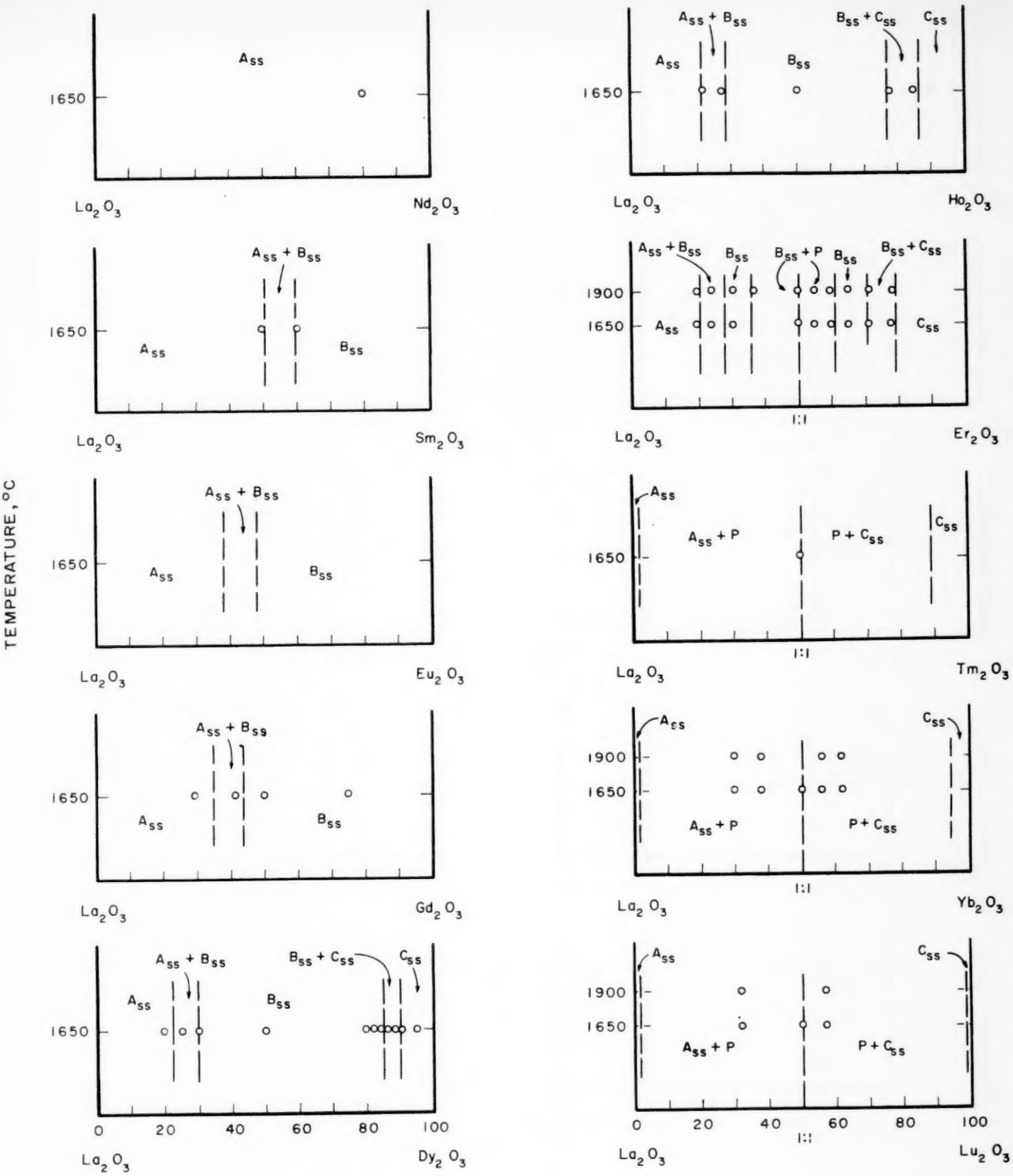

FIGURE 7. *Predicted subsolidus phase diagrams for* La_2O_3*-rare-earth oxide binary systems.*

Circles indicate compositions studied. Diagrams applicable only for indicated temperatures.

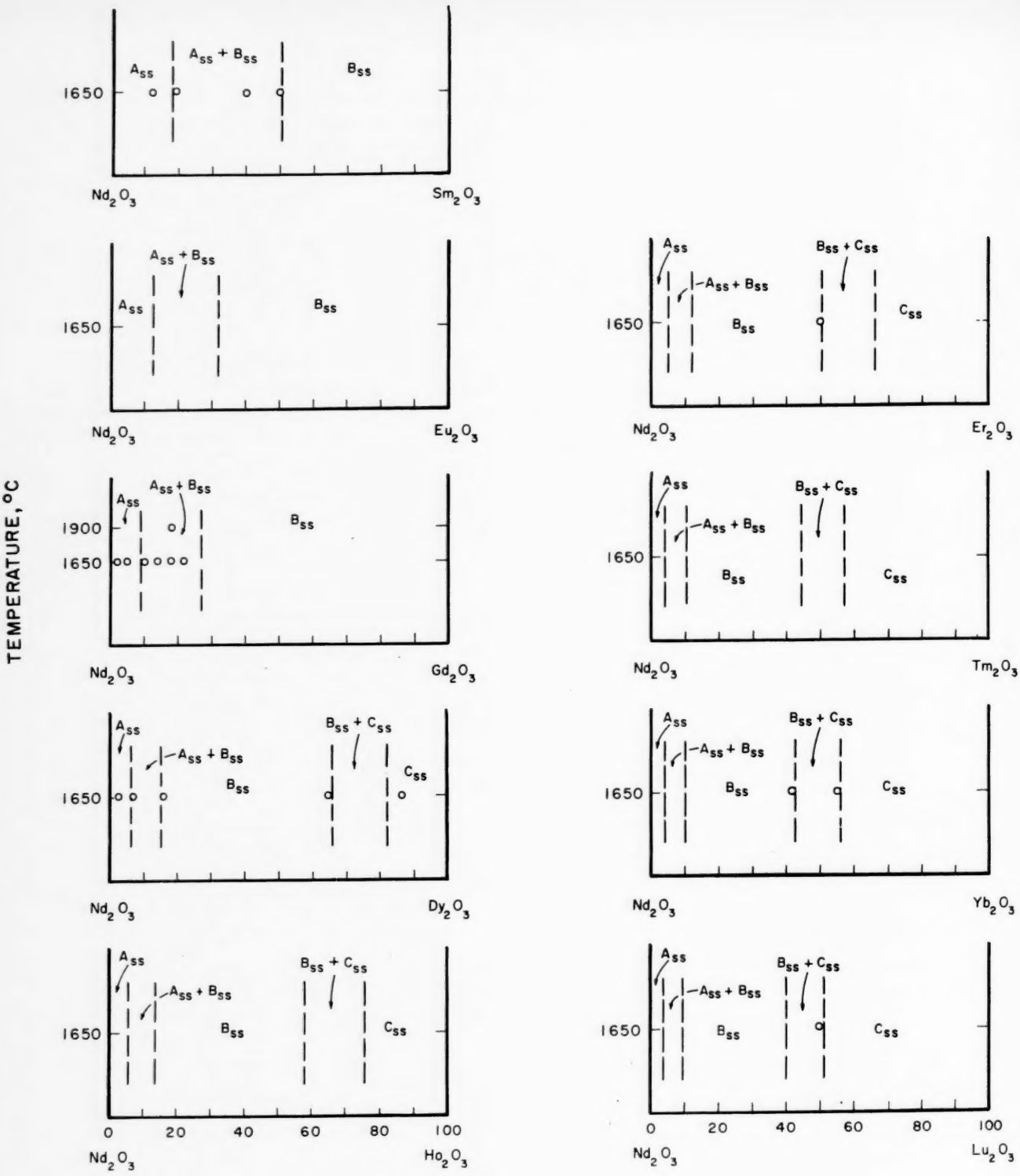

FIGURE 8. *Predicted subsolidus phase diagrams for Nd_2O_3-rare-earth oxide binary systems.*

Circles indicate compositions studied. Diagrams applicable only for indicated temperatures.

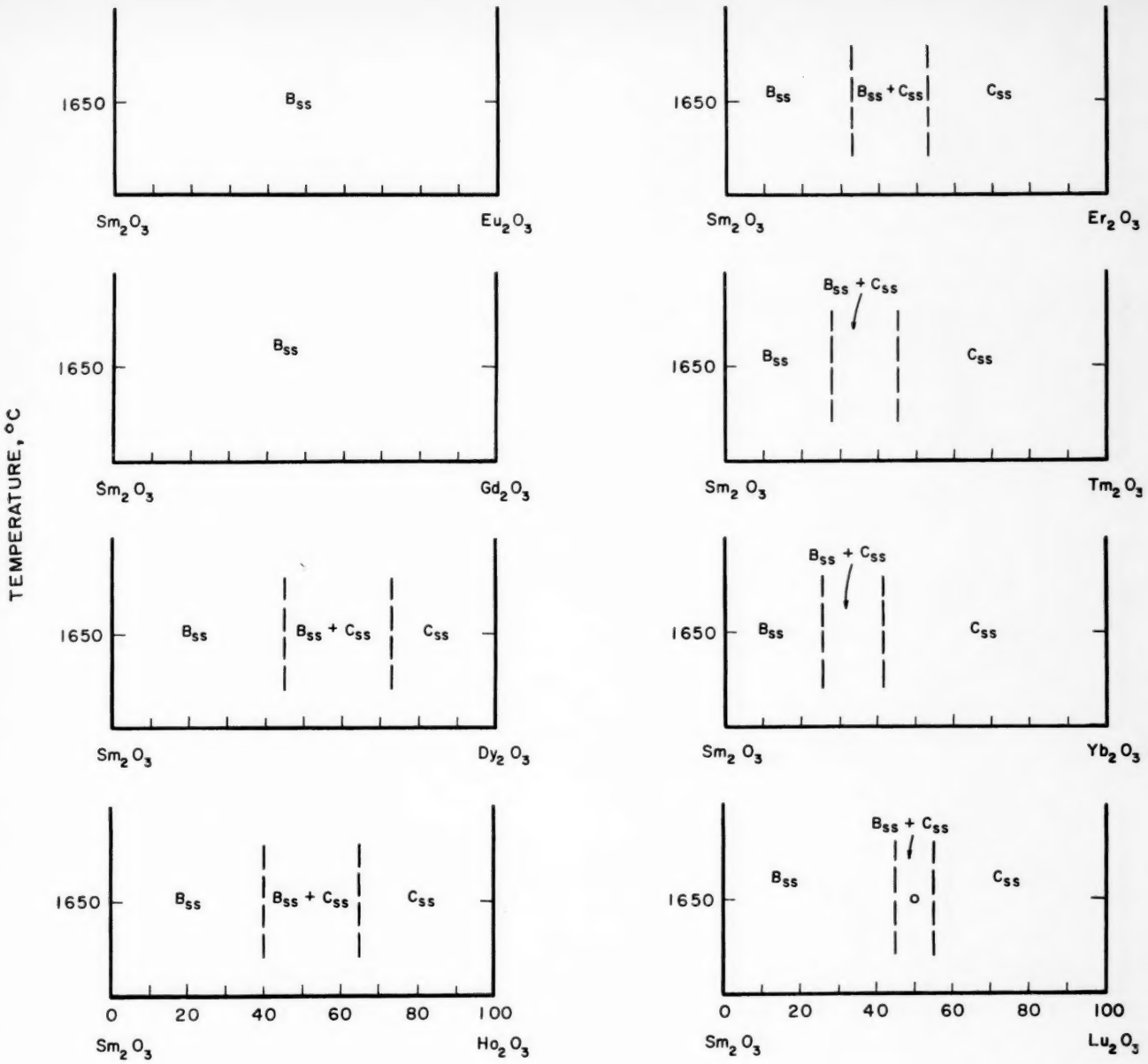

FIGURE 9. *Predicted subsolidus phase diagrams for* Sm_2O_3*-rare-earth oxide binary systems.*

Circles indicate compositions studied. Diagrams applicable only for indicated temperatures.

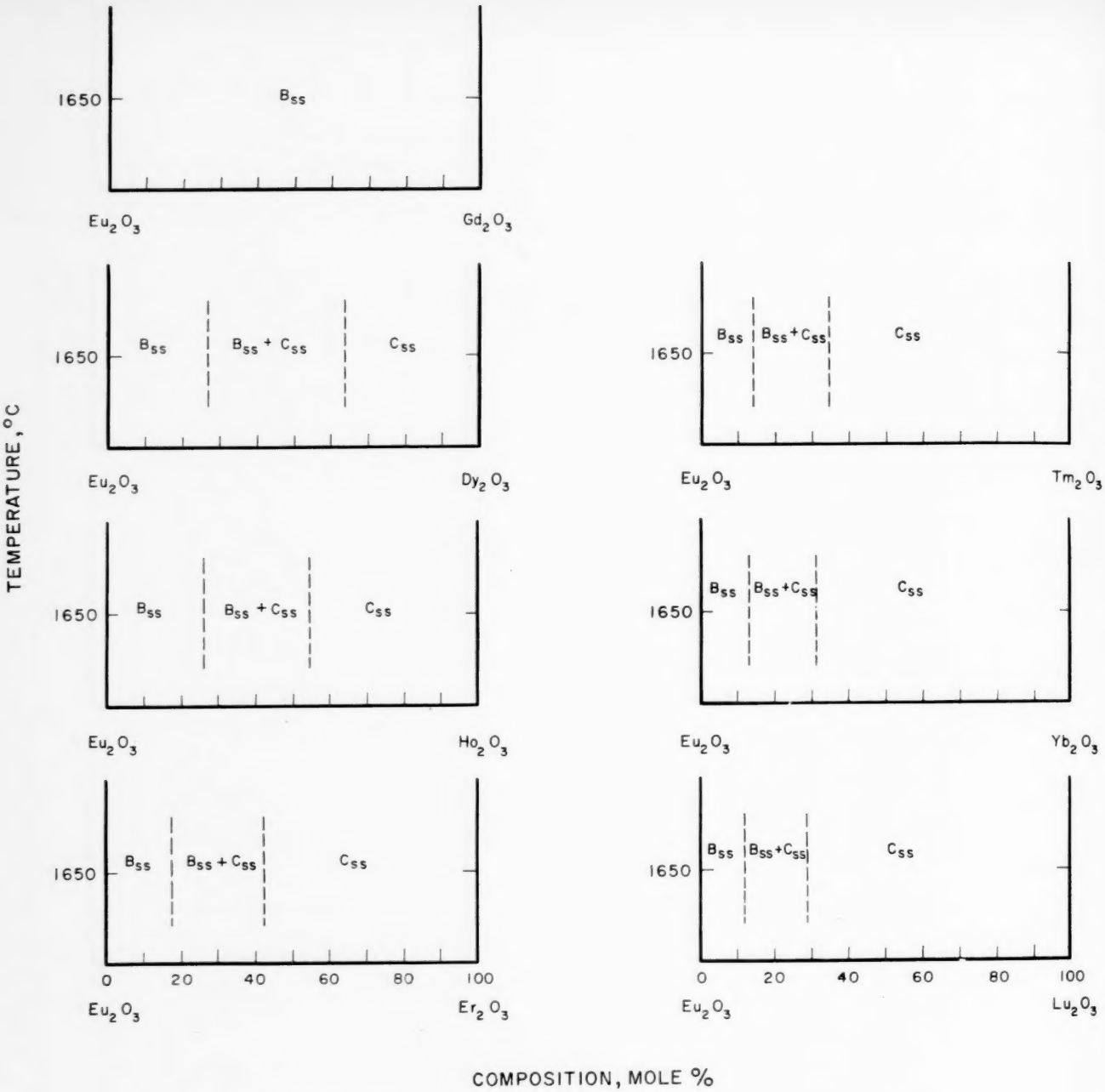

FIGURE 10. *Predicted subsolidus phase diagrams for* Eu_2O_3*-rare-earth oxide binary systems.*

Diagrams applicable only for indicated temperatures.

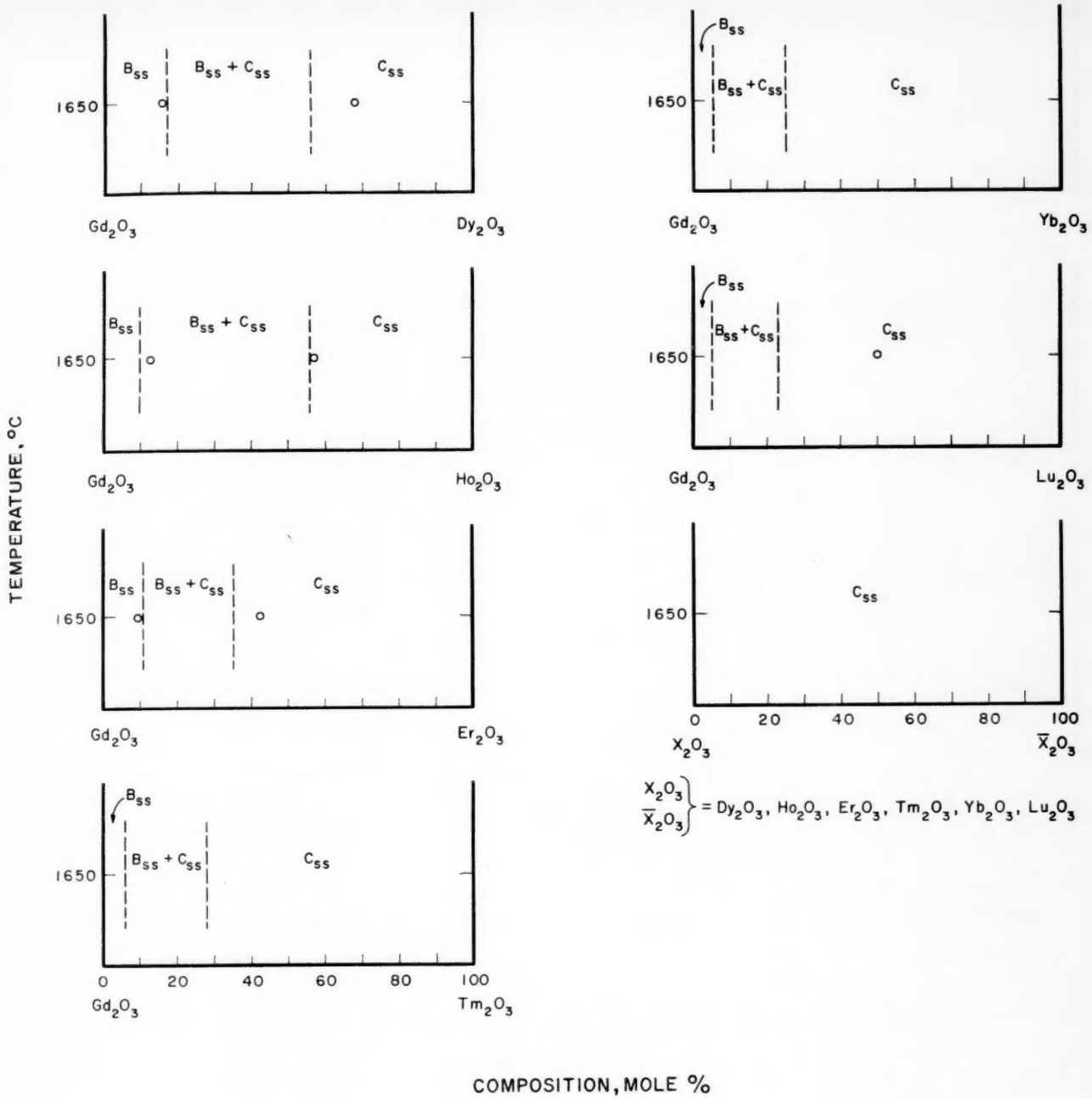

FIGURE 11. *Predicted subsolidus phase diagrams for Gd_2O_3-rare-earth oxide binary systems and for binary systems involving only C-type rare earth oxides.*

Circles indicate compositions studied. Diagrams applicable only for indicated temperatures.

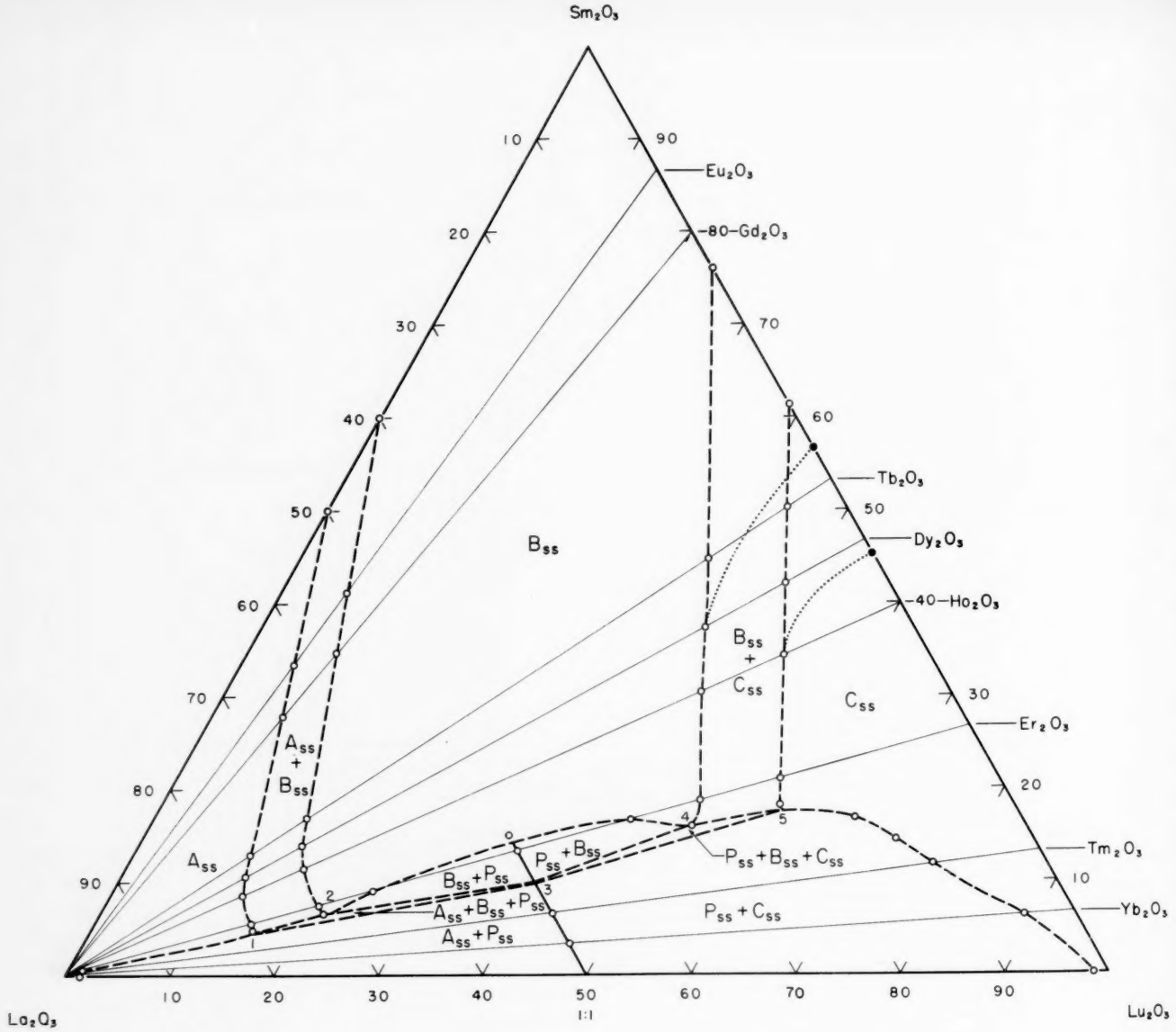

FIGURE 12. *Predicted subsolidus phase diagram for the* La_2O_3-Sm_2O_3-Lu_2O_3 *ternary system.*

TABLE 1.—*Mixed oxide systems forming the A-, B-, or C-structure types*

System	Specimen composition	Average radius [a]			Tolerance factor, *t*	Heat treatment		Phases identified by X-ray diffraction [b]	Remarks
		Large cation	Small cation	Mixture		Temp	Time		
	Mole %	*A*	*A*	*A*		° *C*	*hr*		
La_2O_3-Nd_2O_3	20:80	1.14	1.04	1.060		1,650	6	A_{ss}	
La_2O_3-Sm_2O_3	50:50	1.14	1.00	1.070	0.75	1,650	6	A_{ss}	
	40:60	1.14	1.00	1.056		1,650	6	B_{ss}	
La_2O_3-Gd_2O_3	70.6:29.4	1.14	.97	1.090		1,650	6	A_{ss}	
	63.5:36.5	1.14	.97	1.078		1,650	6	$A_{ss}+B_{ss}$	B_{ss} phase present in small amounts.
	50:50	1.14	.97	1.055	.76	1,650	6	B_{ss}	
	25:75	1.14	.97	1.013		1,650	6	B_{ss}	
La_2O_3-Dy_2O_3	80:20	1.14	.92	1.096		1,650	6	A_{ss}	
	75:25	1.14	.92	1.085		1,650	6	$A_{ss}+B_{ss}$	B_{ss} phase present in small amounts.
	70:30	1.14	.92	1.074		1,650	6	B_{ss}	
	50:50	1.14	.92	1.030	.77	1,650	6	B_{ss}	
	20:80	1.14	.92	.964		1,650	6	B_{ss}	
	18:82	1.14	.92	.960		1,650	6	B_{ss}	
	16:84	1.14	.92	.955		1,650	6	B_{ss}	
	14:86	1.14	.92	.951		1,650	6	$B_{ss}+C_{ss}$	
	12:88	1.14	.92	.946		1,650	6	$B_{ss}+C_{ss}$	
	10:90	1.14	.92	.942		1,650	6	$B_{ss}+C_{ss}$	
	5:95	1.14	.92	.931		1,650	6	C_{ss}	
La_2O_3-Ho_2O_3	78.3:21.7	1.14	.91	1.090		1,650	6	$A_{ss}+B_{ss}$	B_{ss} phase present in small amounts.
	73:27	1.14	.91	1.078		1,650	6	$A_{ss}+B_{ss}$	
	50:50	1.14	.91	1.025	.78	1,650	6	B_{ss}	
	22.6:77.4	1.14	.91	.962		1,650	6	$B_{ss}+C_{ss}$	
	14.8:85.2	1.14	.91	.944		1,650	6	$B_{ss}+C_{ss}$	
Nd_2O_3-Sm_2O_3	88:12	1.04	1.00	1.035		1,650	6	A_{ss}	
	81:19	1.04	1.00	1.032		1,650	6	$A_{ss}+B_{ss}$	B_{ss} phase present in smal amounts.
	60:40	1.04	1.00	1.024		1,650	6	$A_{ss}+B_{ss}$	
	50:50	1.04	1.00	1.020	.72	1,650	6	$A_{ss}+B_{ss}$	
Nd_2O_3-Gd_2O_3	98:2	1.04	.97	1.039		1,650	6	A_{ss}	
	95:5	1.04	.97	1.037		1,650	6	A_{ss}	
	90:10	1.04	.97	1.033		1,650	6	A_{ss}	Pattern of pellet surface indicated $A_{ss}+B_{ss}+C_{ss}$; $B_{ss}+C_{ss}$ phase nonequilibrium.
	86:14	1.04	.97	1.030		1,650	6	$A_{ss}+B_{ss}$	
	82:18	1.04	.97	1.027		1,650	6	$A_{ss}+B_{ss}$	
						1,900	.083	$A_{ss}+B_{ss}$	
	78:22	1.04	.97	1.025		1,650	6	$A_{ss}+B_{ss}$	
Nd_2O_3-Dy_2O_3	97:3	1.04	.92	1.036		1,650	6	A_{ss}	
	93:7	1.04	.92	1.032		1,650	6	$A_{ss}+B_{ss}$	
	84:16	1.04	.92	1.021		1,650	6	B_{ss}	
	35:65	1.04	.92	.962		1,650	6	B_{ss}	
	13.3:86.7	1.04	.92	.936		1,650	6	C_{ss}	
Nd_2O_3-Er_2O_3	50:50	1.04	.89	.965	.75	1,650	6	B_{ss}	
Nd_2O_3-Yb_2O_3	58:42	1.04	.86	.964		1,650	6	B_{ss}	
	45:55	1.04	.86	.941		1,650	6	$B_{ss}+C_{ss}$	
Nd_2O_3-Lu_2O_3	50:50	1.04	.85	.945	.77	1,650	6	$B_{ss}+C_{ss}$	
Sm_2O_3-Lu_2O_3	50:50	1.00	.85	.925	.75	1,650	6	$B_{ss}+C_{ss}$	Average cation radius of B_{ss}~ 0.935A.
Gd_2O_3-Dy_2O_3	84:16	.97	.92	.962		1,650	6	B_{ss}	
	32:68	.97	.92	.936		1,650	6	C_{ss}	
Gd_2O_3-Ho_2O_3	86.7:13.3	.97	.91	.962		1,650	6	$B_{ss}+C_{ss}$	C_{ss} phase present in small amounts.
	43.3:56.7	.97	.91	.936		1,650	6	C_{ss}	
Gd_2O_3-Er_2O_3	90:10	.97	.89	.962		1,650	6	B_{ss}	
	57.5:42.5	.97	.89	.936		1,650	6	C_{ss}	
Gd_2O_3-Lu_2O_3	50:50	.97	.85	.910	.75	1,650	6	C_{ss}	
Dy_2O_3-Lu_2O_3	50:50	.92	.85	.885		1,650	6	C_{ss}	
La_2O_3-Nd_2O_3-Sm_2O_3	24:56:20	1.07	1.00	1.056		1,900	.167	A_{ss}	No 1,650° C heat.
	22.5:52.5:25	1.07	1.00	1.053		1,900	.333	A_{ss}	No 1,650° C heat.
	18:42:40	1.07	1.00	1.042		1,650	6	$A_{ss}+B_{ss}$	
	15:35:50	1.07	1.00	1.035	.73	1,650	6	B_{ss}	
La_2O_3-Nd_2O_3-Gd_2O_3	18:12:70	1.10	.97	1.009		1,650	6	B_{ss}	
La_2O_3-Nd_2O_3-Dy_2O_3	56:24:20	1.11	.92	1.072		1,650	3	A_{ss}	
	52.5:22.5:25	1.11	.92	1.063		1,650	3	$A_{ss}+B_{ss}$	
La_2O_3-Dy_2O_3-Er_2O_3	50:8.3:41.7	1.14	.895	1.018	.78	1,900	.167	B_{ss}	No 1,650° C heat.
						1,900	.333	B_{ss}	No 1,650° C heat.
Nd_2O_3-Gd_2O_3-Sm_2O_3	50:33.3:16.7	1.04	.98	1.010	.73	1,650	3	B_{ss}	
Nd_2O_3-Gd_2O_3-Dy_2O_3	10:54:36	1.04	.95	.959		1,650	3	B_{ss}	
Sm_2O_3-Gd_2O_3-Ho_2O_3	25:50:25	.98	.91	.963		1,900	.167	B_{ss}	No 1,650° C heat.

[a] Based on radii given by Ahrens [4].
[b] A=hexagonal A-type rare-earth oxide structure, B=monoclinic B-type rare-earth oxide structure, C=cubic C-type rare-earth oxide structure.

TABLE 2. *Mixed oxide systems forming perovskite-type compounds.*

System	Specimen composition	Average radius [a]			Tolerance factor, t	Heat treatment		Phases identified by X-ray diffraction [b]	Remarks
		Large cation	Small cation	Mixture		Temp	Time		
	Mole %	*A*	*A*	*A*		*°C*	*min*		
La_2O_3-Er_2O_3	80:20	1.14	0.89	1.090		1,650	360	$A_{ss}+B_{ss}$	Nonequilibrium.
						1,900	5	A_{ss}	
	75.2:24.8	1.14	.89	1.078		1,650	360	$A_{ss}+B_{ss}+P$	Nonequilibrium.
						1,900	5	$A_{ss}+B_{ss}$	
	69:31	1.14	.89	1.063		1,650	360	$B_{ss}+P$	Nonequilibrium.
						1,900	5	B_{ss}	
	63:37	1.14	.89	1.048		1,900	5	$B_{ss}+P$	No X-ray pattern for 1,650° C heat.
	57:43	1.14	.89	1.033		1,650	360	P	Second phase present, probably B_{ss}.
						1,900	5	$B_{ss}+P$	
	50:50	1.14	.89	1.015	0.79	1,650	360	P	
						1,900	6	P	
						1,900	30	P	
	45:55	1.14	.89	1.003		1,650	360	$B_{ss}+P$	
						1,900	5	$B_{ss}+P$	
	40:60	1.14	.89	0.990		1,650	360	$B_{ss}+C_{ss}$	Nonequilibrium.
						1,900	5	$B_{ss}+C_{ss}+P$	Nonequilibrium.
						1,900	16	$B_{ss}+P$	
	35:65	1.14	.89	.978		1,900	5	$B_{ss}+C_{ss}$	Nonequilibrium, no 1650° C heat.
						1,900	22	$B_{ss}+C_{ss}$	Amount of C_{ss} phase reduced relative to previous 1,900° C heat—C_{ss} nonequilibrium.
	28.8:71.2	1.14	.89	.962		1,650	360	$C_{ss}+P$	Nonequilibrium.
						1,900	6	$B_{ss}+C_{ss}$	
	21.6:78.4	1.14	.89	.944		1,650	360	$C_{ss}+P$	Nonequilibrium.
						1,900	5	$B_{ss}+C_{ss}$	
La_2O_3-Tm_2O_3	50:50	1.14	.87	1.005	.79	1,650	360	P	
La_2O_3-Yb_2O_3	70:30	1.14	.86	1.056		1,650	180	$A_{ss}+P$	
						1,900	5	$A_{ss}+P$	
	62:38	1.14	.86	1.034		1,650	180	$A_{ss}+P$	
						1,900	5	$A_{ss}+P$	
	50:50	1.14	.86	1.000	.80	1,650	360	P	
	44:56	1.14	.86	.983		1,650	180	$C_{ss}+P$	
						1,900	5	$C_{ss}+P$	
	38:62	1.14	.86	.966		1,650	180	$C_{ss}+P$	
						1,900	5	$C_{ss}+P$	
La_2O_3-Lu_2O_3	68:32	1.14	.85	1.047		1,650	180	$A_{ss}+P$	
						1,900	5	$A_{ss}+P$	
	50:50	1.14	.85	0.995	.80	1,650	360	P	
	43:57	1.14	.85	.975		1,650	180	$C_{ss}+P$	
						1,900	5	$C_{ss}+P$	
La_2O_3-Nd_2O_3-Yb_2O_3	49:21:30	1.11	.86	1.035		1,900	10	$A_{ss}+P$	No 1,650° C heat.
La_2O_3-Nd_2O_3-Lu_2O_3	30:20:50	1.10	.85	0.975	.79	1,900	5	P	No 1,650° C heat.
	25:25:50	1.09	.85	.970	.78	1,900	5	$P+C_{ss}$	No 1,650° C heat, nonequilibrium.
						1,900	15	$P+C_{ss}$	No 1,650° C heat, nonequilibrium, amount of C_{ss} phase reduced relative to previous heat.
	15:35:50	1.07	.85	.960	.78	1,650	360	P	
	10:40:50	1.06	.85	.955	.77	1,650	360	$P+B_{ss}+C_{ss}$	Nonequilibrium.
						1,900	10	$P+B_{ss}+C_{ss}$	Nonequilibrium, amount of P phase reduced relative to previous heat.
						1,960	10	$B_{ss}+C_{ss}$	
	5:45:50	1.05	.85	.950	.77	1,650	360	$P+B_{ss}+C_{ss}$	P′ phase probably nonequilibrium.

[a] Based on radii given by Ahrens [4].
[b] A=hexagonal A-type rare earth oxide structure, B=monoclinic B-type rare earth oxide structure, C=cubic C-type rare earth oxide structure, P=orthorhombic distorted perovskite type compound.

6. References

[1] R. S. Roth and S. J. Schneider, Phase equilibria in systems involving the rare-earth oxides. Pt. I. Polymorphism of the trivalent rare-earth oxides, J. Research NBS **64A,** 309 (1960).

[2] J. M. Goldschmidt, F. Ulrich, and T. Barth, Geochemical distribution of the elements, IV. On the crystal structure of the oxides of the rare-earth metals. Skrifter Norske Videnskaps-Akad. Oslo. I. Mat.-Naturv. Kl. No. 5 (1925).

[3] M. W. Shafer and R. Roy, Rare earth polymorphism and phase equilibria in rare-earth oxide-water systems, J. Am. Ceram. Soc. **42,** 563 (1959).

[4] L. H. Ahrens, The use of ionization potentials, Part 1. Ionic radii of the elements, Geochim. et Cosmochim. Acta **2,** 155–169 (1952).

[5] S. J. Schneider and R. S. Roth, Perovskite-type compounds in binary rare earth oxide systems, J. Am. Ceram. Soc. **43,** 115 (1960).

[6] R. S. Roth, Classification of perovskite and other ABO_3-type compounds, J. Research NBS **58,** 75 (1957) RP2736.

[7] J. M. Goldschmidt, T. Barth, G. Lunde, and W. Zachariasen, Geochemische Verteilungsgesetze der Elements. VII Skrifter Norske Videnskaps-Akad. Oslo I. Mat.-Naturv. Kl. No. 2 (1926).

[8] D. H. Templeton and C. H. Dauben. Lattice parameters of some rare earth compounds and a set of crystal radii, J. Am. Chem. Soc. **76,** 5237 (1954).

WASHINGTON, D.C. (Paper 64A4–54)

JOURNAL OF RESEARCH of the National Bureau of Standards—A. Physics and Chemistry
Vol. 64A, No. 4, July–August 1960

Some Observations on the Calcium Aluminate Carbonate Hydrates

Elmer T. Carlson and Horace A. Berman

(April 7, 1960)

Two calcium aluminate carbonate hydrates, previously reported in the literature, were prepared and various properties determined. The compound $3CaO \cdot Al_2O_3 \cdot CaCO_3 \cdot 11H_2O$, was prepared by precipitation from mixtures of solutions of calcium aluminate, calcium hydroxide and sodium carbonate; and, in less pure form, by several other means. It forms thin hexagonal plates having refractive indices 1.532 and 1.554. From X-ray diffraction, cell parameters, calculated on the assumption of hexagonal symmetry, are $a=8.716$, $c=7.565$. On continued exposure to atmospheric carbon dioxide it is decomposed to calcium carbonate and hydrated alumina.

The compound $3CaO \cdot Al_2O_3 \cdot 3CaCO_3 \cdot 32H_2O$, was prepared by precipitation from mixtures of ammonium bicarbonate, calcium aluminate, and calcium hydroxide in aqueous sucrose solution. It crystallized as spherulites of minute needles. Other methods produced individual crystals, some tubular, but only in minute quantities or mixed with other phases. X-ray diffraction indicates isomorphism with $3CaO \cdot Al_2O_3 \cdot 3CaSO_4 \cdot 32H_2O$. $3CaO \cdot Al_2O_3 \cdot 3CaCO_3 \cdot 32H_2O$ is, in general, less stable than the monocarbonate complex.

The needle-form "silicoaluminate" reported by Flint and Wells was re-examined. It was concluded that the phase probably contains CO_2 as well as SiO_2, but the exact composition is in doubt.

1. Introduction

The existence of two series of calcium aluminate complex salts has been known for many years. One series may be represented by the general formula $3CaO \cdot Al_2O_3 \cdot CaX \cdot nH_2O$, the other by $3CaO \cdot Al_2O_3 \cdot 3CaX \cdot mH_2O$, in which X is one of a number of divalent anions (or two units of a monovalent anion), n is 10 to 12, and m is about 30. The former series crystallizes typically as thin hexagonal plates, though the symmetry may be lower than hexagonal; the latter series usually occurs as long, slender needles. Perhaps the most familiar example of the first series is the calcium aluminate hydrate, $3CaO \cdot Al_2O_3 \cdot Ca(OH)_2 \cdot 12H_2O$ (more commonly written $4CaO \cdot Al_2O_3 \cdot 13H_2O$); whereas the acicular series is typified by the well-known aluminate sulfate, $3CaO \cdot Al_2O_3 \cdot 3CaSO_4 \cdot 32H_2O$.

The literature relative to this interesting class of compounds up to 1951, has been reviewed by Steinour [1] [1]. Some years earlier, at the Symposium on the Chemistry of Cement in Stockholm, F. E. Jones [2] summarized the existing data on the calcium aluminate complex salts, including two "carboaluminates" which had been prepared by G. E. Bessey. The formulas assigned were $3CaO \cdot Al_2O_3 \cdot CaCO_3 \cdot 11H_2O$ and $3CaO \cdot Al_2O_3 \cdot 3CaCO_3 \cdot 27H_2O$. More recently the low-carbonate compound was the subject of a study by Turriziani and Schippa [3] (who indicated the water content as 10.8 H_2O), and its occurrence has also been reported by one of the present authors [4]. The high-carbonate compound has been prepared by Buttler [5], who found by X-ray methods that it is isomorphous with the "sulfoaluminate" of analogous composition.

It may be appropriate at this point to consider briefly the nomenclature of these compounds. The term "sulfoaluminate" has become firmly established through many years of usage, and it was therefore natural to refer to the more recently discovered carbonate analogs as carboaluminates. These names, unfortunately, do not correctly represent the relationship of the varous atoms involved. Although our knowledge of the crystal structure is incomplete, it seems clear that the sulfoaluminates might more correctly be called "aluminate sulfates", and the analogous "carboaluminates", "aluminate carbonates." Thus, for example, the compound $3CaO \cdot Al_2O_3 \cdot 3CaCO_3 \cdot nH_2O$ (or $6CaO \cdot Al_2O_3 \cdot 3CO_2 \cdot nH_2O$) would be called hexacalcium aluminate tricarbonate hydrate. Inasmuch as this terminology is rather cumbersome, the compounds will generally be referred to in this paper by formula rather than by name. The older terms sulfoaluminate and carboaluminate will be avoided except when needed in referring to earlier work.

The two aluminate carbonates are of some practical interest because of their possible relation to the chemistry of cement hydration. The compound $3CaO \cdot Al_2O_3 \cdot CaCO_3 \cdot 11H_2O$ has, in fact, been noted among the hydration products of aluminous cement [4, 6].

2. Procedures

The various reaction mixtures were prepared from reagent grade chemicals, except as noted below. Calcium hydroxide solutions were made from calcium oxide, freshly obtained by heating calcium carbonate. Calcium aluminate solutions were prepared by shaking monocalcium aluminate, $CaO \cdot Al_2O_3$, with water for 30 to 40 min., followed by filtration. The anhydrous aluminate used for this purpose was made by heating a mixture of calcium carbonate and alumina

[1] Figures in brackets indicate the literature reference at the end of this paper.

(either hydrated or anhydrous) for several hours at about 1,250° C, and was used within a short time after cooling. In some cases, an aluminous cement was substituted for the $CaO{\cdot}Al_2O_3$, and the shaking with water was continued for periods up to 3 hrs. By either method, concentrations up to 2.0 g Al_2O_3 and 1.2 g CaO per liter, or occasionally higher, were obtained. Such solutions are metastable, and usually start to become cloudy within the time required for an accurate analysis. An estimate of concentration based on titration with hydrochloric acid, in the presence of phenolphthalein, was therefore used as a basis for calculating the desired proportions in the mixtures, to permit use of the solution while still fresh. The actual concentration was later determined gravimetrically.

X-ray diffraction patterns by the powder method were made on a Geiger counter diffractometer, with copper Kα radiation.

Infrared spectra were obtained on pressed pellets, with the sample in the amount of 0.3 to 0.4 percent dispersed in KBr. A Beckmann IR–4 infrared spectrometer with sodium chloride optics was used. The spectra include a small amount of absorption due to adsorbed water.

3. Results and Discussion

3.1. $3CaO{\cdot}Al_2O_3{\cdot}CaCO_3{\cdot}11H_2O$

The compound $3CaO{\cdot}Al_2O_3{\cdot}CaCO_3{\cdot}11H_2O$ was prepared by mixing solutions of calcium aluminate, calcium hydroxide, and sodium carbonate, (or bicarbonate) following the method of Turriziani and Schippa [3]. The calcium aluminate solution was prepared from aluminous cement, as described in the previous section. Two liters of the aluminate solution and 8 to 9 liters of saturated calcium hydroxide were mixed and stirred a few seconds, after which sodium carbonate (3.50 to 3.75 g Na_2CO_3 in 250 ml of water) was added slowly with continued stirring. The mixture was allowed to stand about two months, after which the precipitate was filtered off and dried over saturated magnesium chloride solution (33% R.H.) until the water content, determined by ignition loss, was constant (requiring about 2 months). Details relative to two such preparations are given in table 1 (preparations 1.1 and 1.2). The molar ratios of these preparations, computed from results of analyses, are close to the theoretical composition $3CaO{\cdot}Al_2O_3{\cdot}CaCO_3{\cdot}11H_2O$. The small deviations probably are not quantitatively significant, as both preparations were observed to contain minute amounts of calcite ($CaCO_3$), gibbsite ($Al_2O_3{\cdot}3H_2O$), and tricalcium aluminate hexahydrate ($3CaO{\cdot}Al_2O_3{\cdot}6H_2O$).

The compound crystallizes in the form of minute hexagonal plates, which when viewed on edge appear to be needles showing positive elongation. In the preparations described above, the crystals were too thin to be distinguished except when observed edgewise. The low- and high-refractive indices were 1.532 ± 0.003 and 1.554 ± 0.003, respectively.

The X-ray diffraction pattern obtained for $3CaO{\cdot}Al_2O_3{\cdot}CaCO_3{\cdot}11H_2O$ (preparation 1.1) is given in table 2. Certain weak reflections believed to be due to the known extraneous phases have been omitted from the tabulation. Assuming a hexagonal lattice, probable *hkl* values have been tabulated and the following unit cell parameters calculated: $a = 8.71_6$ A, $c = 7.56_5$ A. The expected *d*-spacings are calculated from these parameters, and compared with both the observed *d*-spacings and the *d*-spacings published by Turriziani and Schippa [3]. It should be emphasized that the planes and parameters calculated in this manner are only a first approximation to the actual structure. Although there is good agreement between most of the observed and calculated *d*-spacings, those calculated for the *hkl* values referred to in footnote (c) of table 2 do not agree with the observed spacings as closely as the others. The true unit cell is probably larger and more complex, perhaps in the manner suggested by Buttler, Dent Glasser, and Taylor for $3CaO{\cdot}Al_2O_3{\cdot}Ca(OH)_2{\cdot}12H_2O$ [7].

TABLE 1. *Preparation of* $3CaO{\cdot}Al_2O_3{\cdot}CaCO_3{\cdot}11H_2O$

Preparation No.	1.1	1.2	1.3	1.4
Total volume of mixture, liter	10.2	10.2	5.6	5.8
Original concentration of mixture, calculated:				
CaO, g/liter	1.129	1.158	1.142	1.147
Al_2O_3, g/liter	0.358	0.355	0.347	0.240
Na_2CO_3, g/liter	0.342	0.337	0.519	0.705
Molar ratio, CaO: Al_2O_3	5.74	5.93	5.98	8.70
Molar ratio, CO_2: Al_2O_3	0.92	0.91	1.44	3.06
Final concentration of solution: [a]				
CaO, g/liter	0.387	0.414	0.291	0.328
Al_2O_3, g/liter	0.007	0.008	0.007	0.005
Molar ratios in precipitate (dried at 33% R.H.):				
CaO: Al_2O_3	4.05	3.96	4.43	5.80
CO_2: Al_2O_3	1.02	0.98	1.57	3.47
H_2O: Al_2O_3	10.6	10.7	11.0	9.1
Solid phases in precipitate	Nearly all $3CaO{\cdot}Al_2O_3{\cdot}CaCO_3{\cdot}11H_2O$. Very small amounts of calcite and $3CaO{\cdot}Al_2O_3{\cdot}6H_2O$.	Same as 1.1	$3CaO{\cdot}Al_2O_3{\cdot}CaCO_3{\cdot}11H_2O$ and calcite.	$3CaO{\cdot}Al_2O_3{\cdot}CaCO_3{\cdot}11H_2O$ and calcite

[a] Other constituents not determined.

TABLE 2. *X-ray diffraction pattern of* $3CaO \cdot Al_2O_3 \cdot CaCO_3 \cdot 11H_2O$

Observed *d*-spacings	Relative intensity	Probable *hkl* [a]	Calculated *d*-spacings [a]	*d*-spacings observed by T and S [b]	Remarks
7.567	100	001	7.565	7.740	
		100	7.548		
4.360	6	110	4.359		May be a line of $Al_2O_3 \cdot 3H_2O$.
3.985	6				
		002	3.783		
3.784	44	111	3.776	3.790	
		200	3.774		
3.661	2				
3.458	6				
2.858	30	112	2.857	2.890	
		210	2.853		
2.777	8				May be a line of $C_3A \cdot 6H_2O$.
[2.725 [d]	14	[c] 202	2.672		
2.654]	4	[c] 211	2.669]		
2.524	18	003	2.522	2.530	
		300	2.516		
2.488	18				
[2.441 [d]	18	[c] 103	2.392	2.430]	
2.419]	24	[c] 301	2.388	2.366	
2.339	22				
2.295	4				
2.238	4	[c] 212	2.276		
2.165	6	113	2.183	2.177	
		220	2.180		
2.116	8			2.118	Designated as 310 or 302 by Turriziani and Schippa.
		302	2.097		
2.096	6	203	2.093		
		310			
2.065	2				
2.024	2				
2.012	6	311	2.018	2.023	
1.992	2				
1.943	10			1.955	Designated as 004 by Turriziani and Schippa.
1.907	2				
		004	1.891		
1.890	4	213	1.889		
		222	1.888		
		400	1.887		
1.861	8				
		[c] 104	1.835		
1.824	12	[c] 312	1.833		
		[c] 401	1.831		
[1.661 [d]	12	402			
1.652	16	321	1.688	1.685	
1.642]	12	410	1.648	1.665	
		223			
1.602	4	[c] 313	1.611		
		[c] 411	1.610		
1.580	4	322	1.575	1.586	
		214	1.576		
		005	1.513		
		304	1.512		
1.512	6	403	1.511		
		412	1.510		
		500			
		115	1.430		
1.436	4	224	1.428		
		323	1.424		
		420			
1.410	2	[c] 205	1.404		
1.381	4	[c] 314	1.403		
		413	1.379		

[a] *hkl* are assigned on the assumption of a hexagonal lattice. The expected *d*-spacings are calculated from the unit cell parameters $a=8.716$ and $c=7.565$, which were in turn calculated from the observed *d*-spacings. See discussions.
[b] See ref [3].
[c] See discussion in text concerning the *hkl* values marked.
[d] The bracketed *d*-spacings may correspond to one or several of the corresponding *hkl* values tabulated, and vice versa.

A differential thermal analysis curve for preparation 1.1 is shown in figure 1, top curve. The most notable feature is the endothermic effect at about 220° C, followed by a smaller one at 260° C. These are believed to be associated with the loss of water of hydration. The thermal effects at the higher temperatures are not as well defined, but it may be assumed that the carbon dioxide is expelled in this range. The departures here may be interpreted

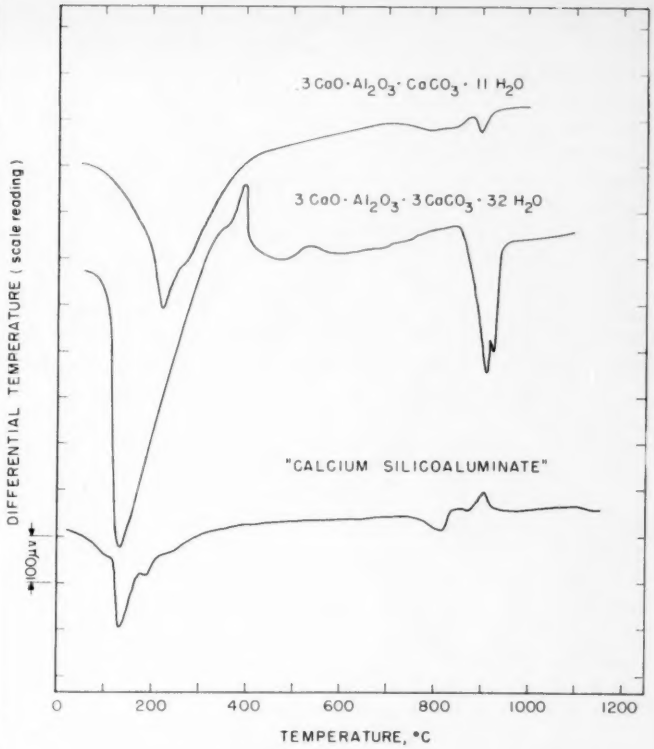

FIGURE 1. *Differential thermal analysis curves for the calcium aluminate carbonate hydrates and silicoaluminate.*

either as two endotherms separated by a brief recovery, or as a single broad endotherm culminating at 895° C, with a superimposed exotherm at 875°. The curve given by preparation 1.2 shows only minor deviations from that of 1.1, and both are similar to that given by Turriziani and Schippa [3].

A portion of the infrared absorption spectrum for preparation 1.1 is shown in the top curve of figure 2. While no attempt has been made to analyze the spectrum in detail, it may be noted that the multiple band between 2.5 and 4 μ and the smaller one at about 6.1 μ are probably due to combined or adsorbed water. The effect at 6.1 μ may be largely eliminated, and the one at lower wave length partially so, by preliminary heating of the sample at 110° C. It is therefore inferred that the effect at 6.1 μ is associated with adsorbed water, and the larger band at 2.5 to 4 μ with both combined and adsorbed water.

The double absorption band at 7.0 to 7.3 μ is believed to be associated with the carbonate group. Calcite and aragonite show a moderately broad band between 6.5 and 7.0 μ, from which it may be inferred that the bonding here is somewhat different. Heating the material at 110° C changes the doublet into a single band, but does not change its position. The rest of the spectrum is essentially unchanged by the heat treatment.

$3CaO \cdot Al_2O_3 \cdot CaCO_3 \cdot 11H_2O$ was also prepared by exposing calcium aluminate solutions to atmospheric carbon dioxide, both at room temperature (25 to 30° C) and at 1° C. In no case was a pure preparation obtained in this manner, small amounts of cal-

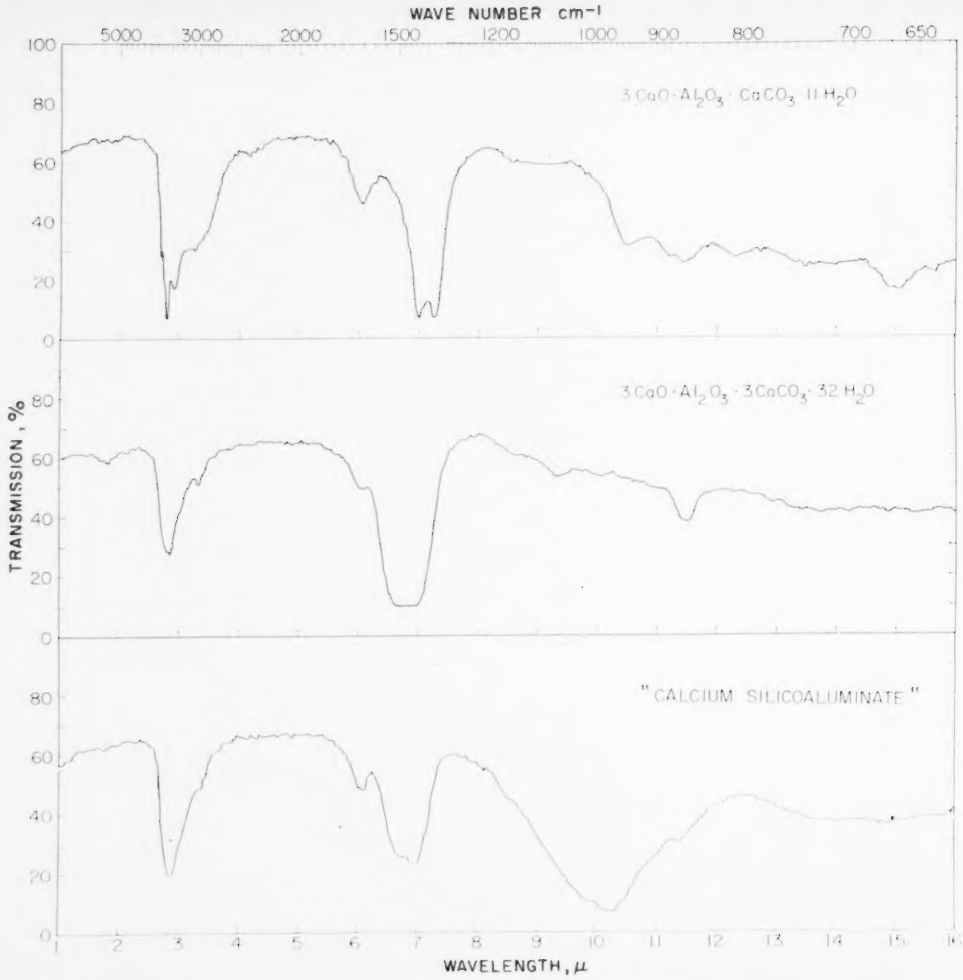

FIGURE 2. *Infrared absorption spectra for the calcium aluminate carbonate hydrates and silicoaluminate.*

cium carbonate and hydrated alumina being formed at the same time. On continued exposure, the aluminate carbonate that had formed was entirely decomposed, the products being calcite, aragonite, gibbsite, and bayerite. The decomposition may be represented by the equation,

$$3CaO\cdot Al_2O_3\cdot CaCO_3\cdot 11H_2O + 3CO_2 \rightarrow 4CaCO_3 + Al_2O_3\cdot 3H_2O + 8H_2O$$

(calcite or aragonite) (gibbsite or bayerite)

The conditions favoring one form of calcium carbonate or alumina over the other were not investigated. The reactions were slower at 1° C than at room temperature, but apparently followed the same course.

From the foregoing, it is clear that $3CaO\cdot Al_2O_3\cdot CaCO_3\cdot 11H_2O$ in aqueous suspension is not stable in the presence of carbon dioxide at pressures as high as the partial pressure of carbon dioxide in ordinary air. If the compound has a range of stable existence it must be in equilibrium with carbon dioxide at lower pressure. The probability that it does have a limited region of stability is suggested by the following experiments. A mixture of finely ground anhydrous tricalcium aluminate and calcium carbonate in equimolar ratio was made up to a paste with water in a vessel cooled with ice water. The paste was packed into a glass vial and examined after 7 days moist storage at room temperature. The X-ray diffraction pattern of the hardened paste indicated almost complete conversion to $3CaO\cdot Al_2O_3\cdot CaCO_3\cdot 11H_2O$, with very small amounts of calcite and $3CaO\cdot Al_2O_3\cdot 6H_2O$. Similar results were obtained if calcium carbonate was present in excess; or if the mixture was shaken with excess water in a stoppered flask instead of being made into a paste; or if the temperature of storage was lowered to 1° C. The overall reaction may be simply represented by the equation,

$$3CaO\cdot Al_2O_3 + CaCO_3 + 11H_2O \rightarrow 3CaO\cdot Al_2O_3\cdot CaCO_3\cdot 11H_2O$$

No attempt was made to determine the actual mechanism.

In another series of experiments, various calcium

aluminate hydrates were covered with calcium hydroxide solutions of appropriate concentration and exposed to the atmosphere in unstoppered bottles for 10 weeks. The aluminates used were $CaO \cdot Al_2O_3 \cdot 10H_2O$, $2CaO \cdot Al_2O_3 \cdot 8H_2O$, $4CaO \cdot Al_2O_3 \cdot 13H_2O$, and $3CaO \cdot Al_2O_3 \cdot 6H_2O$. All were altered completely during this period except $3CaO \cdot Al_2O_3 \cdot 6H_2O$ at 1° C; in the latter case a small amount of the original material remained. The final products were chiefly calcite and bayerite, but aragonite and gibbsite also were present in some cases. $3CaO \cdot Al_2O_3 \cdot CaCO_3 \cdot 11H_2O$ was observed during the earlier stages except when $CaO \cdot Al_2O_3 \cdot 10H_2O$ was the starting material. It persisted longer in those held at 1° C than in those at room temperature, and in two cases there was still some present after 10 weeks.

In general, then, it appears that the calcium aluminate hydrates in contact with water are attacked by atmospheric carbon dioxide with the formation of $3CaO \cdot Al_2O_3 \cdot CaCO_3 \cdot 11H_2O$, which in turn is decomposed to calcium carbonate and alumina. However, when atmospheric carbon dioxide is excluded, calcite can react with calcium aluminate to form $3CaO \cdot Al_2O_3 \cdot CaCO_3 \cdot 11H_2O$. Presumably there is a point of equilibrium at some carbon dioxide concentration lower than that of the atmosphere, but this has not been investigated.

3.2. $3CaO \cdot Al_2O_3 \cdot 3CaCO_3 \cdot 32H_2O$

Several attempts were made to prepare $3CaO \cdot Al_2O_3 \cdot 3CaCO_3 \cdot 32H_2O$ by the same technique used successfuly in preparing the monocarbonate complex; that is, from solutions of calcium aluminate, calcium hydroxide, and sodium carbonate. Preparations 1.3 and 1.4, table 1, are representative of a series in which the initial ratios of CaO and CO_2 to Al_2O_3 were progressively increased. All these preparations showed the X-ray diffraction pattern and differential thermal analysis peaks of $3CaO \cdot Al_2O_3 \cdot CaCO_3 \cdot 11H_2O$ and calcite. The intensities of the calcite peaks relative to those of the aluminate complex increased with the calcium carbonate content of the preparations. Optical examination showed crystals of $3CaO \cdot Al_2O_3 \cdot CaCO_3 \cdot 11H_2O$ and very fine particles of calcite. No $3CaO \cdot Al_2O_3 \cdot 3CaCO_3 \cdot 32H_2O$ was observed. Details of composition are given in table 1.

The other method employed, in which atmospheric carbon dioxide was allowed to react with calcium aluminate solutions, proved more successful. After numerous experiments it was concluded that the conditions favoring the formation of the needle-form compound are rather critical. Favorable results were obtained by the action of atmospheric carbon dioxide on a calcium aluminate solution containing 0.5 to 0.7g Al_2O_3 and 0.4 to 0.6g CaO per liter. Such solutions were prepared by the action of water on $CaO \cdot Al_2O_3$, followed by dilution of the filtrate with water and calcium hydroxide solution. The diluted solution was cooled to 10 to 20° C, and air was bubbled through at a moderate rate. In a short time, usually about 20 min, the needle crystals could be observed, and at that point, more calcium hydroxide could be added to increase the yield. Despite all precautions, the preparations always contained either calcite or $3CaO \cdot Al_2O_3 \cdot CaCO_3 \cdot 11H_2O$ in small amounts. Increased contamination resulted if the solutions were not freshly prepared, if the temperature exceeded 20° C, or if the volume aerated exceeded 200 ml. It was therefore difficult to prepare more than a few milligrams of reasonably pure material at a time. The crystals obtained were long, slender needles, similar in appearance to those of $3CaO \cdot Al_2O_3 \cdot 3CaSO_4 \cdot 32H_2O$. The high and low indices of crystals that had been dried over magnesium perchlorate were 1.480 and 1.456. These may be compared with the indices 1.464 and 1.458 for the sulfoaluminate, reported by Lerch, Ashton, and Bogue [8]. The ratio of CaO to Al_2O_3 was in approximate agreement with the formula, but the amount of precipitate available was too small for an accurate determination of the CO_2 content.

Small amounts of $3CaO \cdot Al_2O_3 \cdot 3CaCO_3 \cdot 32H_2O$ were also formed when calcium aluminate solutions derived from an aluminous cement were allowed to stand overnight in open beakers. Such preparations always contained large amounts of $3CaO \cdot Al_2O_3 \cdot CaCO_3 \cdot 11H_2O$ as well as other crystals and amorphous material, but they were of interest because of the relatively large size of the needle crystals. In several instances the larger crystals were clearly tubular in shape, as may be seen in the photomicrograph, figure 3. In this picture, the gas

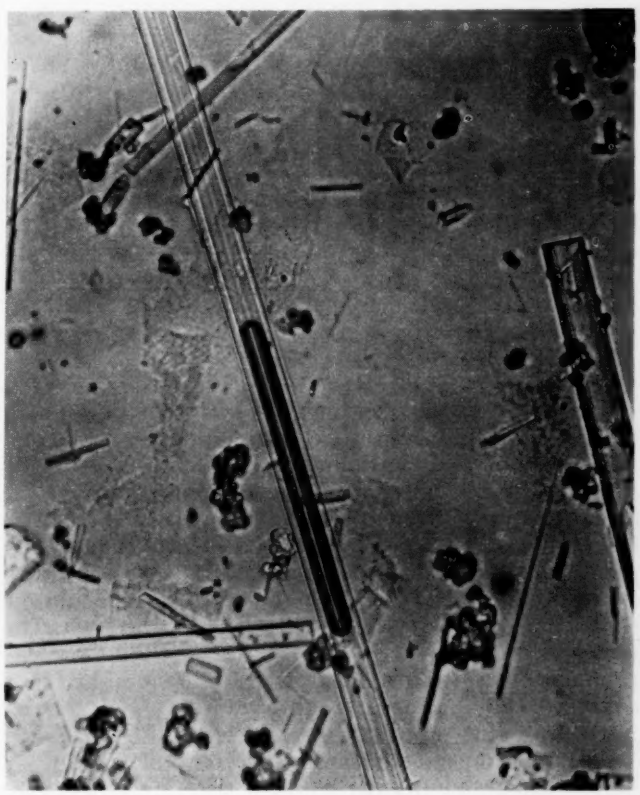

FIGURE 3. *Photomicrograph showing tubular crystals of* $3CaO \cdot Al_2O_3 \cdot 3CaCO_3 \cdot 32H_2O$.

Magnification, × 310. Largest crystal contains entrapped bubble.

bubble, which aids in discerning the tubular habit, presumably consists of ether vapor derived from the drying treatment. Such bubbles were gradually absorbed by the immersion liquid, and disappeared entirely in a few minutes.

For reasons not yet understood, the crystals formed in this manner had somewhat higher indices of refraction, namely, 1.490 and 1.470. The X-ray diffraction pattern, however, appeared to be identical with those of the previous preparation.

The difficulties attending preparation of $3CaO{\cdot}Al_2O_3{\cdot}3CaCO_3{\cdot}32H_2O$ led to a modified procedure designed to permit a high concentration of CaO while inhibiting precipitation of $CaCO_3$. The CaO was dissolved in aqueous solutions of sucrose (ordinary granulated sugar) ranging from 2 to 10 percent. After clarification by settling, the CaO concentration was determined by titration. A calculated volume of calcium aluminate solution was then poured into the lime-sucrose solution (no precipitate being formed at this point), after which a weighed quantity of ammonium bicarbonate, dissolved in water, was added. A flocculent precipitate formed, consisting of minute spherulites of uniform size, apparently formed of needles too small to be resolved by the microscope. Details of three such precipitation experiments are given in table 3.

TABLE 3. *Preparation of* $3CaO{\cdot}Al_2O_3{\cdot}3CaCO_3{\cdot}32H_2O$

Preparation No.	3.1	3.2	3.3
Total volume of mixture ml	1,000	1,000	1,000
Original concentration of mixture, calculated:			
CaO g/liter	1.94	3.41	6.16
Al_2O_3 g/liter	.46	.69	1.15
NH_4HCO_3 g/liter	.80	1.33	2.40
Sucrose g/liter	16	35	50
Final concentration of solution: [a]			
CaO g/liter	1.05	1.85	3.48
Molar ratios in precipitate (dried at 79% R.H.):			
$CaO: Al_2O_3$	5.90	5.88	6.00
$CO_2: Al_2O_3$			3.02
$H_2O: Al_2O_3$			31.9

[a] Other constituents not determined.

The three products appeared identical under the microscope. Thus in this method the initial concentration of the solution appears not to be critical. It may also be noted that it was not necessary to cool the solutions below room temperature. From the analysis of preparation 3.3, after drying to constant weight over saturated ammonium chloride solution (79% R.H.), the composition was calculated to be 6.00 CaO:1 Al_2O_3:3.02 CO_2:31.9 H_2O, or in whole numbers, $3CaO{\cdot}Al_2O_3{\cdot}3CaCO_3{\cdot}32H_2O$. Approximately 3 molecules of water were lost on drying over magnesium perchlorate. The X-ray pattern of this preparation is given in table 4.

The differential thermal analysis curve (fig. 1, middle curve) shows, as its most prominent feature, a large endothermic effect at 135° C, evidently resulting from expulsion of water of hydration. This endotherm is followed by an exotherm at 390°, the reason for which has not been investigated. The small exotherm near 500° likewise remains unexplained. The endotherm at 910° may be assumed to be caused by liberation of CO_2, but the reason for the slight irregularity just above that point is not known.

TABLE 4. *X-ray powder diffraction patterns of* $3CaO{\cdot}Al_2O_3{\cdot}3CaCO_3{\cdot}32H_2O$ *and "silicoaluminate"*

$3CaO{\cdot}Al_2O_3{\cdot}3CaCO_3{\cdot}32H_2O$		"Calcium silicoaluminate"	
d	I	d	I
A		A	
9.41	100	9.69	100
5.43	27	5.56	25
5.31	4		
4.83	20	4.94	10
4.62	26	4.68	8
3.80	42	3.85	13
3.52	20	3.57	5
3.37	27	3.44	14
3.13	4	3.20	6
2.962	8	3.00	4
2.700	35	2.88	9
2.653	11	2.77	7
2.605	5	2.74	9
2.529	7	2.66	5
2.507	67	2.58	9
2.466	3	2.54	15
2.413	4		
2.339	6		
2.310	4	2.184	11
2.152	31	2.157	4
2.098	19	2.130	7
2.049	3	2.056	3
1.996	5	2.034	4
1.977	3		
1.913	7	1.948	3
1.879	12	1.917	5
1.822	9		
1.768	7	1.786	2
1.758	2		
1.739	2		
1.711	2	1.723	2
1.684	4		
1.646	4	1.665	3
1.622	7	1.645	2
1.582	2	1.597	2
1.568	2		
1.541	2	1.559	2
1.532	4		
1.483	5		
1.465	3		

The infrared absorption spectrum (fig. 2, middle tracing) shows some similarity to that of $3CaO{\cdot}Al_2O_3{\cdot}CaCO_3{\cdot}11H_2O$, but there are differences in detail. In both spectra there is a large absorption band with a maximum near 3μ, and a small one at 6.1μ. With both preparations, heating at 110° C diminished the effect at 3μ and eliminated that at 6.1μ. In both cases, the absorption bands may probably be ascribed to combined and adsorbed water.

In the spectrum for $3CaO{\cdot}Al_2O_3{\cdot}3CaCO_3{\cdot}32H_2O$, there is a large band at 6.5 to 7μ, also a smaller one near 11.5μ. These are similar in size and position to bands observed for calcite and aragonite, and attributed to the carbonate group. The relationship here appears to be closer than that between $3CaO{\cdot}Al_2O_3{\cdot}CaCO_3{\cdot}11H_2O$ and calcite and aragonite.

3.3. Relation of $3CaO \cdot Al_2O_3 \cdot 3CaCO_3 \cdot 32H_2O$ to Other Compounds of the Same Type

a. $3CaO \cdot Al_2O_3 \cdot 3CaCO_4 \cdot 32H_2O$

The isomorphous relationship between $3CaO \cdot Al_2O_3 \cdot 3CaCO_3 \cdot 32H_2O$ and the analogous sulfate compound has already been mentioned. The possibility of solid solution between the two seemed worth investigating, and a few experiments were directed toward that end. The problem was attacked from two angles. The first procedure consisted of partial substitution of carbonate for sulfate in mixtures known to yield $3CaO \cdot Al_2O_3 \cdot 3CaSO_4 \cdot 32H_2O$ crystals. In every case, the product was a mixture of $3CaO \cdot Al_2O_3 \cdot 3CaSO_4 \cdot 32H_2O$ and $3CaO \cdot Al_2O_3 \cdot CaCO_3 \cdot 11H_2O$, with no observable displacement in the X-ray pattern of either.

The other procedure involved substitution of ammonium sulfate for half of the ammonium bicarbonate in the lime-sucrose-solution method successfully used in preparing $3CaO \cdot Al_2O_3 \cdot 3CaCO_3 \cdot 32H_2O$. A heavy precipitate was obtained but the crystals were so minute that their shape could not be ascertained. There appeared to be two phases, the predominant one having a mean index of refraction below 1.47, the other above 1.48. The X-ray diffraction pattern showed strong lines of $3CaO \cdot Al_2O_3 \cdot 3CaSO_4 \cdot 32H_2O$, together with very weak lines of $3CaO \cdot Al_2O_3 \cdot 3CaCO_3 \cdot 32H_2O$. The results are not entirely conclusive, because of the extreme fineness of the precipitate and the very small differences between the respective indices of refraction andX-ray patterns. Nevertheless, the inference may be drawn that if any solid solution occurs, it is so limited in extent that it cannot be demonstrated by the methods used. The reason for the surprising difference in the relative amounts of the two phases has not been investigated.

b. Hexacalcium Aluminate Hydrate

Preparation of a hexacalcium aluminate hydrate, $6CaO \cdot Al_2O_3 \cdot 33H_2O$(or $3CaO \cdot Al_2O_3 \cdot 3Ca(OH)_2 \cdot 30H_2O$) was reported by Flint and Wells [9] in 1944, but confirmation from other source appears to be lacking. The compound was prepared by mixing lime-sucrose solution with calcium aluminate solution; that is, the method was the same as described above for $3CaO \cdot Al_2O_3 \cdot 3CaCO_3 \cdot 32H_2O$ except that no carbonate was added. In connection with the present study, an attempt was made to prepare the hexacalcium aluminate by following the method of Flint and Wells. A surprisingly small amount of precipitate was obtained, which had, however, a $CaO:Al_2O_3$ ratio close to 6, as expected. The optical properties approximated those reported by Flint and Wells, although the crystals were too small for a precise determination of indices of refraction. Because of the small amount of the precipitate, carbon dioxide was not quantitatively determined, but its presence was noted qualitatively. Further attempts at preparation of hexacalcium aluminate yielded still less precipitate, or none at all. The X-ray pattern of the precipitate proved to be identical with that of $3CaO \cdot Al_2O_3 \cdot 3CaCO_3 \cdot 32H_2O$ from which it is inferred that the material actually was the tricarbonate complex. The carbon dioxide probably was derived from the lime-sucrose solution, which in that instance had been subjected to repeated filtration in an effort to remove the lime remaining in suspension, without exclusion of atmospheric carbon dioxide. Thus the existence of a hexacalcium aluminate hydrate was not confirmed.

c. Calcium Silicoaluminate

Flint and Wells [9] reported the preparation of two calcium silicoaluminates analogous to the sulfoaluminates. One of these, crystallizing as long, hair-like needles, appeared in a number of aqueous lime-alumina-silica mixtures that had been kept for three years or longer. It could not be separated from the other solid phases present for analysis, but because of its marked similarity to $3CaO \cdot Al_2O_3 \cdot 3CaSO_4 \cdot 32H_2O$ it was tentatively assigned the formula $3CaO \cdot Al_2O_3 \cdot 3CaSiO_3 \cdot 30\text{–}32H_2O$. This phase formed slowly and progressively, while the mixtures were kept in rubber-stoppered glass flasks at room temperature over a period of years. Fortunately, four such mixtures, prepared by Flint and Wells, are still available for examination. One, containing a greater proportion of the acicular crystals than the others, was singled out for special study. In addition to the crystals, it contained a large amount of more or less gelatinous material with an average index of refraction about 1.51. Numerous attempts to separate the crystals from the gel were unsuccessful. The high and low indices of the needles were found to be 1.495 and 1.473, and the elongation was negative. These indices are slightly higher and lower, respectively, than those reported by Flint and Wells: $\omega = 1.487$; $\epsilon = 1.479$. The discrepancy may result from different degrees of drying. Because of the radically different nature of the two types of material present, an accurate estimate of the relative amounts was impossible, but the needle phase appeared to be over 50 percent of the total. The X-ray diffraction record showed a strong pattern similar to that of $3CaO \cdot Al_2O_3 \cdot 3CaCO_3 \cdot 32H_2O$, (see table 3). In addition, there were weaker and more diffuse lines corresponding to $2CaO \cdot Al_2O_3 \cdot SiO_2 \cdot nH_2O$ and to hydrated calcium silicate. These have been omitted from the table. The intensities of the latter reflections were smaller than might have been expected from the amount of gel-like material present, hence it must be concluded that this material is poorly crystallized.

By chemical analysis, the overall molar ratio of the nonvolatile components in the precipitate was found to be 5.48 CaO:1 Al_2O_3:2.81 SiO_2. This could be construed to lend good support to the formula proposed by Flint and Wells, were it not for the other solid phases known to be present in significant quantity. Analysis also indicated 0.02 percent SO_3, which was considered negligible. However, there was also a considerable amount of CO_2, which presumably had permeated through or around the

rubber stopper from the atmosphere during the 18-year period of storage. In terms of the molar ratio given above, it amounted to 0.73 mole per mole of Al_2O_3, which is too much to be ignored. Such a quantity of CO_2, if combined as calcite or aragonite, would be conspicuous under the polarizing microscope and readily detectable by X-ray diffraction. Another possible form of combination, $3CaO \cdot Al_2O_3 \cdot CaCO_3 \cdot 11H_2O$, likewise could hardly escape notice if present in the indicated proportion. Since none of these substances was observed, it would be reasonable to infer that the needle crystals contain the CO_2 and that they actually are $3CaO \cdot Al_2O_3 \cdot 3CaCO_3 \cdot 32H_2O$. Unfortunately, this conclusion also fails to fit all the facts. The X-ray patterns show small, but significant, differences; and the amount of CO_2 found is inadequate to account for the large proportion of needle crystals present if the formula showing $3CaCO_3$ is accepted. The chemical analysis can be rationalized by the assumption of a quinary compound (possibly a solid solution) with a composition approximating $3CaO \cdot Al_2O_3 \cdot 1.5CaCO_3 \cdot 1.5CaSiO_3 \cdot nH_2O$. It is recognized that this suggested formula rests on no firmer foundation than does that proposed by Flint and Wells, except that it does account for the CO_2 shown to be present.

A differential thermal analysis curve for the preparation under discussion is shown in figure 1, bottom curve. In comparison with the curve for $3CaO \cdot Al_2O_3 \cdot 3CaCO_3 \cdot 32H_2O$, the endotherm corresponding to loss of water occurs at the same temperature, but that attributed to liberation of CO_2 comes at about 815°, considerably lower than in the tricarbonate compound. This shift is probably due to the presence of silica. The exotherm at about 850° C may represent a lime-silica reaction, but the significance of the other irregularities is not known.

The infrared absorption spectrum (fig. 2, bottom) closely resembles that of $3CaO \cdot Al_2O_3 \cdot 3CaCO_3 \cdot 32H_2O$ in the region of lower wave lengths. The wide absorption band extending from 8 to 12 μ is typical of hydrated calcium silicates.

The results described above are supported by less complete data for three other mixtures prepared by Flint and Wells. Two of them contained the same solid phases as the one discussed, but with the needle phase present in smaller amount. The other was predominantly $3CaO \cdot Al_2O_3 \cdot CaCO_3 \cdot 11H_2O$, with lesser amounts of the needle phase and calcium silicate hydrate. The X-ray patterns showed the stronger lines of the needle phase, with no significant variation in *d*-spacings among the different preparations.

Similar acicular crystals have appeared in smaller amounts in at least 10 aqueous lime-alumina-silica mixtures prepared more recently by one of the authors. The crystals differed somewhat in habit, usually being shorter and thicker, but the indices of refraction were the same, within limits of measurement. It seems significant that in all cases, the acicular crystals were formed only after the mixtures had stood several months or years in rubber-stoppered flasks, thus affording opportunity for slow diffusion of CO_2 from the atmosphere.

The conclusion, then, is that the acicular crystals in question are neither a pure aluminate silicate nor a pure aluminate carbonate, but may contain both $CaCO_3$ and $CaSiO_3$.

Quite recently, Mohri [10] reported the preparation of a compound which he believed to be the same as the silicoaluminate of Flint and Wells, $3CaO \cdot Al_2O_3 \cdot 3CaSiO_3 \cdot 31H_2O$. The product was obtained by hydrating lime-alumina-silica glasses at 20° C, with careful exclusion of CO_2. However, the electron micrographs showed tabular rather than acicular crystals, and the X-ray diffraction patterns showed strong lines in agreement with the pattern of $2CaO \cdot Al_2O_3 \cdot SiO_2 \cdot nH_2O$. Consequently this work cannot be taken unreservedly as a confirmation of the conclusions of Flint and Wells.

3.4. Relation to the Chemistry of Cements

The possible relation of the aluminate carbonates to the hydration of hydraulic cements has scarcely been touched in the present study, but it seems appropriate to point out that the subject deserves further exploration. The components of these compounds are all present in the cements, the aggregates, the water, or the atmosphere to which concrete and mortar are exposed during and after mixing and placing. Hence the formation of aluminate carbonates in such materials, though perhaps only metastably, must be considered a possibility. The occurrence of $3CaO \cdot Al_2O_3 \cdot CaCO_3 \cdot 11H_2O$ in hydrated aluminous cement pastes has been noted above. Schippa [6] found this compound chiefly near the surface of the specimens, as might be expected. The formation of a similar crystalline phase at the interface between aluminous cement and calcareous aggregate was noted by Farran [11], who, however, considered it to be a solid solution between $3CaO \cdot Al_2O_3 \cdot CaCO_3 \cdot 11H_2O$ and $4CaO \cdot Al_2O_3 \cdot 13H_2O$. No report of the formation of such compounds in portland cement has been noted.

From the experimental work recorded above, it appears unlikely that $3CaO \cdot Al_2O_3 \cdot 3CaCO_3 \cdot 32H_2O$ would be formed in hydraulic cements, except perhaps under rather unusual conditions. $3CaO \cdot Al_2O_3 \cdot CaCO_3 \cdot 11H_2O$, however, should form readily, especially near the surface. Under continuous exposure to the atmosphere it would be expected to decompose with formation of calcium carbonate and alumina; but if formed beneath the surface, from reaction with calcareous aggregate, it might persist indefinitely.

4. Summary

Two calcium aluminate carbonate hydrates, previously reported in the literature, have been prepared and various properties determined.

$3CaO \cdot Al_2O_3 \cdot CaCO_3 \cdot 11H_2O$, crystallizes as thin hexagonal plates having refractive indices 1.532 and 1.554. The X-ray diffraction pattern has been tentatively indexed on the assumption of hexagonal symmetry, and the unit cell parameters calculated to be $a=8.716$, $c=7.565$. It was prepared by pre-

cipitation from mixtures of solutions of calcium aluminate, $Ca(OH)_2$, and Na_2CO_3; by the action of atmospheric CO_2 on calcium aluminate solutions, and on calcium aluminate hydrates in aqueous suspension; and by reaction between $3CaO \cdot Al_2O_3$, $CaCO_3$ and water, in paste form. On continued exposure to atmospheric CO_2, it is decomposed to $CaCO_3$ and hydrated Al_2O_3.

$3CaO \cdot Al_2O_3 \cdot 3CaCO_3 \cdot 32H_2O$, crystallizes in the form of needles, which in some cases are shown to be tubular. The lower index of refraction ranges from 1.456 to 1.470, the higher from 1.480 to 1.490 in different preparations. It could not be prepared by the method used most successfully in obtaining $3CaO \cdot Al_2O_3 \cdot CaCO_3 \cdot 11H_2O$; that is, by precipitation with Na_2CO_3. Precipitation by the action of atmospheric CO_2 on calcium aluminate solutions was successful only over a closely restricted range of concentration, temperature, and volume. A more satisfactory procedure was the precipitation by ammonium bicarbonate from a sucrose solution containing calcium aluminate and relatively high concentrations of $Ca(OH)_2$. $3CaO \cdot Al_2O_3 \cdot 3CaCO_3 \cdot 32H_2O$ is, in general, less stable than $3CaO \cdot Al_2O_3 \cdot CaCO_3 \cdot 11H_2O$.

Attempts to prepare solid solutions between the aluminate carbonates and the isomorphous aluminate sulfates were unsuccessful. The same is true regarding attempts at preparation of the hexacalcium aluminate hydrate described by Flint and Wells.

The silicoaluminate, $3CaO \cdot Al_2O_3 \cdot 3CaSiO_3 \cdot 30\text{–}32\text{-}H_2O$, reported by Flint and Wells, has been reexamined. Although the composition still has not been established, it is concluded that the phase in question probably contains CO_2 as well as SiO_2.

The authors acknowledge the invaluable assistance of several members of the staff of the National Bureau of Standards: H. E. Swanson and coworkers, who made the X-ray patterns; C. M. Hunt, who made the infrared measurements; and E. S. Newman, who assisted with the differential thermal analyses.

5. References

[1] H. H. Steinour, Aqueous cementitious systems containing lime and alumina; Research and Develop. Lab., Portland Cement Assoc., Research Dept. Bul. 34 (Feb. 1951).

[2] F. E. Jones, The calcium aluminate complex salts, Proc. of the Symposium on the Chem. of Cements; Stockholm, 1938 (p. 231). Ingeniörs Vetenskaps Akad., Stockholm (1939).

[3] R. Turriziani and G. Schippa, On the existence of hydrated calcium monocarboaluminate (in Italian), Ricerca Sci. **26,** 2792 (1956).

[4] E. T. Carlson, The system lime-alumina-water at 1° C; J. Research NBS **61,** 1 (1958) RP2877.

[5] F. G. Buttler, Personal communication.

[6] G. Schippa, Hydration of aluminous cement (in Italian), Ricerca Sci. **28,** 2120 (1957).

[7] F. G. Buttler, L. S. Dent Glasser, and H. F. W. Taylor, Studies on $4CaO \cdot Al_2O_3 \cdot 13H_2O$ and the related natural mineral hydrocalumite; J. Am. Ceram. Soc. **42,** 121 (1959).

[8] W. Lerch, F. W. Ashton, and R. H. Bogue, The sulfoaluminates of calcium; BS J. Research **2,** 715 (1929) RP54.

[9] E. P. Flint and L. S. Wells, Analogy of hydrated calcium silicoaluminates and hexacalcium aluminate to hydrated calcium sulfoaluminates; J. Research NBS **33,** 471 (1944) RP1623.

[10] J. Mohri, Calcium silicoaluminate; Semento Gijutsu Nenpo **12,** 43–45 (1958).

[11] J. Farran, Mineralogical contribution to the study of the adherence between the hydrated constituents of cements and the embedded materials (in French), Rev. matériaux construct. et trav. publ., C, No. 490, 155; No. 492, 191 (1956).

Washington, D.C. (Paper 64A4–55)

JOURNAL OF RESEARCH of the National Bureau of Standards—A. Physics and Chemistry
Vol. 64A, No. 4, July–August 1960

Acid Dissociation Constant and Related Thermodynamic Quantities for Triethanolammonium Ion in Water From 0 to 50 °C[1]

Roger G. Bates and Guy F. Allen

(February 25, 1960)

Earlier studies of the dissociation constants of monoethanolammonium and diethanolammonium ions and the thermodynamic constants for the dissociation processes have been supplemented by a similar study of triethanolammonium ion from 0° to 50° C. The dissociation constant (K_{bh}) is given by the formula

$$-\log K_{bh} = 1341.16/T + 4.6252 - 0.0045666T$$

where T is in degrees Kelvin. The order of acidic strengths of the ions is as follows: Triethanolammonium > diethanolammonium > monethanolammonium. Conversely, monoethanolamine is the strongest of the three bases. The thermodynamic constants for the dissociation of one mole of triethanolammonium ion in the standard state at 25° C are as follows: Heat content change ($\Delta H°$), 33,450 joule mole^{-1}; entropy change ($\Delta S°$), −36.4 joule deg^{-1} mole^{-1}; heat-capacity change ($\Delta C_p°$), 52 joule deg^{-1} mole^{-1}.

1. Introduction

The dissociation of positively charged weak acids is an isoelectric process, occurring without the creation of new electrostatic charges. There should therefore be no significant electrostatic contribution to the change of heat capacity that accompanies the dissociation. Hence, the thermodynamic constants for dissociation processes of this charge type may be expected to reveal information concerning the nature of the specific chemical interactions that occur between the solvent and the dissolved molecules and ions. In addition, the strengths of organic bases provide a useful insight into the inductive (electron-donating and electron-attracting) powers of substituent groups.

In earlier work [1, 2],[2] the substitution of hydroxyl groups into the substituents of alkylammonium ions was found to reduce the magnitude of the heat-capacity change occurring when 1 mole of the ion dissociates in the standard state to form hydrogen ion and 1 mole of the corresponding ammonia base. Following Everett and Wynne-Jones [3], this result was attributed to a reduction by hydroxyl of the hydrophobic character of the alkyl group. As a consequence of the electron-attracting property of the hydroxyl group, however, the monoethanolamine and diethanolamine are considerably weaker bases than ethylamine and diethylamine.

The study of the dissociation of substituted ammonium ions has now been extended to triethanolammonium. The acidic dissociation constant of this positively charged acid has been determined by electromotive-force measurements at intervals of 5°C from 0° to 50° C. Earlier studies [4, 5] of the dissociation constant of triethanolammonium were confined to a narrow range of temperatures. The standard changes of heat content, entropy, and heat capacity accompanying the dissociation process have been computed from the temperature coefficient of the dissociation constant. As expected, triethanolamine is a weaker base than diethanolamine, which is, in turn, weaker than monoethanolamine.

2. Method

The electromotive force method and many of the experimental techniques have been described in detail elsewhere [1, 6, 7]. The cell used is represented schematically as follows:

$$\mathrm{Pt;H_2(g),\ (HOC_2H_4)_3N{\cdot}HCl}\ (m_1),\ (\mathrm{HOC_2H_4})_3\mathrm{N}\ (m_2),\ \mathrm{AgCl;\ Ag}.$$

The dissociation process can be formulated most simply,

$$\mathrm{BH^+ = B + H^+}, \qquad (1)$$

where $\mathrm{BH^+}$ and B represent, respectively, triethanolammonium ion and triethanolamine. The complete expression by which the acidic dissociation constant, K_{bh}, was determined is

$$-\log K'_{bh} \equiv -\log K_{bh} - \beta m_1 = p_w\mathrm{H} + \log \frac{m_1}{m_2} - \frac{2A\sqrt{m_1}}{1 + Ba^*\sqrt{m_1}}. \qquad (2)$$

The hydrogen ion function p_wH is derived from the emf (E) of the cell without liquid junction by the formula

$$p_w\mathrm{H} \equiv -\log(f_{\mathrm{H}} f_{\mathrm{Cl}} m_{\mathrm{H}}) = (E - E°)F/(2.3026RT) + \log m_1, \qquad (3)$$

where $E°$ is the standard potential of the cell [8], m

[1] Presented in part before the Division of Physical Chemistry at the 137th meeting of the American Chemical Society, Cleveland, Ohio, April 1960.
[2] Figures in brackets indicate the literature references at the end of this paper.

is molality, f is an activity coefficient on the molal scale, and the other symbols have their usual significance.

The following steps in the derivation of eq (2) should be noted:

(1) The mass-law expression for eq (1) is combined with eq (3).

(2) The equilibrium concentrations of BH^+ and B are set equal to m_1 and m_2, respectively, in view of the fact that neither species is a strong enough acid or base to be appreciably solvolyzed.

(3) The variation of the activity coefficient term $f_{BH^+}f_{Cl^-}/f_B$ as a function of ionic strength is expressed by an equation of the Hückel form containing two parameters, a^* and β, and the Debye-Hückel constants, A and B [9].

(4) The ionic strength of each solution is equal to the molality of triethanolammonium chloride (m_1).

3. Procedures and Results

Hydrochloric acid of reagent grade was diluted to about 6N and distilled in an all-glass still; the middle third was collected and redistilled. The twice-distilled acid was diluted to form solutions of molality about 0.1. These stock solutions were standardized gravimetrically by the silver chloride method. Colorless triethanolamine of the best commercial grade was distilled three times in vacuum, the middle fraction of the distillate being retained. The purified product was assayed by titration with the standard solution of hydrochloric acid. The assay value was 100.07 percent of the theoretical figure.

The cell solutions were prepared either by: (1) Adding weighed quantities of the pure triethanolamine to a solution of hydrochloric acid, the molar quantity of amine being approximately twice the number of moles of hydrochloric acid present; or (2) diluting with distilled water solutions prepared in this manner. Before the cells were filled, dissolved air was removed from the buffer solutions by bubbling purified hydrogen through them. Precautions were taken to prevent changes of concentration from occurring as a result of the deaeration.

The solubility of silver chloride in the cell solutions was so low that separation of the electrode compartments and corrections for solubility [6] were unnecessary, as attested by the absence of a gray deposit of silver on the platinum electrode at the conclusion of a run. The temperature of the water bath was measured by a calibrated mercury-in-glass thermometer. It was known to $\pm 0.02°$ C.

The emf data were corrected in the usual manner to 1 atm partial pressure of gaseous hydrogen, and pwH was calculated by eq (3). Each value of pwH given in table 1 is the average of the results obtained from two hydrogen-silver chloride electrode combinations in the same cell. Values of $-\log K'_{bh}$ were calculated by eq (2) for several values of the parameter a^* and were plotted as a function of m_1. Straight-line plots were obtained at each temperature when $a^*=0$ was chosen, as shown in figure 1. The true $-\log K_{bh}$, the intercept of these lines at $m_1=0$, was obtained by the method of least squares.

The values of $-\log K_{bh}$ are summarized in table 2, together with the standard deviations (S.D.) of the intercepts. The last two columns of table 2 list $-\log K_b$ and K_b, where K_b is the basic dissociation constant of triethanolamine obtained from K_{bh} and K_w, the ion-product constant of water [7], by the formula

$$K_b = K_w/K_{bh}. \tag{4}$$

The value of $-\log K_{bh}$ at 25° C (7.762) is to be compared with 7.77 found by Hall and Sprinkle [4] and by Bates and Schwarzenbach [5].

TABLE 1. *pwH at 0° to 50° C for buffer solutions composed of triethanolammonium hydrochloride* (m_1) *and triethanolamine* (m_2)

m_1	m_2	0°	5°	10°	15°	20°	25°	30°	35°	40°	45°	50°
0.09909	0.10481	8.5764	8.4611	8.3569	8.2479	8.1453	8.0473	7.9494	7.8534	7.7615	7.6727	7.5848
.09908	.14403		8.5994	8.4912	8.3857	8.2832	8.1851					
.09908	.10765	8.5882	8.4722	8.3643	8.2589	8.1566	8.0604	7.9599	7.8665	7.7694	7.6784	7.5932
.09379	.09312	8.5408	8.4281	8.3184	8.2112	8.1079	8.0102	7.9113	7.8191	7.7257	7.6375	7.5431
.07923	.08381		8.4363	8.3297	8.2257	8.1239	8.0250	7.9281	7.8325	7.7402	7.6518	
.07896	.08578	8.5643	8.4460	8.3356	8.2319	8.1315	8.0353	7.9321	7.8357			
.07707	.07651	8.5166	8.4056	8.2979	8.1920	8.0911	7.9940	7.8950	7.7987	7.7059	7.6153	7.5286
.07522	.10934		8.5737	8.4641	8.3587	8.2563	8.1582					
.05928	.06440	8.5415	8.4219	8.3151	8.2109	8.1087	8.0097	7.9084	7.8184	7.7235	7.6340	7.5479
.05830	.06166	8.5240	8.4067	8.3001	8.1951	8.0938	7.9962	7.8967	7.8019	7.7089	7.6192	7.5304
.05215	.05178		8.3681	8.2606	8.1562	8.0559	7.9563	7.8612	7.7664			
.03952	.04294	8.5072	8.3905	8.2831	8.1799	8.0782	7.9787	7.8803	7.7889	7.6930	7.6041	7.5170
.03949	.04177	8.4897	8.3771	8.2706	8.1662	8.0651	7.9658	7.8686	7.7740	7.6813	7.5926	7.5054
.03797	.05520		8.5107	8.4044	8.3001	8.1979	8.1020	8.0022	7.9072	7.8162	7.7263	7.6422
.03039	.03018	8.4426	8.3290	8.2227	8.1188	8.0179	7.9192	7.8208	7.7270	7.6354	7.5459	7.4600
.019780	.02029	8.4423	8.3279	8.2214	8.1176	8.0161	7.9198	7.8210	7.7239	7.6358	7.5432	7.4546
.019283	.02095	8.4529	8.3367	8.2304	8.1269	8.0254	7.9279	7.8310	7.7396	7.6445	7.5557	7.4692
.009568	.010120	8.4033	8.2878	8.1857	8.0789	7.9779	7.8806	7.7846	7.6906	7.5992	7.5094	7.4237
.009541	.013869		8.4273	8.3212	8.2175	8.1146	8.0191					7.5560
.007774	.008223	8.3967	8.2796	8.1734	8.0697	7.9668	7.8710	7.7750	7.6793	7.5835	7.4974	7.4091
.005557	.005877	8.3841	8.2657	8.1599	8.0563	7.9556	7.8566	7.7623	7.6673	7.5752	7.4855	7.3964
.003869	.004092	8.3757	8.2584	8.1533	8.0497	7.9483	7.8469	7.7547	7.6586	7.5652	7.4740	7.3880

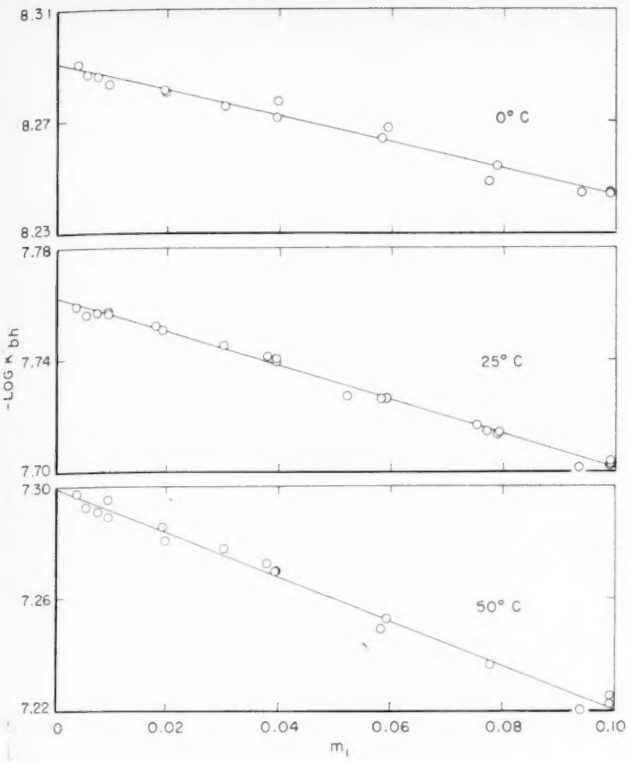

FIGURE 1. *Plots of* $-\log K'_{bh}$ *as a function of* m_1 *at 0°, 25°, and 50° C.*

TABLE 2. *Summary of values for* K_{bh} *and* K_b

t	$-\log K_{bh}$	*S.D.*	$K_{bh}\times 10^5$	$-\log K_b$	$K_b\times 10^7$
° C					
0	8.290_5	±0.0009	0.512	6.652	2.23
5	8.173_4	.0007	.671	6.561	2.75
10	8.067_4	.0009	.936	6.468	3.40
15	7.963_2	.0008	1.088	6.383	4.14
20	7.861_1	.0007	1.377	6.306	4.94
25	7.762_4	.0006	1.728	6.234	5.83
30	7.666_1	.0009	2.16	6.167	6.81
35	7.570_7	.0010	2.69	6.109	7.78
40	7.477_3	.0008	3.33	6.058	9.45
45	7.387_5	.0009	4.10	6.008	9.82
50	7.299_2	.0012	5.02	5.963	10.89

4. Thermodynamic Quantities

The values of $-\log K_{bh}$ given in Table 2 were fitted to an equation of the Harned-Robinson form [10] by the method of least squares. Between 0° and 50° C, K_{bh} is given by the expression

$$-\log K_{bh}=1341.16/T+4.6252-0.0045666\,T \qquad (5)$$

where T is the temperature in deg Kelvin. The average difference between the "observed" K_{bh} at the 11 temperatures and that calculated by eq (5) is 0.0009 unit.

The changes of Gibbs free energy ($\Delta G°$), of enthalpy ($\Delta H°$), of entropy ($\Delta S°$), and of heat capacity (ΔC_p°) for the dissociation of 1 mole of triethanolammonium ion in the standard state were computed from the constants of eq (5) by the following formulas:

$$\Delta G°=2.3026R(A+BT+CT^2), \qquad (6)$$

$$\Delta H°=2.3026R(A-CT^2), \qquad (7)$$

$$\Delta S°=2.3026R(-B-2CT), \qquad (8)$$

$$\Delta C_p^\circ=2.3026R(-2CT). \qquad (9)$$

The values of A, B, and C are, respectively, 1341.16, 4.6252, and −0.0045666. The results are summarized in Table 3. From the standard deviation of log K_{bh}, the uncertainties in the thermodynamic quantities at 25° C are estimated to be as follows: $\Delta G°$, 6 j mole^{-1}; $\Delta H°$, 100 j mole^{-1}; $\Delta S°$, 0.5 j deg^{-1}, mole $^{-1}$; and ΔC_p°, 5 j deg^{-1} mole^{-1}.

TABLE 3. *Thermodynamic quantities for the dissociation of 1 mole of triethanolammonium ion in the standard state*

t	$\Delta G°$	$\Delta H°$	$\Delta S°$	ΔC_p°
° C	*j mole*$^{-1}$	*j mole*$^{-1}$	*j deg*$^{-1}$ *mole*$^{-1}$	*j deg*$^{-1}$ *mole*$^{-1}$
0	43,340	32,200	−40.8	48
5	43,422	32,440	−39.9	49
10	43,740	32,690	−39.0	50
15	43,932	32,940	−38.2	50
20	44,121	33,190	−37.3	51
25	44,305	33,450	−36.4	52
30	44,485	33,710	−35.5	53
35	44,608	33,980	−34.7	54
40	44,832	34,250	−33.8	55
45	44,999	34,530	−32.9	56
50	45,161	34,810	−32.0	56

5. Discussion

The strengths of acids and bases are influenced by polar (inductive) and resonance effects within the molecule, by the possibility of internal hydrogen bonding, and steric factors. It is, however, difficult to impede the addition or removal of a proton by the addition of bulky groups to the molecule. Furthermore, resonance and intramolecular hydrogen bonding do not usually play an important role in the dissociation of the simple aliphatic substituted ammonias. In the Lewis concept, the strength of nitrogen bases is a measure of the availability of a donor electron pair, and the effect of polar substituent groups on the basic strength can sometimes be satisfactorily accounted for in a qualitative way by inductive influences. The electron-attracting properties of the hydroxyl group are no doubt largely responsible for the fact that the ethanolamines are weaker bases than the corresponding ethylamines.

The dissociation of a weak base or acid is, however, fundamentally a protolytic process involving both the acid (or base) in question and the solvent as well. It is quite understandable, therefore, that the extent to which such a reaction proceeds should depend not only on the intrinsic acidic or basic strengths of the two reacting species but also upon other factors which

either limit or enhance the probability that the reacting species will approach so closely that reaction is favored. In this connection, it is well to bear in mind that solvation may well be the initial stage of acidic or basic dissociation. Entirely apart from electronic effects, therefore, dissociation in water may be favored or hindered by the size and shape of the acid or base molecule (steric factors) and by its hydrophilic or hydrophobic character (chemical factors).

When a monobasic cationic acid such as triethanolammonium (BH^+) dissociates, the process is perhaps best regarded as the separation of solvated BH^+ ions into free amine and hydronium ions (H_3O^+). Inasmuch as the amine is uncharged it is presumably not highly effective in orienting the polar water molecules. Hence, the degree of solvation may be strongly influenced by steric and chemical factors which are relatively unimportant with charged species. In the dissociation process water molecules may therefore be released from combination.

These effects are likely to be reflected in the values of the entropy and heat-capacity changes for the dissociation process; release of water molecules should result in an increase of entropy and heat capacity. Any factor, steric or hydrophobic for example, tending to exclude solvent molecules and reduce solvation of the free amine would therefore be expected to make the entropy and heat capacity changes for the process more positive (less negative).

Considerations of this sort led Everett and Wynne-Jones [3] to ascribe the positive heat-capacity change in the dissociation of the methyl-substituted ammonium ions (as compared with $\Delta C_p^\circ = 0$ for ammonium ion [3, 6] to the hydrophobic character of alkyl groups. For the dissociation of monoethanolammonium ion, ΔC_p° is about -5 j deg^{-1} mole^{-1} [1] and for diethanolammonium ion about $+49$ j deg^{-1} mole^{-1} [2], as compared with $+52$ j deg^{-1} mole^{-1} given in table 3 for triethanolammonium ion. These results suggest that increasing substitution of ethanol groups into ammonia has two effects, namely (1) progressively decreasing hydrophobic character (tending to lower ΔC_p°), and (2) progressively greater steric hindrance (tending to raise ΔC_p° by exclusion of solvent). Likewise, a contrary variation of the entropy change and the heat-capacity change, although observed heretofore, has not, to the authors knowledge, yet been satisfactorily explained. A more illuminating comparison than this one could doubtless be made between the ethanolamines and the corresponding ethyl amines, but unfortunately the heat-capacity data needed are unavailable.

6. References

[1] R. G. Bates and G. D. Pinching, J. Research NBS **46,** 349 (1951) RP2205.

[2] V. E. Bower, R. A. Robinson, and R. G. Bates, to be published.

[3] D. H. Everett and W. F. K. Wynne-Jones, Proc. Roy Soc. (London) **169A,** 190 (1938; also **177A,** 499 (1941).

[4] N. F. Hall and M. R. Sprinkle, J. Am. Chem. Soc. **54,** 3469 (1932).

[5] R. G. Bates and G. Schwarzenbach, Helv. Chim. Acta **37,** 1437 (1954).

[6] R. G. Bates and G. D. Pinching, J. Research NBS **42,** 419 (1949) RP1982.

[7] H. S. Harned and B. B. Owen, The physical chemistry of electrolytic solutions, 3d ed. (Reinhold Publishing Corp., New York, N.Y. (1958).

[8] R. G. Bates and V. E. Bower, J. Research NBS **53,** 283 (1954).

[9] R. A. Robinson and R. H. Stokes, Electrolyte solutions, 2d ed., app. 7.1 (Academic Press, New York, N.Y. (1959).

[10] H. S. Harned and R. A. Robinson, Trans. Faraday Soc **36,** 973 (1940).

WASHINGTON, D.C. (Paper 64A4–56)

JOURNAL OF RESEARCH of the National Bureau of Standards—A. Physics and Chemistry
Vol. 64A, No. 4, July–August 1960

Ionization Constants of Four Dinitrophenols in Water at 25 °C

Robert A. Robinson,[1] Marion Maclean Davis, Maya Paabo, and Vincent E. Bower

(February 19, 1960)

Thermodynamic ionization constants of 2,3-, 2,5-, 3,4-, and 3,5-dinitrophenols in aqueous solution at 25° C have been determined by a spectrophotometric method. The respective values found, expressed as pK, are 4.95_9, 5.21_0, 5.42_2, and 6.69_2. pK has also been determined potentiometrically for 2,3- and 3,5-dinitrophenols; the respective values obtained are 4.98 and 6.66. The experimental pK values for all six dinitrophenols are lower than the calculated values based on pK data for phenol and the mononitrophenols.

Spectral absorption curves are presented for the ionized and unionized forms of the four dinitrophenols.

1. Introduction

"Concentration" ionization constants of the six dinitrophenols were determined by Holleman and Wilhelmy [1],[2] and thermodynamic ionization constants have since been determined for all but the 2, 3- and 3,5-isomers. Only the 2,4- and 2,6-isomers are readily obtained commercially at the present time. The remaining isomers were synthesized in this laboratory for a study of the comparative acidic behavior of the six dinitrophenols in benzene.[3] The same materials were used for the work reported in this paper; namely, the determination of thermodynamic pK values for the 2,3- and 3,5-isomers and redetermination of thermodynamic pK values for the 2,5- and 3,4-isomers.

2. Experimental Procedure

2.1. Materials

3,5-Dinitrophenol was made by converting 1,3,5-trinitrobenzene to 3,5-dinitroanisole [1, 2] and then demethylating [3]. The product was recrystallized from water as the dihydrate; this was dehydrated overnight in a vacuum oven, then recrystallized from benzene-cyclohexane and dried at 90° for one hour (mp, 124.3 to 125.0° C).

2,3-, *2,5-*, and *3,4-Dinitrophenols* were prepared simultaneously by nitrating *m*-nitrophenol and then were separated by fractional crystallizations [1, 4]. Finally, each compound was recrystallized twice from the solvent indicated: 2,3-Dinitrophenol (from water), mp 146.5 to 147.0° C; 2,5-dinitrophenol (from 95% ethanol), mp 105.8 to 106.2° C; 3,4-dinitrophenol (from benzene), mp 135.1 to 135.5° C.

Potentiometric weight titrations for 2,3-dinitrophenol and for 3,5-dinitrophenol indicated a purity of not less than 99.8 percent.

2.2. Determination of pK values

The *spectrophotometric procedure* followed in determining the pK values was devised by Robinson and coworkers [5] in a research program one objective of which is to test the applicability of Hammett's equation [6] to substituted phenols.

The pK of the dinitrophenol was calculated from the equation

$$p\mathrm{K}=p\mathrm{H}-\log[(D-D_1)/(D_2-D)]-\log\gamma_{R^-}-\Delta p\mathrm{H}. \quad (1)$$

The spectrophotometric data (see second term on right side of eq (1)) were obtained at 25.0±0.1° C with a Beckman Model DU quartz spectrophotometer, using optical absorption cells 1 cm in length. The symbols D_1, D_2, and D signify the spectral absorbances (optical densities) of solutions containing the same total molar concentration of dinitrophenol present as unionized molecules, phenolate ions, or mixtures of the two, respectively. In measuring the limiting spectral absorbances, the dinitrophenol was dissolved in aqueous hydrochloric acid of $p\mathrm{H}\approx 2$ (for D_1 values) or in aqueous sodium hydroxide of $p\mathrm{H}\approx 12$ (for D_2 values). Measurements of D were made for at least three differently buffered solutions having known pH values which were close to the expected pK value of the dinitrophenol. The absorbances were measured at two or three wavelengths. Phosphate buffer mixtures [7] were used in determining the pK of 3,5-dinitrophenol, and succinate buffer mixtures [8] were used for the remaining dinitrophenols. The compositions and pH values of buffers used are given in tables 2 and 3.

The following modification of Davies' equation [9] was used to calculate γ_{R^-}, the activity coefficient of the phenolate ion:[4]

$$-\log\gamma_{R^-}=A\sqrt{I}/(1+\sqrt{I})-0.2\,I. \quad (2)$$

The final term in eq (1), ΔpH, is a correction applied because the addition of the phenol to the buffer mixtures causes some changes in the pH of

[1] Consultant to the Chemistry Division. Present address: University of New England, Armidale, New South Wales, Australia.
[2] Figures in brackets indicate the literature references at the end of this paper.
[3] M. M. Davis and M. Paabo, work in progress.

[4] The modification consists of substituting 0.2 I for 0.1 I [5]. I symbolizes the ionic strength. The value for the parameter A in the Debye-Hückel-Onsager equation has been recomputed because a more accurate value for the dielectric constant of water is available. The value of A adopted earlier [10] was 0.509; the new value is 0.5115 [11].

the solution, a change which becomes more important as the buffer becomes more dilute [12]. This correction can be put in the form

$$\Delta p\mathrm{H} \approx 0.4343[m_3/(m_1+m_2)]\ (K/K_R) \times[(K_R+h)^2/(K+h)h], \quad (3)$$

where m_1 and m_2 are the molalities of the buffer salts, m_3 is that of the phenol, h is the hydrogen ion concentration, K_R is the ionization constant of the acid of the buffer, and K is the ionization constant of the phenol.

In the *potentiometric determination of* pK for 2,3- and 3,5-dinitrophenols, a 100-ml portion of 0.01-M aqueous solution of each compound was titrated at 25° ± 1° C with 0.1-M sodium hydroxide. The potential was measured between glass and saturated calomel electrodes [13].

Values of pK were computed from the equation

$$p\mathrm{K} = p\mathrm{H} - \log\{([\mathrm{B}^-]+[\mathrm{H}^+])/([HB]-[H^+])\} + \{(0.5115\sqrt{I})/(1+1.5\sqrt{I})\}. \quad (4)$$

The pK value obtained for 2,3-dinitrophenol was 4.98 ± 0.005, and the pK value for 3,5-dinitrophenol was 6.66 ± 0.001.

3. Results and Discussion

Molar absorption curves for the dinitrophenols in aqueous acid and alkali are presented in figures 1 to 3. Optical constants are summarized in table 1.

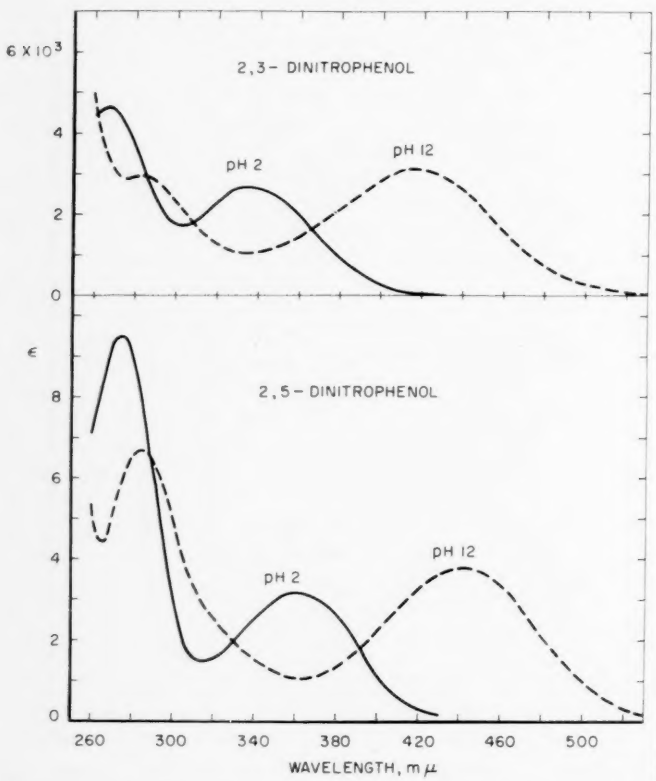

FIGURE 1. *Absorption spectra of 2,3-dinitrophenol and 2,5-dinitrophenol in aqueous acid* ($p\mathrm{H} \approx 2$) *and alkali* ($p\mathrm{H} \approx 12$).

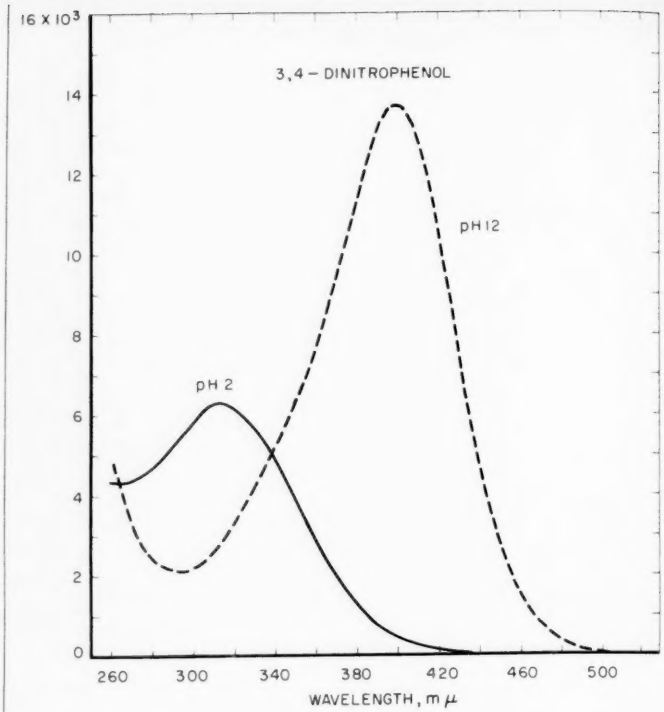

FIGURE 2. *Absorption spectra of 3,4-dinitrophenol in aqueous acid* ($p\mathrm{H} \approx 2$) *and alkali* ($p\mathrm{H} \approx 12$).

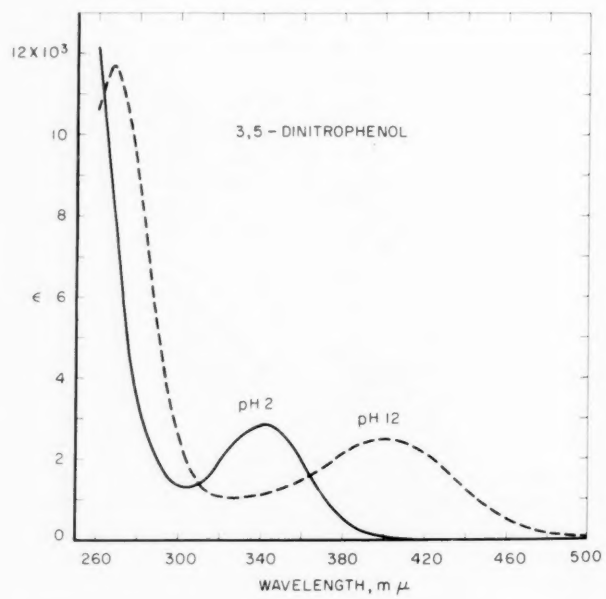

FIGURE 3. *Absorption spectra of 3,5-dinitrophenol in aqueous acid* ($p\mathrm{H} \approx 2$) *and alkali* ($p\mathrm{H} \approx 12$.)

TABLE 1. *Optical constants of dinitrophenols in aqueous acid and alkali*

Compound	Absorption bands				Isosbestic points	
	pH=2		pH=12			
	λ_{max} mμ	ϵ_{max}	λ_{max} mμ	ϵ_{max}	λmμ	ε
2,3-Dinitrophenol	265	4620	282	2930	261	4500
	335	2700	416	[a] 3130	285	2950
					308	1800
					366	1700
2,5-Dinitrophenol	275	9500	285	6700	288	6550
	360	3150	440	[a] 3770	330	2000
					392	1800
3,4-Dinitrophenol	315	6300	400	[a] 13700	264	4300
					338	5000
3,5-Dinitrophenol	343	2900	268	11700	262	11000
			400	[a] 2480	310	1400
					364	1600

[a] G. Kortüm, Z. physik. Chem. **B42,** 39 (1939), reported values in good agreement with these results in the cases of 2,3-dinitrophenol (3160) and 3,5-dinitrophenol (2450), but not in the cases of 2,5-dinitrophenol (4170) or 3,4-dinitrophenol (5250). (See table on p. 64 of ref. cited.)

Data and results for the ionization constants by the spectrophotometric procedure are summarized in tables 2 and 3.

TABLE 2. *Ionization constant of 3,5-dinitrophenol in water at 25° C*

Ionic strength [a]	pH	$-\log \gamma_B^-$	D [b]	$\log \frac{D-D_1}{D_2-D}$	pK	pK (corr.)
	λ=400 mμ D_1=0.037, D_2=1.341					
0.2	6.772	0.118	0.830	0.191	6.699	6.693
.1	6.860	.103	.879	.260	6.703	6.691
.08	6.886	.097	.886	.271	6.712	6.696
.04	6.959	.077	.917	.318	6.718	6.686
.02	7.018	.059	.924	.328	6.749	6.687
	λ=410 mμ D_1=0.017, D_2=1.298					
0.2	6.772	0.118	0.793	0.187	6.704	6.698
.1	6.860	.103	.839	.252	6.711	6.699
.08	6.886	.097	.851	.271	6.712	6.696
.04	6.959	.077	.883	.321	6.716	6.684
.02	7.018	.059	.889	.329	6.748	6.686
Avg						6.69_2
						$K=2.03\times10^{-7}$

[a] The molar concentration of 3,5-dinitrophenol was 5.4×10^{-4}. The buffer solutions contained equimolar KH_2PO_4 and Na_2HPO_4.

[b] The optical absorption cells were 1 cm in length. D_1 and D_2 symbolize, respectively, the spectral absorbance (optical density) of the unionized phenol and the phenol anion, and D, that of a solution containing a mixture of the two.

TABLE 3. *Ionization constants of 2,3-, 2,5-, and 3,4-dinitrophenols in water at 25° C* [a]

Buffer mixture No. [b]	2,3-Dinitrophenol 2.17×10^{-4} M				2,5-Dinitrophenol 1.13×10^{-4} M				3,4-Dinitrophenol 6.8×10^{-5} M			
	D	$\log \frac{D-D_1}{D_2-D}$	pK	pK (corr.)	D	$\log \frac{D-D_1}{D_2-D}$	pK	pK (corr.)	D	$\log \frac{D-D_1}{D_2-D}$	pK	pK (corr.)
	λ=410 mμ D_1=0.019, D_2=0.671				λ=430 mμ D_1=0.010, D_2=0.414				λ=400 mμ D_1=0.023, D_2=0.930			
1	0.513	0.496	4.965	4.962	0.270	0.260	5.201	5.200	0.495	0.035	5.426	5.425
2	.524	.535	4.971	4.966	.276	.287	5.218	5.215	.519	.082	5.424	5.422
3	.534	.576	4.976	4.963	.286	.335	5.216	5.209	.548	.138	5.413	5.409
	λ=420 mμ D_1=0.009, D_2=0.676				λ=440 mμ D_1=0.005, D_2=0.426				λ=410 mμ D_1=0.011, D_2=0.866			
1	0.517	0.504	4.957	4.954	0.275	0.252	5.209	5.208	0.456	0.035	5.426	5.425
2	.527	.540	4.966	4.961	.284	.291	5.215	5.212	.474	.072	5.434	5.432
3	.536	.577	4.974	4.961	.291	.326	5.225	5.218	.500	.126	5.425	5.421
	λ=430 mμ D_1=0.005, D_2=0.632				Avg			5.21_0	Avg			5.42_2
								$K=6.17\times10^{-6}$				$K=3.78\times10^{-6}$
1	0.483	0.506	4.955	4.952								
2	.493	.546	4.960	4.955								
3	.501	.580	4.971	4.958								
	Avg			4.95_9								
				$K=1.10\times10^{-5}$								

[a] Optical absorption cells 1 cm in length were used throughout. D_1 and D_2 signify, respectively, the spectral absorbance (optical density) of the unionized phenol and the phenol anion, and D symbolizes the absorbance of a solution containing both unionized and ionized phenol.

[b] Buffer mixtures Nos. 1, 2, and 3 were mixtures of x-molar sodium hydrogen succinate and x-molar disodium succinate, where x=0.05, 0.025, and 0.01, respectively. The pH values of these buffer mixtures were 5.343, 5.403, and 5.474, respectively.

In table 4, the pK values obtained in this work by the spectrophotometric method are compared with earlier experimental values. pK values for 2,4- and 2,6-dinitrophenols are included in table 4.

TABLE 4. p*K values of dinitrophenols in water at 25° C*

Dinitrophenol	pK, calc [a]	pK, experimental				ΔpK [e]
		This work	Earlier work [b]			
2,3-	5.61	*4.96	4.89 [d]			−0.65
2,4-	4.36		4.00 [d]	4.09 [c]	*4.11 [f]	−.25
2,5-	5.61	*5.21	5.15 [d]	5.22 [g]		−.40
2,6-	4.42		3.57 [d]	*3.71 [b,i]		−.71
3,4-	5.55	*5.42	5.37 [d]	5.42 [g]		−.13
3,5-	6.80	*6.69	6.68 [d]			−.11

[a] Based on the following pK values: Phenol, 9.998; *o*-nitrophenol, 7.210; *m*-nitrophenol, 8.399; *p*-nitrophenol, 7.149. See R. A. Robinson and A. I. Biggs, Trans. Faraday Soc. **51,** 901 (1955); A.I. Biggs, Trans. Faraday Soc. **52,** 35 (1956).

[b] pK values determined at other temperatures are in general harmony with the values cited in this table. For example, L. Michaelis and A. Gyemant, Biochem. Z. **109,** 165 (1920); L. Michaelis and R. Krüger, Biochem. Z. **119,** 307 (1921); R. Riccardi and P. Franzosini, Boll. sci. fac. chim. ind., Bologna **15,** 25 (1957).

[c] $\Delta pK = {}^*pK_{\text{exptl.}} - pK_{\text{calc.}}$

[d] A. F. Holleman and G. Wilhelmy, Rec. trav. chim. **21,** 432 (1902). (R. Bader, Z. physik. Chem. **6,** 289 (1890), determined ionization constants for all of the dinitrophenols except 3,5-dinitrophenol, but only very approximately.)

[e] H. von Halban and G. Kortüm, Z. physik. Chem. **A170,** 351 (1934); see also W. D. Bale and C. B. Monk, Trans. Faraday Soc. **53,** 450 (1957).

[f] R. G. Bates and G. Schwarzenbach, Helv. chim. acta **37,** 1069 (1954).

[g] C. M. Judson and M. Kilpatrick, J. Am. Chem. Soc. **71,** 3110 (1949).

[h] G. Kortüm and H. Wilski, Z. physik. Chem. **2,** 256 (1954); earlier unpublished work of M. Kortüm-Seiler yielding the same result by a different method is cited.

[i] J. F. J. Dippy, S. R. C. Hughes, and J. W. Laxton, J. Chem. Soc. (London) **1956,** 2995.

It is evident that the thermodynamic ionization constants, expressed in pK units, agree well in general magnitude with the corresponding "concentration" ionization constants [1], but the thermodynamic values are from 0.01 to 0.14 pK unit higher. Our pK values for the 2,5- and 3,4-isomers are in excellent agreement with the results of Judson and Kilpatrick (table 4, footnote *g*).

Values of pK for all six dinitrophenols can be calculated from pK data for phenol itself and for the monosubstituted nitrophenols, using the assumption of additivity (see table 4). The experimental pK values are all lower than the calculated values, in agreement with an analogous conclusion of Holleman and Wilhelmy [1]. The disagreement is particularly marked in the case of dinitrophenols substituted in the 2-position.

4. References

[1] A. F. Holleman and G. Wilhelmy, Rec. trav. chim. **21,** 432 (1902).

[2] C. A. Lobry de Bruyn, Rec. trav. chim. **9,** 208 (1890).

[3] A. Hantzsch, Ber. deut. chem. Ges. **40,** 330 (1907).

[4] N. V. Sidgwick and W. M. Aldous, J. Chem. Soc. (London) **119,** 1001 (1921).

[5] (a) R. A. Robinson and A. I. Biggs, Trans. Faraday Soc. **51,** 901 (1955).
(b) R. A. Robinson, Ionization constants of weak acids from spectrophotometric measurements, ch. 16 in The structure of electrolytic solutions, W. J. Hamer, ed. (John Wiley & Sons, Inc., New York, N.Y., 1959).

[6] (a) L. P. Hammett, J. Am. Chem. Soc. **59,** 96 (1937).
(b) L. P. Hammett, Physical organic chemistry, ch. VII (McGraw-Hill Book Co., Inc., New York, N.Y., 1940).

[7] R. G. Bates and S. F. Acree, J. Research NBS **34,** 373 (1945) RP1648.

[8] R. G. Bates, G. D. Pinching, and E. R. Smith, J. Research NBS **45,** 418 (1950) RP2153.

[9] C. W. Davies, J. Chem. Soc. (London) **1938,** 2093.

[10] G. G. Manov, R. G. Bates, W. J. Hamer, and S. F. Acree, J. Am. Chem. Soc. **65,** 1765 (1943).

[11] R. A. Robinson and R. H. Stokes, Electrolyte solutions, app. 7.1, p. 468 (Academic Press, Inc., New York, N.Y., 2d ed., 1959).

[12] R. A. Robinson and A. K. Kiang, Trans. Faraday Soc. **51,** 1398 (1955).

[13] M. M. Davis and H. B. Hetzer, J. Phys. Chem. **61,** 123 (1957).

WASHINGTON, D.C. (Paper 64A4–57)

JOURNAL OF RESEARCH of the National Bureau of Standards—A. Physics and Chemistry
Vol. 64A, No. 4, July–August 1960

Dissociation Constant of Anisic (*p*-Methoxybenzoic) Acid in the System Ethanol-Water at 25 °C

Elizabeth E. Sager and Vincent E. Bower

(March 1, 1960)

The dissociation constant of anisic (*p*-methoxybenzoic) acid in the system ethanol-water was measured at 25° C by a combination of spectrophotometric and electrometric methods. Percentage by weight of ethanol in the solvent system varied from zero to 83.43. The value of K varied correspondingly from 3.22×10^{-5} ($pK=4.492$) to 3.34×10^{-8} ($pK=7.476$).

1. Introduction

A new phase in the technique of measuring dissociation constants of weak acids dates from 1932 when Harned and Ehlers [1] used[1] measurements of the cell Pt; H_2(g, 1 atm), CH_3 COOH (m_1), CH_3 COONa (m_2), NaCl (m_3), AgCl (s); Ag to determine the dissociation constants of acetic acid from 0° to 60° C. In the same year MacInnes and Shedlovsky [2] used conductance measurements to determine the dissociation constant of this acid at 25° C. Since then an immense body of factual information has become available on the dissociation constants of weak acids in aqueous solution. In many instances the variation of the dissociation constant with temperature has been studied. The field of nonaqueous solutions and of mixed solvents with water as one component has, however, been comparatively neglected. The dissociation constant of acetic acid has been measured in 20, 45, 70, and 82 percent dioxane [3 to 6]; in 10 percent and 20 percent methanol [7]; in 50 percent glycerol [8]; and, more recently, over the 0 to 100 percent range of water-methanol system [9]. Again, the dissociation constants of the ammonium and the methylammonium ions have been measured in 60 percent methanol [10]. Other examples could be noted, but they are few compared with the number of determinations that have been made in aqueous solution.

As a contribution to this field, measurements on anisic acid (*p*-methoxybenzoic acid) in the ethanol-water system are now reported. This acid was selected because it is available in a state of high purity, and its dissociation constant in water ($pK_a=4.471$ at 25° C) has already been measured [11]. Moreover, there are data in the literature for a buffer system in ethanol-water mixtures in this dissociation range [12].

[1] Figures in brackets indicate the literature references at the end of this paper.

2. Experimental Procedure

2.1. Materials

Anisic acid, NBS Standard Sample No. 142, was used without further purification. The white, powdered material is sparingly soluble in water, and an original stock solution, about $2\times10^{-2}M$, was made by dissolving a weighed amount in 95 percent ethanol and warming the resulting solution in a water-bath. A second stock solution was prepared for each series by diluting 5 ml of the original solution to 100 ml with water.

Hydrochloric acid of reagent grade was used to control the hydrogen-ion concentration of the solutions employed to determine the limiting spectrophotometric curves of the anisic acid. Standardized sodium hydroxide, free from carbonate, was used to transform the acid completely to the salt. Purified sodium acetate (hydrate) was employed for the acetate buffers. A 1-M stock solution was prepared from which dilutions were made by volumetric procedures. Glacial acetic acid was used to prepare a 1-M stock solution, of which varying small amounts ½ to 4 ml, were used to change the buffer ratio, while keeping the acetate constant. Thus the ratio of the anisic acid to its salt could be measured spectrophotometrically.

Potassium chloride, recrystallized three times from water and dried at 110° C, was used to make all solutions 5×10^{-3} M with respect to chloride for the electromotive force measurements.

The ethanol was tested for impurities and met ACS specifications. Conductivity water was used throughout for all preparations.

2.2. Equipment

A Beckman DU spectrophotometer equipped with a water-jacketed cell compartment was used for the spectrophotometric measurements. The temperature was controlled at 25° C within ±0.05° C. Cylindri-

cal 1-cm absorption cells with removable quartz endplates were used throughout.

Electromotive force measurements of the following cell without liquid junction were made for each ethanol-water mixture.

$$\text{Pt; } H_2(1 \text{ atm}), \text{HA } (m_1), \text{NaA } (m_2),$$

$$\text{KCl } (0.005\ m), \text{AgCl(s); Ag} \qquad \text{(A)}$$

The cell was a simplified version, much reduced in size, of that described by Bates [13, 14]. The volume of the cell is only 10 ml and the solution is therefore quickly saturated with hydrogen. Data required for the correction of the electromotive force of the cells to 1 atm partial pressure of hydrogen were calculated from values of the vapor pressures of alcohol-water system given in International Critical Tables [15].

3. Calculation of Dissociation Constants From Spectral Absorbance Data and Electromotive Force Measurements

3.1. Absorbance Measurements

Anisic acid shows well-defined absorbance in the ultraviolet. When the acid is transformed to the salt the absorbance shifts to lower wavelengths. The shift, however, is a small one and consequently absorbance values must be read from curves of very steep slope for making the calculations. Also, when alcohol is introduced into the water system, there is a slight hypsochromic effect, both bands for the acid and for the salt shifting toward lower wavelengths. Therefore it was necessary to determine carefully the so-called "limiting" curves which represent the transformation to all acid or to all salt in ethanol-water mixtures. For each series a slightly different isosbestic point exists; thus, the complete spectrum was examined for behavior and stability of each system by extensive measurements throughout the ultraviolet.

The reaction may be simply represented as the acid dissociating to the ions, namely,

$$HA \rightleftharpoons [H^+] + [A^-].$$

According to the law of absorption, at any given wavelength,

$$\text{Molar absorbance} = A/(bM), \qquad (1)$$

in which A is the absorbance of the sample (−log transmittancy), b is the depth of solution in centimeters through which the radiant energy passes, and M is the molar concentration of the absorbing compound. Molar absorbance is expressed in liters mole^{-1} cm^{-1}.

The values of molar absorbance of anisic acid and its sodium salt are shown in figure 1, the solid lines 1 and 2 representing the compound in water, and the broken lines 3 and 4 representing the material in 83.43 percent by weight of ethanol.

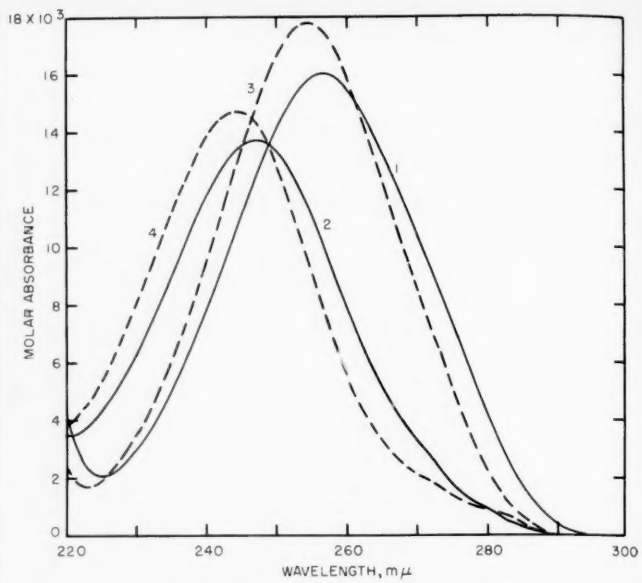

FIGURE 1. *The limiting curves of anisic acid and its salt in water (curves 1, 2) and in 83.43 percent by weight ethanol (curves 3, 4).*

In water the acid shows maximum molar absorbance of about 16,000 liters mole^{-1} cm^{-1} at a wavelength of 257 mμ and the salt shows a maximum of about 13,000 liters mole^{-1} cm^{-1} at 247 mμ. The two species have the same absorption at 249 mμ, the isosbestic point. In 83.43 percent ethanol by weight, the maximum molar absorbance of the acid increases to 17,800 liters mole^{-1} cm^{-1}, at 254.6 mμ, while the maximum of the salt increases to 14,700 liters mole^{-1} cm^{-1}, at 244.2 mμ, with the isosbestic point at 246.4 mμ. Figure 2 shows the series of curves for different degrees of dissociation of anisic

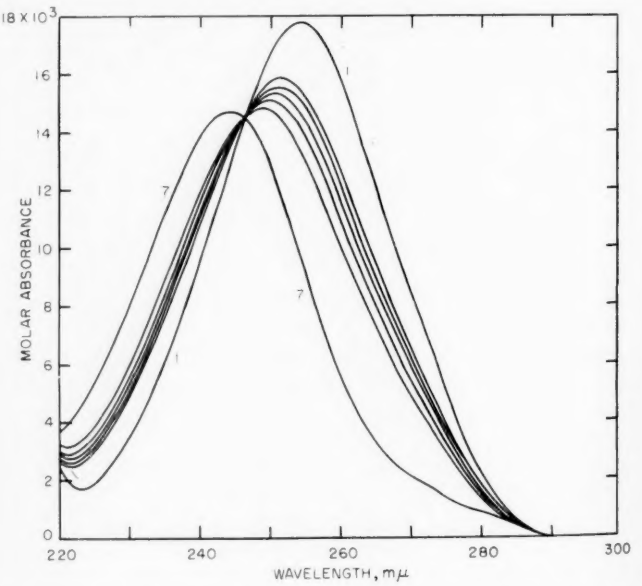

FIGURE 2. *Spectrophotometric curves representing the dissociation of anisic acid in 83.43 percent ethanol by weight.*

Curve 1, Anisic acid; curve 7, the sodium salt.

acid in 83.43 percent ethanol by weight. It is typical of the other series studied, but in the illustrated series the slopes of the curves are steeper and therefore involve greater experimental errors than in the other series. All series exhibited well-defined isosbestic points.

3.2. Calculation of Ratio of Salt to Acid

In any given series, the amounts of undissociated acid and of the salt are proportional to their respective absorbance values. If α represents the amount of salt, then at any step in the dissociation,

$$\alpha=\frac{A_{HA}-A}{A_{HA}-A_{A^-}}, \tag{2}$$

in which A with appropriate subscripts represents the absorbance of the acid, the absorbance of the partially dissociated acid, and the absorbance of the salt. The ratio $\alpha/(1-\alpha)$ may be calculated directly, but when the absorbance values are taken from such steep curves where experimental errors are large, it is wise to examine the α values at several wavelengths so that any trend in the values or influence of the buffering system may be determined. For this reason an average α at 16 wavelengths was used and the ratio $\alpha/(1-\alpha)$ calculated afterwards.

3.3. Calculation of *p*K

After the spectrophotometric observations were completed, each solution and its companion buffer solution were measured by electromotive force methods.

The pK of anisic acid on the thermodynamic scale is given by

$$p\mathrm{K}=-\log[\mathrm{H}^+]-\log\frac{\alpha}{1-\alpha}-\log\frac{\gamma_{A^-}}{\gamma_{HA}}, \tag{3}$$

where γ represents the activity coefficient of the ionic or molecular species denoted by the subscripts. For a cell of type A

$$-\log[\mathrm{H}^+]\gamma_H\gamma_{Cl}=(E-E^\circ)/(2.303RT/F)+\log m_{Cl}+\log\gamma_{Cl}, \tag{4}$$

where R, T, and F are, respectively, the gas constant, the absolute temperature, and the faraday, and where E° is the standard potential of the silver-silver chloride electrode in the particular alcohol-water system [16].

By combination,

$$p\mathrm{K}=pw\mathrm{H}-\log\frac{\alpha}{1-\alpha}-\log\frac{\gamma_{A^-}}{\gamma_{Cl^-}\gamma_{HA}}, \tag{5}$$

which is essentially the method of calculation employed by Bates and Schwarzenbach [17]. Inasmuch as the last term of eq (5) is approximately zero at low and moderate ionic strengths eq (5) simplifies to

$$p\mathrm{K}_a\approx pw\mathrm{H}-\log\frac{\alpha}{1-\alpha}. \tag{6}$$

The calculations of the dissociation constant of anisic acid in water and in nine ethanol-water mixtures are shown in table 1. In column 1 the weight percent of ethanol is given and in column 2 the average α for each solution as determined by the spectrophotometric measurements. Values of log $\alpha/(1-\alpha)$ are in column 3 and values of pwH, from electromotive force measurements, are listed in column 4. From columns 3 and 4 the pK of anisic acid is derived as shown in column 5 with the average for each series in column 6. As the dielectric constant of each mixture decreases, the value of pK increases as the ethanol content increases.

It was not our intention to determine the dissociation constants of acetic acid in the ethanol-water system since it has already been reported [1]. The ratio of acetate to acetic acid was known from the volumetric preparation of the buffer systems, but because the amounts of acetate and acetic acid added by pipet are small, the experimental error is expected to be large. Electromotive force measurements were made on the buffering solutions with and without anisic acid. At the concentrations used, the anisic acid had no observable effect upon pwH. From the *emf* measurements, then, the pK of acetic acid could be calculated according to the relation:

$$p\mathrm{K}=pw\mathrm{H}-\log\frac{\text{salt}}{\text{acid}} \tag{7}$$

The buffer ratios are shown in column 7 with the corresponding values of $-$log (salt/acid) in column 8. The pK values of acetic acid in the same series of ethanol-water system are given in column 9 and averaged in column 10. Our data show slightly higher values than those found by Grunwald and Berkowitz, but it should be noted that the values for both anisic acid and for acetic acid in water are in reasonable agreement with published values.

To test the validity of eq 7, by which Bates and Schwarzenbach found that $p\mathrm{K}_a$ was independent of ionic strength in the case of a buffering system of this charge type, several experiments were made using equimolar solutions of acetate-acetic acid buffer at 0.015, 0.025, and 0.055 ionic strengths in several ethanol-water mixtures. The resulting absorbance curves were the same within the experimental error, and the pwH values also agreed within the experimental error. The fact that $p\mathrm{K}_a$ remains constant, as the ionic strength is varied, suggests the soundness of the assumption that log γ_{Cl^-} and log γ_{A^-} are representable by the same function. It also reveals the use of the acidity function pwH in combination with spectrophotometric measurements to be the valid and promising method that Bates and Schwarzenbach contend it to be.

TABLE 1. *Dissociation of anisic acid in ethanol-water systems with acetic acid-sodium acetate buffers*

Wt. % ethanol	Averaged α in %	$\log \alpha/(1-\alpha)$	*pw*H	*p*K of Anisic acid, (*pw*H-log $\alpha/(1-\alpha)$)	Average *p*K	Buffer ratio, $\frac{\text{salt}}{\text{acid}}$	Log $\frac{\text{salt}}{\text{acid}}$	*p*K of acetic acid (*pw*H-log salt/acid)	Average *p*K
0.00	48.2	−0.032	4.456	4.488		0.02/.04	−0.301	4.757	
	54.9	.085	4.590	4.505		.02/.03	−.176	4.766	
	65.1	.270	4.760	4.490		.01/.01	.000	4.760	
	65.3	.274	4.762	4.488		.02/.02	.000	4.762	
	65.0	.268	4.762	4.494		.05/.05	.000	4.762	
	79.0	.575	5.063	4.488	4.492	.02/.01	.301	4.762	4.762
7.64	53.0	.051	4.706	4.655		.02/.03	−.176	4.882	
	57.1	.124	4.799	4.675		.02/.025	−.097	4.896	
	62.3	.218	4.873	4.655		.02/.02	.000	4.873	
	76.7	.517	5.152	4.635	4.655	.02/.01	.301	4.851	4.874
15.43	42.1	−.139	4.712	4.851		.02/.04	−.301	5.013	
	49.1	−.016	4.836	4.852		.02/.03	−.176	5.012	
	59.2	.161	5.013	4.852		.02/.02	.000	5.013	
	74.4	.463	5.304	4.841	4.849	.02/.01	.301	5.003	5.010
23.28	40.7	−.164	4.991	5.155		.02/.03	−.176	5.167	
	45.5	−.079	5.065	5.144		.02/.025	−.097	5.162	
	51.9	.033	5.165	5.132		.02/.02	.000	5.165	
	58.3	.145	5.283	5.138		.02/.015	.124	5.159	
	67.1	.309	5.466	5.157	5.145	.02/.01	.301	5.165	5.163
31.58	30.2	−.365	5.048	5.413		.02/.04	−.301	5.349	
	36.0	−.251	5.169	5.420		.02/.03	−.176	5.345	
	46.2	−.067	5.352	5.419		.02/.02	.000	5.352	
	62.3	.218	5.652	5.434		.02/.01	.301	5.351	
	76.7	.517	5.925	5.408	5.419	.02/.005	.602	5.323	5.344
40.13	31.1	−.346	5.364	5.710		.02/.03	−.176	5.540	
	41.1	−.157	5.505	5.662		.02/.02	.000	5.505	
	48.1	−.034	5.673	5.707		.02/.015	.124	5.549	
	57.9	.138	5.850	5.712		.02/.01	.301	5.549	
	72.7	.425	6.117	5.692	5.697	.02/.005	.602	5.515	5.531
49.18	29.6	−.377	5.602	5.979		.02/.03	−.176	5.778	
	38.6	−.203	5.773	5.976		.02/.02	000	5.773	
	45.3	−.082	5.895	5.977		.02/.15	.124	5.771	
	55.8	.101	6.069	5.968		.02/.01	.301	5.768	
	71.0	.388	6.371	5.983	5.976	.02/.005	.602	5.769	5.779
58.76	29.5	−.379	5.866	6.245		.02/.03	−.176	6.042	
	38.6	−.202	5.993	6.195		.02/.02	.000	5.993	
	45.3	−.082	6.157	6.239		.02/.015	.124	6.033	
	55.1	.088	6.338	6.250		.02/.01	.301	6.037	
	70.6	.380	6.615	6.235	6.235	.02/.005	.602	6.013	6.020
68.99	29.3	−.383	6.188	6.571		.02/.03	−.176	6.364	
	38.1	−.212	6.376	6.588		.02/.02	.000	6.376	
	44.2	−.102	6.488	6.590		.02/.015	.124	6.364	
	55.0	.087	6.681	6.584		.02/.01	.301	6.380	
	70.1	.369	6.919	6.550	6.577	.02/.005	.602	6.314	6.359
83.43	30.7	−.354	7.144	7.498		.02/.03	−.176	7.320	
	35.2	−.266	7.285	7.551		.02/.025	−.097	7.382	
	40.5	−.168	7.243	7.411		.02/.02	.000	7.243	
	47.0	−.053	7.410	7.463		.02/.015	.124	7.286	
	55.7	.099	7.556	7.457	7.476	.02/.01	.301	7.255	7.297

4. References

[1] H. S. Harned and R. W. Ehlers, J. Am. Chem. Soc. **54,** 1350 (1932); **55,** 652 (1933).
[2] D. A. MacInnes and T. Shedlovsky, J. Am. Chem. Soc. **54,** 1429 (1932).
[3] H. S. Harned and G. L. Kazanjian, J. Am. Chem. Soc. **58,** 1912 (1936).
[4] S. S. Danyluk, H. Taniguchi and G. J. Janz, J. Phys. Chem. **61,** 1679 (1957).
[5] H. S. Harned and L. D. Fallon, J. Am. Chem. Soc. **61,** 2377 (1939).
[6] H. S. Harned, J. Phys. Chem. **43,** 275 (1939).
[7] H. S. Harned and N. D. Embree, J. Am. Chem. Soc. **57,** 1669 (1935).
[8] H. S. Harned and F. H. M. Nestler, J. Am. Chem. Soc. **68,** 966 (1946).
[9] T. Shedlovsky and R. L. Kay, J. Phys. Chem. **60,** 151 (1956).
[10] D. H. Everett and W. F. K. Wynne-Jones, Trans. Faraday Soc. **48,** 531 (1952).
[11] J. F. J. Dippy and F. R. Williams, J. Chem. Soc. 1888 (1943).
[12] E. Grunwald and B. J. Berkowitz, J. Am. Chem. Soc. **73,** 4939 (1951).
[13] R. G. Bates and G. D. Pinching, J. Research NBS **42,** 419 (1949) RP1982.
[14] R. G. Bates and S. F. Acree, J. Research NBS **30,** 129 (1943) RP1524.
[15] International Critical Tables III, 290.
[16] I. T. Oiwa, The Science Reports of the Tohoku University, Series 1, Vol. XLI, No. 2 (Oct. 1957).
[17] R. G. Bates and G. Schwarzenbach, Helv. Chim. Acta **37,** 1069 (1954).

WASHINGTON, D.C.

(Paper 64A4–58)

JOURNAL OF RESEARCH of the National Bureau of Standards—A. Physics and Chemistry
Vol. 64A, No. 4, July–August 1960

Preparation of Sulfur of High Purity

Thomas J. Murphy, W. Stanley Clabaugh, and Raleigh Gilchrist

(March 28, 1960)

A method is described for producing sulfur that contains less than 1.3×10^{-5} mole fraction of liquid-soluble, solid-insoluble impurities as determined by the freezing point depression. This corresponds to a purity of 99.999 mole percent. Many of the impurities, including organic matter, are removed by oxidation with sulfuric and nitric acids. The nonvolatile impurities are removed on distilling the sulfur. The residual sulfuric acid is removed by a special extraction with distilled water.

Methods are described for determining small amounts of the following impurities: Selenium, tellurium, arsenic, iron, carbon, sulfuric acid, and residue after ignition.

1. Introduction

The boiling point of sulfur is one of the fixed points on the International Temperature Scale. The sulfur used for determining this temperature must be as pure as possible and, expecially, free of impurities that would affect its boiling point. Analysis of sulfur to be used by Harold F. Stimson of this Bureau in a study of the factors affecting the precise determination of this fixed temperature point showed that the main impurity was organic matter. Inspection of several other samples of so-called pure sulfur revealed that they all contained various amounts of organic impurities.

Several attempts to purify sulfur by methods which are described in the literature always resulted in sulfur that contained appreciable amounts of organic impurities. This was especially true for sulfur that had been recrystallized from carbon disulfide. When roll sulfur containing 140 parts of carbon per million was purified by the method of Von Wartenburg [1],[1] which consists of heating the sulfur at 200° C for 48 hr in an atmosphere of nitrogen and then distilling it, the sulfur was found to contain organic matter to the extent of 53 parts of carbon per million parts of sulfur.

Some of the same sulfur purified by the method of James [2], which consists of agitating the sulfur at a temperature above its melting point with about 2 percent of its weight of concentrated sulfuric acid for a period ranging from 15 min to 2 hr and allowing the mixture to separate into two layers, was found to contain 60 parts of carbon per million of sulfur.

The method of Bacon and Fanelli [3], in which sulfur is boiled with 1 percent of magnesium oxide and then decanted, was not tried because Yeisen [4] reported that magnesium salts are somewhat soluble in sulfur and these salts might affect the boiling point of sulfur.

This paper describes a reliable method for purifying sulfur and the analytical methods used to establish its purity.

[1] Figures in brackets indicate literature references at the end of this paper.

2. Method of Purification Adopted

The starting material was commercial roll sulfur which was found by the analytical methods described later to contain 76 parts of nonvolatile matter, 11 parts of iron, 140 parts of carbon, and less than 1 part of selenium, 1 part of tellurium, and 0.5 part of arsenic per million parts of sulfur. In addition to the above impurities, bits of wood and other foreign matter were present.

The sulfur was freed of this obvious foreign matter by filtering the melted sulfur through a glass filtering funnel of coarse porosity. About 2.5 kg of the filtered sulfur was transferred to a 2-liter, round-bottom Pyrex flask that was equipped with two necks, each having standard taper 24/40 ground-glass joints. About 300 ml of concentrated sulfuric acid was added to the flask and the mixture was heated until the sulfur melted. A motor-driven glass stirrer was inserted through one of the necks. The mixture was heated to 150° C and continuously stirred. Concentrated nitric acid was added in about 2-ml portions at intervals of about 10 to 15 min for a period of 6 hr.

It should be pointed out that the reaction of hot sulfur with sulfuric and nitric acids produces a bluish-black color in the acid layer. This color masks the color produced by the action of hot sulfuric acid on the organic material, making it difficult to tell when all of the organic impurity is removed. However, with all the various samples of sulfur tried, the treatment described above sufficed to reduce the amount of organic impurity to a very low concentration.

The acid-sulfur mixture was allowed to cool to room temperature, then the acid was poured off, and the sulfur was rinsed several times with distilled water. Since some of the acid remains entrapped in the sulfur, the sulfur was remelted and allowed to cool, and again rinsed several times with distilled water. This procedure of remelting, cooling, and rinsing was repeated four or five times to remove most of the sulfuric and nitric acids.

An air-cooled reflux tube, about 40 cm long, was then attached to one of the necks, and a gas delivery tube sealed through a standard taper joint was

placed in the other neck. The lower end of the delivery tube was about 1 in. above the bottom of the flask. The sulfur was then boiled at such a rate that its vapors condensed within a few inches of the top of the reflux tube. A current of helium or water-pumped nitrogen was continually passed through the boiling sulfur. This stream of gas aided in sweeping out the vapors of water, nitric, and sulfuric acids. This refluxing was continued for about 4 hr. The sulfur was cooled and the reflux tube was replaced with a bent air-cooled condenser. The sulfur was then distilled. The first 100-ml portion was discarded and a portion of about 100 ml was allowed to remain in the distilling flask.

To further reduce the acid and water content of the sulfur, the distilled sulfur was melted and transferred to 400-ml glass cylindrical ampoules. Each ampoule was filled to slightly less than one-half of its volume and then placed on its side until the sulfur solidified. Solidifying the sulfur with the ampoules in this position was necessary to prevent the ampoules from breaking when the sulfur was remelted for subsequent treatment. The glass ampoules were constructed of 50-mm tubing and were about 20 cm long; the necks were about 15 cm long and made of 10-mm glass tubing.

About 80 ml of water was added to each 400-ml ampoule, which contained about 200 ml of sulfur. The air remaining in the ampoule was displaced with water-pumped nitrogen, which prevented the formation of sulfuric acid from the reaction of the oxygen present with the melted sulfur. The ampoules were then sealed and placed on their sides in an oven heated to 125° C. After the sulfur had melted, each ampoule was shaken to extract residual sulfuric acid into the water. The ampoules were again placed on their sides to cool. After cooling, the tips of the ampoules were broken open, and the water was poured off and titrated with 0.02N sodium hydroxide solution to determine the sulfuric acid content. Eighty milliliters of water was again added to each ampoule and the process was repeated until no change in acid was noted. Three extractions were sufficient in most cases to reduce the sulfuric acid to less than 0.0002 percent.

This extraction process removed the excess acid, but the sulfur contained entrapped water in addition to any water that might have been dissolved in it. To remove the water remaining in the ampoule after the last extraction the ampoule was sealed to a vacuum system. A trap immersed in a dry ice bath was sealed between the ampoule and the vacuum pump. The sulfur was slowly melted while the system was being evacuated and the pumping was continued until the pressure in the system was reduced to 10 mm of mercury. The pumping was interrupted and water-pumped nitrogen was admitted to a pressure of 100 mm of mercury, and the system was again evacuated to a pressure of 10 mm of mercury. The sulfur was maintained in the molten state throughout these operations. Water-pumped nitrogen was then admitted until the pressure was 1 atm. The ampoule was sealed off and placed on its side for the sulfur to solidify. Figure 1 shows a photograph of a sealed ampoule containing sulfur and water and a sealed ampoule containing the final purified product.

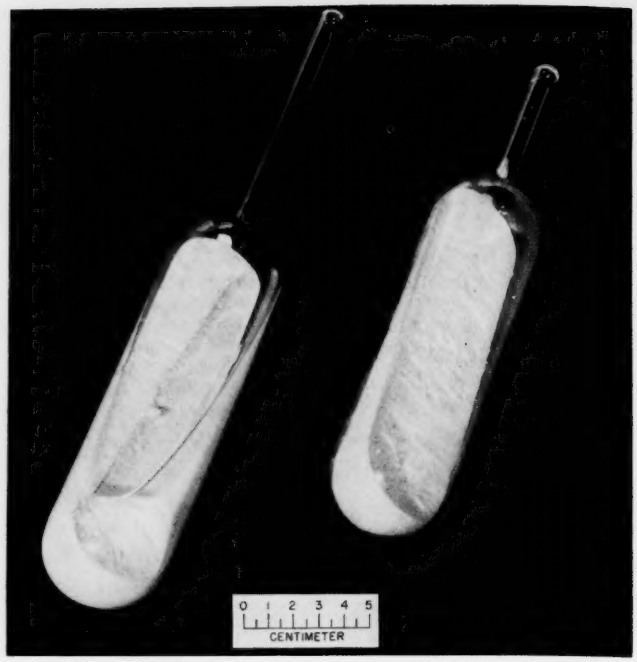

FIGURE 1. *Photograph of a sealed ampoule containing sulfur and water (left) and a sealed ampoule containing the purified sulfur (right).*

3. Estimation of Absolute Purity

The thermodynamic properties of this purified sulfur were measured by West [5] by means of an adiabatic calorimeter. The mole-fraction of liquid-soluble, solid-insoluble impurity was calculated to be 1.3×10^{-5} from the freezing point depression. This corresponds to a purity of 99.999 mole percent of sulfur.

4. Methods for Determining Impurities in the Sulphur

4.1. Separation and Determination of Selenium and Tellurium

The selenium and tellurium were separated from the sulfur by dissolving the sulfur in cold liquid bromine and extracting the selenium and tellurium bromides in cold water. The selenium and tellurium were precipitated as the elements [6]. The elements were dissolved in hydrobromic acid and separated by distillation.

Recommended Procedure

Dissolve 50 g of sulfur in 55 ml of chilled bromine. Cool the solution in an ice bath, transfer it to a separatory funnel, and add 10 ml of cold distilled water. Shake the mixture for 1 min, or until the solution begins to get warm. Draw off the lower layer containing the sulfur bromide, and pass the aqueous

layer through a wetted filter paper to catch any globules of sulfur bromide. Repeat the extraction of the sulfur bromides with cold distilled water several times, combine the water extracts, and dilute the resulting solution to a volume of 100 ml.

Pass a stream of sulfur dioxide into the aqueous extract, to reduce the excess bromine to bromide. Add 0.5 g of hydrazine sulfate and allow the solution to stand overnight to precipitate selenium and tellurium. Filter the solution through a glass microfiltering crucible of fine porosity and wash the precipitate with distilled water. Dissolve the mixed precipitate in about 30 ml of colorless concentrated hydrobromic acid to which a drop of bromine is added. Dilute the solution so obtained to a volume of 50 ml with concentrated hydrobromic acid, and transfer it to a 100-ml distilling flask. Distill 25 ml of this solution into 25 ml of water, and destroy the excess bromine in the distillate with sulfur dioxide, as described above. To this solution add 0.5 g of hydroxylamine hydrochloride and 2 ml of 0.05-percent solution of gum arabic, and place the solution on the steam bath for 1 hr. Cool the solution and compare its red turbidity with control solutions containing known amounts of selenium. Selenium in an amount as small as 0.05 mg can easily be determined; this corresponds to 1 ppm in the sulfur.

Pour the solution, which remains in the distilling flask after the elimination of selenium, into a beaker and compare its yellow color with control solutions containing known amounts of tellurium in equal volumes of concentrated hydrobromic acid. Tellurium in an amount as small as 0.05 mg can easily be determined; this corresponds to 1 ppm in the sulfur.

4.2. Determination of Arsenic

Arsenic was determined by the standard Gutzeit method [7].

Recommended Procedure

Dissolve 3 g of sulfur in 3.5 ml of liquid bromine. Add 75 ml of diluted nitric acid (1+9),[2] and heat the resulting solution to boiling. Continue to boil the solution until reaction ceases. Concentrate the solution as far as possible on the steam bath, add a small amount of bromine to dissolve any free sulfur, and add 5 ml of diluted nitric acid (1+1). This treatment with bromine and nitric acid converts the sulfur to sulfuric acid. The nitric acid also oxidizes any arsenic present to the quinquevalent state so that it will not be volatilized in the subsequent evaporations. Heat the solution to boiling and finally evaporate it until fumes of sulfuric acid are evolved.

Determine the arsenic content by the standard Gutzeit method [7], comparing the stain produced with those of known amounts of arsenic. Arsenic in an amount as small as 0.002 mg can be determined; this corresponds to 0.7 ppm in the sulfur.

[2] Throughout this paper dilutions are indicated by the volumes of concentrated acid and water mixed to prepare a diluted reagent. Diluted nitric (1+x) means a diluted acid prepared by mixing 1 volume of the concentrated acid with x volumes of water.

4.3. Determination of Residue After Ignition

Recommended Procedure

Burn 50 g of the sulfur in a tared dish, in a well-ventilated hood, ignite the residue at a temperature of 550° to 650° C, cool it in a desiccator, and weigh it.

4.4. Determination of Iron

Recommended Procedure

Add 10 ml of diluted hydrochloric acid (1+1) to the residue obtained in section 4.3. Digest the mixture on the steam bath and evaporate to dryness. Dissolve the resulting residue in 2 ml of concentrated hydrochloric acid and dilute the solution to a volume of 50 ml. Add 30 to 50 mg of crystalline ammonium persulfate and 3 ml of a 30-percent solution of ammonium thiocyanate. Compare the red color with that produced by known amounts of iron. Iron in an amount as small as 0.05 mg can be easily determined; this corresponds to 1 ppm in the sulfur.

4.5. Determination of Total Carbon

Organic impurities, reported as carbon, were determined by ascertaining the amount of carbon dioxide produced on burning a weighed portion of the sulfur. If the amount of carbon dioxide is large, more than 1 mg, it can be absorbed in a tared soda-lime tube and determined gravimetrically. If the amount is small, less than 1 mg, it can be absorbed in diluted ammonium hydroxide and determined turbidimetrically.

a. Apparatus

The apparatus used for determining small amounts of carbon dioxide is shown in figure 2. The U-tube, A, contains soda-lime to remove carbon dioxide from the oxygen which is used for combustion. The 125-ml wash bottle, B, contains concentrated sulfuric acid to remove water. The 250-ml round-bottom flask, C, is fitted with a delivery tube which reaches to about 1 in. from the bottom of the flask. The sulfur is placed in this flask. Washing towers, D, E, and F, each contain 200 ml of 30-percent hydrogen peroxide to absorb the sulfur dioxide formed on combustion. Tower D is chilled in an ice bath. The 125-ml wash bottle, G, contains 50 ml of diluted ammonium hydroxide (1+9) to absorb the carbon dioxide which is formed in the combustion. The protective U-tube, H, contains soda-lime. Ball and socket joints are used for connections and all joints are lubricated with phosphoric acid.

If the amount of carbon dioxide to be determined is greater than 1 mg, flask G is replaced with a gas washing tower containing sulfuric acid, a U-tube containing magnesium perchlorate, and a tared U-tube containing soda-lime and magnesium perchlorate.

b. Recommended Procedure

(1) *For Small Amounts of Carbon (less than 1 mg as* CO_2*).* Assemble the apparatus shown in figure 2, but without the ammonia solution in G. Weigh between

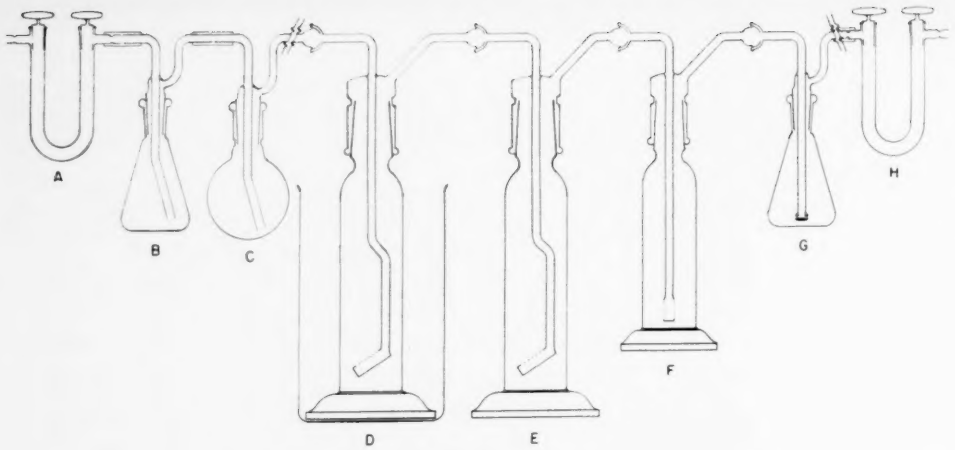

FIGURE 2. *Apparatus used in determining carbon in sulfur.*

75 and 100 g of sulfur and place it in flask C. Sweep out the entire apparatus with oxygen for at least 2 hr and then add the ammonia solution to flask G.

Regulate the stream of oxygen to a rate of about 10 ml per minute and heat the outside of flask C until the sulfur ignites. Continue burning until all the sulfur is consumed and then heat the bottom and lower sides of the flask to dull red heat. Continue passing the oxygen for at least ½ hr.

Remove flask G and add 5 ml of 10-percent barium chloride solution. Transfer the resulting solution to a Nessler tube and compare the turbidity to controls containing known amounts of carbonate in an equal volume of solution.

(2) *For Larger Amounts of Carbon (more than 1 mg as* CO_2*).* Assemble the apparatus shown in figure 2, but for flask *G*, substitute the tower containing sulfuric acid, the U-tube containing magnesium perchlorate, and the tared U-tube containing the soda-lime and magnesium perchlorate.

Follow the procedure outlined above for the addition and ignition of the sulfur.

Remove the tared U-tube containing the soda-lime and absorbed CO_2 and weigh it. The amount of carbon dioxide is determined from the increase in weight of the soda-lime tube.

4.6. Determination of Sulfuric Acid

Sulfuric acid was determined by placing a known weight of sulfur in an ampoule with water, expelling the air with nitrogen, sealing the ampoule, melting the sulfur, and extracting the sulfuric acid into the water. The water is removed by decantation and the acid content is determined by titration with 0.02 *N* sodium hydroxide solution.

Repeated extractions failed to reduce the sulfuric acid content of the purified material below 0.0002 percent. However, since some or all of this acid may have been formed on the surface of the sulfur by atmospheric action or by a slow reaction with the water [8] the actual amount of sulfuric acid in the sulfur may have been less than the value obtained.

5. Analytical Results

Table 1 gives the results of the determination of the impurities in the sulfur taken as the starting material and in that obtained as the final product of purification.

6. Summary

Commercial roll sulfur was purified by a nitric acid—sulfuric acid oxidation method. The total impurities in this sulfur were reduced to 1.3×10^{-5} mole percent. The organic matter was reduced to 0.0002 percent as carbon.

TABLE 1. *Determination of impurities*

Impurity	Amount of impurity in starting material	Amount of impurity in the purified product
	%	%
Total carbon	0.014	0.0002
Nonvolatile matter	.0076	.0003
Iron	.0011	.0001
Selenium	<.0001	(1)
Tellurium	<.00005	(1)
Arsenic	<.00005	(1)
Sulfuric acid		.0002

[1] Not determined.

7. References

[1] H. von Wartenburg, Z. anorg. Chem. **251,** 166 (1943).
[2] Hector G. James, and Imperial Chemical Industries, British Patent No. 523, 465, June 15, 1940.
[3] Raymond F. Bacon and Rocco Fanelli, Ind. Eng. Chem. **34,** 1043–1048 (1942).
[4] Frank M. Yeisen (to Niagara Research Corp.) U.S. Patent No. 2, 459, 764, Jan. 1949.
[5] Estal D. West, J. Am. Chem. Soc. **81,** 29 (1959).
[6] W. Smith, Ind. Eng. Chem. **7,** 849 (1915).
[7] Am. Chem. Soc., Reagent Chemicals, Am. Chem. Soc. Specifications (Am. Chem. Soc., Wash., D.C., 1955).
[8] Elemér Schulek, Endre Koros, and László Maros, Magyar Tudományos Akad. Kém. Tudományok Osztályának, Közleményei **7,** 91 (1955).

WASHINGTON, D.C. (Paper 64A4–59)

JOURNAL OF RESEARCH of the National Bureau of Standards—A. Physics and Chemistry
Vol. 64A, Nc. 4, July–August 1960

Tritium-Labeled Compounds IV. D-Glucose-*6*-*t*, D-Xylose-*5*-*t*, and D-Mannitol-*1*-*t*

Horace S. Isbell, Harriet L. Frush, and Joseph D. Moyer

(April 13, 1960)

Methods are presented for the preparation of D-glucose-*6*-*t*, D-xylose-*5*-*t*, and D-mannitol-*1*-*t* by the reduction of suitable compounds with lithium borohydride-*t* in anhydrous tetrahydrofuran, followed by hydrolysis of the products. The starting materials for the reductions are, respectively, 1,2-*O*-isopropylidene-D-glucurono-6,3-lactone, 5-aldo-1,2-*O*-isopropylidene-D-*xylo*-pentofuranose, and 2,3:5,6-di-*O*-isopropylidene-D-mannofuranose. The apparatus and procedure for carrying out the reductions in a closed system are described.

1. Introduction and Discussion

This report is one of a series on the production and use of tritium-labeled carbohydrates.[1] Previous papers from this laboratory have described convenient apparatus for handling tritium in a closed system [2],[2] and methods for analyzing nonvolatile tritium compounds [3, 4]. A method for preparing lithium borohydride-*t* [2], a versatile reductant for introducing tritium into organic compounds, was also given. The usefulness of this compound, in aqueous pyridine, for preparing position-labeled carbohydrates has already been demonstrated [5]; this paper describes its use in the reduction of certain carbohydrate derivatives in an anhydrous solvent.

The equations illustrate the preparation of D-glucose-*6*-*t*, D-xylose-*5*-*t*, and D-mannitol-*1*-*t* by reduction of suitable compounds with lithium borohydride-*t* in anhydrous tetrahydrofuran. Previously, Sowden had reduced 1,2-*O*-isopropylidene-D-glucurono-6,3-lactone (I) in the preparation of D-glucose-*6*-C^{14} [6]. The reduction, originally carried out with sodium borohydride in water, was improved by Roseman, who used lithium aluminum hydride in anhydrous ether [7]. Crystalline 5-aldo-1,2-*O*-isopropylidene-D-*xylo*-pentofuranose (II) [8, 9] was prepared as a starting material for the synthesis of D-glucose-*6*-C^{14} [8]. Earlier, Sowden had reduced this substance (II), prepared from D-glucose-*1*-C^{14}, with hydrogen and Raney nickel and obtained D-xylose-*1*-C^{14} [10]. Reduction of 5-aldo-1,2-*O*-isopropylidene-D-*xylo*-pentofuranose with lithium borohydride-*t* in tetrahydrofuran, and subsequent hydrolysis, yields D-xylose-*5*-*t*. The reduction of 2,3:5,6-di-*O*-isopropylidene-D-mannofuranose (III) [11] has been used in this laboratory for several years as a means for analyzing lithium borohydride-*t*. The reduction takes place nearly quantitatively, and the specific activity of the D-mannitol-*1*-*t*, readily obtained on hydrolysis, can be used as a measure of the specific activity of the lithium borohydride-*t*.

[1] Project sponsored by the Division of Research of the Atomic Energy Commission. See [1] for a general description of the work.
[2] Figures in brackets indicate the literature references at the end of this paper.

Synthesis of D-Glucose-*6*-*t*

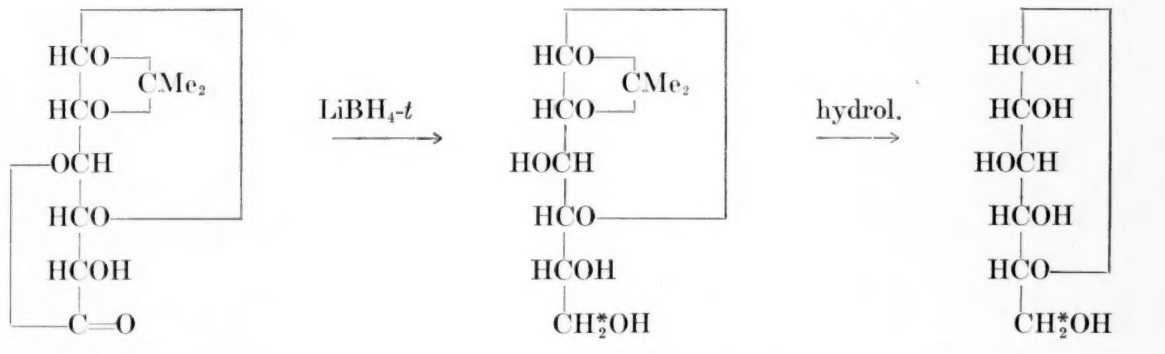

1,2-*O*-isopropylidene-D-glucurono-6,3-lactone

I

1,2-*O*-isopropylidene-D-glucose-*6*-*t*

α-D-glucose-*6*-*t*

Synthesis of D-Xylose-*5-t*

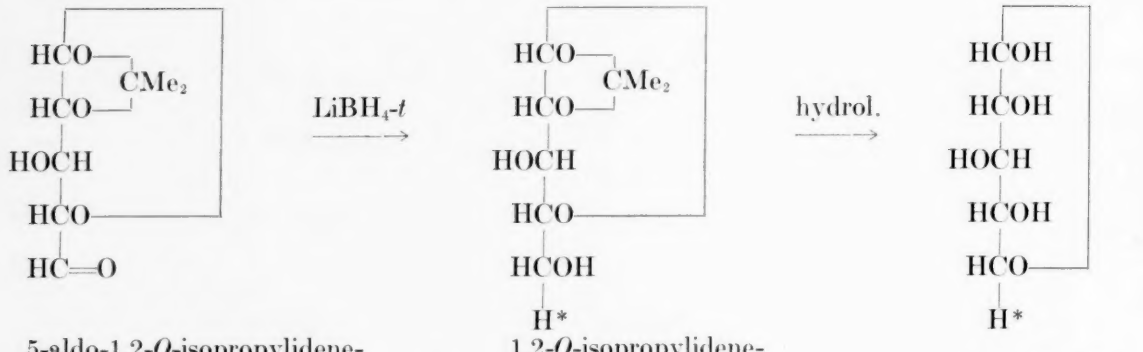

5-aldo-1,2-*O*-isopropylidene-D-*xylo*-pentofuranose

1,2-*O*-isopropylidene-D-xylofuranose-*5-t*

α-D-xylose-*5-t*

II

Synthesis of D-Mannitol-*1-t*

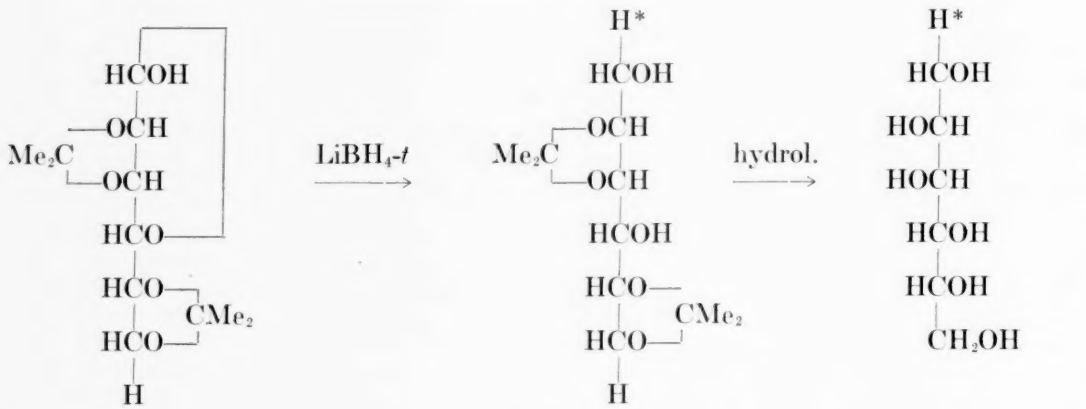

2,3:5,6-di-*O*-isopropylidene-D-mannofuranose

2,3:5,6-di-*O*-isopropylidene-D-mannitol-*1-t*

D-mannitol-*1-t*

III

2. Experimental Details

2.1. Apparatus and Materials

The general-purpose manifold and apparatus for working with tritium in a closed system are described in [2]. The reaction flask, used in conjunction with the manifold in the preparations described here, is shown in figure 1. The following starting materials for the reductions were prepared by the methods given in the references cited: 2,3-*O*-isopropylidene-D-glucurono-6,3-lactone [6], 5-aldo-1,2-*O*-isopropylidene-D-*xylo*-pentofuranose [8], 2,3:5,6-di-*O*-isopropylidene-D-mannofuranose [11], and lithium borohydride-*t* [2]. Anhydrous tetrahydrofuran and solutions of lithium borohydride-*t* therein were prepared by the methods previously described [2].

2.2. Analysis of Tritium Compounds

All analyses of tritium-containing materials were made with a 2π, windowless, gas-flow, proportional counter. Low-activity materials were assayed by the method of Isbell and coworkers [3], in films of sodium *O*-(carboxymethyl) cellulose (CMC) with the proportional counter operated at 2,000 v. The films were made on 2-in., stainless-steel planchets and counted to a statistical error of less than 1 percent (more than 10,000 counts). The specific activity of the material, s, in μc/mg, was obtained from the relationship:

$$s=(mak)/m',$$

where a is the observed counts per second, corrected for background, m is the total solids in the CMC

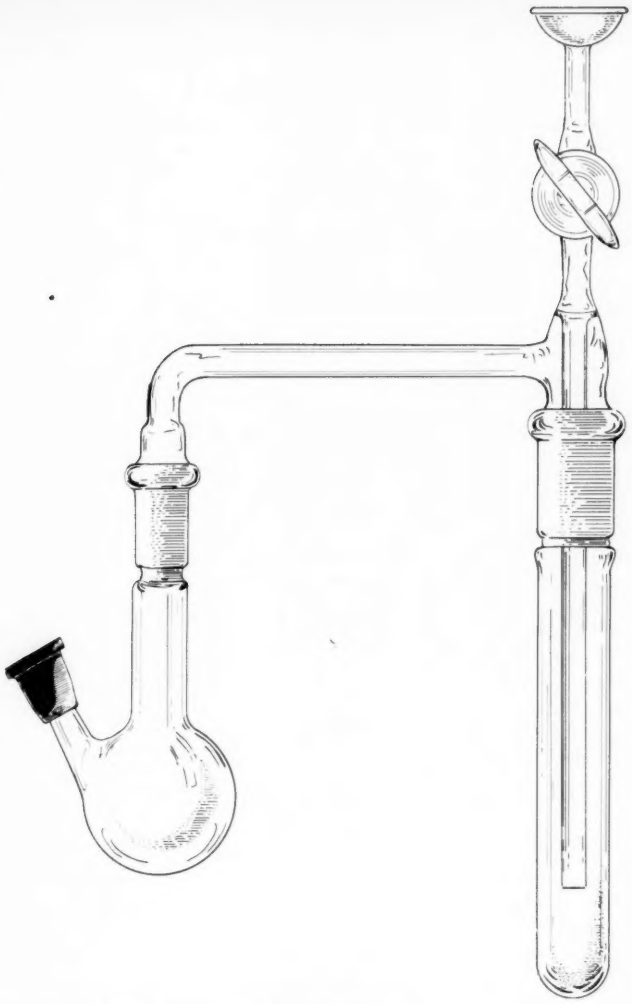

FIGURE 1. *Apparatus for conducting reductions with lithium borohydride-t.*

A, A 50-ml, round-bottomed reaction flask having a rubber-capped side-arm for introducing reagents.
B, Trap for use in cooling-bath.

film, m' is the weight of the radioactive sample, and k is an empirical factor (4.45×10^{-5}) independently determined under the conditions employed. High-activity materials were assayed in formamide solutions,[3] and the proportional counter was operated at 1,750 v. Under the conditions used, 1 count per second corresponds to 0.128 μc of tritium per milliliter of the formamide solution counted.

2.3. α-D-Glucose-6-*t*

Two millimoles of 1,2-*O*-isopropylidene-D-glucurono-6,3-lactone (432 mg) and a magnetic stirring bar were placed in flask A of figure 1. The flask and trap were connected to the general-purpose manifold of [2], and the system was made vacuum-tight and evacuated. The connection to the manifold was then closed, and the reaction flask was cooled in a shallow ice-bath set on a magnetic stirrer. The stirrer was started, and 5 ml of anhydrous tetrahydrofuran was injected into the flask by means of a hypodermic needle; this was followed by a solution of 2.0 millimoles of lithium borohydride-*t* (having a total of 80 mc of radioactivity) in approximately 4 ml of anhydrous tetrahydrofuran. After the solution had remained for 3 hr at 0°, 5 ml of water was injected, and the mixture was allowed to stand at room temperature overnight. The reaction mixture was then frozen in liquid nitrogen, and the hydrogen-*t* that was present was removed through the manifold. The mixture was warmed to room temperature, and 5 ml of water containing 1 millimole of nonradioactive sodium borohydride was added (in order to reduce any aldehyde groups that had escaped reduction with the lithium borohydride-*t*). After 30 min, the solution in flask A was frozen, and freeze-dried by cooling B in a dry-ice bath and evacuating the system through the manifold. Water was added to the residue by means of a hypodermic needle, and the solution was again freeze-dried. This process was repeated once more.

Finally, flask A was removed from the system, and the residue was dissolved in 20 ml of 1-percent hydrochloric acid. The solution was heated for 30 min in a boiling-water bath in order to hydrolyze the isopropylidene group, and was then passed through 20 ml of mixed anion- and cation-exchange resins.[4] The effluent was concentrated in a rotary still, and all boric acid was removed as methyl borate by repeated addition and evaporation of methanol. The resulting product was dissolved in water, and the solution was passed through a column containing 5 ml of mixed anion- and cation-exchange resins. The conductivity of the solution, measured with a purity meter,[5] was found to be low, in accordance with the absence of ionic impurities. A radioassay of an aliquot of the solution in formamide showed the presence of 33.5 mc of radioactivity in the product. The solution was evaporated almost to dryness in a rotary vacuum still. The residue was dissolved in 1 ml of methanol, and 2-propanol was added almost to the point of incipient turbidity. Crystallization of α-D-glucose-*6-t* was induced by seeding with the nonradioactive sugar. The crystals were separated, recrystallized, and assayed in a CMC film by means of the proportional counter. The product weighed 289 mg and had an activity of 29.5 mc. By co-crystallization of the mother liquor with nonradioactive D-glucose, about 2 mc of α-D-glucose-*6-t* of lower activity was recovered. Thus, the yield of D-glucose-*6-t*, based on the 1,2-*O*-isopropylidene-D-glucurono-6,3-lactone, was 85.7 percent; the radiochemical yield (31.5 mc) was 39.4 percent, based on the lithium borohydride-*t*.

[3] The method for radioassay in formamide solutions was developed earlier in this laboratory for the assay of carbon-14 [12]. Although the counting-efficiency for tritium is extremely low, the reproducibility of the method is excellent.

[4] Amberlite IR120–H, Rohm & Haas Co., Philadelphia, Pa., and Duolite A–4, Chemical Process Co., Redwood City, Calif.
[5] Supplied by Barnstead Still & Sterilizer Co., Boston, Mass.

2.4. α- -Xylose-5-*t*

Four millimoles of crystalline 5-aldo-1,2-*O*-isopropylidene-D-*xylo*-pentofuranose were reduced with 2 millimoles of lithium borohydride-*t* (containing 63.5 mc of radioactivity) by the technique described for the preparation of D-glucose-*6-t*. A crystalline substance, presumably 1,2-*O*-isopropylidene-D-*xylo*-pentofuranose-*5-t*, separated after the reduction. This intermediate compound was not purified, but was converted to D-xylose-*5*-t by heating it with 1-percent hydrochloric acid in a boiling-water bath for 1 hr. The solution was de-ionized in the manner previously described, and an aliquot was counted in formamide; the solution contained 26.1 mc of radioactivity. The labeled sugar was crystallized by concentrating the solution to a sirup and diluting it with ethanol and 2-propanol. After recrystallization, the α-D-xylose-*5-t* weighed 450 mg and had an activity of 53 μc/mg. The yield, based on the weight of the 5-aldo-1,2-*O*-isopropylidene-D-*xylo*-pentofuranose, was 75 percent; the radiochemical yield was 38 percent.

2.5. D-Mannitol-*1-t*

One millimole of 2,3:5,6-di-*O*-isopropylidene-D-mannofuranose (260 mg) was reduced with 0.5 millimole of lithium borohydride-*t* containing 16 mc of tritium, by the techniques described in section 2.3. The crystals that separated were recrystallized from water, with the addition of methanol. The purified D-mannitol-*1-t* weighed 175 mg and had an activity of 43 μc/mg. The chemical yield was 95 percent, and the radiochemical yield, 31.3 percent.

3. References

[1] NBS Tech. News Bull. **43,** 130 (1959).
[2] H. S. Isbell and J. D. Moyer, J. Research NBS **63A,** 177 (1959).
[3] H. S. Isbell, H. L. Frush, and R. A. Peterson, J. Research NBS **63A,** 171 (1959).
[4] H. S. Isbell, H. L. Frush, and N. B. Holt, J. Research NBS **64A,** 363 (1960).
[5] H. S. Isbell, H. L. Frush, N. B. Holt, and J. D. Moyer, J. Research NBS **64A,** 177 (1960).
[6] J. C. Sowden, J. Am. Chem. Soc. **74,** 4377 (1952).
[7] S. Roseman, J. Am. Chem. Soc. **74,** 4467 (1952).
[8] R. Schaffer and H. S. Isbell, J. Research NBS **56,** 191 (1956) RP2667.
[9] R. Schaffer and H. S. Isbell, J. Am. Chem. Soc. **79,** 3864 (1957).
[10] J. C. Sowden, J. Am. Chem. Soc. **73,** 5496 (1951).
[11] K. Freudenberg and R. M. Hixon, Ber. deut. chem. Ges. **56,** 2119 (1923).
[12] A. Schwebel, H. S. Isbell, and J. D. Moyer, J. Research NBS **53,** 221 (1954) RP2537.

WASHINGTON, D.C. (Paper 64A4–60)

JOURNAL OF RESEARCH of the National Bureau of Standards—A. Physics and Chemistry
Vol. 64A, No. 4, July–August 1960

Tritium-Labeled Compounds V. Radioassay of Both Carbon–14 and Tritium in Films, With a Proportional Counter[1]

Horace S. Isbell, Harriet L. Frush, and Nancy B. Holt

(March 28, 1960)

A convenient procedure is described for the radioassay of both carbon-14 and tritium in water-soluble, nonvolatile compounds by means of a windowless, gas-flow, proportional counter. The materials are counted in uniform films of sodium *O*-(carboxymethyl)cellulose that are "infinitely thick" to the radiation of tritium but not to the radiation of carbon-14. Films of uniform thickness are obtained by new techniques which are described in detail.

If only carbon-14 is present, its absolute activity can be calculated conveniently by means of an empirically established curve for the counting-efficiency. If both carbon-14 and tritium are present, the films are counted in the proportional counter and are then recounted in the presence of a screen that stops all radiation from tritium but only a portion of that from carbon-14. From a film with a thickness of 0.8 mg/cm², approximately 43 percent of the radiation of carbon-14 is counted. Of this emerging radiation, approximately 50 percent passes through a screen of ¼-mil double-aluminized "Mylar." By use of suitable calibration curves for counting-efficiency, carbon-14 and tritium in the same sample can be calculated from the counts with, and without, the screen.

Satisfactory analyses can be made with samples containing less than 0.001 microcurie of carbon-14 and 0.005 microcurie of tritium. The method is suitable for the radioassay of a wide variety of labeled materials.

1. Introduction and Discussion

Many chemical reactions can be studied by means of double labeling with radioisotopes, as, for instance, with carbon-14 and tritium. However, maximal use of methods employing carbon-14 and tritium has thus far been hampered by the lack of convenient procedures for determining the two radioisotopes in the same sample. Satisfactory analyses of materials containing both carbon-14 and tritium can be made with scintillation counters, but these are expensive and not generally available.

In a previous report from this laboratory, a convenient procedure was described for the radioactivity assay of tritium in water-soluble, nonvolatile compounds by means of a 2π, windowless, gas-flow, proportional counter [1].[2] The sample to be analyzed is contained in a film of sodium *O*-(carboxymethyl)-cellulose that is "infinitely thick" to the radiation of tritium. It seemed possible that this method might be so modified that it could be used for the radioassay of carbon-14 and, especially, of carbon-14 and tritium in the same sample. This paper reports such a method.[3]

Radiation from carbon-14 has considerably greater energy than that from tritium.[4] Consequently, it is impracticable to prepare films that are "infinitely thick" to this radiation. Films that are "infinitely thick" only to the radiation from tritium absorb amounts of that from carbon-14 which are dependent upon film thickness. However, it was found that, by means of an experimentally determined curve for counting-efficiency, absolute determinations of carbon-14 in films of sodium *O*-(carboxymethyl)cellulose (CMC) could be made with high efficiency and good accuracy.[5]

In order to determine carbon-14 and tritium in the *same* film, advantage was taken of the fact that the radiation from tritium is completely stopped by a screen that permits passage of a considerable fraction of the radiation from carbon-14. By use of experimentally determined counting-efficiences, carbon-14 and tritium can be conveniently determined in the same film from the counts with, and without, a suitable screen.

The radioactivity of tritium-containing materials decreases significantly in the course of several months, and hence a table of the change in activity with time is included for the convenience of the analyst (see table 4, p. 367). This table is based on a half-life value for tritium of 12.26 yr [7].

2. Materials and Apparatus

2.1. Radioactive Materials

D-Glucose-*1*-C^{14} was prepared by the method previously described [8] and was standardized by

[1] Part of a project on the development of methods for the production of radioactive carbohydrates, sponsored by the Division of Research of the Atomic Energy Commission.

[2] Figures in brackets indicate the literature references at the end of this paper.

[3] The comparative counting of carbon-14 in films of agar has been reported [2]. The described technique differs considerably from that reported here.

[4] The maximum range of the radiation from carbon-14 is about 28 mg/cm² (see ref. [3] p. 7), whereas that from tritium is only about 0.7 mg/cm² [4]. A film with a thickness of 28 mg/cm² is difficult to dry to constant weight, and tends to crack and peel. Factors affecting the assay and standardization of *beta*-ray emitters are discussed in ref. [5].

[5] This procedure for the counting of carbon-14 supplements the more convenient, but less sensitive, formamide counting-method previously developed in this laboratory [6].

radioassay of a formamide solution of it in a proportional counter [6]. D-Glucose-*1-t* [9], was assayed in a proportional counter [10] by comparing its activity in a sulfuric acid-phosphoric anhydride solution with that of the NBS standard tritium oxide sample No. 4926.

2.2. CMC Stock Solution

The stock solution used with materials of high specific activity consisted of 1.5 g of sodium *O*-(carboxymethyl)cellulose (CMC),[6] 0.5 g of anhydrous D-glucose, 0.2 g of phenol, 5 mg of a dye (*p*-rosaniline hydrochloride), and sufficient water to give 100 ml of solution. The solution was conveniently prepared by mixing the materials with slightly less than the desired amount of water and allowing the mixture to stand for 24 hr or longer. When the CMC had dissolved, the addition of water was completed. The added phenol prevented the growth of bacteria and molds, and the dye revealed the degree of uniformity of the film. In the stock solution used with samples of low specific activity, part or all of the D-glucose, which acts as an organic "ballast" material and plasticizer, was omitted.

2.3. Equipment for Counting

Most of the radioactivity measurements were made at 2000 v with a commercial, 2π, windowless, gas-flow, proportional counter.[7] The commercial counting gas (consisting of 90% of argon and 10% of methane) was dried, before use, by successive passage through soda-lime, anhydrous calcium sulfate, and phosphoric anhydride.

A few measurements of carbon-14 in films were made by means of a commercial "pancake-type" Geiger-Müller tube,[8] in order to confirm the applicability of this equipment to the radioassay of carbon-14 in CMC films.

Stainless-steel, cupped, flat-bottomed, counting planchets, 2 in. in diameter, supplied for use with the proportional counter, were modified by enclosing a 5-cm² area in a shallow, circular groove (cut on a lathe) beyond which the CMC solution did not spread.[9]

The screen used for stopping the radiation of tritium, in the radioassay of tritium and carbon-14, is shown in figure 1. Double-aluminized "Mylar" film,[10] ¼-mil in thickness, and having a weight of of 0.9 mg/cm² was cemented to a circular, aluminum frame that fitted over the top of the planchet. (The thickness of the foil was determined by weighing a sample of known area.) The ability of this foil to stop the radiation from tritium completely was

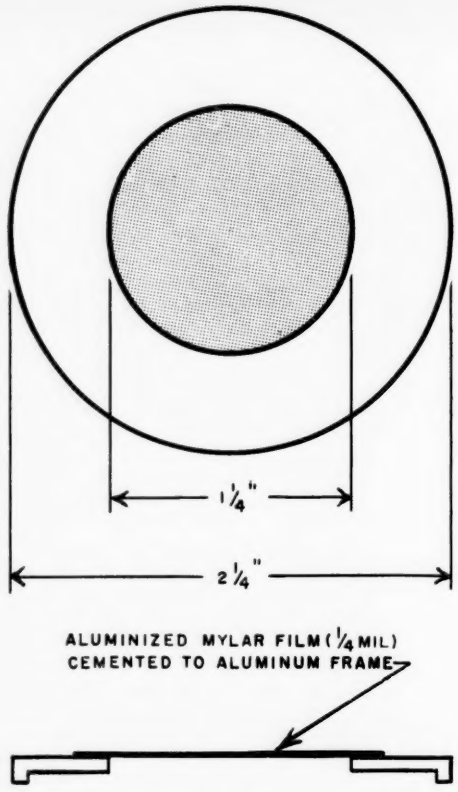

FIGURE 1. *Screen for counting carbon-14 in the presence of tritium.*

tested by comparing the background count in the absence of radioactive material with that found when the screen shielded a film containing D-glucose-*1-t*. The counts were the same, within the statistical error of measurement.

2.4. Preparation of Films and Counting of Their Activity

The planchets were polished by rubbing them, immediately before use, with a dry, 3:1 mixture of infusorial earth and Versene [the tetrasodium salt of (ethylenediamine)tetraacetic acid]; excess cleaning powder was removed by means of a stream of air.[11] This treatment gives a surface on which the liquids used can spread readily.

For every preparation of the CMC stock solution, the exact weight of the total solids per gram of solution was determined by evaporating weighed quantities of the solution (about 1 g), contained in each of several 2-in. planchets, under the conditions used in the analysis. The weight of the residue per gram of the stock solution was used in calculating the weight (m) of total solids in the films made from the stock solution and radioactive materials. A known weight of the sample to be analyzed was dissolved in about 2 ml of the CMC stock solution, and the total weight was determined.[12] A known weight of

[6] Medium-viscosity product, CMC-12MP, of Hercules Powder Co., Wilmington, Del.
[7] Model PC-3, Nuclear Measurements Corp., Indianapolis, Ind.
[8] No. 1007T of Anton Electronics Laboratory, Inc., Brooklyn, N.Y.
[9] For the preparation of films, an area on a planchet, circumscribed by a fine groove, is somewhat less convenient than the 2-in., cupped planchet employed for the counting of tritium only [1]. However, the curved edge of the cupped planchet causes a somewhat uneven distribution of the material. Although unimportant in the counting of tritium, this irregularity in distribution is undesirable in films containing carbon-14, which is counted from *less* than infinite thickness. In the counting of carbon-14 alone, or of carbon-14 and tritium together, the planchets described here should be used.
[10] Supplied by Hastings & Co., Inc., Philadelphia, Pa.
[11] Rinsing the planchet with water or other solvent impairs the effectiveness of the treatment.
[12] Because of the high viscosity of the CMC stock solution, extreme care must be taken to obtain a homogeneous solution with the radioactive material.

this radioactive solution (about 200 mg) was carefully spread over the inscribed circle of each of several planchets, cleaned as described above. (These weights are most conveniently determined from the weights of a 200-*lambda* pipet, first, filled with the solution, and then, emptied.) Each planchet was covered with an inverted, 6-in. Petri dish [13] and allowed to stand at room temperature overnight. The slow evaporation of the solvent left a uniform film, which was heated under an infrared light for 30 min. It was then conditioned by storing it for at least 1 hr in a desiccator over a saturated solution of potassium acetate (in contact with solid potassium acetate). Any planchet in which the edges of the film deviated from the circumscribed area was discarded.

After being conditioned, the films were counted in the windowless, proportional counter operated at 2,000 v. The counter was flushed with the counting gas for 30 sec at the start, and for 10 sec between the counting periods. After a preliminary counting period of 1 min, which was disregarded, the activity of the sample was counted, for 3 periods of 100 sec or longer, to give a total count of at least 10,000. If the counting rates for the several periods changed progressively, the film was reconditioned by storing it for 1 hr or longer over the saturated potassium acetate; it was then re-counted. The counts were corrected for background (determined by counting a film which had been prepared in the usual manner but which contained no added radioactive material).

2.5. Determination of Counting-Efficiencies

By means of empirical calibrations of counting-efficiencies, it is possible to calculate the absolute activity of carbon-14 from the count given by a film of known weight. Figure 2 and table 1 show experimentally determined relationships between the counting-efficiency for carbon-14 (i.e., cps/dps) and the weight of the film under the various conditions employed in this laboratory. Each point was determined by counting 5 films, of known weight, each containing a known amount of carbon-14. The films were prepared, as described in section 2.4, from weighed amounts of a radioactive solution containing known amounts of solids per gram. Each planchet was counted by three different methods. The counting-efficiencies of curve I (E_m) were determined with the windowless, gas-flow, proportional counter; those of curve II (E'_m) were determined in the same manner, with the film covered by the Mylar screen of figure 1; those of curve III (E''_m) were determined with the thin-window, Geiger-Müller tube. For routine analyses, a reference table of values of E_m, E'_m, and E_m/E'_m was prepared from the curves, for use with films of various thicknesses (see table 2). Having once been determined, the values for counting-efficiencies can be used until a change is made in the equipment or procedure. It is advisable to determine counting-efficiencies by the several methods *with the same films*. The ratio E_m/E'_m for a given film-thickness is then independent of the absolute activity in the film.

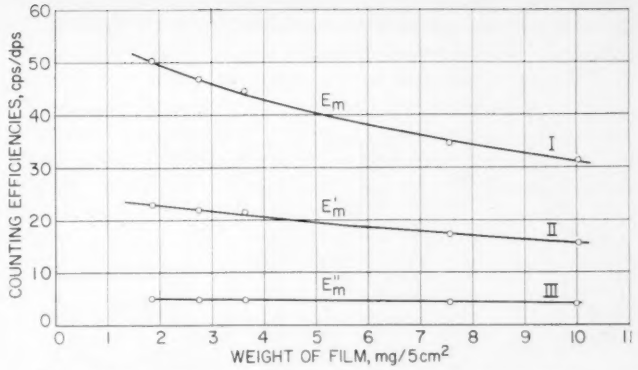

FIGURE 2. *Counting efficiencies for carbon-14 in films.*

I. Film without screen.
II. Film covered with aluminized Mylar screen.
III. Film counted with a thin-window, "pancake-type" Geiger-Müller tube.

2.6. Determination of Carbon-14

The absolute activity of the carbon-14 in a film is given by the equation,

$$x = \frac{a}{37{,}000\, E_m}, \qquad (1)$$

where x is the activity in microcuries, a is the observed counts per second (cps), and E_m is the appro-

[13] Controlled evaporation is necessary in order to obtain uniform films. When the planchets were allowed to stand in the open air, the films that formed were thicker in the middle than at the edges; and when the planchets were rather closely covered (with small Petri dishes), the films were thicker at the edges than in the middle. In contrast, the films that formed under the 6-in. Petri dishes were of nearly uniform thickness.

TABLE 1. *Counting rates of carbon-14 in CMC films*

Weight of solution [a]	Activity		Weight of film [b] (m)	Count without screen			Count with screen			E_m/E'_m
				Observed count [c] (a)	Standard deviation [d]	Counting efficiency (E_m)	Observed count [c] (a')	Standard deviation [d]	Counting efficiency (E'_m)	
mg	$\mu c \times 10^3$	*dps*	*mg*	*cps*	%	*cps/dps*	*cps*	%	*cps/dps*	
100.4	3.851	142.5	1.84	71.7	±2.0	0.5032	32.2	±0.4	0.2259	2.23
150.6	5.777	213.7	2.75	99.8	0.7	.4670	45.7	.7	.2138	2.18
198.6	7.618	281.9	3.63	125.2	2.0	.4441	58.6	.7	.2079	2.14
154.4 [e]	5.738	212.3	7.57	73.5	1.5	.3462	35.7	.8	.1682	2.06
200.6 [e]	7.454	275.8	9.84	85.2	0.9	.3089	42.2	.2	.1530	2.02

[a] The radioactive solution was prepared by mixing 200.1 mg of an aqueous solution of D-glucose-1-C^{14} having an activity of 0.964 μc with sufficient CMC stock solution to give a total weight of 25.130 g. The film from 1 g of this solution weighed 18.29 mg and contained 0.003836 μc.

[b] Each film had an area of 5 cm^2.

[c] Average of 5 films at each thickness.

[d] $\sqrt{\Sigma d^2/(n-1)}$, where d^2 is the square of the deviation from the mean and n is the number of films counted. Results expressed as percent of count.

[e] D-Glucose was added to the radioactive CMC solution. The film from 1 g of the resulting solution weighed 49.05 mg and contained 0.003716 μc.

TABLE 2. *Typical counting-efficiencies for carbon-14 in films, under the conditions described*[a]

m	E_m	E'_m	E_m/E'_m
mg			
3.0	0.461	0.214	2.15
3.1	.457	.213	2.15
3.2	.454	.212	2.14
3.3	.450	.211	2.13
3.4	.447	.210	2.13
3.5	.444	.209	2.12
3.6	.441	.208	2.12
3.7	.438	.207	2.12
3.8	.435	.206	2.11
3.9	.432	.205	2.11
4.0	.429	.204	2.10
4.1	.426	.203	2.10
4.2	.424	.202	2.10
4.3	.421	.201	2.09
4.4	.418	.200	2.09
4.5	.415	.199	2.09
4.6	.413	.198	2.09
4.7	.410	.197	2.08
4.8	.408	.196	2.08
4.9	.405	.195	2.08
5.0	.403	.194	2.08

[a] Table derived from data such as that of table 1 and fig. 2 in the range of film thickness most commonly used for the analysis of carbon-14 and tritium in mixtures.

priate counting-efficiency. If the Geiger-Müller tube is used, the absolute activity of the carbon-14 is likewise calculated from eq (1), but with values for E_m''. There is little difference in the precision of the two methods, but the windowless counter is preferable because it is more sensitive.

2.7. Determination of Carbon-14 and Tritium in the Same Sample

In a previous paper, it was shown that the absolute activity of tritium in an "infinitely thick" film may be calculated from the equation,

$$y=mka, \tag{2}$$

where y is the activity in microcuries, m is the weight of the film in milligrams, a is the counts per second measured with the windowless proportional counter, and k is an empirical constant determined with labeled material of known tritium-content. The factor k, for use with the 5-cm² area of the planchet, was determined by the method previously reported. With the equipment used in this study, $k=1.94\times10^{-4}$ (with a standard deviation of $\pm1.6\%$).[14]

When *both* carbon-14 and tritium are present in the sample, the films are counted in the windowless, proportional counter and are then re-counted after insertion of the Mylar screen (which entirely stops the radiation from tritium but permits passage of a fraction of that from carbon-14). Carbon-14 is then calculated from the equation,

$$x=\frac{a'}{37{,}000\,E'_m}, \tag{3}$$

in which a' is the observed count with the screen in place, and E'_m is the appropriate counting-efficiency. The activity of the tritium present is calculated by the following equation, in which allowance is made for the radiation from carbon-14,

$$y=mk[a-a'E_m/E'_m]. \tag{4}$$

In order to determine the accuracy of the method, a mixture of carbon-14- and tritium-labeled compounds, each of known radioactivity, was analyzed; the results are summarized in table 3. The average amounts of carbon-14 and tritium found differed from the known amounts present by 0.70 percent and 1.65 percent, respectively. The results for thin films and for excessively thick films were less satisfactory than those cited in table 3.

3. Comments on the Film-Counting Method

Although the *comparative* counting of carbon-14 in thin layers has long been an accepted and useful technique, general application of the method has not been satisfactory because of uncertainties regarding the thickness of the sample (see ref. [3], p. 29). *Agglomeration* or *crystallization* of materials on the planchet leads to unpredictable variations in the count. The technique described here for the preparation of films has several unique features: (a) The process described for cleaning the planchet produces a surface on which the aqueous solution spreads readily; (b) the use of a thickening agent tends to inhibit crystallization on the planchet; (c) the added coloring matter enables the uniformity of the film to be judged readily; (d) controlled evaporation affords a uniform film; (e) conditioning of the film after drying avoids difficulty (that is otherwise occasionally encountered) with electrostatic charges on the planchet; (f) the presence of "ballast material" in the film makes possible the counting of even highly radioactive materials in films of known

[14] Nine films, infinitely thick with respect to the radiation of tritium, and containing 0.01401 μc of tritium per milligram of solids, gave an average count of 72.3 cps. The standard deviation was ±1.09 cps or ±1.6 percent.

TABLE 3. *Analysis of a mixture containing known amounts of carbon-14 and tritium* [a]

Weight of film (m)	C^{14} content	Tritium content	Count without screen (a)	Count with screen (a')	E'_m [b]	E_m/E'_m [b]	k [c]	C^{14} found [d]	Diff. from known	Tritium found [e]	Diff. from known
mg	$\mu c\times10^3$	$\mu c\times10^2$	*cps*	*cps*				$\mu c\times10^3$	%	$\mu c\times10^2$	%
4.50	7.16	5.47	171.0	52.3	0.199	2.09	1.94×10^{-4}	7.10 [f]	−0.8	5.39 [g]	−1.5

[a] Average of results for 7 films.
[b] Value taken from table 2.
[c] See p. 366 and footnote 14.
[d] Calculated by eq (3), p. 366, from a' and E'_m.
[e] Calculated by eq (4), p. 366, from m, a, a', E_m/E'_m, and k.
[f] The standard deviation was ±1.7 percent.
[g] The standard deviation was ±3.5 percent.

thickness. In the range of thickness from 0.4 to 1 mg/cm², good reproducibility and uniformity of the film are readily achieved; whereas, in the extremely thin layers necessary for counting highly radioactive substances *alone*, uncertainties as to film thickness and uniformity are relatively great. With the equipment used, the film-counting method is adequate for determining less than 0.001 μc of carbon-14 or 0.005 μc of tritium.

Hendler [11] has developed, for carbon-14, a linear relationship between an "absorption correction factor" and the weight of the film. Hendler's relationship is useful for correcting counts, observed at one film-weight, to comparable counts at a desired (reference) film-weight; it also provides an excellent means for detecting errors in the measurement of counting-efficiency by means of the deviation from a linear relationship. The data presented here are in accord with Hendler's relationship. However, for routine analyses, the *direct* use of counting-efficiencies is adequate and convenient.

TABLE 4. *Decrease of tritium with time* [a]

Time	Activity remaining	Time	Activity remaining	Time	Activity remaining
Days	%	*Days*	%	*Days*	%
0	100.0	250	96.20	500	92.55
10	99.85	260	96.06	510	92.41
20	99.69	270	95.91	520	92.27
30	99.54	280	95.76	530	92.13
40	99.38	290	95.61	540	91.98
50	99.23	300	95.46	550	91.84
60	99.08	310	95.32	560	91.70
70	98.92	320	95.17	570	91.56
80	98.77	330	95.02	580	91.42
90	98.62	340	94.88	590	91.27
100	98.46	350	94.73	600	91.13
110	98.31	360	94.58	610	90.99
120	98.16	370	94.43	620	90.85
130	98.01	380	94.29	630	90.71
140	97.86	390	94.14	640	90.57
150	97.71	400	94.00	650	90.43
160	97.56	410	93.85	660	90.29
170	97.40	420	93.71	670	90.15
180	97.25	430	93.56	680	90.01
190	97.10	440	93.42	690	89.87
200	96.95	450	93.27	700	89.73
210	96.80	460	93.13	710	89.59
220	96.65	470	92.98	720	89.46
230	96.50	480	92.84	730	89.32
240	96.35	490	92.70		

[a] Based on a half-life of 12.262 yr [7] and the fundamental decay law:

$$\ln N/N_0 = -\lambda t.$$

(See for example p. 16 of ref. [12].)

The authors are grateful to Ruth Ann Peterson for valuable assistance in part of the experimental work reported here.

4. References

[1] H. S. Isbell, H. L. Frush, and R. A. Peterson, J. Research NBS **63A,** 171 (1959).
[2] C. C. McCready, Nature **181,** 1406 (1958). See also, H. Campbell, H. A. Glastonbury, and M. D. Stevenson, Nature **182,** 1100 (1958).
[3] M. Calvin, C. Heidelberger, J. C. Reid, B. M. Tolbert, and P. F. Yankwich, Isotopic carbon (J. Wiley & Sons, Inc., New York, N.Y., 1949).
[4] J. Rydberg, Acta Chem. Scand. **12,** 399 (1958).
[5] W. B. Mann and H. H. Seliger, Preparation, maintenance, and application of standards of radioactivity, NBS Circ. 594, p. 28 (1958).
[6] A. Schwebel, H. S. Isbell, and J. D. Moyer, J. Research NBS **53,** 221 (1954) RP2537.
[7] W. M. Jones, Phys. Rev. **100,** 124 (1955).
[8] H. S. Isbell, J. V. Karabinos, H. L. Frush, N. B. Holt, A. Schwebel, and T. T. Galkowski, J. Research NBS **48,** 163 (1952) RP2301.
[9] H. S. Isbell, H. L. Frush, and N. B. Holt, J. Research NBS **64A,** 135 (1960).
[10] H. S. Isbell and J. D. Moyer, J. Research NBS **63A,** 177 (1959).
[11] R. W. Hendler, Science **130,** 772 (1959).
[12] M. D. Kamen, Isotopic tracers in biology, 3d edition (Academic Press Inc., New York, N.Y., 1957).

WASHINGTON, D.C. (Paper 64A4–61)

Publications of the National Bureau of Standards*

Selected Abstracts

Non-self-adjoint boundary value problems in ordinary differential equations, W. Greub and W. C. Rheinboldt, *J. Research NBS* **64B,** *No. 2, 83 (1960).*

It is shown that the theory of non-self-adjoint linear ordinary differential equations can be simplified and unified, if, instead of specifying linear boundary conditions in the conventional way, one merely specifies the linear subspace determined by the boundary conditions. If this is done, the corresponding linear space of the adjoint problem is the orthogonal complement of the original space with respect to the scalar product defined by the right-hand side of Green's boundary formula.

Half-round inductive obstacles in rectangular waveguide, D. M. Kerns, *J. Research NBS* **64B,** *No. 2, 113 (1960).*

Formulas are derived for the accurate calculation of the lowest-mode, lumped-element representation of perfectly conducting half-round inductive obstacles in rectangular waveguide. These obstacles consist of either one or two opposed semicircular cylindrical indentations extending across the narrow sides of the waveguide. They seem especially suitable for use as precise calculable standards of reflection or impedance in waveguide. Using essentially well-known methods, the desired parameters are expressed as functionals of the unknown obstacle currents, which are determined by integral equations. Explicit formulas are obtained for the values of the parameters under the assumption of n-term Fourier sine-series expansions for the obstacle currents; rapid convergence is indicated by numerical evaluations for $n=1$, 2, and 3. In the process of obtaining expressions suitable for numerical calculation, an expansion (believed to be new) of the Green's function of the problem is obtained and the sums of certain infinite series of Bessel's functions occurring in this expansion are expressed in terms of definite integrals. A brief numerical table of these sums, sufficient for the evaluation of the $n=1$ approximation, is included.

Relation of turbulence theory to ionspheric scatter propagation experiments, A. D. Wheelon, *J. Research NBS* **64D,** *No. 4, 301 (1960).*

This paper attempts to relate turbulence theories to radio measurements on VHF ionospheric forward scatter circuits. To this end, the single scattering description of the electromagnetic response of electron density irregularities and the corresponding transmission expression are evaluated. Statistical distributions of signal levels are found to agree with a scattering model. The several theories for turbulent mixing of the electron density are then summarized. A turbulence mixing model is compared favorably with experimental data on absolute signal levels and their diurnal and seasonal variations. Scattering heights in the ionosphere responsible for the signals are also consistent with these theories. Frequency and distance dependence scaling laws are compared briefly with the data. The scatter signal behavior during sudden ionospheric disturbances is also explained. No attempt is made to compare meteoric and turbulence scatter contributions to the measured quantities in this paper. Approximately 30 references are given.

Propagation of oblique incidence over cylindrical obstacles, M. P. Bachynski, *J. Research NBS* **64D,** *No. 4, 311 (1960).*

Investigations of propagation of short electromagnetic waves at oblique incidence over smooth, perfectly conducting cylindrical obstacles are described. It is shown that the effect of oblique incidence can be considered as a change in the effective radius of curvature of the diffracting obstacle. The power in the shadow region of a cylindrical obstacle decreases with angle of obliqueness for horizontally polarized waves and can decrease, remain constant, or increase with angle of obliqueness for vertically polarized waves depending on the geometry of the propagation link. In all cases, vertical polarization gives a stronger field in the shadow region than horizontal polarization. In addition, it is shown that the diffracted field behind an obstruction of uniform radius of curvature is the same as that behind an obstacle of uniformly varying radius of curvature, provided the effective radius is the same.

Diffraction by smooth conical obstacles, H. E. J. Neugebauer and M. P. Bachynski, *J. Research NBS* **64D**, *No. 4, 317 (1960)*

Expressions obtained earlier for the calculation of diffraction due to conducting obstacles with smooth cylindrical surfaces are generalized to oblique incidence and to surfaces of conical shape. The derivation is based on a generalized concept of the Green's function and on the use of corrective factors that take the same place as corrections introduced by other authors into the theory of diffraction by apertures. The final expressions for conical obstacles and oblique incidence are very similar to those for cylindrical obstacles. The results are compared with scale model measurements.

Mode theory and the propagation of ELF radio waves, J. R. Wait, *J. Research NBS* **64D,** *No. 4, 387 (1960).*

The mode theory of propagation of electromagnetic waves at extremely-low-frequencies (1.0 to 3,000 cps) is treated in this paper. Starting with the representation of the field as a sum of modes, approximate formulas are presented for the attenuation and phase constants. Certain alternate representations of the individual modes are mentioned. These are used as a basis for describing the physical behavior of the field at large distances from the source, particularly near the antipode of the source. At the shorter distances, where the range is comparable to the wavelength, the spherical-earth mode series is best transformed to a series involving cylindrical wave functions. This latter form is used to evaluate the near field behavior of the various field components. The effect of the earth's magnetic field is also evaluated using a quasi-longitudinal approximation. In general it is indicated that if the gyrofrequency is less than the effective value of the collision frequency, the presence of the earth's magnetic field may be neglected for ELF. When this condition is not met the attenuation may be increased somewhat. The influence of an inhomogeneous ionosphere is also briefly considered and finally, the propagation of ELF pulses are treated. It is suggested that certain observed characteristics of ELF waveforms may be attributed to the inclination of the current channel in the lightning discharge.

Half-wave cylindrical antenna in a dissipative medium: current and impedance, Ronold King and C. W. Harrison, *J. Research NBS* **64D,** *No. 4, 365 (1960).*

An integral equation for the distribution of current along a cylindrical antenna in a conducting dielectric is derived. It is shown that the boundary conditions for an antenna in such a medium are formally the same as for an antenna in free space. The equation is solved for the current I and the driving-point impedance Z by means of a technique that achieves sufficiently high accuracy in the leading terms of an iteration procedure so that the higher-order terms do not need to be evaluated. Moreover, these leading terms consist only of trigonometric functions with complex coefficients. The electromagnetic field in the infinite dissipative medium may be computed easily and in closed form since the current in the antenna is expressed in such simple terms.

A numerical analysis is made to determine the properties of an antenna with an electrical length of one-half wavelength

in the medium with conductivity σ and relative dielectric constant ϵ_r. Universal curves are given of $I/\sqrt{\epsilon_r}$ with $\sigma/\omega\epsilon_0\epsilon_r$ as the parameter and of $Z\sqrt{\epsilon_r}$ with $\sigma/\omega\epsilon_0\epsilon_r$ as the variable in the range $0 \leq \sigma/\omega\epsilon_0\epsilon_r \leq 0.4$. A table of numerical values of the impedance is given for media such as an isotropic ionosphere, dry salt, dry earth, wet earth, and lake water.

Quantum-mechanical calculation of the probability of an exchange reaction for constrained linear encounters, J. Mazur and R. J. Rubin, *J. Chem. Phys.* **31,** *No. 5, 1395 (1959).*

A numerical procedure suitable for use with a high-speed computing machine is developed for calculating the average quantum-mechanical probability of the exchange reaction BC+A→B+CA for constrained linear encounters at temperature T when BC is initially in its ground or first excited vibrational state. The average refers to the average over the relative momentum frequency distribution of collisions between BC and A at temperature T. The procedure, which involves the numerical solution of the time-dependent Schrödinger equation, is sufficiently general so that any three-atom potential energy surface may be used. Two sample calculations have been performed using a simple potential energy surface. The results of these quantum-mechanical calculations for the average probability of reaction are compared with the corresponding classical quantities which are obtained in an elementary fashion.

Monte Carlo calculations of gamma ray backscattering, M. J. Berger and D. J. Raso, *Radiation Research* **12,** *No. 1, 20 (1960).*

Monte Carlo calculations have been performed to determine the backscattering of gamma rays from semi-infinite media (hydrogen, water, concrete, iron, tin, and lead). Radiation with energies of 0.05, 0.1, 0.2, 0.5, 1.0, or 2.0 Mev was assumed to be incident isotropically or at angles of 0° (perpendicular incidence), 30°, 60°, or 90° (grazing incidence). 5,000 photon histories were followed for each case on an IBM 704 computer. The information obtained includes the number albedo and energy albedo and the energy spectrum and angular distribution of the reflected radiation.

On the diffraction of electromagnetic pulses by curved conducting surfaces, J. R. Wait and A. M. Conda, *Can. J. Phys.* **37,** *1384 (1959).*

Starting with the known steady state solutions for diffraction by a perfectly conducting convex surface, the corresponding transient responses are derived using Fourier-Laplace inversion. Explicit results are given for an incident wave which varies with time as a step function.

New wavelengths for some helium (He I) lines, W. C. Martin, *J. Opt. Soc. Am.* **50,** *No. 2, 174 (1960).*

New vacuum wavelengths for nine lines of He I in the near ultraviolet and visible regions are given. They were obtained by measurement relative to 5462.2707 A and 4359.5625 A of Hg^{198} I with an evacuated Fabry-Perot interferometer. Liquid-nitrogen cooled helium lamps were used. Interference fringes were obtained for the helium line 5017 A with spacers up to 50 mm in length. The wavelength of this line, which was used as a reference wavelength in some previous work on the Rydberg constant, is found to be 5017.0772 ± 0.0003 A (vac.) relative to the stated values for the two standards.

Geomagnetic effects of high-altitude nuclear explosions, A. G. McNish, *J. Geophys. Research* **64,** *No. 12, 2253 (1959).*

Two high-altitude nuclear explosions detonated near Johnston Island in August 1958 produced distinct geomagnetic effects at Honolulu, Palmyra Island, Fanning Island, Jarvis Island, and Apia. No other operating magnetic observatories exhibited discernible effects. The effects at the first four observatories are attributed to overhead currents caused by increased ionization of the atmosphere by gamma rays and their secondaries from the detonations. The effects at Apia are attributed to charged particles from the detonations and Compton electrons released from the air around the detonation.

Determination of piezoelectric properties as a function of pressure and temperature, J. E. McKinney and C. S. Bowyer, *J. Acoust. Soc. Am.* **32,** *No. 1, 56 (1960).*

Piezoelectric data on a mixed titanate system (82% $BaTiO_3$, 9.1% $CaTiO_3$, 3.6% $PbTiO_3$, and 4.4% TiO_2) was obtained from an apparatus intended to measure the dynamic compressibility of materials. The calibration constant of the apparatus involves the piezoelectric and dielectric constants of the ceramics used as transducers. The method is discussed and an operating equation for the apparatus derived. Piezoelectric and dielectric constants have been measured over a fairly extensive temperature and pressure range and an apparent phase transition observed near 5° C. This transition corresponds to that found in pure barium titanate, and might be due to imperfect mixing of the titanates that leaves a small amount of pure barium titanate present. The method described appears more sensitive for the detection of changes in crystal symmetry in such materials than either X-ray or dielectric measurements.

Line shape and *f* value in the OH $^2\Sigma^+ - {}^2\pi$ transition, T. Carrington, *J. Chem. Phys.* **31,** *No. 5, 1243 (1959).*

Line shape and f value in the ultraviolet transition $^2\Sigma^+ - {}^2\pi$ of OH have been studied by the curve of growth method, and rough direct measurements of line width have been made. The lines $Q_1 6$, $P_1 6$, $R_1 6$, $Q_{21} 6$, and $S_1 6$ fit a curve of growth indicating a collision broadening width of 0.02 ± 0.02 cm^{-1} at 2,600° K and 1 atm in flame gases of the approximate composition O_2 60%, H_2O 20% and CO_2 20%. For the $Q_1 6$ line, the f value is $(11.7 \pm 3) \times 10^{-4}$. This corresponds to a radiative lifetime for the free molecule of 5.5×10^{-7} sec, in excellent agreement with the earlier work of Oldenberg. Brief discussions are given of theoretical limitations on the use of the curve of growth, and of the qualitative factors to be considered in explaining the observed line width.

Experimental and theoretical investigation of the magnetic properties of iron oxide recording tape, E. D. Daniel and I. Levine, *J. Acoust. Soc. Am.* **32,** *No. 1, 1 (1960).*

Part A gives the results of remanent magnetization tests made under ordinary and anhysteretic conditions, and shows that the major anhysteretic properties of a recording tape can be expressed in terms of three easily measured constants. The design of the test equipment is discussed and test results are listed for 13 representative types of tape. Part B reviews some of the theories of fine particle magnets that can be applied to recording tape, and gives an extensive treatment of remanent magnetization based upon the Preisach diagram. Some aspects of the Preisach diagram treatment may be of interest to workers outside the magnetic recording field. The anhysteretic properties are important in hf biased recording and a second paper describes how these properties can be used to predict certain recording performance characteristics.

Determination of the recording performance of a tape from its magnetic properties, E. D. Daniel and I. Levine, *J. Acoust. Soc. Am.* **32,** *No. 2, 258 (1960).*

This is the second of two papers. The first (I) dealt with the general magnetic properties of recording tape. The present paper gives an analysis of hf-biased recording based upon the anhysteretic properties of the tape as specified in I. Calculations of performance are compared with the results of absolute measurements carried out on a conventional recording machine, and on large scale models. Satisfactory agreement is obtained when the theory is corrected to take into account a loss attributed largely to a dynamic form of demagnetization which takes place during recording. The corrected theory can be used to compare tape performance under a variety of operating conditions without reference to a particular test recorder. Attention is confined to recorded wavelengths which are large compared with coating thickness.

Departures from the Saha equation under varying conditions of Lyman continuous opacity, S. R. Pottasch and R. N. Thomas, *Astrophys. J.* **130,** *No. 3, 941 (1959).*

A general method for determining the departure from the Saha equation in a hydrogen atmosphere is presented. The usually stated, vague condition of "high opacity in the Lyman continuum" is not sufficient to insure LTE; departures from LTE may amount to several orders of magnitude even under this condition (fig. 2). For illustration, application of the method is made to an atmosphere of constant T_e and n_e (fig. 1) and to an approximate chromospheric model (fig. 3).

Vibration-rotation bands of ammonia. IV. The stretching fundamentals and associated bands near 3ν, W. S. Benedict, E. K. Plyler, and E. D. Tidwell, *J. Chem. Phys.* **32,** *No. 1, 32 (1960).*

High-resolution spectra of NH_3, yielding 1,800 lines between 3,060–3,580 cm^{-1}, are presented. Analysis of the μ_3 fundamental is complete through $J'=9$ and presents no unexpected features. Resolution of the K-substructure in the ν_1 fundamental shows that several perturbations are present. The most important of these, fnvolving a Fermi resonance with the parallel component on $2\nu_4$, and a Coriolis resonance with its perpendicular componet, are clarified. Lines in both components of $2\nu_4$ are identified through $J'=6$, and a strong Coriolis interaction between the $l=0$ and $l=2$ states is observed and discussed.

Electron impact studies of aromatic hydrocarbons, I. Benzene, napthalene, anthracene, and phenanthrene, M. E. Wacks and V. H. Dibeler, *J. Chem. Phys.* **31,** *No.* **6, 1557 (1959).**

A systematic survey of ionization-dissociation processes of fused-ring aromatic compounds is initiated. Mass spectra and appearance potentials of the singly and doubly charged molecule ions are reported.
The observed ionization potentials of benzene (9.38 ev), naphthalene (8.26 ev), anthracene (7.55 ev), and phenanthrene (8.03 ev) are compared with available spectroscopic data, with values obtained from molecular orbital calculations, and with other electron impact data. The empirical method of group equivalents is extended to the calculation of the ionization potentials of the fused-ring aromatic compounds.

Value of the Rydberg constant, W. C. Martin, *Phys. Rev.* **116,** *No. 3, 654 (1959).*

The spectroscopic measurements of Houston and of Chu pertinent to the Rydberg constant have been adjusted to a new wavelength value (5015.6779$\pm$0.0003A in air) for the helium line used as a standard by them. This new wavelength, based primarily on recent measurements by the author and by Series and Field, replaces the value 5015.675A accepted by Houston and Chu. The adjustment brings their data into good agreement with spectroscopic observations relative to the cadmium primary standard made by Drinkwater, Richardson, and Williams. Cohen's conclusion in 1952 that the disagreement of Houston's and Chu's results with those of Drinkwater, Richardson, and Williams was due to a discrepancy in the two standards is thus verified.
In addition, a reappraisal of the data of Chu and of Drinkwater, Richardson, and Williams has resulted in a treatment of their observations substantially different from that given by Cohen. The value of the Rydberg constant resulting from a weighted averaging of all the data, $R_\infty=109737.312\pm0.008$ cm^{-1}, is, however, in excellent agreement with the presently accepted value, 109737.311 ± 0.012 cm^{-1}, calculated by Cohen from the data of Drinkwater, Richardson, and Williams.

Confidence intervals for the expectation of a Poisson variable, E. L. Crow and R. S. Gardner, *Biometrika* **46,** *441 (1959).*

A table of "optimum" two-sided confidence intervals for the mean of a Poisson variable is presented for confidence coefficients 80, 90, 95, 99, and 99.9 percent and all values of the variable 0 through 300. The intervals are compared in length with other existing or possible systems of intervals for the Poisson mean. The method of calculation is stated, and an interesting property of Poisson probability sums useful in the calculation is derived.

Electron characteristic energy losses in some intermetallic compounds, B. Gauthe, *Phys. Rev.* **114,** *No. 5, 1265 (1959).*

Measurements have been made of the characteristic energy losses of 30-kev electrons in transmission through thin films of indium, indium antimonide, cadmium telluride, and zinc telluride; for comparison, the electron energy losses in antimony, cadmium, tellurium, and zinc have been reinvestigated. The energy loss spectra in these intermetallic compounds appear significantly different from a simple superposition or average of the energy loss spectra of the component metals. Some detailed interpretations of the characteristic energy losses in In and in InSb are suggested.

Adsorption, diffusion, and evaporation of carbon monoxide or tungsten, R. Klein, *J. Chem. Phys.* **31,** *No. 5, 1306 (1959).*

The surface migration, adsorption, and evaporation processes for carbon monoxide on tungsten have been examined with a field emission microscope operating at liquid helium temperature. Surface migration, both in the Van der Waals' layer and the chemisorbed layer, has been investigated. The desorption process is observed both visually and by consideration of the preexponential factor of the Fowler-Nordheim expression for the whole emitting point.

Studies of borate minerals. VI: Veatchite, J. R. Clark, M. E. Morse, A. Perloff, and G. Burley, *Am. Mineralogist* **44,** *No. 11–12, 1141 (1959).*

Veatchite is a hydrated strontium borate originally described by Switzer (1938). In the present study X-ray precession patterns have been correlated with crystal habit and indices of refraction to yield the following data: monoclinic, space group $A2/a-C_{2h}^6$ (or less likely, $Aa-C_s^4$), $a=20.81\pm0.04$, $b=11.74\pm0.03$, $c=6.63_7\pm0.02$ Å, $\beta=92°02'\pm05'$, $V=1620$ Å^3; dominant forms {100}, {111}, {h11} with $h=2, 3, 4$; cleavage perfect parallel to (100) and (011); optical orientation $Z=b$, $X=c$, $Y\wedge a=-2°$. Previous chemical analyses considered together with the present crystallographic data show that the correct formula is $SrO{\cdot}3B_2O_3{\cdot}2H_2O$, one of two possibilities proposed by Switzer and Brannock (1950). For eight [$SrO{\cdot}3B_2O_2{\cdot}2H_2O$] per cell, the calculated density is 2.86 g.cm.$^{-3}$; an observed density of 2.78 ± 0.03 g.cm.$^{-3}$ was obtained on the Berman balance for a 2.4 mg. sample of excellent single crystals. X-ray powder pattern data are given with calculated interplanar spacings for $d\geq2.300$ A.

The adhesion of electrodeposited nickel to chromium at elevated temperatures, W. E. Reid, Jr., and F. Ogburn, *J. Electrochem. Soc.* **107,** *No. 2, 91 (1960).*

The use of a composite coating of electrodeposited nickel and chromium to protect molybdenum from oxidation at elevated temperatures has certain practical limitations. Examination of the composite coating showed that the problems of blister formation, weakening of the bond between nickel and chromium, and edge separation were interrelated. Blisted formation was eliminated and edge separation reduced slightly by an improved treatment of the chromium surface prior to nickel plating. The weakening of the bond between nickel and chromium appears to be inherent to the coating system.

Chloride content of the diffusion layer at a silver anode, P. A. Krasley, *J. Electrochem. Soc.* **107,** *No. 2, 139 (1960).*

The depletion of chloride in the diffusion layer of a silver electrode was investigated. A microporous silver electrode was used, and the diffusion layer was drawn off through the pores of the electrode. The maximum reduction of chloride ion obtained was about 80 percent.

Chemical structure and stability relationships in polymers, B. G. Achhammer, M. Tryon, and G. M. Kline, *Kunststoffe Combined with German Plastics Digest* **49,** *No. 11, 600 (1959)*; *Modern Plastics* **37,** *No. 4, 131 (1959).*

Stability of polymers is usually considered in terms of a material's ability to withstand specified conditions and still retain the physical properties required for use of the material in a given application. Admitting that the retention of desired physical properties is a matter of practical concern, it is necessary to recognize the basic problem in stability of polymers as being degradation of a chemical structure involving environment and available energy. Resultant changes in chemical structure then determine the material's physical properties.

On the convergence of the Rayleigh quotient iteration for the computation of characteristic roots and vectors, VI. (Usual Rayleigh quotient for nonlinear elementary divisors), A. M. Ostrowski, *Arch. Rat. Mech. Anal.* **4,** *No. 2, 153 (1959).*

In this paper the classical Rayleigh quotient iteration is discussed for eigenvalues with nonlinear elementary divisors. The convergence of the method is only then satisfactory, if it is combined with the accelerating methods of Steffensen and Householder, but in this last case it turns out to be at least as good as the method of the generalized Rayleigh quotient.

The weighted compounding of two independent significance tests, M. Zelen and L. S. Joel, *Ann. Math. Stat.* **30,** *No. 4, 885 (1959).*

Suppose an experimenter wishes to combine the results of two independent statistical tests made on the same null hypothesis into a single combined test. The tests may have arisen from several sets of independent data or from independent tests made on the same data. Often it is difficult to pool the data from both tests and resort must be made to combining the tests themselves.
The object of this paper is to discuss a proposed test for combining two such independent tests, each based on the variance-ratio or F-distribution. A method for combining the two tests is proposed which weights one test relative to the other.

Sauter theory of the photoelectric effect, U. Fano, K. W. McVoy, and J. R. Albers, *Phys. Rev.* **116,** *No. 5, 1147 (1959).*

Results of Sauter are expressed in the form of a transition matrix which determines the photoelectric effect cross section for arbitrary X-ray polarization and arbitrary initial and final orientations of the electron spin. The structure of the matrix elements accounts for curious properties of the cross section in terms of interference between orbital and spin currents. Expansion of the wave functions into powers of $Z/137$ simplifies the calculation of the transition matrix, reduces it to a special case of the bremsstrahlung theory in Born approximation, and explains discrepancies between results of earlier calculations. Analytical and graphical data are given on the photoemission of polarized electrons by circularly polarized X-rays.

High-frequency limit of bremsstrahlung in the Sauter approximation, U. Fano, *Phys. Rev.* **116,** *No. 5, 1156 (1959).*

The expansion in powers of $Z/137$ utilized in the Sauter theory of the photoelectric effect yields a nonzero cross section proportional to Z^3 at the high-frequency limit of the bremsstrahlung spectrum, and also at the low electron energy limit of the pair production spectrum. These cross sections are related to the Sauter photoelectric cross section by detailed balancing. The results apply equally when the effects of spin orientations and X-ray polarization are considered.

Interference of orbital and spin currents on bremsstrahlung and photoelectric effect, U. Fano, K. W. McVoy, and J. R. Albers, *Phys. Rev.* **116,** *No. 5, 1159 (1959).*

The matrix elements of the Born approximation theory of bremsstrahlung are resolved into sums of terms classified according to whether the radiation interacts with orbital or with spin currents and on the basis of additional spin effects which result from electron motion before and after the emission. Observable features of angular distribution, X-ray polarization, and spin orientation can be interpreted as effects of interference between the separate terms. The results are applicable to corresponding features of the photoelectric effect.

Bremsstrahlung and the photoelectric effect as inverse processes, K. W. McVoy, and U. Fano, *Phys. Rev.* **116,** *No. 5, 1168 (1959).*

The bremsstrahlung matrix element at the short-wavelength limit of the spectrum is calculated to lowest order in $a \equiv Z/137$, for an unscreened Coulomb field. The result, valid for relativistic incoming electrons, is shown to be exactly $\alpha^{-1}m^{-\frac{1}{2}}$ times the complex conjugate of Sauter's relativistic matrix element for the K-shell photoelectric effect. These matrix elements are the leading terms in an expansion of the exact matrix elements in powers of α, and they are found to be derivable from the first two terms of the expansions in powers of α of the electron wave functions. In this sense their structure is completely analogous to that of the Bethe-Heitler bremsstrahlung matrix element.
This simple relation between the matrix elements derives from an approximate equality (through first order in α between the Coulomb wave functions for bound and zero-momentum continuum states, which can be understood as due to the neglect of the Coulomb binding energy, a second-order quantity in α.
Finally, the range of validity of Sauter's approximation is examined in detail. The lower bound of this (energy) range is found to be simply related to the radius of convergence of the expansion of the photoeffect matrix element in powers of α.

Balmer decrements: the diffuse nebulae, S. R. Pottasch, *Astrophys. J.* **131,** *No. 1, 202 (1960).*

The possibility that diffuse nebulae may have a total optical depth of the order of unity is considered. The Balmer decrement is found as a function of the total optical depth of a plane atmosphere in $H\alpha$, assuming that the atmosphere has a constant temperature and density (less than 10^5 electrons/cm^3) and is optically thick to Lyman line radiation. It is found that the $H\alpha/H\beta$ ratio increases with increasing optical depth in $H\alpha$.
The observations of $H\alpha/H\beta$ in diffuse nebulae are high enough as to make any other interpretation beside that of optical thickness in $H\alpha$, appear doubtful.

Fusion of polymer networks formed from linear polyethylene: Effect of intermolecular order, L. Mandelkern, D. E. Roberts, J. C. Halpin, and F. P. Price, *J. Am. Chem. Soc.* **82,** *46 (1960).*

Specimens of linear polyethylene have been crosslinked at a variety of temperatures both above and below the melting point by either high energy electrons or by Co^{60} γ-rays. The melting points and the specific volume-temperature behavior of these specimens have been examined as functions of radiation dose and irradiation temperature. In general, the two types of radiation give the same results. Both the melting point depression and the reduction in crystallinity are more sensitive to radiation dose when the irradition is carried out above the melting temperature than when it is performed below this temperature. The observed effects are explicable in terms of a recent theory of Flory which envisages that the configurational entropy of an amorphous polymer network is sensitive to the degree of order present when the crosslinks were introduced. These considerations lead to the conclusion that intermolecular order present in a highly crystalline polymer is maintained to some degree in the melt, if the crosslinks are introduced in the crystalline state. Consequently the melting temperatures of networks formed in this manner are significantly higher than those of networks formed when randomly arrayed chains. Furthermore, it was found that the melting temperatures of both types of networks, when immersed in a large excess of liquid, are depressed in accordance with the well-known melting point relation, provided cognizance is taken of the amount of liquid imbibed.

Electrophoretic deposition of metals, metalloids, and refractory oxides, V. A. Lamb and W. R. Reid, *Plating* **47,** *No. 3, 291 (1960).*

Operating conditions are defined for electrophoretically depositing a number of metals, metalloids, and refractory oxides. Conversion of the deposits to practical coatings requires treatments such as chemical reduction and sintering. Further development of the latter steps is necessary before practical coatings can be achieved. Coatings of titanium-nickel alloys on steel may warrant further investigation.

Relative measurement of the photodetachment cross section for H^-, S. J. Smith and D. S. Burch, *Phys. Rev.* **116,** *No. 5, 1125 (1959).*

The spectral dependence of the photodetachment cross section for the negative ion of atomic hydrogen has been measured in the range from 4,000 Å to 13,000 Å with approximately 300 Å resolution. Measurements were made with 25 band pass filters, each measurement taken relative to the value obtained with a control filter at 5,280 Å. A probable error of about 2 percent is attached to the relative value obtained for each filter. The results are in significant disagreement with available calculated cross sections.

Isotope exchange processes in solid nitrogen under electron bombardment, R. Klein and E. M. Horl, *J. Chem. Phys.* **32,** *No. 1, 307 (1960).*

Investigations were carried out on the isotope exchange in solid nitrogen layers during electron bombardment at 4° and 20° K with mixtures of $N^{14}N^{14}$ and $N^{15}N^{15}$ molecules. The samples were analyzed after bombardment for their $N^{14}N^{15}$ content, and the yield per 100 ev in terms of the number of $N^{14}N^{15}$ molecules produced (G value) measured. For undiluted nitrogen at 4.2° K, a value of the order of 0.2 was obtained. A discussion of the elementary processes involved in the exchange is presented.

Theory of flame propagation in solid nitrogen at low temperatures, S. G. Reed and C. M. Herzfeld, *J. Chem. Phys.* **32,** *No. 1, 1 (1960).*

A theory for a flame in a solid whose speed is controlled by diffusion of radicals and heat is applied to slowly propagating flashes observed in solid nitrogen deposited at 4° K from a microwave discharge. Reasonable agreement is obtained with observed speeds.

Use of the equation of hydrostatic equilibrium in determining the temperature distribution in the outer solar atmosphere, S. R. Pottasch, *Astrophys. J.* **131,** *No. 1, 68 (1960).*

The temperature distribution from 1.0043 (3,000 km) to 20 solar radii in the sun's atmosphere is computed from the observed density distribution in this region and the assumption of hydrostatic equilibrium. The temperature distribution shows a maximum between 1.1 and 3 solar radii and a decrease in temperature thereafter. This decrease in temperature is consistent with Chapman's suggestion of thermal conduction only if loss of energy by radiation is included. Inclusion of a radiative energy loss also is shown to invalidate Parker's argument against hydrostatic equilibrium out to large distances from the sun.

Apparent temperatures measured at melting points of some metal oxides in a solar furnace, J. J. Diamond and S. J. Schneider, *J. Am. Ceram. Soc.* **43,** *No. 1, 1 (1960).*

Six metal oxides (Al_2O_3, TiO_2, Nb_2O_5, Ta_2O_5, La_2O_3 and Dy_2O_3) were melted in a solar furnace and the apparent temperatures at their melting points measured by means of a conventional optical pyrometer. The apparent temperatures of three of them (Al_2O_3, TiO_2 and Nb_2O_5) were 2,025°, 1,840°, and 1,497° C, respectively, in close agreement with the melting points as determined by other investigators using other methods. The apparent temperatures of the other three varied widely and bore no relation to their melting points. The method does not, therefore, have general utility for the measurement of unknown melting points.

Perovskite-type compounds in binary rare earth oxide systems, S. J. Schneider and R. S. Roth, *J. Am. Ceram. Soc.* **43,** *No. 2, 115 (1960).*

A survey was made of the solid state reactions that occur in equi-molar mixtures of oxides of the trivalent rare earth ions. It was determined that a perovskite-type compound of the form $A^{+3}B^{+3}O_3$ occurred as a stable phase only in the following binaries: $La_2O_3 = Er_2O_3$, $La_2O_3 = Tm_2O_3$, $La_2O_3 = UYb_2O_3$ and $La_2O_3 = Lu_2O_3$. A correlation between compound formation and tolerance factor was made.

Use of disodium *m*-benzenedisulfonate as a hardening agent in Watts nickel bath, W. H. Metzger, P. A. Krasley, and F. Ogburn, *Plating* **47,** *No. 3, 285 (1960).*

A request from the Bureau of Engraving and Printing for an electrodeposit of nickel that was harder and more free of stress than those currently obtained from a Watts bath operated at 5 amp/dm², 50° C, and *p*H 5.0 resulted in a recommendation for the use of disodium *m*-benzene-disulfonate as an addition agent. The electrodeposits made in the presence of this agent had the physical properties required by BEP for their new printing plates, while production conditions remained the same. The agent increases deposit hardness to a maximum of 350 VHN at a concentration of 0.3 g/l and above, under the operating conditions stated. The stress varies from 20,000 psi tensile to 5,000 psi compressive over a range of concentration of the additive from zero to 0.4 g/l. This agent causes hardness to vary inversely with *p*H in the range studied (*p*H 4.0–5.0). The relative stability of the agent appears unaffected by conventional purification procedures. Intercomparisons with two spiral contractometers and four coils show that, within the 10 percent experimental error, significant variations can be accounted for in the surface condition of the coils, the "stop-off" procedure inside the coil, and the mechanical differences between individual contractometers.

Some evidence for structural anomalies in pure cristobalite, R. F. Walker, S. J. Schneider, and R. S. Roth, *J. Am. Ceram. Soc.* **42,** *No. 12, 642 (1959).*

Some evidence is produced for the occurrence of structural anomalies in cristobalite of at least 99.998 percent purity. The anomalies were observed only in samples subjected to heat-treatment over a limited temperature range. In somewhat less pure material (about 99.8 percent) the anomalies could be detected in samples treated over a wider range of temperature. There appeared to be a definite connection between the structural anomalies and the "multiple peak" phenomenon encountered during differential thermal analysis of the samples. Some of the difficulties in attempting to rationalize the observations in terms of the cristobalite-tridymite relationships are discussed.

Other NBS Publications

Journal of Research, Section 64B, No. 2, April–June 1960. 75 cents.

Non-self-adjoint boundary value problems in ordinary differential equations. Werner Greub and Werner C. Rheinboldt. (See above abstract.)

Criteria for the existence and equioscillation of best Tchebycheff approximations. John R. Rice.

Note on the solution of Riccati's differential equation. H. Herbert Howe.

On a generalization of the index notation for absolute tensors of arbitrary order. Edmund H. Brown.

Upper and lower bounds for the center of flexure. Lawrence E. Payne.

Half-round inductive obstacles in rectangular waveguide. D. M. Kerns. (See above abstract.)

Journal of Research, Section 64D, No. 4, July-August 1960. 70 cents.

Relation of turbulence theory to ionospheric scatter propagation experiments. Albert D. Wheelon. (See above abstract.)

Propagation at oblique incidence over cylindrical obstacles. M. P. Bachynski. (See above abstract.)

Diffraction by smooth conical obstacles. H. E. J. Neugebauer and M. P. Bachynski. (See above abstract.)

Characteristics of 488 megacycles per second radio signal reflected from the moon. B. C. Blevis and J. H. Chapman.

The use of polarization fading of satellite signals to study the electron content and irregularities in the ionosphere. C. Gordon Little and Robert S. Lawrence.

Note on a test of the equivalence theorem for sporadic *E* propagation. J. W. Wright and T. N. Gautier.

Daytime attenuation rates in the very low frequency band using atmospherics. W. L. Taylor.

Measured electrical properties of snow and glacial ice. A. D. Watt and E. L. Maxwell.

Some extremely low frequency phenomena. E. T. Pierce.

Mode theory and the propagation of extremely low frequency radio waves. James R. Wait. (See above abstract.)

Studies of natural electric and magnetic fields. G. D. Garland and T. F. Webster.

Natural electromagnetic energy in frequencies below slow tail sferios band. Wallace H. Campbell.

Possible application of the system loss concept at extremely low frequencies. Kenneth A. Norton.

Measurements of the spectrum of radio noise from 50 to 100 cycles per second. M. Balser and C. A. Wagner.

Half-wave cylindrical antenna in a dissipative medium: current and impedance. Ronold King and Charles W. Harrison. (See above abstract.)

Standard X-ray diffraction powder patterns, H. E. Swanson, M. I. Cook, T. Isaacs, and E. H. Evans, NBS Circ. 539, Vol. 10 (1960) 40 cents.

Properties of high-temperature ceramics and cermets—Elasticity and density at room temperature, S. M. Lang, NBS Monograph 6 (1960) 20 cents.

Precise measurement of heat of combustion with a bomb calorimeter, R. S. Jessup, NBS Monograph 7 (1960) 25 cents.

Conductive flooring for hospital operating rooms, T. H. Boone, F. L. Hermach, E. H. MacArthur, and R. C. McAuliff, NBS Monograph 11 (1960) 20 cents.

Tabulation of data on receiving tubes, C. P. Marsden, W. J. Keery, and J. K. Moffitt, NBS Handb. 68 (1959) $1.00.

Survey of Central Radio Propagation Laboratory research in tropospheric propagation 1948–1956, J. W. Herbstreit and P. L. Rice, NBS Tech. Note 26 (PB151385) (1959) $4.00.

Distribution of incoming lettermail at the Baltimore, Maryland City Post Office, B. M. Levin and A. E. Newman, NBS Tech. Note 33 (PB151392) (1959) $2.50.

A multiplet table of astrophysical interest, C. E. Moore, NBS Tech. Note 36 (PB151395) (1959) $4.00.

Application of RF micropotentiometers for calibration of signal generators to 1,000 Mc, L. F. Behrent, NBS Tech. Note 37 (PB151396) (1960) 50 cents.

Design and construction of a liquid hydrogen temperature refrigeration system, D. B. Chelton, J. W. Dean, and B. W. Birmingham, NBS Tech. Note 38 (PB151397) (1960) 75 cents.

Helium refrigeration and liquefaction using a liquid hydrogen refrigerator for precooling, D. B. Chelton, J. W. Dean, and T. R. Strobridge, NBS Tech. Note 39 (PB151398) (1960) 50 cents.

Mean electron density variations of the quiet ionosphere I—March 1959, J. W. Wright and L. A. Fine, NBS Tech. Note 40–1 (PB151399–1) (1960) $1.25.

Mean electron density variations of the quiet ionosphere 2—April 1959, J. W. Wright and L. A. Fine, NBS Tech. Note 40–2 (PB151399–2) (1960) $1.25.

Expendable modules as bases for disposal-at-failure maintenance, R. O. Stone, P. Meissner, and K. M. Schwarz, NBS NBS Tech. Note 41 (PB151400) (1960) $2.25.

Identification of textile coatings by infrared spectroscopy, F. H. Forziati, R. T. Hite, and M. K. Wharton, Am. Dyestuff Reptr. **49,** No. 4, 29 (1960).

Propagation and production of electromagnetic waves in a plasma, R. Gallet, Nuovo Cimento Suppl. **13,** No. 1, 234 (1959).

Fading rate recorder for propagation research, J. W. Koch, W. B. Harding, and R. J. Jansen, Electronics **32,** No. 51, 78 (1959).

Matrix algebra for calculating multicomponent mixtures, F. Ordway, Portland Cement Assoc. J. Research and Develop. Labs. **2,** No. 1, 28 (1960).

Leonard Euler's integral: A historical profile of the gamma function, P. J. Davis, Am. Math. Mo. **66,** 849 (1959).

Gages for measuring the thickness of chromium on the internal surface of small-bore tubes, V. A. Lamb and P. A. Krasley, Plating **47,** No. 2, 176 (1960).

Characteristics of deposits, W. H. Metzger, Jr., Symp. Electroless Nickel Plating, ASTM Spec. Tech. Pub. **265,** p. 13 (1959). Turbulent motion, G. B. Schubauer and C. M. Tchen, Sec. B, Vol. V, Princeton Ser., High speed aerodynamics and jet propulsion, Turbulent flows and heat transfer, p. 75 (Princeton Univ. Press, Princeton, N.J., 1959).

Efficient harmonic generation, G. F. Montgomery, Proc. IRE **48,** No. 2, 251 (1960).

The ninth plenary assembly of the CCIR, J. W. Herbstreit, IRE Proc. **48,** 45 (1960).

Effect of fluorides on infrared transmittance of certain silicate glasses, G. W. Cleek and T. S. Scuderi, J. Am. Ceram. Soc. **42,** No. 12, 599 (1959).

Condltions at the ionization and shock fronts in collisions of gas clouds—Bright rims in diffuse nebulae, pt. VI, S. R. Pottasch, Rev. Modern Phys. **30,** No. 3, 1053 (1958).

Spectral emittance of ceramic-coated and uncoated specimens of Inconel and stainless steel, J. C. Richmond and J. E. Stewart, J. Am. Ceram. Soc. **42,** No. 12, 633 (1959).

Mismatch errors in cascade-connected variable attenuators, G. E. Schafer and A. Y. Rumfelt, IRE Trans. Microw. Theory Tech. **MTT-7,** No. 4, 447 (1959).

A study of 17–7 PH stainless steel, N. L. Carwile and S. J. Rosenberg, WADC Tech. Rept. 58–653 (1959) (available from the Office of Technical Services, Department of Commerce, Washington 25, D.C.).

High-altitude observation techniques, D. M. Gates, Letter Sci. **131,** 266 (1960).

The relation between confidence intervals and tests of significance—a teaching aid, M. G. Natrella, Am. Stat. **14,** No. 1, 20 (1960).

The effect of the earth's magnetic field on m.u.f. calculations, K. Davies, J. Atmospheric and Terrest. Phys. **16,** 187 (1959).

Surface area and exchange capacity relation in a Florida kaolinite, W. C. Ormsby and J. M. Shartsis, J. Am. Ceram. Soc. **43,** No. 1, 44 (1960).

Standard frequency transmission and time signals, W. D. George, Proc. 2d all-IRIG Symp., prepared by Secretariat, Inter-Range Instrumentation Group, Oct. 1958 (White Sands Missile Range, New Mexico) p. 141, IRIG Document No. 107–58 (1959).

Atomistic approach to the rheology of sand-water and clay-water mixtures, W. A. Weyl and W. C. Ormsby, Ch. 7, Vol. III Rheology—Theory and applications, Ed. by F. R. Eirich, p. 249 (Academic Press, New York, N.Y., 1960).

Diffusion of particles in turbulent flow, C. M. Tchen, Adv. Geophys. 6: Atmospheric diffusion and air pollution, p. 165, Proc. Symp. Oxford, England, Aug. 1958 (Academic Press Inc., New York, N.Y., 1959).

Atmospheric tides and ionospheric electrodynamics, M. L. White, J. Geophys. Research **65,** 153 (1960).

LaRecherche sur les radicaux libres au National Bureau of Standards, H. P. Broida, J. chim. phys. **56,** No. 2392, 813 (1959).

Are life testing procedures robust? M. Zelen and M. C. Dannemiller, Proc. 6th Natl. Symp. Reliability and Quality Control in Electron. Jan. 11–13, 1960, Inst. Radio Engrs. Inc., p. 185 (1960).

Reception of space diversity transmitters, J. W. Koch, Wireless World (England) **65,** No. 10, 512 (1959).

Improved NBS abrasive jet method for measuring abrasion resistance of coatings, A. G. Roberts, ASTM Bull. No. 244, 48 (TP52) (1960).

Flame-spread measurements by the radiant panel flame-spread method, D. Gross, Forest Products J. **X,** No. 1, 33 (1960).

Réactions en chaine de radicaux gelés, J. L. Jackson, J. chim. phys. **56,** No. 2392, 771 (1959).

Étude spectroscopique des produits de la decharge électrique dan L'Azote condensés a l'état solide à très basse temperature, prevues en faveur de l'existence d'Azote triatomique dans le solide, M. Peyron, E. M. Horl, H. W. Brown, and H. P. Brodia, J. chim. phys. **56,** No. 2392, 736 (1959).

What price accurate test methods? A. T. McPherson, ASTM Bull. (ACR Notes Column) No. 244, 7 (1960).

An analysis of time variations in tropospheric refractive index and apparent radio path length, M. C. Thompson, H. B. Janes, and A. W. Kirkpatrick, J. Geophys. Research **65,** 193 (1960).

Neutron detection by reactions induced in scintillators, C. O. Muehlhause, pt. I, Fast Neutron Physics, sec. III. B, p. 387 (Interscience Pub., New York, N.Y., 1960).

A relationship between the lower ionosphere and the [OI] 5577 nightglow emission, J. W. McCaulley and W. S. Hough, J. Geophys. Research **64,** No. 12, 2307 (1959).

Many changes reflected in new dry cell standard, W. J. Hamer, Mag. of Standards **31,** No. 3, 81 (1960).

Étude aux infrarouges de certains solides condensés à partir de decharges en phase gazeuse, K. B. Harvey and H. W. Brown, J. Chim. Phys. **56,** No. 2392, 745 (1959).

Water penetration testing machine for sole leather, T. J. Carter, J. Am. Leather Chemists, Assoc. **LV,** No. 3, 139 (1960).

A note regarding the mechanism of UHF propagation beyond the horizon, A. D. Watt, E. F. Florman, and R. W. Plush, Letter Proc. IRE **48,** 252 (1960).

A model of the F region above h_{max}F2, J. W. Wright, J. Geophys. Research **65,** 185 (1960).

Interference of antioxidant in the determination of low polymer in SBR synthetic rubber, L. T. Milliken and F. J. Linnig, J. Polymer Sci. **XLI,** No. 138, 544 (1959).

**Publications for which a price is indicated (except for NBS Technical Notes) are available only from the Superintendent of Documents, U.S. Government Printing Office, Washington 25, D.C. (foreign postage, one-fourth additional). Technical Notes are available only from the Office of Technical Services, U. S. Department of Commerce, Washington 25, D.C. (order by PB number). Reprints from outside journals and the NBS Journal of Research may often be obtained directly from the authors.*

UNITED STATES
GOVERNMENT PRINTING OFFICE
DIVISION OF PUBLIC DOCUMENTS
WASHINGTON 25, D.C.

OFFICIAL BUSINESS

PENALTY FOR PRIVATE USE TO AVOID PAYMENT OF POSTAGE, $300 (GPO)

JOURNAL OF RESEARCH of the National Bureau of Standards Vol. 64A, No. 4 July–August 1960
A. Physics and Chemistry

Contents

	Page
Gamma irradiation of hexafluorobenzene. R. E. Florin, L. A. Wall, and D. W. Brown.	269
Behavior of isolated disturbances superimposed on laminar flow in a rectangular pipe. Grover C. Sherlin.	281
Standard of spectral radiance for the region of 0.25 to 2.6 microns. Ralph Stair, Russell G. Johnston, and E. W. Halbach.	291
Photovoltaic effect produced in silicon solar cells by X- and gamma rays. Karl Scharf.	297
Phase equilibria in systems involving the rare-earth oxides. Part I. Polymorphism of the oxides of the trivalent rare-earth ions. R. S. Roth and S. J. Schneider.	309
Phase equilibria in systems involving the rare-earth oxides. Part II. Solid state reactions in trivalent rare-earth oxide systems. S. J. Schneider and R. S. Roth.	317
Some observations on the calcium aluminate carbonate hydrates. Elmer T. Carlson and Horace A. Berman.	333
Acid dissociation constant and related thermodynamic quantities for triethanolammonium ion in water from 0 to 50 °C. Roger G. Bates and Guy F. Allen.	343
Ionization constants of four dinitrophenols in water at 25 °C. Robert A. Robinson, Marion Maclean Davis, Maya Paabo, and Vincent E. Bower.	347
Dissociation constant of anisic (*p*-methoxybenzoic) acid in the system ethanol-water at 25 °C. Elizabeth E. Sager and Vincent E. Bower.	351
Preparation of sulfur of high purity. Thomas J. Murphy, W. Stanley Clabaugh, and Raleigh Gilchrist.	355
Tritium-labeled compounds IV. D-Glucose-*6-t*, D-xylose-*5-t*, and D-mannitol-*1-t*. Horace S. Isbell, Harriet L. Frush, and Joseph D. Moyer.	359
Tritium-labeled compounds V. Radioassay of both carbon-14 and tritium in films, with a proportional counter. Horace S. Isbell, Harriet L. Frush, and Nancy B. Holt.	363
Publications of the National Bureau of Standards.	369

For sale by the Superintendent of Documents, U.S. Government Printing Office, Washington 25, D.C. Price 70 cents (single copy)
Subscription price: $4.00 a year; $0.75 additional for foreign mailing.
UNITED STATES GOVERNMENT PRINTING OFFICE, WASHINGTON : 1960